Evolution of Coronal Mass Ejections through the Heliosphere

by

Ying Liu

Submitted to the Department of Physics
in partial fulfillment of the requirements for the degree of

Doctor of Philosophy

at the

MASSACHUSETTS INSTITUTE OF TECHNOLOGY

June 2007

Author .....
Department of Physics
May 21, 2007

Certified by .....
John W. Belcher
Professor of Physics
Thesis Supervisor

Certified by .....
John D. Richardson
Principal Research Scientist
Thesis Supervisor

Accepted by .....
Thomas J. Greytak
Associate Department Head for Education

Evolution of Coronal Mass Ejections through the Heliosphere

by

Ying Liu

Submitted to the Department of Physics
on May 21, 2007, in partial fulfillment of the
requirements for the degree of
Doctor of Philosophy

Abstract

This thesis studies the evolution of coronal mass ejections (CMEs) in the solar wind. We develop a new method to determine the magnetic field orientation of CMEs using Faraday rotation. A radio source occulted by a moving magnetic flux rope gives two basic Faraday rotation curves, consistent with Helios observations. The axial component of the magnetic field produces a gradient in the Faraday rotation pattern obtained from multiple radio sources along the flux rope, which allows us to determine the CME field orientation and helicity 2 - 3 days before CMEs reach the Earth. We discuss implementation of the method by the Mileura Widefield Array.

We present the first direct evidence that magnetic clouds (MCs) are highly flattened and curved due to their interaction with the ambient solar wind. The cross-sectional aspect ratio of MCs is estimated to be no smaller than 6 : 1. We offer a simple model to extract the radius of curvature of the cross section. Application of the model to observations shows that the cross section tends to be concave-outward at solar minimum while convex-outward near solar maximum.

CMEs expand in the solar wind, but their temperature decreases more slowly with distance than an adiabatic profile. The turbulence dissipation rate, deduced from magnetic fluctuations within interplanetary CMEs (ICMEs), seems sufficient to produce the temperature profile. We find that the ICME plasma is collision dominated and the alpha-proton differential speed is quickly reduced. However, the alpha particles are preferentially heated with a temperature ratio $T_\alpha/T_p = 4$ - 6. These findings impose a serious problem on particle heating and acceleration within ICMEs.

Both case studies and superposed epoch analysis demonstrate that plasma depletion layers (PDLs) and mirror-mode waves occur in the sheath regions of ICMEs with preceding shocks. A theoretical analysis shows that shock-induced temperature anisotropies can account for many observations made in interplanetary shocks, planetary bow shocks and the termination shock in the heliosphere. A comparative study of these shocks and corresponding sheaths reveals some universal processes, such as temperature anisotropy instabilities, magnetic field draping and plasma depletion. These results underscore important physical processes which alter the ICME environment.

Thesis Supervisor: John W. Belcher
Title: Professor of Physics

Thesis Supervisor: John D. Richardson
Title: Principal Research Scientist

Acknowledgments

Looking back, I realize that my Ph.D. program would not have gone as smoothly without help from many people. First, my thesis supervisor, Prof. John Belcher, offered me remarkable support and encouragement during my study. He taught me how to define a research topic, which is essential for a scientific researcher. I am also fortunate to have worked with Dr. John Richardson who always carefully read my manuscripts and gave me valuable comments. He showed me how to present research results clearly and effectively. I have also benefitted a lot from his great ideas.

Thanks are also due to Alan Lazarus, Justin Kasper, Justin Ashmall, Anne MacAskill, Mike Stevens and Leslie Finck for their helpful discussion and technical assistance. It has been a great pleasure working with the Space Plasma Group.

I am also grateful to Bruno Coppi and Adam Burgasser for serving on my thesis committee. They have monitored my thesis work and provided constructive comments in the past two years. Their sharp physical intuition is always impressive.

Finally, I would like to give my special thanks to my family and my fiancee, Weiyu, for their persistent love and support. Without them, it would not be possible for me to take such a long journey of doing physics!

The thesis work was supported in part under NASA contract 959203 from the Jet Propulsion Laboratory to MIT.

Contents

List of Figures

List of Tables

Chapter 1

Introduction

Coronal mass ejections (CMEs) are spectacular eruptions in the solar corona in which 10^{15} to 10^{16} g of plasma is hurled into interplanetary space with 10^{31} to 10^{32} ergs of energy. The ejected material in the solar wind is called interplanetary coronal mass ejections (ICMEs). ICMEs are a key link between activities at the Sun and disturbances in the heliosphere. They can cause interplanetary shocks and significant geomagnetic disturbances. CMEs have been studied for three decades by remote sensing of these events at the Sun and by in situ measurements of their plasma properties when they encounter spacecraft. In this chapter we review our current knowledge of CMEs and ICMEs and describe the motivation and organization of the thesis.

1.1 CMEs at the Sun

The phrase "coronal mass ejection" was initially coined to describe bright features moving outward over minutes to hours, as detected by a white-light coronagraph. The coronagraphs record the photospheric radiation (or white light) scattered by electrons (the so-called Thomson scattering) in the ionized coronal plasma, so the observed features are essentially a density structure. The first recorded CMEs were observed on 14 December 1971 and 8 February 1972 using the white-light coronagraph aboard the Seventh Orbiting Solar Observatory (OSO 7). Subsequent observations by the SOLWIND, Solar Maximum Mission (SMM) and Large Angle Spectrometric Coronagraph Observatory (LASCO) reveal that CMEs are a common phenomenon in the solar atmosphere.

1.1.1 Basic Properties

Many CMEs have a three-part structure: a leading loop-like high-density shell, a trailing dark cavity with a sharp boundary and a bright interior feature (usually an erupted prominence). Figure 1-1 displays a CME observed by LASCO [Brueckner et al., 1995] on 27 February 2000, which clearly shows the three-feature topology.

CMEs maintain their structural integrity through the field view of LASCO[1], suggesting that they are organized by the magnetic field.

"Halo CMEs" are defined as the events that are directed toward or away from the Earth; they appear as expanding, circular brightenings that completely surround the coronagraph occulting disk [Howard et al., 1982]. Observations of associated activity on the solar disk are necessary to distinguish whether a halo CME is launched from the frontside or backside of the Sun. Other CMEs, which span large apparent angles ($\geq 120°$) but do not appear as complete halos, are called "partial halo" CMEs. The cutoff at 120° is selected somewhat arbitrarily. Halo-type CMEs occur at about 10% the rate of all CMEs; full halo CMEs are detected at a rate of $\sim 4\%$ of all CMEs [Webb, 2002]. Halo-type CMEs are known to be the drivers of many space weather phenomena such as major storms and solar energetic particle events.

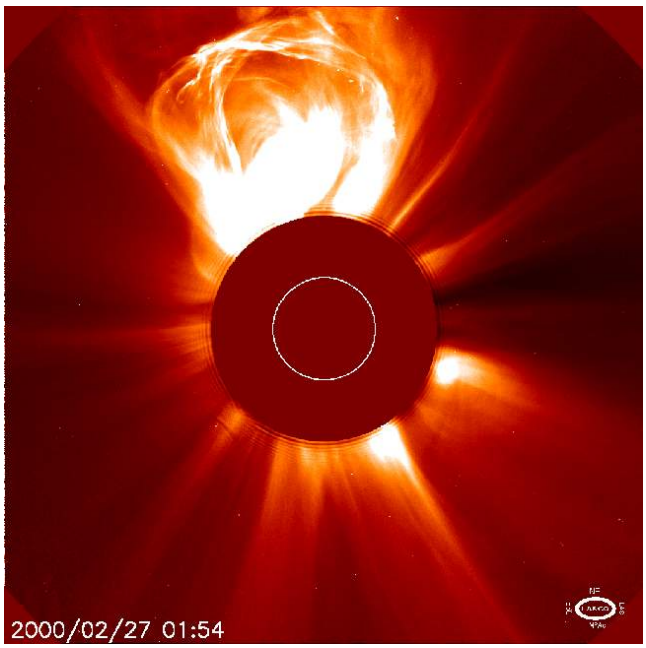

Figure 1-1: 27 February 2000 CME observed by LASCO/C2. The field of view of the LASCO/C2 image is 12×12 $R_\odot$ with a pixel size of $11''.2$; the occulting disk has a radius of 1.7 $R_\odot$. The white circle represents the size and position of the solar disk.

Table 1.1 lists physical properties of CMEs established by observations of SOLWIND, SMM and LASCO. This tabulation is adapted from Gosling [1997], Hundhausen [1997], St. Cyr et al. [2000], Forbes [2000] and Webb [2002]. The frequency of occurrence of CMEs tends to track the solar activity level, with ~ 3.5 per day at solar maximum and ~ 0.2 per day during solar minimum. The apparent opening angle is about $\sim 70°$ on average; this angular size would correspond to a scale of about 1.1 AU at 1 AU if it is conserved during the propagation of CMEs in the solar wind. The

[1]The LASCO instrument has three optical systems: an internally occulted coronagraph (C1 with a field of view of 1.1-3.0 $R_\odot$) and two externally occulted coronagraphs (C2 with field of view of 1.7-6.0 $R_\odot$, and C3 with field of view 3.7-32.0 $R_\odot$).

Table 1.1: Properties of CMEs

Frequency of occurrence	About 3.5 events day^{-1} during solar maximum and about 0.2 events day^{-1} near solar minimum
Average (median) angular size	72° (50°)
Speed of leading edge	50 to 2000 km s^{-1}, with an average 400 km s^{-1}
Volume involved	10^{30} cm^3
Mass ejected	5×10^{15} g
Average kinetic energy	10^{30} to 10^{31} ergs
Average potential energy	7.1×10^{30} ergs (from SMM)
Average mechanical energy	1.4×10^{31} ergs (from SMM)
Heating and radiation	10^{32} ergs
Energy density	100 ergs cm^{-3}

apparent speed, ranging from 50 to 2000 km s^{-1}, is determined from the height of the leading edge over the solar limb as a function of time. The volumes, masses and energies of CMEs require difficult instrument calibrations and often have large uncertainties. The kinetic energy, $nm_pv^2/2$, gravitational energy, nm_pgh, and thermal energy, nk_BT, can be estimated by assuming a coronal density $n \sim 10^9$ cm^{-3}, solar surface gravity $g \sim 2.5 \times 10^4$ cm s^{-2}, average height $h \sim 10^{10}$ cm and a temperature $T \sim 2 \times 10^6$ K, where m_p is the proton mass, v is the plasma speed, and k_B is Boltzmann's constant. The energy density required by an eruption is of the order of 100 ergs cm^{-3}. The magnetic energy density, $B^2/8\pi$, is ~ 400 ergs cm^{-3} for an average field strength of 100 G, as is appropriate for an eruption in an active region. The magnetic energy density exceeds the required energy density, so the eruption must be driven by the magnetic field.

1.1.2 Mechanism of Initiation

CMEs are probably triggered by a loss of stability or equilibrium of the coronal magnetic field [e.g., Forbes, 2000]. Magnetic flux emergence from the convection zone and/or the large-scale magnetic footpoint displacement on the solar surface induce stresses which build up in the magnetic field. When these stresses exceed a threshold, a stable equilibrium cannot be maintained, and this eventually leads to an eruption of the field.

A loss of equilibrium can result from stressing the closed magnetic fields in a helmet streamer. Helmet steamers are large-scale, quasi-static structures in the solar corona. They also exhibit a three-part structure similar to CMEs: the high-density dome, the low-density cavity below the dome and a quiescent prominence (called a filament when observed against the solar disk) within the cavity.

Observations show that more than half of all CMEs are associated with eruptive prominences [e.g., Simnett, 2000; Wu et al., 2000]. Another common phenomenon related to CMEs is soft X-ray arcades which often develop after the CME material

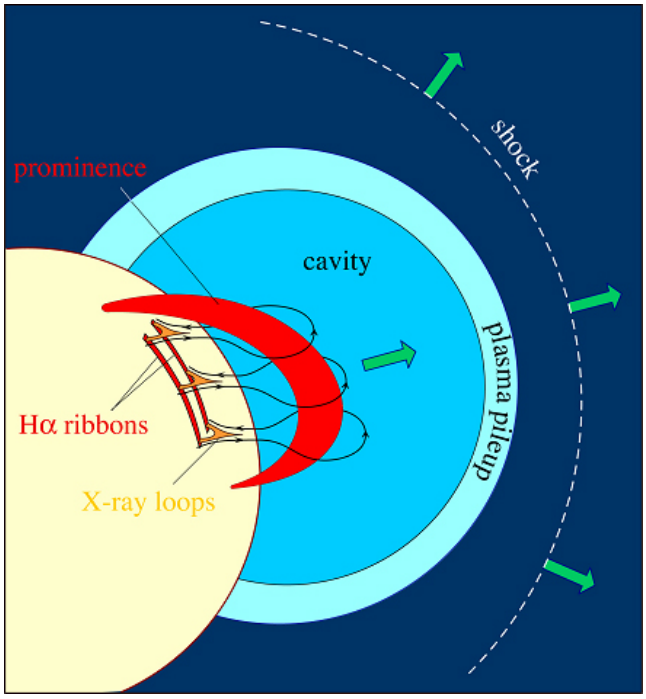

Figure 1-2: Schematic diagram showing the relationship between various features associated with a CME. The region labeled as "plasma pileup" refers to the outer circular arc seen in coronagraphs; the dark cavity and the bright feature inside the cavity (a prominence) are also indicated. After Forbes [2000].

has left the surface [e.g., Webb, 1992]. These soft X-ray loops are the CME counterparts of the flare loops but exhibit a motion pattern different from that of flare loops. Hα emission lasting for many hours, a "long duration event" (LDE), is also associated with a CME. The interrelationship between the diverse features is shown in Figure 1-2. The CME phenomenon can be explained in two steps. First, a helmet streamer is destabilized due to emerging flux or shuffling of the field line footpoints, which lifts the prominence inside the cavity and induces a CME. The rapid motion of the leading edge of the CME piles up material ahead and creates a shock wave. Second, the upward motion of the prominence pushes inward the antiparallel field lines below the prominence and magnetic reconnection occurs. The energy released in the reconnection site is transported downward along the newly formed loops (visible in soft X-rays) to heat the chromosphere, which as a result accounts for the brightening of the two Hα ribbons. This picture makes good physical sense and relates a diversity of observations, but note that not all CMEs have the various features described above.

CMEs illustrated in this cartoon are powered by a sudden release of magnetic energy stored in the corona. Models based on this mechanism are called "storage models". Aly [1991] and Sturrock [1991] show that magnetic topology in a force-free state cannot have more magnetic energy than the fully open configuration (which corresponds to the eruption of a CME), known as the Aly-Sturrock energy constraint.

Any storage model has to get around the Aly-Sturrock energy constraint. Four representative categories of these models have been classified [Forbes, 2000; Forbes et al., 2006]:

• *Ideal MHD models which attempt to explain the CME eruption in terms of only an ideal MHD process.* In these models, magnetic reconnection does not play a role in the field eruption, so it is not clear how a closed field state transits to the open state. Some models of this class, for example, Manchester et al. [2004], artificially remove plasma from a flux rope to destabilize the closed field configuration and trigger a CME; the physical meaning of this process still needs to be established.

• *Resistive MHD models which invoke magnetic reconnection to trigger a CME.* Prior to a CME, the reconnection rate must be slow (say, slower than the photospheric motion scale) so that energy can be stored in the field. After energy has built up, an increase in the plasma resistivity leads to a rapid reconnection which expels a flux rope [Mikić and Linker, 1994]. Obviously, an anomalous resistivity is required at the time of eruption. This anomalous resistivity is likely to be created by micro-instabilities in a current sheet [e.g., Heyvaerts and Priest, 1975], but its precise nature still needs to be determined.

• *Hybrid models which initiate the eruption by an ideal MHD process but need magnetic reconnection to sustain the eruption.* An ideal MHD process, e.g., a slow change in the photospheric field [Lin et al., 1998; Linker et al., 2003], is first needed to create the sudden formation of a current sheet below a flux rope (a process now referred to as a "catastrophe"). This process replaces the onset of a micro-instability needed in resistive MHD models. The total magnetic energy stored in the new system is still less than that corresponding to the fully opened field, so the flux rope cannot escape unless magnetic reconnection occurs in the current sheet. More specifically, the second step is to get around the Aly-Sturrock constraint by invoking the non-ideal process of magnetic reconnection. The reconnection rate needed for the eruption is estimated by Lin and Forbes [2000]. These models assume an axially symmetric flux rope detached from the solar surface. Whether a current sheet can form through the catastrophic process below a curved flux rope with ends tied to the photosphere remains to be investigated.

• *Non-force-free models which use small deviations from a force-free field caused by gravity to trigger an eruption.* If gravity is important, then the field is no longer force-free. The weight of the prominence material acts like a rigid wall to confine the magnetic field; with such a confinement the magnetic energy can exceed that of the open-field configuration [Low and Smith, 1993]. Thus the Aly-Sturrock constraint can be circumvented. When this wall is suddenly removed, the field springs outward and a CME forms.

The storage models, although widely accepted, have to resolve the Aly-Sturrock energy problem as discussed above. Other possible ways around the constraint include

flux injection models and *breakout models*. Chen [1996] proposes a flux injection model in which the eruption of a flux rope system is triggered by an increase in the poloidal magnetic flux of the rope. The basic hypothesis of this model, which differs from the storage-release paradigm, is that the magnetic energy responsible for the eruption resides below the photosphere and is dynamically injected into the corona. Similarly, assuming an increase in the current of a flux rope, Wu et al. [2000] find that the outward Lorentz force ($\mathbf{j} \times \mathbf{B}$) resulting from the current destabilizes a helmet streamer and finally launches a CME. These models require a rapid increase in the magnetic energy during an eruption. Even though they do not address why the magnetic energy should suddenly increase, these models reproduce the height-time curve of CMEs that erupt from the pre-existing flux rope. They can also explain the three-part structure of CMEs.

Most reconnection-driven models assume a sheared filament channel below which reconnection occurs at the neutral line, producing a twisted flux rope. In breakout models, reconnection occurs at a null point *above* the filament channel, which removes the overlying flux and thus reduces the magnetic tension so that the filament can expand outward [Antiochos et al., 1999; MacNeice et al., 2004]. Thus the distinguishing character of breakout models is to postulate a reconnection external to the filament channel, between its overlying flux and neighboring flux systems. Consequently, a breakout model requires a multipolar flux distribution at the photosphere. The breakout models have drawn attention recently in that active regions where eruptions occur are often magnetically complex. The breakout mechanism, although not operative in a truly bipolar field, is compatible with a wide range of magnetic structures. It should be noted that all reconnection models predict a similar evolution once the eruption is well underway. A convincing observation to verify the breakout model would be detection of reconnection before a CME. No such an event has been detected so far, given the complexity of a 3-D active region.

Most models favor the idea that CMEs originate from a helical coronal magnetic field in the form of a flux rope. The helical flux rope offers a structure that naturally supports the prominence material and explains the three-part structure commonly observed in CMEs. In these flux-rope driven models, magnetic flux and helicity are central to the evolution of CMEs [Kumar and Rust, 1996]. However, the CME eruption does not always require the existence of a flux rope. Instead, a helical flux rope is produced as a consequence of magnetic reconnection during the eruption [e.g., Mikić and Linker, 1994]. Magnetic reconnection is necessary to trigger the loss of the field equilibrium in the absence of a helical structure since no curvature force is associated with the field. The flux rope geometry, whatever its origin, can be used to determine the field orientation of CMEs based on Faraday rotation (see Chapter 2).

Many models rely on the Lorentz force $\mathbf{j} \times \mathbf{B}$ to drive a CME. If the magnetic field that erupts has its origin in the magnetic dynamo region located at the base of the convection zone, an interesting question would be where the current density comes from. In most cases the magnetic energy density greatly exceeds the thermal and gravitational energy densities (see section 1.1.1), so the current associated with the field must be either force-free or confined to a current sheet. One possibility is that the current density is created by the photospheric surface flows which stress the

magnetic field. These flows are ~ 1 km s^{-1} or less and sufficient to store the energy of 10^{32} ergs needed for a CME over a period of several days. The other possibility is that the current comes along with the field as it emerges from the convection zone. As the motion of the field line may accompany the flux emergence, it is difficult to distinguish between the two processes. It is also hard to measure the current density since it is proportional to derivatives of the magnetic field.

The relationship between solar flares and CMEs is becoming clearer. CMEs are not generally associated with impulsive flares [Gosling, 1993]. CMEs which are associated with flares often appear to start before the flare onset [Hundhausen, 1999]. More recent observations show that soft X-ray emissions from flares increase with CME speed, particularly for fast CMEs [Zhang et al., 2002]. These results are at variance with the previous suggestion that the impulsive heating of the corona by flares is the energy source fueling CMEs. As suggested by Švestka [1995], the difference between flare-associated and non-flare-associated CMEs lies in the magnetic field strength in the region where the eruption occurs, but for both cases the cause of CMEs is the same. More specifically, the association of CMEs with flares is governed by the free energy in the magnetic structure available for the eruption: the more the free energy, the better the correlation.

Note that CME models cover a broad spectrum. Although it is generally believed that the energy driving CMEs originates from the coronal magnetic field, there is no consensus on the mechanism leading to the loss of the field equilibrium. Observations, including vector magnetograms in filament channels and active regions combined with high-resolution multi-wavelength imaging and spectroscopy, will test these theoretical and computational models and help to further clarify the relationship between CMEs and solar flares. New missions such as STEREO and Solar-B will provide these measurements. Ground-based radio arrays, which make Faraday rotation observations to determine the CME magnetic field (see Chapter 2), will be crucial for testing CME models.

1.2 CMEs in the Solar Wind

After an abrupt formation in the solar corona, a CME propagates into the interplanetary medium. The interplanetary manifestations, or the ejected material in the solar wind, have been termed ICMEs. Combined in situ measurements and remote observations, such as those made by the Helios spacecraft and by SOLWIND, have established the association between CMEs at the Sun and the interplanetary ejecta, though a clear one-to-one association is not fully proven. In situ measurements of the solar wind plasma and magnetic field reveal that ICMEs have signatures different from the ambient solar wind. The identification of ICMEs, still a subjective art, is primarily based on these signatures. This section describes the signatures currently used to identify ICMEs, the criteria for the identification, and the geoeffectiveness (how effective ICMEs are in producing geomagnetic storms) of ICMEs.

1.2.1 Signatures

Recent measurements from ACE, WIND and Ulysses, together with joint observations of the Sun by SOHO, have greatly advanced our understanding of ICMEs. Their signatures and the implications for understanding the nature of ICMEs are summarized and discussed as follows.

• *Unusual temperature behavior of ions and electrons.* The ion temperature is usually lower than normal for the observed solar wind speed. This depressed temperature may result from the expansion of ICMEs as revealed by a declining speed profile across the ICME interval. The expansion speed of ICMEs is typically of the order of the Alfvén speed. As ICMEs move through the ambient medium, the low ion temperature is not necessarily accompanied by a declining speed profile [Webb et al., 2000]. A good criterion for identifying ICMEs, developed by Richardson and Cane [1995], is to compare the ICME proton temperature with an expected solar wind temperature. The expected temperature T_{exp} (in units of 10^3 K) is calculated from the relationship between the temperature T_p and speed v (in km s^{-1}) for the ambient solar wind [Lopez and Freeman, 1986]:

$$T_{exp} = \begin{cases} (0.031v - 5.1)^2 & v < 500 \text{ km s}^{-1}, \\ 0.51v - 142 & v \geq 500 \text{ km s}^{-1}. \end{cases} \tag{1.1}$$

ICMEs usually have $T_p < 0.5T_{exp}$. An ICME example is shown in Figure 1-3; the declining speed and low proton temperature are evident within the ICME interval. This relationship can be applied to various radial distances, say, within 20 AU, by assuming a temperature dependence on the distance [Liu et al., 2005; Wang and Richardson, 2004]; at larger distances, identification of ICMEs using this relationship must be done with caution due to the solar wind heating by pickup ions.

Similarly, Neugebauer and Goldstein [1997] define a "thermal index" $I_{th} = (500v + 1.75 \times 10^5)/T_p$. If $I_{th} > 1$, the plasma is likely to be associated with an ICME, but it may or may not be the case when $I_{th} < 1$.

The electrons show a strange behavior across the ICME plasma. The electron temperature T_e is often larger than the proton temperature within ICMEs with a typical ratio $T_e/T_p \sim 3$ [Liu et al., 2005], so the thermal pressure is dominated by the electron component. However, T_e tends to be lower than the proton temperature in the sheath regions of ICMEs with preceding shocks [Skoug et al., 2000], analogous to planetary magnetosheaths. A possible explanation is that protons resonate at their gyro-frequency with magnetic fluctuations induced at the preceding shock and thus gain energy from the fluctuations, while electrons cannot do so. Another commonly reported feature of electrons is a polytropic index $\gamma_e < 1$ inside ICMEs (determined from $T_e n_e^{1-\gamma_e} = \text{const}$), which remains a puzzle.

• *Magnetic field signatures, magnetic clouds, and Forbush decreases.* The magnetic field inside ICMEs is often strong and has a reduced variance. Combined with the low proton temperature, the strong field leads to a low proton beta (the proton

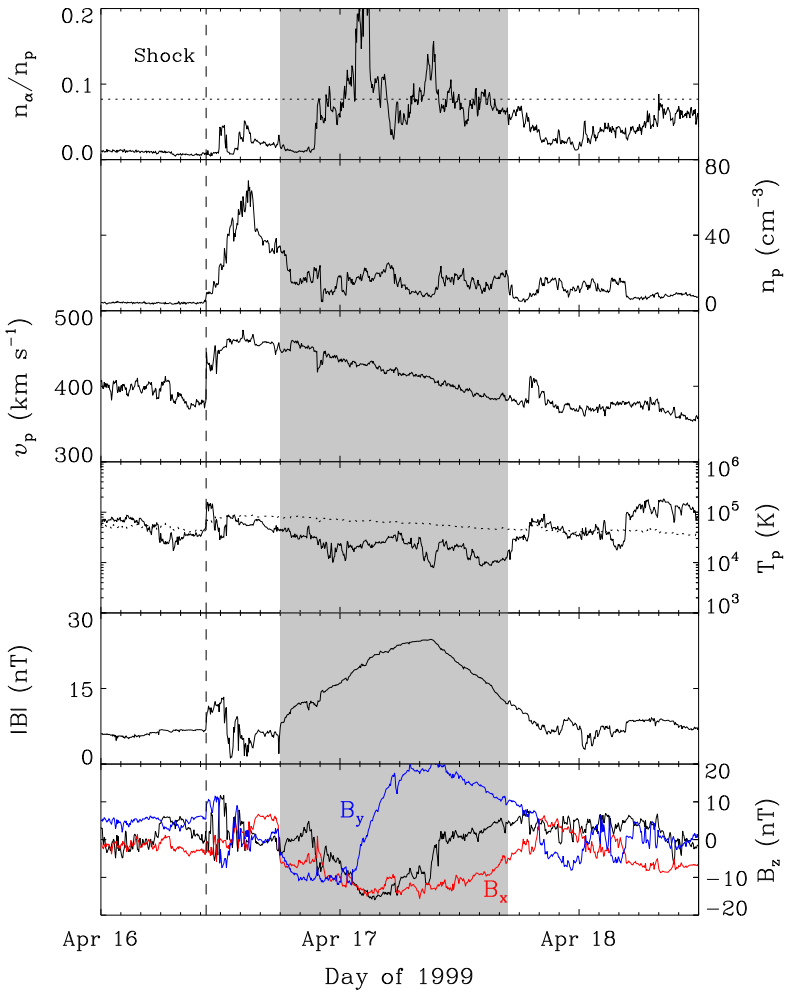

Figure 1-3: Solar wind plasma and magnetic field parameters measured by ACE for a 2.5-day interval in 1999. From top to bottom, the panels show the alpha-to-proton density ratio, proton density, bulk speed, proton temperature, magnetic field strength and components in the geocentric solar ecliptic (GSE) coordinates. The shaded region shows an ICME. The dashed line indicates the arrival time of the ICME-driven shock. Dotted lines denote the 8% level of the alpha/proton density ratio (top panel) and the expected proton temperature (fourth panel), respectively.

thermal pressure divided by the magnetic pressure), typically less than 0.1. A special subset of ICMEs, characterized by a strong magnetic field, a smooth and coherent rotation of the magnetic field vector and a depressed proton temperature, have been termed "magnetic clouds" (MCs) [Burlaga et al., 1981]. The rotation of the magnetic field can be well fitted by a flux rope geometry, allowing the determination of the 3-D structure of an MC based on a single cut through the structure. Although the flux rope configuration has been widely accepted, other possibilities such as a plasmoid structure cannot be completely excluded [Vandas et al., 1993a,b]. MCs are of inter-

est because their magnetic structure is well organized. MCs comprise only $\sim$ 30% of ICMEs [Gosling, 1990]. This percentage has a solar cycle dependence: $\sim$ 100% of ICMEs are MCs near solar minimum and $\sim$ 15% at solar maximum [Cane and Richardson, 2003]. It should be noted that this percentage depends on the identification criteria of ICMEs. Jian et al. [2006] claim that all ICMEs contain an MC structure which is encountered by spacecraft only 30% of the time; their use of a pressure signature to identify ICMEs is under debate.

Depressed fluxes of low energy cosmic rays, know as "Forbush decreases", are observed within ICMEs and their sheath regions. While the strong magnetic fields screen these particles from ICMEs, the intensity decrease inside the sheath region may result from particle scattering by magnetic fluctuations [e.g., Badruddin et al., 1991; Ifedili, 2004]. Plasma in the sheath regions of ICMEs with preceding shocks may be unstable to temperature anisotropy instabilities, leading to enhanced magnetic turbulence. The contribution of this study to the understanding of the sheath region is given in Chapters 5 and 6; other features like field line draping and plasma depletion will also be investigated.

The ICME example shown in Figure 1-3 can be qualified as an MC given the strong field, smooth rotation in the B_y component and the low proton temperature. Magnetic fluctuations are apparent in the sheath between the forward shock and the ICME interval.

• *Compositional anomalies.* Compositional anomaly signatures identified within ICMEs include helium abundance enhancement relative to protons [Hirshberg et al., 1972; Borrini et al., 1982] and enhanced charge states of oxygen [e.g., Galvin, 1997; Henke et al., 2001] and iron [e.g., Bame et al., 1979; Fenimore, 1980]. Enhanced helium abundance has been observed in ICMEs since the early space era. The alpha-to-proton density ratio n_α/n_p rarely exceeds 0.08 except within or in the vicinity of an ICME. A helium enhancement is present in the ICME displayed in Figure 1-3. The cutoff in the density ratio which best identifies ICMEs is not well determined; Richardson and Cane [2004] suggest $\sim$ 0.06 for the ICME level. This signature is important for the identification of ICMEs since measurements of the helium abundance are routinely available. Note that the occurrence of high helium abundances is often patchy and sometimes does not coincide with the field and temperature signatures; it is also absent in many high-latitude ICMEs. The cause of the helium enhancement is still not well understood. Neugebauer and Goldstein [1997] ascribe it to a "sludge removal phenomenon" whereby the helium settling at the base of the solar wind flux tube is cleared out by the CME eruption. This speculation has not yet been tested.

Relative to the ambient solar wind, ICMEs may also have enhanced ion charge states. Roughly 50% - 70% ICMEs have enhanced iron charge states with the average charge $\langle Q \rangle_{Fe} > 12$ and increased oxygen charge states with $O^7/O^6 > 1$ [Richardson and Cane, 2004]. Other composition anomalies can be found in Richardson and Cane [2004]. The ion charge states tend to be frozen-in near the Sun when the time scales of ionization and recombination become larger than the solar wind expansion time. Thus they provide important information for the thermal environment of CMEs and their interplanetary counterparts. In general, the enhanced charge states suggest a

hot source for CMEs with respect to the ambient solar wind. We note, however, that a small subset of ICMEs have intervals with unusually low ion charge states, such as He^+ [Gosling et al., 1980; Burlaga et al., 1998]. The singly charged He particles imply that these "cold" events originate from a low temperature region, possibly a cool, dense prominence in the solar atmosphere.

The charge state signatures appear to be a good indicator of ICMEs. Interestingly, the solar wind composition seems also dependent on the speed; expected levels for the ambient solar wind are formulated by Richardson and Cane [2004] based on the speed dependence. A potential ICME can thus be identified by comparing the observed composition signatures with those expected from the speed, akin to the ICME identification with the temperature criterion. Note that the charge state anomalies sometimes occur in the trailing portion outside ICMEs, making it difficult to identify the boundaries solely based on the anomalies.

• *Bidirectional streaming electrons and protons.* Bidirectional electrons (BDEs) are observed in the suprathermal ($>$ 100 eV) electron "strahl" (beam) that flows from the solar corona into the solar wind [Gosling et al., 1987], and are widely used signatures for identifying ICMEs. Bidirectional anisotropies in low energy protons (35-1600 keV) are also thought to be an indicator of an ICME [Marsden et al., 1987]. These features are considered to be indicative of closed magnetic field loops that are connected either to the Sun or to themselves. BDEs are sometimes intermittent or even absent inside an ICME. The physical interpretation is that the ICME field lines have reconnected with the ambient field [Gosling et al., 1995a], which is considered evidence for the disconnection of ICMEs from the Sun and the modulation of the heliospheric flux by ICMEs. BDE observations are not available for most solar wind data bases.

• *Association with a preceding shock.* ICMEs with speed exceeding the fast magnetosonic speed in the solar wind drive a shock ahead of them. The association of ICMEs with preceding shocks is indicated by the passage of interplanetary shocks followed by the arrival of the ejecta several hours later. Almost all shocks inside 2-3 AU are generated by ICMEs, but not every shock is followed by an ICME. A preceding shock with sharp increases in the plasma density, speed, temperature and the field strength can be seen in Figure 1-3.

It should be noted that the above signatures do not usually occur simultaneously and few ICMEs have all of them. These signatures are largely based on solar wind observations at 1 AU. Some of them may not persist during the ICME propagation in the ambient solar wind, and as a result it is difficult to identify ICMEs in the outer heliosphere.

1.2.2 Identification

Despite these many ICME signatures, no universal scheme is used to identify ICMEs. Individual ICMEs rarely show all the signatures described above and no single dis-

tinctive feature is detected in all ICMEs [Richardson and Cane, 1993]. In addition, these characteristics may not persist across the entire ICME but may come and go within one ICME. Therefore, the identification of ICMEs remains a subjective undertaking. This is not surprising since these signatures arise from different physical circumstances, as discussed above. Here we discuss a practical approach to identify ICMEs.

MCs show a well-organized field structure, so their identification is relatively easy. Magnetic field signatures, including enhanced field strength and reduced variance relative to the ambient medium, can be readily seen within an MC. The field rotation can also be seen by displaying the field components. Many MCs have a transition in the B_z (or B_N depending on the coordinates[2]) component from southward (negative) to northward (positive) or the other way around, indicative of a dipolar field; MCs with this field rotation have an axis roughly close to the ecliptic plane. The axis of MCs could also be perpendicular to the ecliptic plane. Another way to see the field rotation is to display the magnetic field vector projected onto the maximum variance plane obtained from minimum variance analysis (MVA) of the fields within an MC [e.g., Bothmer and Schwenn, 1998, also see Chapter 3]. Note that a good MVA requires a clear separation among the eigenvalues of the covariance matrix of the magnetic field. MCs, by definition, have a low proton temperature, so one also needs to look at the proton temperature. It is still not clear as to how low the temperature must be in order to qualify as an MC. One could simply compare the MC temperature with the ambient temperature, but a better way is to use the ratio of the expected to observed temperatures as described above.

The field signatures can help to identify the boundaries of an MC (or an ICME in general). In principle, the boundary between an ICME and the ambient solar wind should be a tangential discontinuity in the absence of magnetic reconnection. In this case, the boundaries can be identified with little ambiguity. In most cases, however, the boundaries are less distinct and are hard to identify solely based on the field signatures; other signatures are needed.

Several MC lists have been compiled from different data sets. Bothmer and Schwenn [1998] give an MC list based on the Helios data. The WIND MC list formulated by R. P. Lepping can be found at `http://lepmfi.gsfc.nasa.gov/mfi/mag_cloud_pub1.html`. The ACE MC list is at `http://www.bartol.udel.edu/~chuck/ace/ACElists/obs_list.html`, maintained by C. W. Smith. MCs have not been identified systematically from the Voyager data, but several of them can be found in Burlaga and Behannon [1982].

Generic ICMEs are difficult to identify because no necessary and sufficient condition to define an event has been found. Identification based on only one signature may give false events (non-ICME intervals), while identification based on many signatures would omit many ICMEs. Another complication is that ICMEs may have different boundaries in plasma, magnetic field and other signatures. The most practical ap-

[2]In GSE coordinates, **x** points from the Earth to the Sun, **z** is perpendicular to the ecliptic plane and points to the north, and **y** completes the right-handed triad. In RTN coordinates, **R** points from the Sun to the spacecraft, **T** is parallel to the solar equatorial plane and points to the planet motion direction, and **N** completes the right-handed triad.

proach is to examine as many signatures as possible and reach a consensus based on the grouping of several signatures. Fortunately, a significant fraction of ICMEs do include multiple signatures and their identification would produce little dispute, although the exact locations of the boundaries may still be subject to debate.

Various lists of ICMEs have been developed based on different criteria. Cane and Richardson [2003] develop a near-Earth ICME list for the time period 1996 through 2002. In compiling this list, they first identify possible ICMEs based on the temperature criterion described above, and then incorporate complementary signatures such as reduced fluctuations of the magnetic field, shocks, compositional anomalies, and Forbush decreases. They do not take into account the helium abundance or BDEs. Liu et al. [2005] make a survey of ICMEs observed by the Helios 1 and 2, Ulysses, WIND and ACE spacecraft, which together cover heliocentric distances from 0.3 to 5.4 AU; they mainly use the criteria of depressed proton temperature and enhanced helium abundance. The temperature and helium data are routinely available. Another advantage is that the alpha-to-proton density ratio will not change as ICMEs propagate in the solar wind, making it a good identifier for ICMEs at large distances from the Sun [Paularena et al., 2001; Richardson et al., 2002]. Wang and Richardson [2004] use the temperature criterion to identify ICMEs from Voyager 2 data out to 30 AU. Both of these surveys incorporate other signatures to determine the ICME boundaries. A near-Earth ICME list has also been given by Jian et al. [2006] from WIND and ACE data during 1995-2004 using a pressure signature. Other lists identified but not published include the Ulysses ICME list which can be found at `http://swoops.lanl.gov/cme_list.html`.

These lists are influenced by the selection criteria. Comparison of the lists (including the MC lists) shows that even when events appear on multiple lists the time boundaries may not be the same. Also note that these lists are largely based on plasma and magnetic field signatures. Although compositional anomalies and BDEs may be reliable signatures, they are often not used since those data are not always available.

1.2.3 Geoeffectiveness

Because of their energetics and global scale, CMEs produce large disturbances in the solar wind that are the primary cause of geomagnetic storms. Studies using in situ measurements of WIND and ACE together with solar observations from SOHO, TRACE and Yohkoh have established that CMEs typically drive the storms in two ways. First, CMEs are often associated with a sustained southward magnetic field. Southward fields can induce magnetic reconnection at the dayside of the magnetopause [Dungey, 1961], which allows a strong coupling between the CME energy and the magnetosphere. The southward fields may be either in the ejecta themselves reaching the Earth in the form of an MC, or result from the distortion of the ambient field by the ejecta, or both. Second, fast CMEs can generate interplanetary shocks, a key source of energetic particles; the pressure increase associated with CME-driven shocks or CMEs themselves can significantly compress the magnetosphere, which makes them more geoeffective.

Large nonrecurrent geomagnetic storms are induced by fast CMEs [e.g., Gosling et al., 1991]; even some recurrent storms are enhanced by CMEs [Crooker and Cliver, 1994]. Halo CMEs are particularly effective because they suggest the launch of a disturbance toward the Earth. A good example of the geoeffectiveness of a halo CME is the January 1997 event, which caused a large geomagnetic storm leading to the demise of the Telstar 4 satellite. LASCO has now observed a sufficient number of these events to permit a statistical study. Examining LASCO halo CMEs from 1996 to June 1998, St. Cyr et al. [2000] find that 43% of halo CMEs (40 out of 92) may be directed toward the Earth; timing analysis of these CMEs with the K_p geomagnetic storm index indicates that 71% (15 out of 21) of intense storms ($K_p \geq 6$) could be accounted for by frontside halo CMEs. Webb et al. [2001] study 89 frontside full-halo CMEs observed from 1996 - 2000 and find that about 70% of the halos are associated with shocks and/or other ejecta signatures at 1 AU; magnetic clouds or cloud-like structures are involved with 60% - 70% of the halos. The average travel time from the onsets of these CMEs to the onsets of the storms at the Earth is about 3.3 days. Analyses of the relation between halo CMEs and geomagnetic storms also show a strong correlation near solar minimum and a decreased association during solar maximum [Brueckner et al., 1998; Webb et al., 2000].

Note that for an intense magnetic storm to occur there must be a sustained period of strong southward magnetic fields to provide an efficient transfer of energy and momentum from the solar wind to the magnetosphere. Only half of the frontside halos studied by Webb et al. [2001] could be well associated with moderate or intense storms, when averaged over the period of 1996 - 2000. Confirming this result, Webb [2002] finds that $\sim 70\%$ (15 out of 21) of the most intense storms ($D_{st} \geq -150$ nT) are associated with one or more halo CMEs. Southward fields can also be associated with corotating interaction regions (CIRs) preceding high-speed streams. Case studies indicate that, even in simple events, the magnetosphere's response to an MC closely follows the southward field. Frontside halo CMEs without strong southward fields may not create large storms.

1.3 Motivation

Although CMEs/ICMEs have been studied by remote sensing and in situ measurements for thirty years, there is still substantial progress to be made. There are several important limitations to most studies that have been performed thus far.

First, the coronal magnetic field cannot be measured currently, making it hard to verify various CME initiation models and to predict the southward magnetic field for space weather purposes. The fact that the magnetic field is frozen-in with the plasma does not allow determination of the field orientation from while-light coronagraph images. As described above, when CMEs contain a prolonged southward magnetic field, the solar wind and the magnetosphere are strongly coupled and large geomagnetic storms occur; these geomagnetic storms produce large auroral currents and high fluxes of energetic particles which can disrupt power systems and satellite operations. A major problem in our ability to forecast these events and mitigate potential dam-

age is that the magnetic field direction in these CMEs cannot be measured until they reach the satellites at the L1 point in front of the Earth, providing a warning time of only 30 minutes.

Second, the vast majority of in situ data analysis has been limited to single point observations. ICMEs, however, are 3-D and their structure can only be inferred from multi-point measurements. Various flux-rope fitting techniques have been proposed to describe the in situ measurements, but these models may significantly underestimate the true dimension and thus the magnetic flux and helicity of ICMEs given their assumptions and many free parameters. In addition, spacecraft are sporadically distributed at different heliospheric distances and are rarely radially aligned. It is thus hard to track specific ICMEs through the heliosphere; models of transient structure evolution in the solar wind cannot be quantitatively tested or constrained in the absence of observations of plasma features over a range of radial distances. The global morphology and propagation of ICMEs in interplanetary space are not well understood.

Third, our limited understanding of the physical processes within ICMEs and their surroundings makes it difficult to interpret observations or relate features that may occur in different environments. The low-temperature nature of ICMEs makes the ICME plasma collision-dominated since the Coulomb collision time is proportional to $T^{1.5}$. The strong collisions will fail ideal MHD modeling of the ICME propagation in the heliosphere. Kinetic properties of ions, in the presence of collisions, would be distinct from those in the ambient solar wind but they have not been investigated. The sheath region between an ICME and its preceding shock is similar to planetary magnetosheaths and the heliosheath. This resemblance may reveal important physical processes, such as plasma depletion and mirror mode waves, that may be universal in these sheath regions. Properties and implications of these features need to be studied to give a comprehensive view of ICMEs and their related phenomena.

1.4 Organization of Thesis

Based on the above analysis, this thesis focuses on the determination of the CME magnetic field orientation, the global morphology of MCs, the thermodynamic state and kinetic properties of the ICME plasma, the sheath regions of ICMEs, and finally a comparative study of various shocks and sheaths in the heliosphere. The thesis is laid out as follows.

Chapter 2 gives a new method to determine the magnetic field orientation of CMEs based on Faraday rotation (FR). A flux rope, force-free or non-force-free, is shown to reproduce the FR curves across the CME plasma as observed by the Helios spacecraft. We show that a 2-D FR mapping can disentangle flux rope configurations, which gives the field orientation and helicity 2-3 days before CMEs reach the Earth. Application of this method by future large radio arrays, such as the Mileura Widefield Array (MWA), is also discussed.

Chapter 3 studies the global structure of MCs in terms of the transverse size and curvature. We show that the cross section of MCs (or ICMEs in general) are highly

flattened due to their interaction with the ambient solar wind. We present a simple model to investigate the curvature of the cross section and apply this model to solar wind observations at solar minimum and maximum. It is shown that MCs tend to be concave outward at solar minimum while convex outward near solar maximum.

Chapter 4 investigates the thermodynamic state and kinetic properties of the ICME plasma by using a combined survey of ICMEs from 0.3 - 20 AU. ICMEs are shown to be continuously heated during their expansion in the solar wind. We deduce the turbulence dissipation rate and show that it may be sufficient for the ICME heating. It is demonstrated that the ICME plasma is collision dominated. The reduced alpha-proton relative speed is consistent with strong collisions. However, we find a preferential heating of alpha particles relative to protons within the ICME plasma, which imposes a serious problem on particle heating and acceleration in ICMEs. We also compare the ICME plasma with the ambient solar wind.

Chapter 5 examines the sheath regions between ICMEs and their preceding shocks. Using a case study and statistical analysis we show that the sheath region is often characterized by plasma depletion layers and mirror mode waves, similar to planetary magnetosheaths. Different classes of ICMEs, with or without forward shocks, MCs or non-MCs, are compared in the association with these features. Implications of these features are discussed for a variety of crucial physical processes in the solar wind.

Chapter 6 performs a comparative study of interplanetary shocks, planetary bow shocks, the termination shock and their associated sheath regions in the heliosphere. We generalize some universal processes in these sheaths, such as temperature anisotropy instabilities, magnetic field draping and plasma depletion. We further show, based on a theoretical analysis, that shock-induced temperature anisotropies can explain magnetic fluctuations observed downstream of these shocks. These results help us better understand ICMEs and their surroundings.

Chapter 7 briefly summarizes the main results of the thesis and describes future work based on the studies.

Chapter 2

Determination of CME Magnetic Field Orientation

We describe a new method to measure the magnetic field orientation of coronal mass ejections (CMEs) using Faraday rotation (FR). Two basic FR profiles, Gaussian-shaped with a single polarity or "N"-like with polarity reversals, are produced by a radio source occulted by a moving flux rope depending on its orientation. These curves are consistent with the Helios observations, providing evidence for the flux-rope geometry of CMEs. Many background radio sources can map CMEs in FR onto the sky. We demonstrate with a simple flux rope that the magnetic field orientation and helicity of the flux rope can be determined from the mapping 2-3 days before it reaches the Earth, which is of crucial importance for space weather forecasting. An FR calculation based on global magnetohydrodynamic (MHD) simulations of CMEs in a background heliosphere shows that FR mapping can also resolve a CME geometry curved back to the Sun. We discuss implementation of the method using data from the Mileura Widefield Array (MWA).

2.1 Introduction

CMEs are recognized as primary drivers of interplanetary disturbances. The ejected materials are often associated with large southward magnetic fields which can reconnect with geomagnetic fields and produce storms in the terrestrial environment [Dungey, 1961; Gosling et al., 1991]. Determination of the CME magnetic field orientation is thus of crucial importance for space weather forecasting. However, nearly all atoms are ionized at the coronal temperature $\sim 2\times10^6$ K, making it difficult to detect the coronal magnetic field through Zeeman splitting of spectral lines as is routinely done for the photospheric field. A typical way to estimate the coronal magnetic field above $2R_\odot$ ($R_\odot$ being the solar radius) is theoretical extrapolation using the photospheric fields as boundary conditions, which can only be checked by comparison to the field strength measured from radio bursts and the orientation determined from soft X-ray observations. The field orientation is also hard to infer from white-light coronagraph images. Spacecraft near the first Lagrangian point (L1) measure the

local fields but can only give a warning time of ~ 30 minutes for arrival at the Earth [Vogt et al., 2006; Weimer et al., 2002].

A possible method to measure the coronal magnetic field is Faraday rotation (FR), the rotation of the polarization plane of a radio wave as it traverses a magnetized plasma. The first FR experiment was conducted in 1968 by Pioneer 6 during its superior solar conjunction [Levy et al., 1969]. The observed FR curve features a "W"-shaped profile over a time period of 2-3 hours with rotation angles up to 40° from the quiescent baseline. This FR event was interpreted as a coronal streamer stalk of angular size 1-2° [Woo, 1997], but Pätzold and Bird [1998] argue that the FR curve is produced by the passage of a series of CMEs. Joint coronagraph observations are needed to determine whether an FR transient is caused by CMEs. Subsequent FR observations by the Pioneer and Helios spacecraft reveal important information on the quiet coronal field [Stelzried et al., 1970; Pätzold et al., 1987] and magnetic fluctuations [Hollweg et al., 1982; Efimov et al., 1996; Andreev et al., 1997; Chashei et al., 1999, 2000]. FR fluctuations are currently the only source of information for the coronal field fluctuations. Independent knowledge of the electron density, however, is needed in order to study the background field and fluctuations.

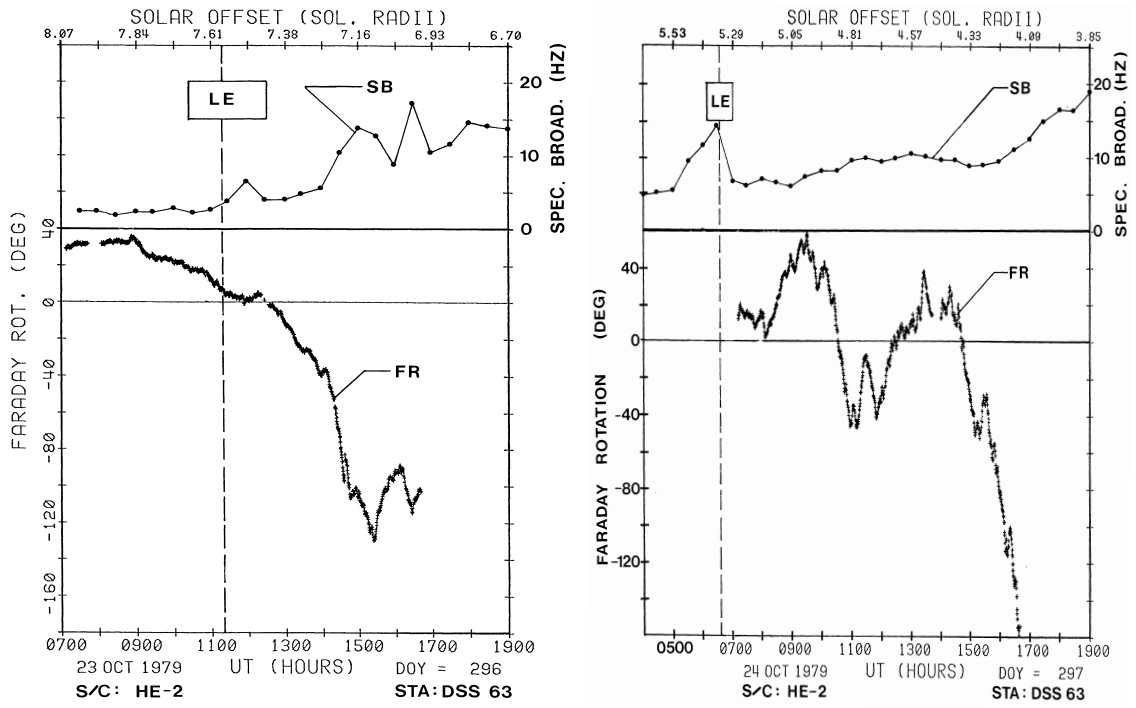

Figure 2-1: Time profiles of FR (bottom) and spectral broadening (top) of the Helios 2 signal during the CMEs of 23 October 1979 (left) and 24 October 1979 (right) recorded at the Madrid station DSS 63. The apparent solar offset of Helios 2 is given at the top. The dashed vertical line indicates the arrival time of the CME leading edge with uncertainties given by the width of the box "LE". Large deviations in FR following the leading edge indicate the arrival of the CME's bright core. Reproduced from Bird et al. [1985].

Joint coronagraph and FR measurements of CMEs were also conducted when the Helios spacecraft, with a downlink signal at a wavelength $\lambda = 13$ cm, was occulted by CME plasma. Bird et al. [1985] establish a one-to-one correspondence between the SOLWIND white-light transients and FR disturbances for 5 CMEs. Figure 2-1 displays the time histories of FR and spectral broadening for two CMEs. Note that the spectral broadening is proportional to the plasma density fluctuations; the increased spectral broadening is consistent with the enhanced density fluctuations within CMEs and their sheath regions (see Chapter 5). The FR through the 23 October 1979 CME shows a curve (note a data gap) which seems not to change sign during the CME passage; a single sign in FR indicates a monopolar magnetic field. The 24 October 1979 CME displays an FR curve which is roughly "N"-like across the zero rotation angle, indicative of a dipolar field. Other CMEs in the work of Bird et al. [1985] give similar FR curves, either an "N"-type or a waved shape around the zero level. Based on a simple slab model for CMEs, the mean transient field magnitude is estimated to be 10 - 100 mG scaled to $2.5R_{\odot}$, which seems larger than the mean background field. The CME field geometry, as implied by these FR curves, will be discussed below. These features demonstrate why radio occultation measurements are effective in detecting CMEs.

FR experiments using natural radio sources, such as pulsars and quasars, have also been performed. FR observations of this class were first conducted by Bird et al. [1980] during the solar occultation of a pulsar. The advantage of using natural radio sources is that many of these sources are present in the vicinity of the Sun and provide multiple lines of sight which can be simultaneously probed by a radio array. We can thus make a two-dimensional (2-D) mapping of the solar corona and the inner heliosphere with an extended distribution of background radio sources.

In this chapter we show a new method to determine the magnetic field orientation of CMEs using FR. This method enables us to acquire the field orientation 2 - 3 days before CMEs reach the Earth, which will greatly improve our ability to forecast space weather. The data needed to implement this technique will be available from the Mileura Widefield Array (MWA) [Salah et al., 2005]. The magnetic structure obtained from MWA measurements with this method will fill the missing link in coronal observations of the CME magnetic field and also place strong constraints on CME initiation theories.

2.2 Faraday Rotation

The FR technique uses the fact that a linearly polarized radio wave propagating through a magnetized plasma can be split into the left-hand and right-hand circularly polarized waves with wave vectors given by [Sturrock, 1994]

$$k_L = \frac{\omega}{c}\left[1 - \frac{\omega_p^2}{\omega(\omega + \Omega_e)}\right]^{1/2}, \tag{2.1}$$

$$k_R = \frac{\omega}{c}\left[1 - \frac{\omega_p^2}{\omega(\omega - \Omega_e)}\right]^{1/2}, \tag{2.2}$$

where ω is the angular frequency of the radio wave, c is the speed of light, ω_p is the plasma frequency, and Ω_e is the electron gyrofrequency. It is clear that the R wave travels faster than the L wave. For this reason, there will be a progressive phase change between the two polarized components as the wave propagates. For a wave traveling along a path $\mathbf{s}$ at a time t, the electric field vector can be written as

$$\mathbf{E}_L = E_0\left[\cos(\mathbf{k}_L \cdot \mathbf{s} - \omega t) + i\sin(\mathbf{k}_L \cdot \mathbf{s} - \omega t)\right] \tag{2.3}$$

for the left-hand component, and

$$\mathbf{E}_R = E_0\left[\cos(\mathbf{k}_R \cdot \mathbf{s} - \omega t) - i\sin(\mathbf{k}_R \cdot \mathbf{s} - \omega t)\right] \tag{2.4}$$

for the right-hand component, where E_0 is the amplitude of each component. The combined wave is obtained by superposing the two components

$$\mathbf{E} = \frac{1}{2}(\mathbf{E}_L + \mathbf{E}_R) = E_0 \cos\left[\frac{(\mathbf{k}_L + \mathbf{k}_R)\cdot\mathbf{s}}{2} - \omega t\right]\cos\left[\frac{(\mathbf{k}_L - \mathbf{k}_R)\cdot\mathbf{s}}{2}\right] + \tag{2.5}$$

$$iE_0 \cos\left[\frac{(\mathbf{k}_L + \mathbf{k}_R)\cdot\mathbf{s}}{2} - \omega t\right]\sin\left[\frac{(\mathbf{k}_L - \mathbf{k}_R)\cdot\mathbf{s}}{2}\right]. \tag{2.6}$$

The rotation angle Ω of the combined electric vector can be obtained from

$$\tan\Omega = \tan\left[\frac{(\mathbf{k}_L - \mathbf{k}_R)\cdot\mathbf{s}}{2}\right], \tag{2.7}$$

which gives

$$\frac{d\Omega}{d\mathbf{s}} = \frac{1}{2}(\mathbf{k}_L - \mathbf{k}_R). \tag{2.8}$$

For $\omega \gg \omega_p, \Omega_e$, the above equation can be approximated as

$$\frac{d\Omega}{ds} = \frac{\omega_p^2 \Omega_e}{2c\omega^2}. \tag{2.9}$$

Substituting $\Omega_e = \frac{eB}{m_e}$ and $\omega_p = \sqrt{\frac{n_e e^2}{\epsilon_0 m_e}}$ into the above equation, we obtain the total rotation angle over the propagation path $\Omega = \lambda^2 RM$, where λ is the wavelength of the radio wave. The rotation measure, RM, is expressed as

$$RM = \frac{e^3}{8\pi^2\epsilon_0 m_e^2 c^3}\int n_e \mathbf{B}\cdot d\mathbf{s}, \tag{2.10}$$

where e is the electron charge, ϵ_0 is the permittivity of free space, m_e is the electron mass, n_e is the electron density, $\mathbf{B}$ is the magnetic field, and $d\mathbf{s}$ is the vector incremental path defined to be positive toward the observer. FR responds to the magnetic field, making it a useful tool to probe the coronal transient and quiet magnetic fields.

Note that the polarization vector may undergo several rotations across the coronal plasma. Measurements at several frequencies are needed to break the degeneracy; observations as a function of time can also help to trace the rotation through its cycles.

2.3 Modeling the Helios Observations

In situ observations of CMEs from interplanetary space indicate that CMEs are often threaded by magnetic fields in the form of a helical flux rope [Burlaga et al., 1981; Burlaga, 1988; Lepping et al., 1990]. This helical structure either exists before the eruption [Chen, 1996; Kumar and Rust, 1996; Gibson and Low, 1998; Lin and Forbes, 2000], as needed for supporting prominence material, or is produced by magnetic reconnection during the eruption [e.g., Mikić and Linker, 1994]. The flux rope configuration reproduces the white-light appearance of CMEs [Chen, 1996; Gibson and Low, 1998]. This well-organized structure will display a specific FR signature easily discernible from the ambient medium, but direct proof of the flux-rope geometry of CMEs at the Sun has been lacking.

2.3.1 Force-Free Flux Ropes

Here we model the Helios observations using a cylindrically symmetric force-free flux rope [Lundquist, 1950] with

$$\mathbf{B} = B_0 J_0(\alpha r)\hat{z} + B_0 H J_1(\alpha r)\hat{\phi} \tag{2.11}$$

in axis-centered cylindrical coordinates $(\hat{r}, \hat{\phi}, \hat{z})$ in terms of the zeroth and first order Bessel functions J_0 and J_1 respectively, where B_0 is the field magnitude at the rope axis, r is the radial distance from the axis, and H specifies the left-handed (-1) or right-handed (+1) helicity. We take $\alpha r_0 = 2.405$, the first root of the J_0 function, so α determines the scale of the flux-rope radius r_0. The electron density is obtained by assuming a plasma beta $\beta = 0.1$ and temperature $T = 10^5$ K, as implied by the extrapolation of in situ measurements [Liu et al., 2005, also see Chapter 4]. Combining equations (2.10) and (2.11) with a radio wave path gives the FR.

For simplicity, we consider a frame with the x-y plane aligned with the flux-rope cross section at its center and the z axis along the axial field. Figure 2-2 shows the diagram of the flux rope with the projected line of sight. The flux rope, initially at $4R_\odot$ away from the Sun with a constant radius $r_0 = 3.6R_\odot$ and length $20R_\odot$, moves with a speed $v = 500$ km s^{-1} in the x direction across a radio ray path. The radio signal path makes an angle θ with respect to the plane and ϕ with the motion direction when projected onto the plane. The magnetic field strength at the rope axis is adopted to be $B_0 = 25$ mG, well within the range estimated from the Helios observations [Bird et al., 1985].

The resulting FR curves are displayed in Figure 2-3. A radio source occulted by the moving flux rope gives two basic types of FR curves, Gaussian-shaped and "N"-shaped

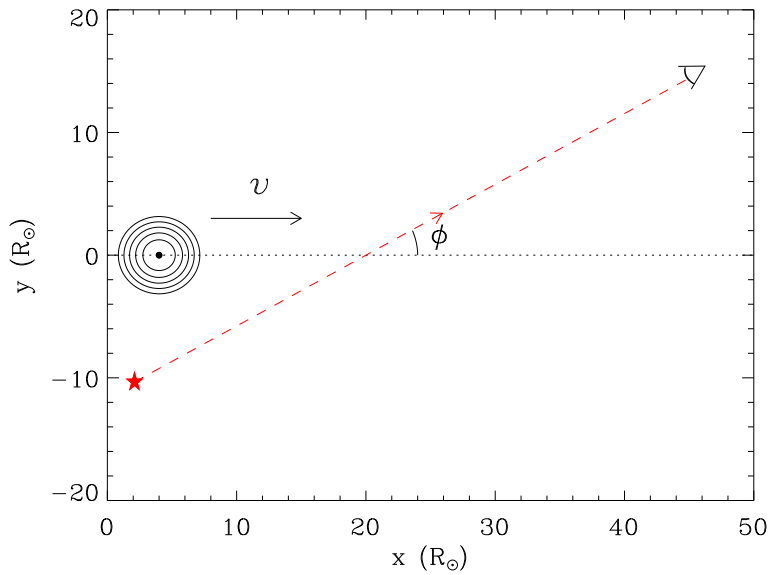

Figure 2-2: Schematic diagram of a force-free flux rope and the line of sight from a radio source to an observer projected onto the plane of the flux-rope cross section. The flux rope moves at a speed v across the line of sight which makes an angle ϕ with the motion direction.

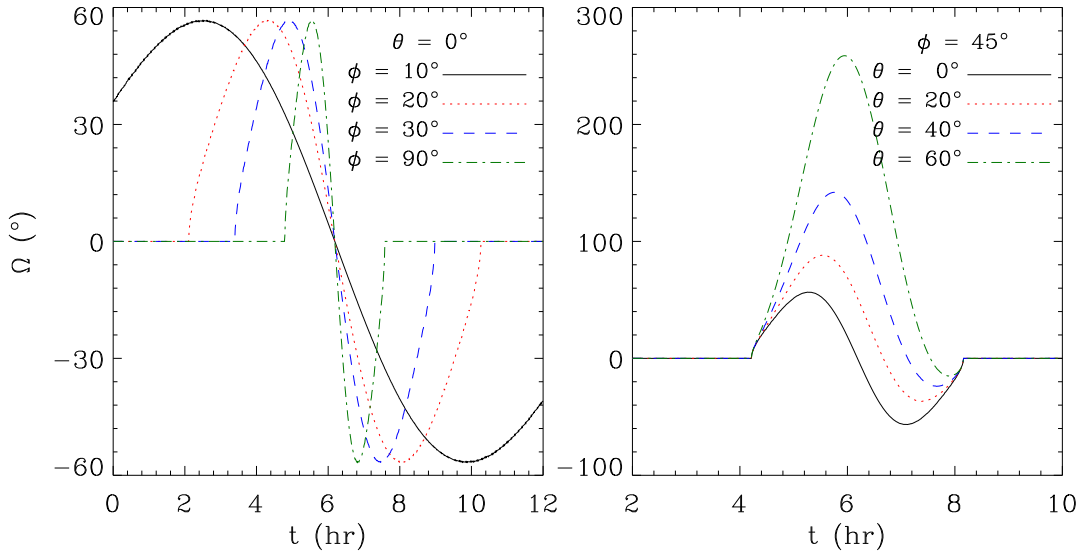

Figure 2-3: FR at $\lambda = 13$ cm through the force-free flux rope as a function of time. Left is the rotation angle with θ fixed to 0° and $\phi = [10°, 20°, 30°, 90°]$, and right is the rotation angle with ϕ fixed to 45° and $\theta = [0°, 20°, 40°, 60°]$.

(or inverted "N") depending on the orientation of the radio wave path with respect to the flux rope. When the radio signal path is roughly along the flux rope (say, for $\phi =$ 45° and $\theta = 60°$ as shown in the right panel), the axial field overwhelms the azimuthal

field along the signal path, so the FR curve would be Gaussian-like, indicative of a monopolar field. For a signal path generally perpendicular to the flux rope, the azimuthal field dominates and changes sign along the path, so the rotation curve would be "N" or inverted "N" shaped with a sign change (left panel), suggestive of a dipolar field. These basic curves are consistent with the Helios measurements. Two adjacent flux ropes with evolving fields could yield a "W"-shaped curve as observed by Pioneer 6 [Levy et al., 1969; Pätzold and Bird, 1998]. The time scale and magnitude of the observed FR curves are also reproduced. When $\theta = 0°$, the line of sight is within the plane. Varying ϕ gives a variety of time scales of FR, ranging from ~ 3 to more than 10 hours, but the peak value of FR is fixed at $\sim 57°$. These numbers are consistent with the Helios data shown in the right panel of Figure 2-1. When θ is close to 90°, the observer would be looking along the flux rope. The axial field produces a strong FR, but decreasing θ will diminish the rotation angle and make the curve more and more "N"-like. The time scale, however, remains at 4 hours. For $\phi = 45°$ and $\theta = 40°$, the rotation angle is up to 140°, in agreement with the Helios data shown in the left panel of Figure 2-1.

2.3.2 Non-Force-Free Flux Ropes

A non-force-free flux rope could give more flexibility in the field configuration. Consider a magnetic field that is uniform in the z direction in terms of rectangular coordinates. Since $\nabla \cdot \mathbf{B} = 0$, the magnetic field can be expressed as

$$\mathbf{B} = \left(\frac{\partial A}{\partial y}, -\frac{\partial A}{\partial x}, B_z \right), \tag{2.12}$$

where the vector potential is defined as $\mathbf{A} = A(x, y)\hat{\mathbf{z}}$. Combined with $\nabla \times \mathbf{B} = \mu_0 \mathbf{j}$, the above equation becomes

$$\frac{\partial^2 A}{\partial x^2} + \frac{\partial^2 A}{\partial y^2} = -\mu_0 j_z, \tag{2.13}$$

where μ_0 is the permeability of free space, and $\mathbf{j}$ is the current density. The MHD equilibrium, $\mathbf{j} \times \mathbf{B} - \nabla p = 0$, gives

$$\frac{\partial^2 A}{\partial x^2} + \frac{\partial^2 A}{\partial y^2} = -\mu_0 \frac{d}{dA} \left(p + \frac{B_z^2}{2\mu_0} \right) = -\mu_0 j_z \tag{2.14}$$

after a comparison with equation (2.13), where p is the plasma thermal pressure. Equation (2.14) is known as the Grad-Shafranov equation. We see from this equation that p, B_z and hence j_z are a function of A alone. An interesting proof is also given by Schindler et al. [1973], who use the fact that any distribution function that is expressed as a function of the constants of motion satisfies the steady state Vlasov equation; for the assumed 2-D form of the model, the constants of motion are the particle Hamiltonian and the z component of the canonical momentum.

A Maxwellian distribution would suggest a reasonable form of e^A for the current

density, or

$$\nabla^2 \tilde{A} = e^{-2\tilde{A}} \tag{2.15}$$

in properly scaled units. With this choice, equation (2.14) has the solution [Schindler et al., 1973]

$$\tilde{A} = \ln\left[\alpha \cos\tilde{x} + \sqrt{1+\alpha^2}\cosh\tilde{y}\right], \tag{2.16}$$

This nonlinear solution has been called the periodic pinch since it has the form of a 2-D neutral sheet perturbed by a periodic chain of magnetic islands centered in the current sheet. Here $\tilde{A}$, $\tilde{x}$ and $\tilde{y}$ are dimensionless quantities, and α is a free parameter that can be used to control the aspect ratio of the magnetic islands. A similar problem in the gravity system (where Jean's equation applies) is a thin self-gravitating disk for which Poisson's equation may be written as $\nabla^2\Phi \sim e^{-\Phi}$. Here Φ is the gravitational potential, and solutions of this equation would give the vertical density profile of the disk.

From equations (2.12), (2.14) and (2.16) we obtain

$$j_z = -\frac{B_0}{\mu_0 L_0}\exp\left(\frac{-2A}{B_0 L_0}\right), \tag{2.17}$$

$$B_x = B_0 \frac{\sqrt{1+\alpha^2}\sinh(y/L_0)}{\alpha\cos(x/L_0)+\sqrt{1+\alpha^2}\cosh(y/L_0)}, \tag{2.18}$$

$$B_y = B_0 \frac{\alpha\sin(x/L_0)}{\alpha\cos(x/L_0)+\sqrt{1+\alpha^2}\cosh(y/L_0)}, \tag{2.19}$$

where B_0 and L_0 are scales of the field magnitude and length, respectively. The axial field B_z and the thermal pressure can be obtained from $\frac{d}{dA}(p+\frac{B_z^2}{2\mu_0}) = j_z$ which gives

$$p + \frac{B_z^2}{2\mu_0} = \frac{B_0^2}{2\mu_0}\exp\left(\frac{-2A}{B_0 L_0}\right) + \frac{B_1^2}{2\mu_0}, \tag{2.20}$$

where B_1 is an arbitrary constant. Assuming a factor ε in the partition of the total pressure, we have

$$p = \varepsilon\frac{B_0^2}{2\mu_0}\left[\left(\alpha\cos\frac{x}{L_0}+\sqrt{1+\alpha^2}\cosh\frac{y}{L_0}\right)^{-2}+\frac{B_1^2}{B_0^2}\right], \tag{2.21}$$

$$B_z = \pm\sqrt{1-\varepsilon}B_0\left[\left(\alpha\cos\frac{x}{L_0}+\sqrt{1+\alpha^2}\cosh\frac{y}{L_0}\right)^{-2}+\frac{B_1^2}{B_0^2}\right]^{1/2}. \tag{2.22}$$

Adjusting the parameters α and ε gives a variety of flux rope configurations, circular and non-circular, force-free and non-force-free.

A flux rope of this kind is displayed in Figure 2-4. As can be seen, this flux rope lies within a current sheet. To single out the flux rope, we require $0 \le x \le 2\pi L_0$ and $-\pi L_0/2 \le y \le \pi L_0/2$ initially, where $L_0 = 1.5R_\odot$. The flux rope is still $20R_\odot$ long, moving with $v = 500$ km s^{-1} across the line of sight. Other parameters are assumed to be $B_0 = 10$ mG, $B_1 = 0$, $\alpha = 2$, $\varepsilon = 0.1$, and the temperature $T = 10^5$ K. Figure 2-5

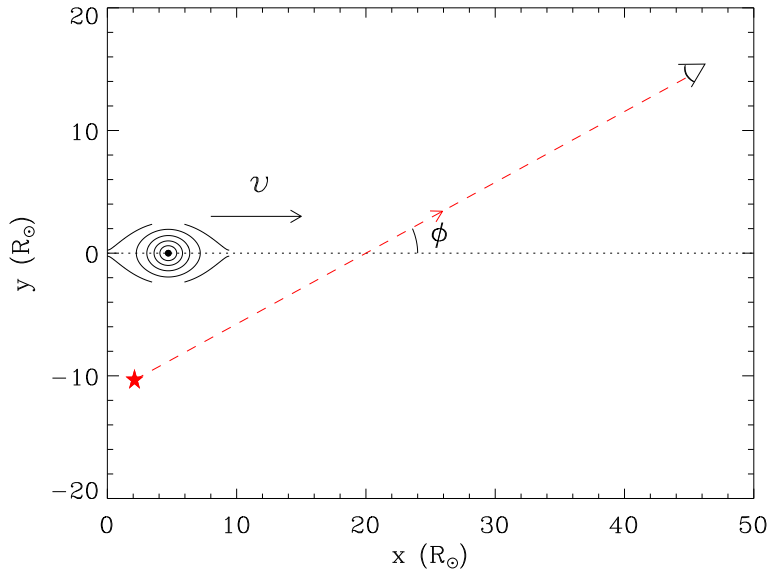

Figure 2-4: Same format as Figure 2-2, but for a non-force-free flux rope embedded in a current sheet.

shows the calculated FR. These curves are generally similar to those for a cylindrically symmetric force-free flux rope. Unlike the force-free flux-rope counterpart, the FR curves show a smooth transition from the zero angle to peak values. In addition, they are narrower in width, which may result from fields and densities which are more concentrated close to the axis. Note that the field magnitude is $\sim$ 40 mG at the axis of the non-force-free flux rope. These profiles can also qualitatively explain the Helios observations.

The above results suggest that CMEs at the Sun manifest as flux ropes, confirming what previously could only be inferred from in situ data [Burlaga, 1988; Lepping et al., 1990]. They also reinforce the connection of CMEs observed by coronagraphs with magnetic clouds identified from in situ measurements.

2.4 2-D Mapping of CMEs

As demonstrated above, even a single radio signal path can give hints on the magnetic structure of CMEs. Ambiguities in the flux rope orientation cannot be removed based on only one radio ray path. The power of the FR technique lies in having multiple radio sources, especially when a 2-D mapping of CMEs onto the sky is possible.

2.4.1 A Single Flux Rope

For a flux-rope configuration shown in Figure 2-6, the magnetic field is azimuthal close to the rope edge and purely axial at the axis. The rotation measure would be positive through the part of the rope with fields coming toward an observer and negative through the part with fields leaving the observer, so the azimuthal field

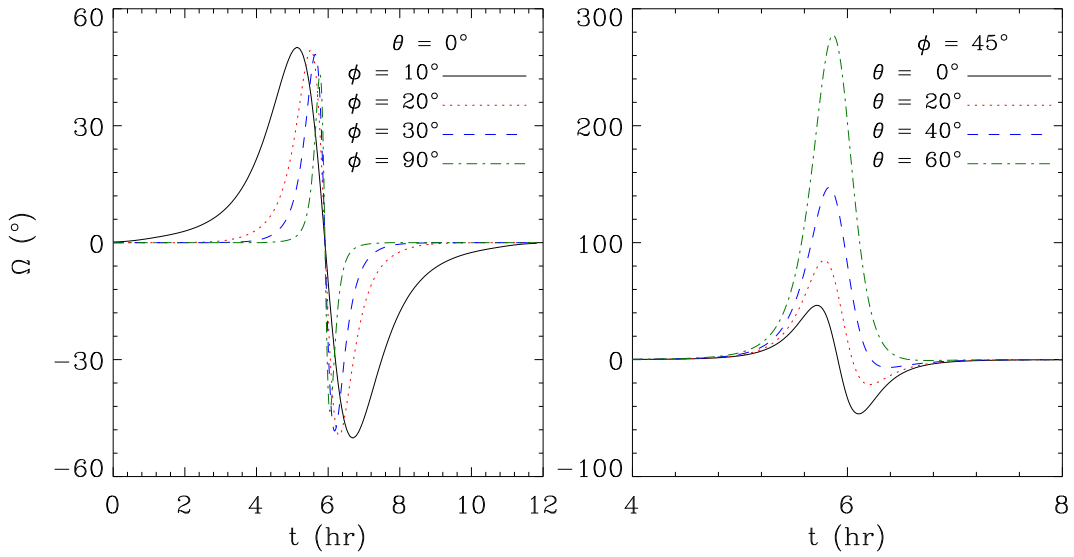

Figure 2-5: Same format as Figure 2-3, but for crossings of the non-force-free flux rope.

orientation can be easily recognized with data from multiple lines of sight (radio ray paths). A key role is played by the axial component, which tells us the helicity of the flux rope. Consider a force-free flux rope for simplicity. For points on a line parallel to the rope axis within the flux rope, the field direction as well as the magnitude is the same. The fields on this line would make different angles with a variety of radio signal paths since the signal path is always toward the observer. To make it clearer, we mark two points on the axis of the flux rope. It is evident that the two angles θ_1 and θ_2, between the axial field and lines of sight across the axis at the two points, are distinct. The dot product between the field and the unit vector of the line of sight is positive on the left side while negative on the right side. As long as the axial field component is strong enough, these different angles will lead to a gradient in the rotation measure along the rope.

Assuming an observer sitting at the Earth, we calculate the FR pattern projected onto the sky for a force-free flux rope viewed from many radio sources. A flux rope has two possibilities for the axial field direction, with each one accompanied by either a left-handed or right-handed helicity. Plotted in Figure 2-7 are the four possible configurations as well as their rotation measure patterns. The angle θ_y defines the azimuthal angle of a line of sight with respect to the Sun-Earth (observer) direction in the solar ecliptic plane, while θ_z is the elevation angle of the line of sight with respect to the ecliptic plane. The flux rope, with axis in the ecliptic plane and perpendicular to the Sun-Earth direction, is centered at $10R_\odot$ from the Sun and has a radius of $r_0 = 8R_\odot$ and length $50R_\odot$. The magnetic field magnitude is assumed to be 10 mG at the rope axis. The gradient effect in the rotation measure along the flux rope is apparent in Figure 2-7 and it produces a one-to-one correspondence between the flux-rope configuration and the rotation measure pattern. The four configurations of

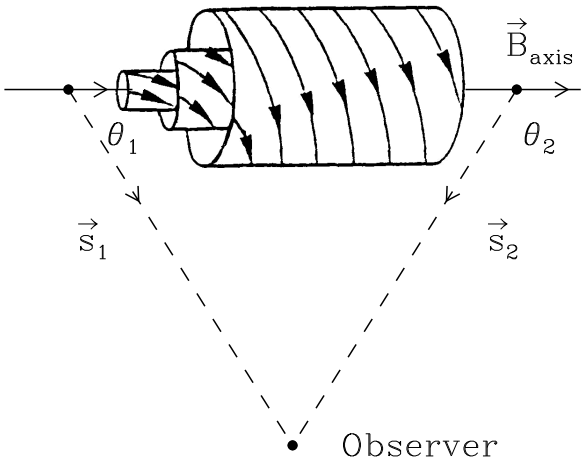

Figure 2-6: Idealized sketch of a flux rope showing the magnetic field orientation. Two lines of sight, with unit vectors $\vec{s}_1$ and $\vec{s}_2$ respectively, make different angles with the flux-rope axis.

a flux rope can thus be uniquely determined from the global behavior of the rotation measure, which gives the axial field orientation and the helicity. In order to fully resolve the flux rope, we have assumed $\sim$ 80 radio sources per square degree in the field of view, but in practice a resolution of 250 times lower can give enough information for the field orientation and helicity (see Figure 2-8).

The FR mapping obtained from multiple radio sources can also help to determine the speed and orientation of CMEs as they move away from the Sun. This mapping is similar to coronagraph observations. While the polarized brightness (Thomson-scattered, polarized component of the coronal brightness) is sensitive to the electron density, FR reacts to the magnetic field as well as the electron density and thus may be able to track CMEs to a larger distance than white light imaging. Figure 2-8 gives snapshots at different times of a tilted flux rope moving outward from the Sun. A Sun-centered coordinate system is defined such that the x axis extends from the Sun to the Earth, the z axis is normal to and northward from the solar ecliptic plane, and the y axis lies in the ecliptic plane and completes the right-handed set. A force-free flux rope, initially centered at (2, 2, 2)$R_\odot$ in this frame and oriented at 30° from the ecliptic plane and 70° from the Sun-Earth line, moves at a speed 500 km s^{-1} from the Sun along the direction with elevation angle 10° and azimuthal angle 20°. The flux rope evolution is constructed by assuming a power law dependence with distance R (in units of AU) for the rope size and physical parameters, i.e.,

$$r_0 = 0.2 \times R^{0.78} \text{ AU}$$

for the rope radius,

$$B_0 = 15 \times R^{-1.5} \text{ nT}$$

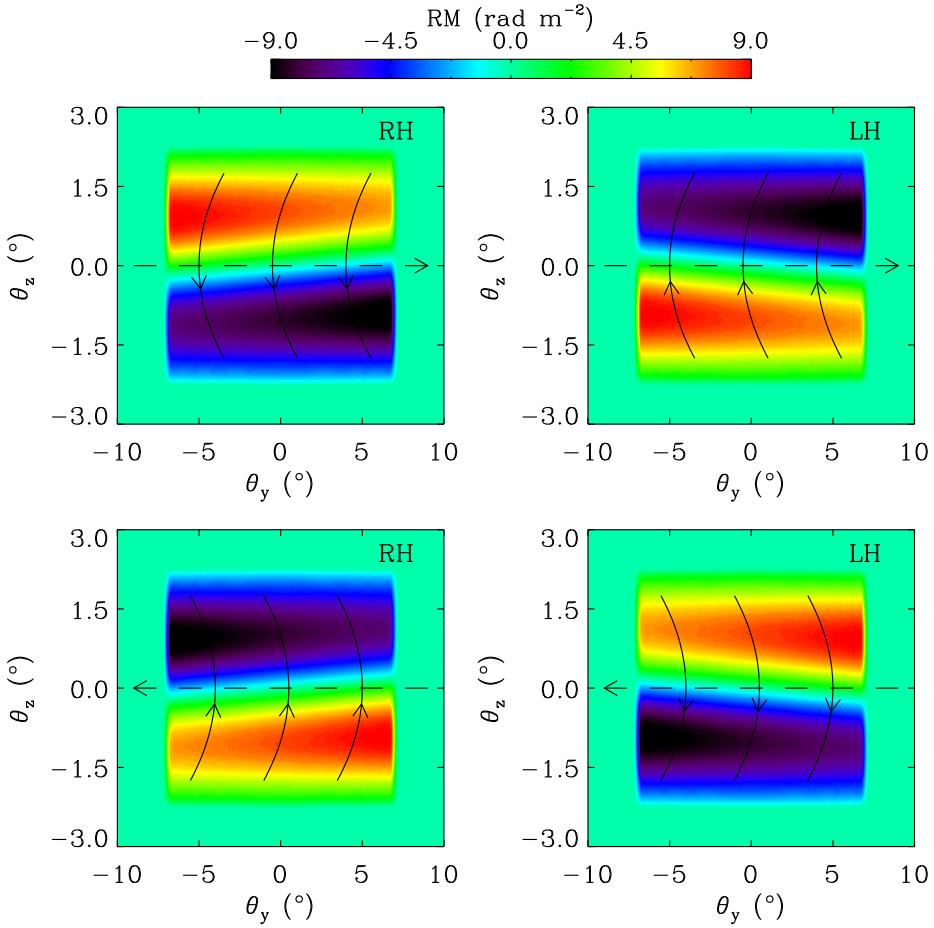

Figure 2-7: Mapping of the rotation measure corresponding to the four configurations of a flux rope projected onto the sky. The color shading indicates the value of the rotation measure. The arrows show the directions of the azimuthal and axial magnetic fields, from which a left-handed (LH) or right-handed (RH) helicity is apparent. Each configuration of the flux rope has a distinct rotation measure pattern.

for the field magnitude at the axis, and

$$T = 3 \times 10^4 \times R^{-0.72} \text{ K}$$

for the temperature. The rope length is kept at 3 times the rope diameter, and the plasma β is kept at 0.1. Similar power-law dependences have been identified by a statistical study of ICME evolution in the solar wind [Liu et al., 2005, also see Chapter 4], but note that the transverse size of the flux-rope cross section could be much larger than the radial width (see Chapter 3).

The 2-D mapping has a pixel size of about 3.2 degrees. Even at such a low resolution, the flux rope can be recognized several hours after appearance at the Sun. The orientation of the flux rope with respect to the ecliptic plane is apparent in the first few snapshots, but note that this elevation angle may be falsified by the

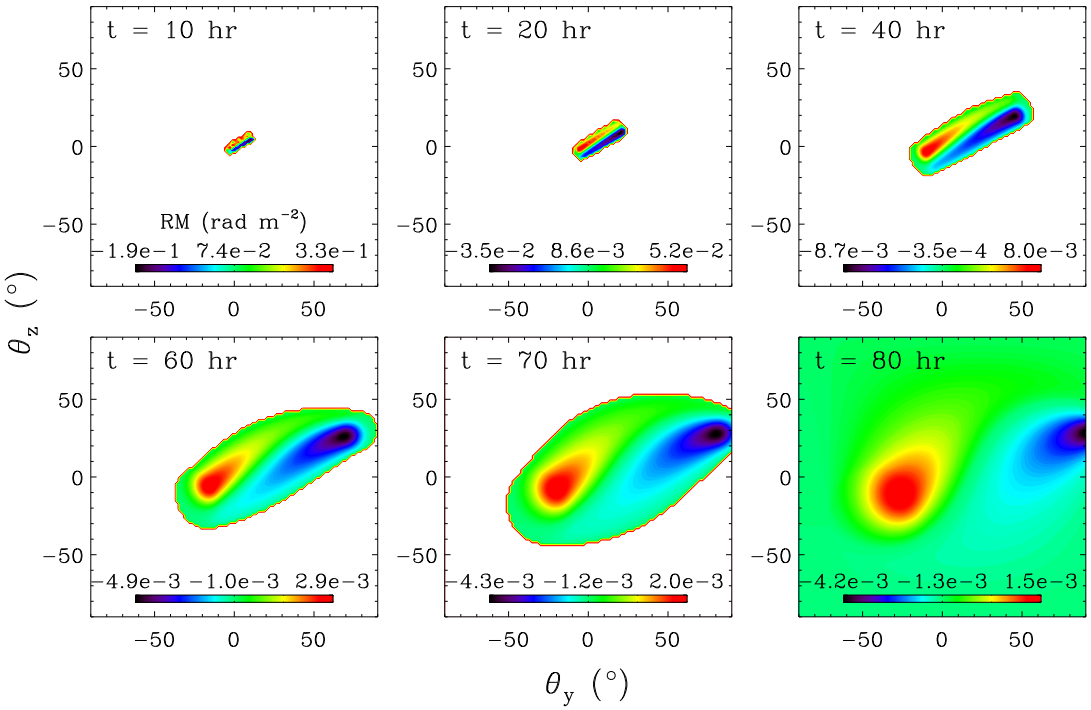

Figure 2-8: FR mapping of the whole sky at a resolution of ~ 3.2 degrees as a tilted flux rope moves away from the Sun. Note that the motion direction of the flux-rope center is not directly toward the Earth. Values of the rotation measure for each panel are indicated by the color bar within the panel. Also shown is the time at the top for each snapshot.

projection effect. The gradient effect in the rotation measure along the flux rope is discernable at 10 hours and becomes clearer around 20 hours. A right-handed helicity with axial fields skewed upward can be obtained from this gradient after a comparison with Figure 2-7 (top left). When the flux rope is closer to the Earth, its appearance projected onto the sky becomes more and more deformed. Finally, when the Earth is within the flux rope (around 80 hours), an observer would see two spots with opposite polarities produced by the ends of the flux rope.

Note that the above conclusions are not restricted to cylindrically symmetric force-free flux ropes. We have also used the non-force-free solutions of the steady state Vlasov-Maxwell equations (see section 2.3.2), which unambiguously give the same picture. The FR technique takes advantage of an axial magnetic field coupled with the azimuthal component, which is the general geometry of a flux rope. This robust feature makes possible a precise determination of the CME field orientation. A curved flux rope with turbulent fields, however, may need caution in determining the axial field direction (see below).

2.4.2 MHD Simulations with Background Heliosphere

The above FR calculation does not take into account the background heliosphere. In this sense, the 2-D mapping may be considered as a difference imaging between the transient and background heliospheres. Here we use for the FR calculation 3-D ideal MHD simulations of a CME propagating into a background heliosphere [Manchester et al., 2004]. The simulations are performed using the so-called Block Adaptive Tree Solar-Wind Roe Upwind Scheme (BATS-R-US) at the University of Michigan. A specific heating function is assumed to produce a global steady-state model of the corona that has high-latitude coronal holes (where fast winds come from) and a helmet streamer with a current sheet at the equator. A twisted flux rope with both ends anchored in the photosphere is then inserted into the helmet streamer. Removal of some plasma in the flux rope destabilizes the flux rope and launches a CME. A 3-D view of the flux rope resulting from the simulations is displayed in Figure 2-9. The magnetic field, as represented by colored solid lines extending from the Sun, winds to form a helical structure within the simulated CME. The field has a strong toroidal (axial) component close to the axis but is nearly poloidal (azimuthal) at the surface of the rope.

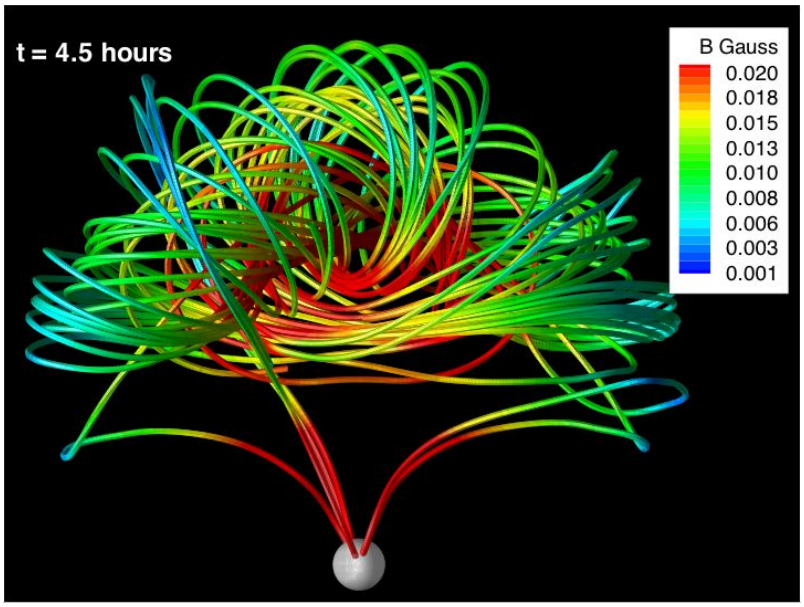

Figure 2-9: A 3-D rendering of the CME magnetic field lines at 4.5 hours after initiation. The color shading indicates the field magnitude and the white sphere represents the Sun.

A fundamental problem in CME studies which remains to be resolved is whether CMEs are magnetically connected to the Sun as they propagate through interplanetary medium. Most theoretical modeling assumes a twisted flux rope with two ends anchored to the Sun [Chen, 1996; Kumar and Rust, 1996; Gibson and Low, 1998]. This scenario is suggested by energetic particles of solar origin observed within a magnetic cloud [Kahler and Reames, 1991]. An isolated plasmoid is also a possible

structure for CMEs [Vandas et al., 1993a,b]. The FR mapping is capable of removing this ambiguity in that it can easily capture a flux-rope geometry bent toward the Sun. To show this capability, we calculate the FR mapping of the simulated CME with the background heliosphere. The MHD model gives a time series of data cubes of $300R_{\odot}$ in length. We subtract the background from the rotation measure of the CME data to avoid possible effects brought about by the finite domain. Figure 2-10 shows the difference mapping of the rotation measure at a resolution of ~ 3.2 degrees when the CME propagates a day ($\sim 70R_{\odot}$) away from the Sun. The simulation data are rotated such that the observer (projected onto the origin) can see the flux rope curved to the Sun. The coordinates, θ_y and θ_z, are defined with respect to the observer. A flux rope extending back to the Sun is apparent in the difference image. The outer arc with positive rotation measures is formed by the azimuthal magnetic field pointing to the observer while the inner arc with negative rotation measures originates from the field with the opposite polarity. The rotation measure difference is positive near the Sun, which is due to a pre-existing negative rotation measure that becomes less negative after the CME eruption.

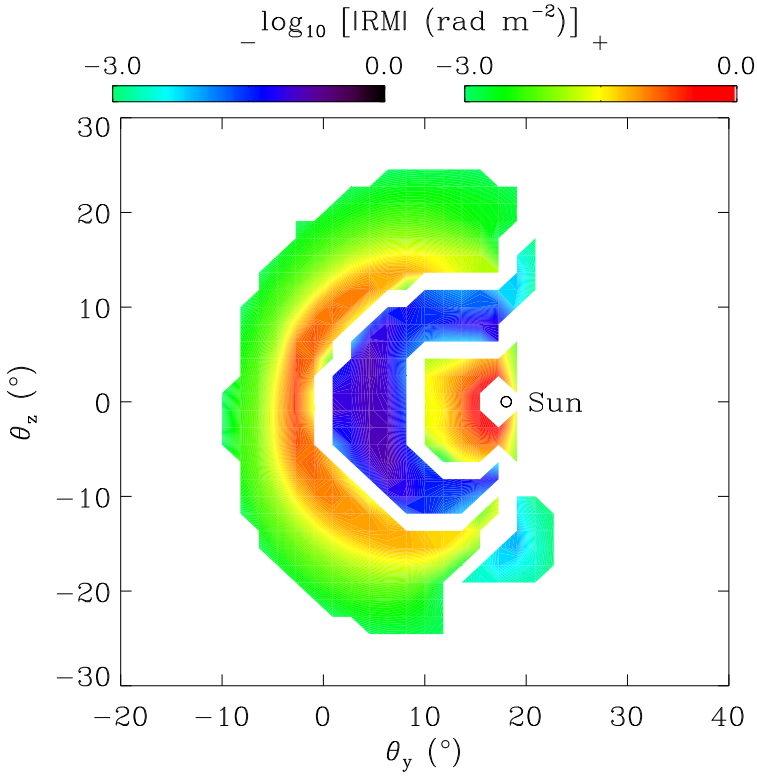

Figure 2-10: Mapping of the rotation measure difference between the MHD simulation at 24 hours and the steady state heliosphere. The two color bars indicate the logarithmic scale of the absolute value of the negative (-) and positive (+) rotation measure, respectively.

A closer look at the image would also reveal asymmetric legs of the flux rope. This effect, indicative of a right-handed helicity, is created by the different view angles as

described above. The nose of the flux rope does not show a clear gradient in the rotation measure because the view angles of this part are similar. In the case of the two legs directed to the observer, two spots with contrary magnetic polarities will be seen, so the curved geometry may also help to clarify the field helicity.

2.5 Implementation by MWA

The present results pave the way for interpreting future FR observations of CMEs by large radio arrays, particularly those operating at low frequencies [Oberoi and Kasper, 2004; Salah et al., 2005]. The MWA - Low Frequency Demonstrator, specially designed for this purpose at 80-300 MHz, will feature wide fields of view, high sensitivity and multi-beaming capabilities [Salah et al., 2005]. Figure 2-11 shows the planned physical layout of the array. This array will be installed in Western Australia (26.4°S, 117.3°E), a radio quiet region. The basic unit is an antenna dipole; 8000 of them are assembled into 500 tiles and then 64 nodes. The array will spread out ~ 1.5 km in diameter, achieving ~ 8000 m^2 of collecting area at 150 MHz and a field of view from 15° at 300 MHz to 50° at 80 MHz. The point source sensitivity will be about 20 mJy for an integration time of 1 s.

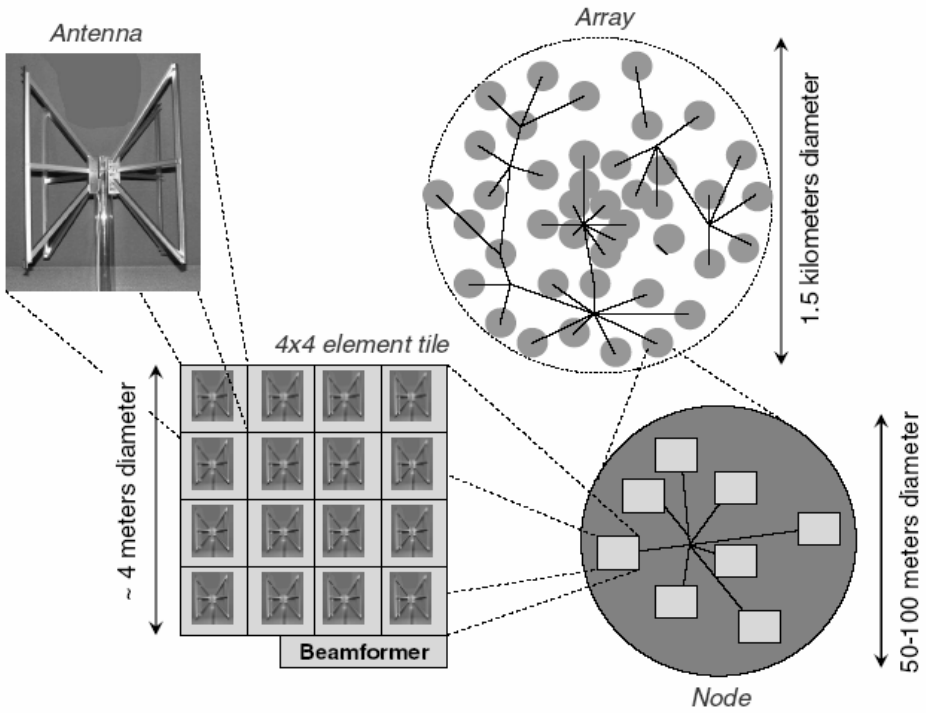

Figure 2-11: Schematic diagram of the physical layout of the MWA. Reproduced from Salah et al. [2005].

The array is expected to monitor $\sim$ 300 background radio sources within 13° elongation ($\sim 50R_\odot$) from the Sun, providing a sufficient spatial sampling of the

inner heliosphere. In addition, this array will be able to capture a rotation measure of 10^{-2} rad m^{-2} and thus is remarkably sensitive to the magnetic field. Such an array can provide higher sensitivity and resolution than previously available. Science operations of this array will start in 2009.

2.6 Summary and Discussion

We have presented a new method to determine the magnetic field orientation of CMEs based on FR. Our FR calculations, either with a simple flux rope or global MHD modeling, demonstrate the exciting result that the CME field orientation can be obtained 2-3 days before CMEs arrive at the Earth, substantially longer than the warning time achieved by local spacecraft measurements at L1.

The FR curves through the CME plasma observed by Helios can be reproduced by a flux rope moving across a radio signal path. Two basic FR profiles, Gaussian-shaped with a single polarity or "N"-like with polarity reversals, indicate the orientation of the flux rope with respect to the signal path. Force-free and non-force-free flux ropes generally give the same picture, except some trivial differences reflecting the field and density distributions within the flux rope. The FR calculation with a radio signal path, combined with the Helios observations, shows that CMEs at the Sun appear as flux ropes.

2-D FR mapping of a flux rope using many radio sources gives the field orientation as well as the helicity. The orientation of azimuthal fields can be readily obtained since they yield rotation measures with opposite polarities. The axial component of the magnetic field creates a gradient in rotation measure along the flux rope, with which the flux rope configurations can be disentangled. Time-dependent FR mapping is also calculated for a tilted flux rope propagating away from the Sun. The orientation of the flux rope as a whole and its projected speed onto the sky can be determined from the snapshots of the flux rope mapped in FR. We further compute the FR mapping for a curved flux rope moving into a background heliosphere obtained from 3-D ideal MHD simulations. The FR mapping can resolve a CME curved back to the Sun in addition to the field orientation. Difference imaging is needed to remove the FR contribution from the background medium.

Note that the above results are a first-order attempt to predict what may be seen in FR. An actual CME likely shows a turbulent behavior and may have multiple structures along the line of sight; the rotation measure, an integral quantity along the line of sight, could display similar signatures for different structures. Therefore, interpretation of the FR measurements will be more complex than suggested here. However, having an instantaneous, global map of the rotation measure that evolves in time will be vastly superior to a time profile along a single line of sight, and comparison with coronagraph observations and actual measures of geoeffectiveness (e.g., the D_{st} index) for a series of real events will eventually lead to the predictive capability proposed in this work.

It should be emphasized that this new method can determine the magnetic field orientation of CMEs without knowledge of the electron density. The electron den-

sity could be inferred from Thomson scattering measurements made by the SECCHI instrument (suite of wide angle coronagraphs) on STEREO which has stereoscopic fields of view [Howard et al., 2000]. With the joint measurements of the electron density, the magnetic field strength can be estimated. Implementation of our method by the MWA and SECCHI would imply a coming era when the impact of the solar storm on the Earth can be predicted with small ambiguities. It could also fill the missing link in coronal observations of the CME magnetic field, thus providing strong constraints on CME initiation theories.

The content of this chapter has been accepted for publication in the *Astrophysical Journal* [see Liu et al., 2007b].

Chapter 3

Constraints on the Global Structure of Magnetic Clouds

We present direct evidence that magnetic clouds (MCs) have highly flattened and curved cross section resulting from their interaction with the ambient solar wind. Lower limits on the transverse size are obtained for three MCs observed by ACE and Ulysses from the latitudinal separation between the two spacecraft, ranging from 40° to 70°. The cross-section aspect ratio of the MCs is estimated to be no smaller than 6 : 1. We offer a simple model to extract the radius of curvature of the cross section, based on the elevation angle of the MC normal distributed over latitude. Application of the model to WIND observations from 1995 - 1997 (close to solar minimum) shows that the cross section is bent concavely outward by a structured solar wind with a radius of curvature of ~ 0.3 AU. Near solar maximum, MCs tend to be convex outward in the solar wind with a uniform speed; the radius of curvature is proportional to the heliographic distance of MCs, as demonstrated by Ulysses observations between 1999 and 2003. These results improve our knowledge of the global morphology of MCs in the pre-STEREO era, which is crucial for space weather prediction and heliosphere studies.

3.1 Introduction

As described in Chapter 1, magnetic clouds (MCs) are a subset of ICMEs that are characterized by a strong magnetic field, a smooth and coherent rotation of the field vector, and a depressed proton temperature compared to the ambient solar wind [Burlaga et al., 1981]. MCs drive many space weather events and affect the solar wind throughout the heliosphere, so it is important to understand their spatial structure. In addition, CMEs carry a huge amount of magnetic flux and helicity into the heliosphere; proper estimates of the magnetic flux and helicity, which is crucial to connect the coronal origin and in situ manifestations, also require knowledge of the global structure.

Most in situ observations give information on a single line through an MC; flux-rope fitting techniques have been developed to interpret these local measurements.

Cylindrically symmetric models vary from a linear force-free field [e.g., Burlaga, 1988; Lepping et al., 1990] to non-force-free fields with a current density dependence [e.g., Hidalgo et al., 2002a; Cid et al., 2002]. Elliptical models take into account the expansion and distortion effect of MCs, also based on the linear force-free [Vandas and Romashets, 2003] and non-force-free approaches [e.g., Mulligan and Russell, 2001; Hidalgo et al., 2002b]. The Grad-Shafranov (GS) technique relaxes the force-free assumption and reconstructs the cross section of MCs in the plane perpendicular to the cloud's axis without prescribing the geometry [e.g., Hau and Sonnerup, 1999; Hu and Sonnerup, 2002]. Although useful in describing local observations, these models may significantly underestimate the true dimension, magnetic flux and helicity of MCs [Riley et al., 2004; Dasso et al., 2005]; the ambiguities in their results cannot be removed since they involve many free parameters and assumptions. Multiple point observations are therefore required to properly invert the global structure of MCs.

Indirect evidence, both from observations and numerical simulations, suggests that MCs are highly flattened and distorted due to their interaction with the ambient solar wind. CMEs observed at the solar limb typically have an angular width of 50 - 70° and maintain this width as they propagate through the corona [e.g., Webb et al., 1997; St. Cyr et al., 2000]. At 1 AU, this angular width would correspond to a size of $\sim$ 1 AU, much larger than the ICME's radial thickness of $\sim$ 0.2 AU (see Chapter 4). Shocks driven by fast MCs have a standoff distance which is too large to be produced by a cylindrically symmetric flux rope [Russell and Mulligan, 2002]. The oblate cross section of MCs is also indicated by global magnetohydrodynamic (MHD) simulations of the propagation both in a uniform [e.g., Cargill et al., 2000; Odstrcil et al., 2002; Riley et al., 2003] and structured solar wind [e.g., Groth et al., 2000; Odstrcil et al., 2004; Manchester et al., 2004].

The simulated flux ropes show an interesting curvature which depends on the background solar wind state. Figure 3-1 shows an idealized sketch of the flux-rope cross section in the solar meridianal plane, initially having a radius $r_0 = 1\ r_\odot$ at a height $h_0 = 2\ r_\odot$ from the Sun, where $r_\odot$ represents the solar radius. This configuration corresponds to an angular extent of $\Delta\theta = 60°$ subtended by the rope. At a time t, the axis-centered distance r and polar angle ϕ in the flux-rope cross section translate to the heliographic distance (R) and latitude (θ) assuming kinematic evolution [Riley and Crooker, 2004; Owens et al., 2006]

$$\theta = \arctan\left(\frac{r\sin\phi}{h_0 + r\cos\phi}\right),$$

and

$$R = \sqrt{r^2\sin^2\phi + (h_0 + r\cos\phi)^2} + vt\left[1 + \frac{Ar}{r_0}\cos(\phi - \theta)\right],$$

where v is the solar wind speed and $A = 0.1$ is the ratio of the expansion speed at the rope edge (relative to the rope center) to the solar wind speed. The left flux rope is propagating into a uniform solar wind with a speed of $v = 450$ km s^{-1}, while the right one is propagating into a solar wind with a latitudinal speed gradient $v = 700\sin^2\theta + 400$ km s^{-1}. After 4 days these flux ropes arrive at 1 AU. Due

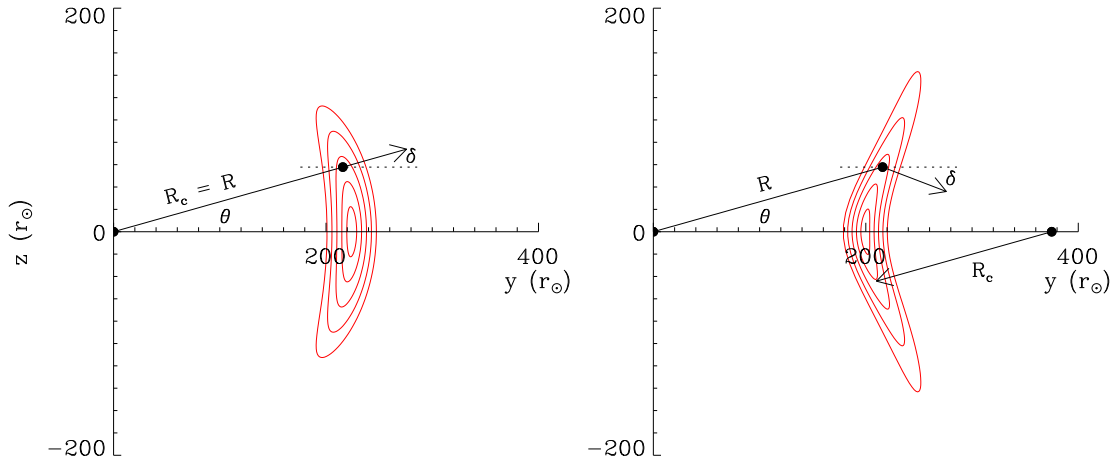

Figure 3-1: Schematic diagram of MCs at 1 AU in the solar meridianal plane with axes perpendicular to the radial and transverse directions, illustrating the large latitudinal extent and curvature in a uniform (left panel, corresponding to solar maximum) and structured solar wind (right panel, corresponding to solar minimum). Contours denote levels of the initial flux-rope radius. The angles, labeled as θ and δ, represent the latitude of a virtual spacecraft and the elevation angle of the flux-rope normal. The distance of the spacecraft and radius of flux-rope curvature are marked as R and R_c, respectively. Note that the transverse size is the width in the direction perpendicular to both the radial and axial directions.

to the expansion of the solar wind, plasmas on different stream lines move apart while the magnetic tension in the flux rope tries to keep them together. Since the flow momentum overwhelms the magnetic force after a few solar radii, the flux rope is stretched azimuthally but its angular extent is conserved, as shown in Figure 3-1. The left case is representative of solar maximum, when the solar wind speed is roughly uniform in the meridianal plane. The right panel represents solar minimum, when fast solar wind originates from large polar coronal holes and slow wind is confined to low latitudes associated with helmet streamers [e.g., McComas et al., 1998]. The flux rope is bent convexly outward by a spherical expansion of the solar wind (left panel) or concavely outward by a structured wind (right panel).

From Figure 3-1, we obtain a simple relationship between the latitude θ of an observing spacecraft and the normal elevation angle δ of the flux rope at the spacecraft

$$\delta = \arcsin\left(\frac{R}{R_c}\sin\theta\right). \tag{3.1}$$

The radius of curvature, R_c, is defined such that it is positive when the flux rope is curved away from the Sun (left panel) and negative when curved toward the Sun (right panel). In the left case, $R_c = R$, so equation (3.1) is reduced to $\theta = \delta$. Since MCs are highly flattened as discussed above, the normal would be along the minimum variance direction of the flux-rope magnetic field. The radius of curvature of MCs can be extracted from equation (3.1) by examining the latitudinal distribution of the

normal elevation angles. Lower limits for the transverse size of MCs can be derived from pairs of spacecraft widely separated in latitude. Ulysses, complemented with a near-Earth spacecraft, is particularly useful for this research since it covers latitudes up to 80° [e.g., Hammond et al., 1995; Gosling et al., 1995b].

This chapter applies the above methodology to give the first direct observational evidence for the large-scale transverse size and curvature of MCs. The data and analysis methods are described in section 3.2. Sections 3.3 and 3.4 give lower limits for the transverse size of MCs and study how they are curved in different solar wind states, respectively. We summarize and discuss the results in section 3.5.

3.2 Observations and Data Analysis

To give a meaningful measure of the transverse size, we need at least two spacecraft separated as widely as possible in the solar meridianal plane. Launched in 1991, Ulysses explores the solar wind conditions at distances from 1 to 5.4 AU and up to 80° in latitude. WIND and ACE have provided near-Earth measurements (within 7° of the solar equatorial plane) since 1994 and 1998, respectively. We first look for MCs in Ulysses data when it is more than 30° away from the solar equator. If we see the same MC at the near-Earth spacecraft, then its transverse width is at least the spacecraft separation. To determine if the spacecraft observe the same MC, we look at the timing and data similarities (similar transient signatures, the same chirality, etc.), and use a one-dimensional (1-D) MHD model to do data alignment.

We require that the MC axis lie close to the solar equatorial plane. Otherwise, the width we invert is the length of the flux rope other than the transverse size of the cross section; this requirement also minimizes the effect of axial curvature. In addition, our curvature study needs MCs not to be aligned with the radial direction. WIND observations in 1995 - 1997 are used to investigate the MC curvature near solar minimum, while Ulysses as well as the near-Earth spacecraft provides observations from 1999 to 2003 for the curvature study near solar maximum.

3.2.1 Coordination of Observations via 1-D MHD Modeling

Single-point observations can only sample MCs at a specific distance. As MCs propagate in the solar wind, they may change appreciably. Models are needed to connect observations at different spacecraft. Studies to compare ICME observations at various locations have been performed, using ICME signatures and an MHD simulation to trace their evolution [e.g., Wang et al., 2001; Richardson et al., 2002; Riley et al., 2003]. We follow the same approach and use a 1-D MHD model developed by Wang et al. [2000] to propagate the solar wind from 1 AU to Ulysses. Momentum and energy source terms resulting from the interaction between solar wind ions and interstellar neutrals can be included in this model, but we drop them since they have a negligible effect on the solar wind propagation within Ulysses' distance. All physical quantities at the inner boundary (1 AU) are set to the average near-Earth solar wind conditions; the MHD equations are then solved by a piecewise parabolic scheme to give a steady

state solar wind solution. Observations at 1 AU (typically 60 days long) containing the ICME data are introduced into the model as perturbations. The numerical calculation stops when the perturbation has traveled to Ulysses. The model output is compared with Ulysses observations. Note that the 1-D model assumes spherical symmetry, so we do not expect the model output to exactly match the Ulysses data. Nevertheless, large stream structures should be similar and allow us to align these data sets.

3.2.2 Minimum Variance Analysis

The axis orientation of MCs is needed to specify their global structure. Minimum variance analysis (MVA) of the measured magnetic field yields useful principle axes [e.g., Sonnerup and Cahill Jr., 1967; Sonnerup and Scheible, 1998]. A normal direction, $\hat{\mathbf{n}}$, can be identified by minimizing the deviation of the field component $\mathbf{B}^m \cdot \hat{\mathbf{n}}$ from $\langle \mathbf{B} \rangle \cdot \hat{\mathbf{n}}$ for a series of measurements of $m = 1, \ldots, N$

$$\sigma^2 = \frac{1}{N} \sum_{m=1}^{N} |(\mathbf{B}^m - \langle \mathbf{B} \rangle) \cdot \hat{\mathbf{n}}|^2, \tag{3.2}$$

where $\langle \mathbf{B} \rangle$ is the average magnetic field vector. Optimizing the above equation under the constraint of $|\hat{\mathbf{n}}|^2 = 1$ results in the eigenvalue problem of the covariance matrix of the magnetic field

$$M_{\mu\nu} = \langle B_\mu B_\nu \rangle - \langle B_\mu \rangle \langle B_\nu \rangle, \tag{3.3}$$

where μ, ν indicate the field components in Cartesian coordinates. Eigenvectors of the matrix, $\hat{\mathbf{x}}^\star$, $\hat{\mathbf{y}}^\star$, $\hat{\mathbf{z}}^\star$, corresponding to the eigenvalues in order of decreasing magnitude, denote the the maximum, intermediate and minimum variance directions. The normal of an elongated flux rope should be along the minimum variance direction (see Figure 3-1); the maximum variance would occur azimuthally since the azimuthal component changes its sign across the flux rope; the intermediate variance direction is identified as the axis orientation due to the non-uniform distribution of the axial field over the flux-rope cross section. The MVA method also gives the chirality of the flux-rope fields as shown in the bottom panels of Figures 3-2, 3-3 and 3-4.

Angular error estimates of the directions can be written as [Sonnerup and Scheible, 1998]

$$\Delta\varphi_{ij} = \sqrt{\frac{\lambda_z(\lambda_i + \lambda_j - \lambda_z)}{(N-1)(\lambda_i - \lambda_j)^2}} \tag{3.4}$$

for $i, j \in \{\hat{\mathbf{x}}^\star, \hat{\mathbf{y}}^\star, \hat{\mathbf{z}}^\star\}$ and $i \neq j$, where λ_i denotes the eigenvalue of the variance matrix, and $\Delta\varphi_{ij}$ represents the angular uncertainty of eigenvector i with respect to eigenvector j. The uncertainty of the normal elevation angle δ is

$$\Delta\varphi_z = \sqrt{(\Delta\varphi_{zx})^2 + (\Delta\varphi_{zy})^2}, \tag{3.5}$$

where we assume that the errors are independent.

Table 3.1: Estimated parameters of MCs at ACE and Ulysses[a]

No.	Year	CME Onset[b]	Start	End	R^c (AU)	θ^c (°)	ϕ^c (°)	Θ^d (°)	Φ^d (°)	Chirality
1	1999	Jul 29, 05:43	Aug 2, 15:36	Aug 3, 10:34	1	5.9	234.3	−42.4 (−48.8)	251.2 (261.5)	L
	1999	-	Aug 19, 00:00	Aug 20, 12:00	4.7	−32.3	87.4	−7.1 (−11.3)	283.9 (261.9)	L
2	2000	Mar 14, 10:08	Mar 19, 03:22	Mar 19, 12:43	1	−7.1	103.0	24.3 (29.2)	51.4 (95.8)	R
	2000	-	Mar 31, 12:00	Apr 1, 07:12	3.7	−50.1	93.1	19.1 (13.6)	112.2 (90.0)	R
3	2001	Nov 6, 16:39	Nov 10, 19:12	Nov 11, 07:55	1	3.3	333.0	−37.8 (−16.5)	151.1 (121.9)	L
	2001	-	Nov 14, 12:00	Nov 15, 14:24	2.3	75.4	39.5	−16.6 (−15.4)	104.7 (103.4)	L
PR[e]	1999	Feb 15, -[f]	Feb 18, 13:55	Feb 19, 11:02	1	−7.0	74.0	0.4 (−30.1)	277.1 (284.7)	L
	1999	-	Mar 3, 21:36	Mar 5, 21:36	5.1	−22.3	85.2	−38.0 (−35.3)	269.3 (265.2)	L

[a] Corresponding to the first and second lines for each case, respectively.
[b] Obtained by extrapolating the quadratic fit of the CME's height-time curve to the solar surface.
[c] Heliographic inertial distance, latitude and longitude of the spacecraft.
[d] Axis elevation angle with respect to the solar equatorial plane and azimuthal angle in RTN coordinates, estimated from MVA (outside parentheses) and the GS technique (inside parentheses).
[e] The case studied by Riley et al. [2003].
[f] No CMEs observed at the Sun on 15 February 1999.

3.2.3 Grad-Shafranov Technique

Initially designed for the study of the terrestrial magnetopause [e.g., Hau and Sonnerup, 1999], the GS technique can be applied to flux-rope reconstruction [e.g., Hu and Sonnerup, 2002]. It assumes an approximate deHoffmann-Teller (HT) frame in which the electric field vanishes everywhere. This reference frame can be obtained by minimizing the residual electric field, provided that plasma velocities relative to the HT frame are substantially smaller than the local Alfvén velocity, a measure of the dynamic effect [Khrabrov and Sonnerup, 1998]. It follows from Faraday's law, $\nabla \times \mathbf{E} = -\frac{\partial \mathbf{B}}{\partial t}$, that the magnetic field is quasi-stationary when viewed in the HT frame. Structures in such a frame obey MHD equilibrium, $\mathbf{j} \times \mathbf{B} - \nabla p = 0$, which can be reduced to the so-called GS equation (see section 2.3.2)

$$\frac{\partial^2 A}{\partial x^2} + \frac{\partial^2 A}{\partial y^2} = -\mu_0 \frac{d}{dA}\left(p + \frac{B_z^2}{2\mu_0}\right)$$

by assuming a translational symmetry along the flux rope (i.e., $\frac{\partial}{\partial z}$=0). The vector potential is defined as $\mathbf{A} = A(x, y)\hat{\mathbf{z}}$, through which the magnetic field is given by $\mathbf{B} = (\frac{\partial A}{\partial y}, -\frac{\partial A}{\partial x}, B_z)$.

The key idea in reconstructing the flux rope is that the thermal pressure p and the axial field B_z are functions of A alone. The flux-rope orientation is determined by the single-valued behavior of the transverse pressure $p_t = p + B_z^2/2\mu_0$ over the vector potential A, which essentially requires that the same field line be crossed twice by an observing spacecraft. Observations yield the transverse pressure, while the vector potential along the spacecraft trajectory ($y = 0$) is derived from $A(x, 0) = -\int B_y(x, 0)dx$. Once the invariant z axis is acquired, the right-hand side of the equation can be derived from the differentiation of the best fit of p_t versus A. This best fit is assumed to hold over the entire flux-rope cross section. Away from the observation baseline, the vector potential A is calculated based on its second order Taylor expansion with respect to y. Since the integration is intrinsically a Cauchy problem, numerical singularities are generated after a certain number of steps. As a result, the transverse size is generally limited to half of the width along the observation line in the integration domain. Detailed procedures can be found in Hau and Sonnerup [1999] and Hu and Sonnerup [2002]. Here we only use this approach to determine the axis orientation of MCs and make a comparison with MVA.

3.3 Lower Limits of the Transverse Extent

Application of the criteria and restrictions given in section 3.2 yields three MCs observed at both ACE and Ulysses with a latitudinal separation larger than 30°. Table 3.1 lists the times, locations, estimated axis orientations and chiralities for ACE and Ulysses observations, respectively. The distance R, latitude θ and longitude ϕ of the spacecraft are given in the heliographic inertial frame. The MC denoted as PR in the table was shown to be observed at both the spacecraft by Riley et al. [2003] through a qualitative comparison between data and an MHD model output; the two

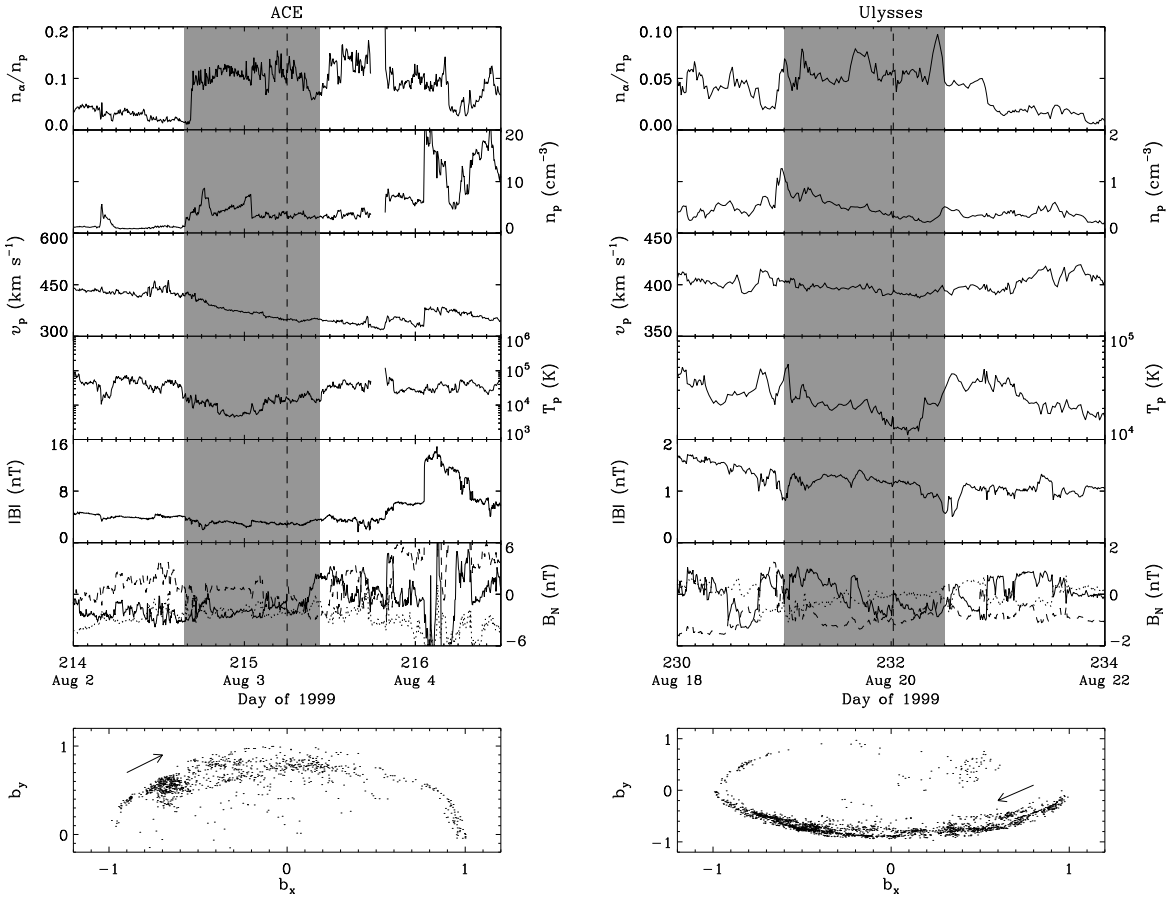

Figure 3-2: Solar wind plasma and magnetic field parameters measured by ACE (left panel) and Ulysses (right panel) for Case 1 in Table 3.1. From top to bottom, the panels show the alpha-to-proton density ratio, proton density, bulk speed, proton temperature, magnetic field strength, magnetic field components (solid line for B_N, dotted line for B_R, dashed line for B_T), and rotation of the normalized magnetic field vector inside the MC in the maximum variance plane. The shaded region shows the MC. Dashed lines denote the separation of the two flux ropes contained in the MC. Arrows in the bottom panels show the direction of the magnetic field rotation.

spacecraft were separated by 15° in latitude. Table 3.1 also gives the CMEs observed at the Sun (adopted from `http://cdaw.gsfc.nasa.gov/CME_list`) that best match the occurrence time calculated from the MC's transit speed at 1 AU. Applications of the MVA method to the normalized magnetic field measurements and the GS technique to the plasma and magnetic field observations within the MCs give the axis orientation, in terms of the elevation (Θ) and azimuthal (Φ) angles. The axis azimuthal angle is given in RTN coordinates, which allows us to see if the axis is perpendicular to the radial direction (i.e., close to 90° or 270°). The magnetic field and velocity vectors inside the MCs are rotated into the heliographic inertial frame in order to have an axis elevation angle with respect to the solar equatorial plane. The estimates of the axis orientation from the MVA and GS methods roughly agree. The

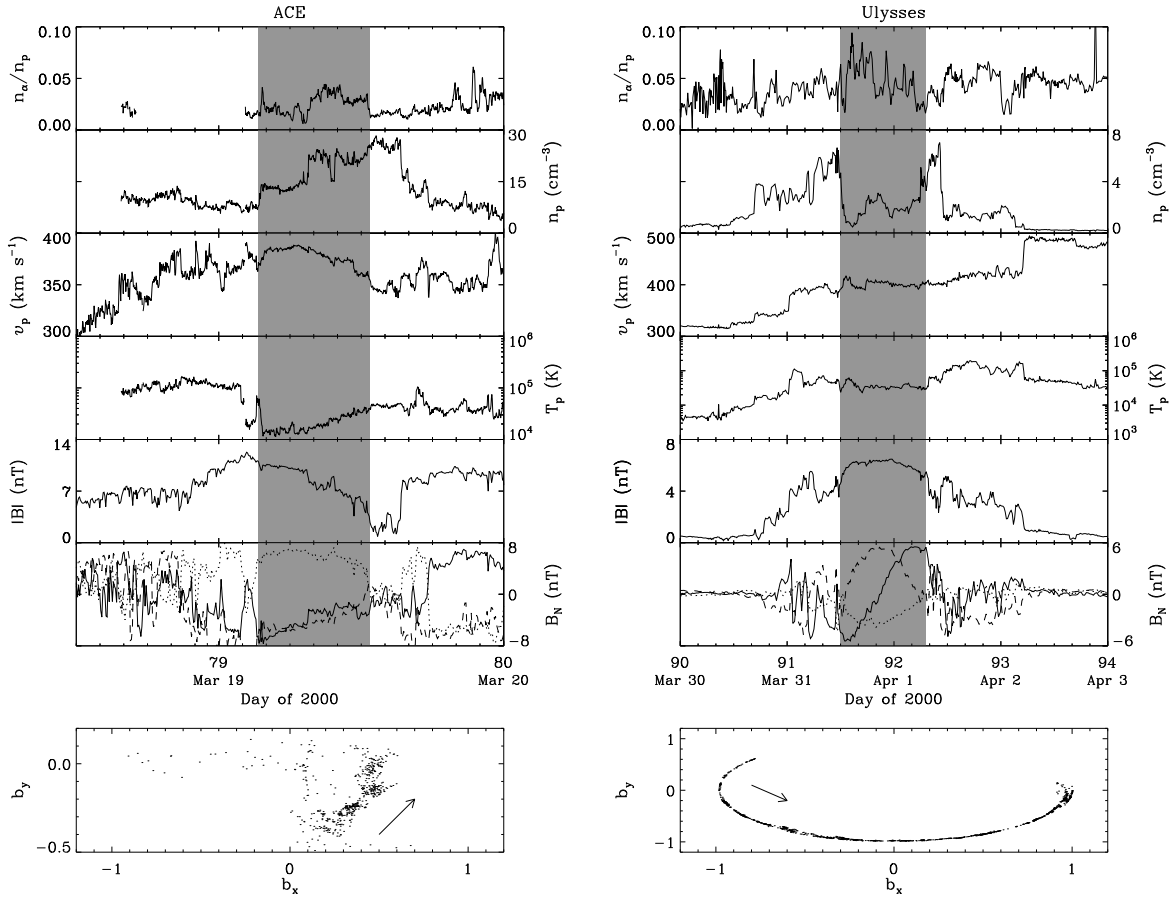

Figure 3-3: Solar wind plasma and magnetic field parameters for Case 2 in Table 3.1. Same format as Figure 3-2.

MCs generally lie close to the solar equator and perpendicular to the radial direction. The MC travel time from ACE to Ulysses is consistent with the observed speeds. They also have the same chirality as listed in Table 3.1.

Figure 3-2 shows the plasma and magnetic field measurements for Case 1 in Table 3.1 at ACE and Ulysses separated by 38° in latitude. Its boundaries are mainly determined from the low proton temperature combined with enhanced helium abundance. The helium enhancement has been shown to be an effective tool to trace ICMEs from 1 AU to Ulysses and Voyager 2 [e.g., Paularena et al., 2001; Richardson et al., 2002]. The MVA of the magnetic field measurements inside the MC at ACE and Ulysses gives an eigenvalue ratio $\lambda_x : \lambda_y : \lambda_z$ of 6 : 1 : 0.8 and 3.2 : 1 : 0.2, respectively. The MC has a relatively large axis elevation angle ($> 40°$) at ACE, probably due to the small separation between λ_y and λ_z; the axis orientation is close to the solar equator at Ulysses. The bottom panels of Figure 3-2 display the normalized magnetic field inside the MC projected onto the maximum variance plane. The majority of the data show a coherent rotation of about 180°; both the rotations indicate a left-handed chirality of the magnetic configuration. Interestingly, the GS reconstruction shows that this case contains two nested flux ropes in both ACE and

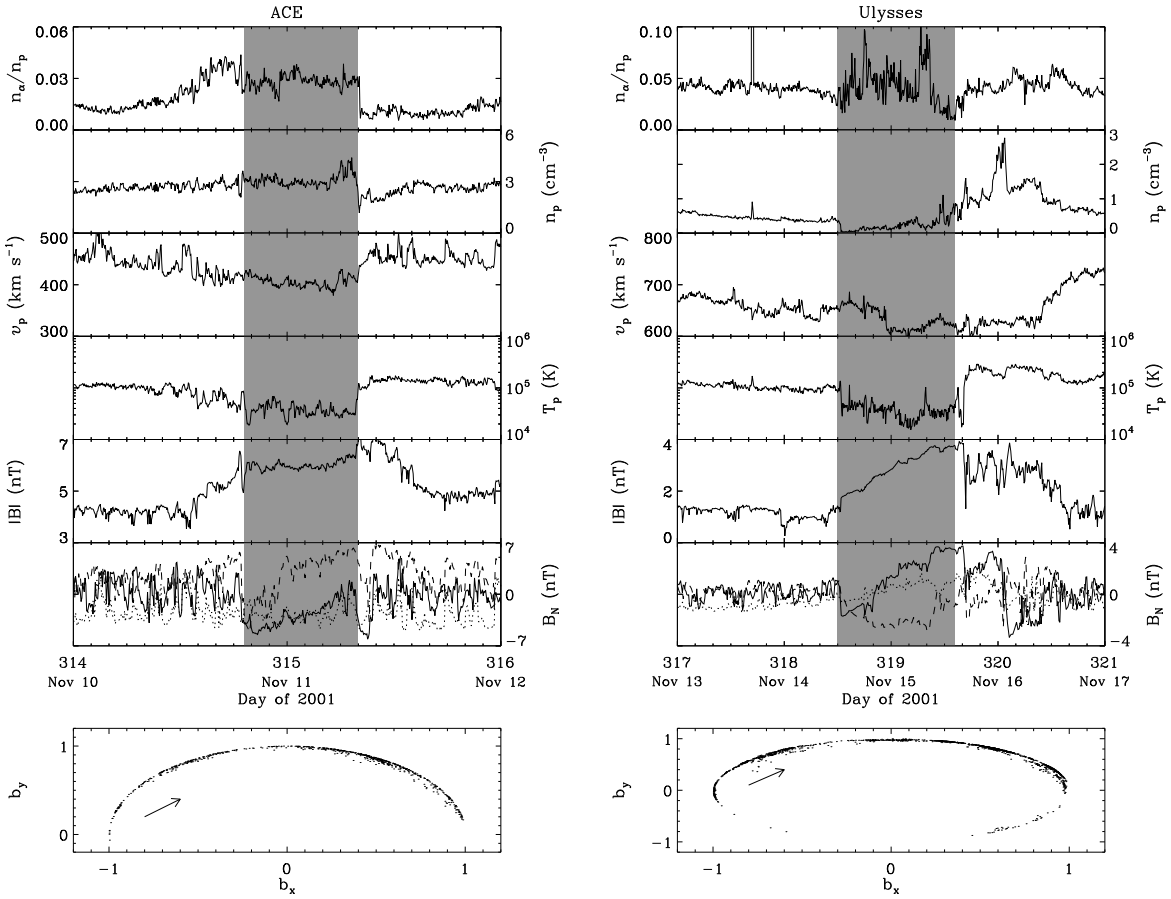

Figure 3-4: Solar wind plasma and magnetic field parameters for Case 3 in Table 3.1. Same format as Figure 3-2.

Ulysses measurements. Marked as a dashed line in Figure 3-2, the separation of the two flux ropes in both ACE and Ulysses observations appears as a discontinuity in the proton density (second panels) and magnetic field components (sixth panels). A shock wave, indicated by simultaneous sharp increases in the proton density, speed, temperature and magnetic field strength, follows the MC at ACE and Ulysses (not shown in the Ulysses data).

Figure 3-3 displays the data for Case 2 at ACE and Ulysses separated by 43° in latitude. ACE and Ulysses are roughly aligned in longitude for this case. The boundaries are determined from the rotation of the magnetic field together with the low proton temperature. This event is also associated with a small bump in the helium/proton density ratio. The eigenvalue ratio $\lambda_x : \lambda_y : \lambda_z$ determined from the MVA is $2.5 : 1 : 0.2$ and $3.2 : 1 : 0.02$ for ACE and Ulysses observations, respectively. It drives a forward shock at Ulysses which may also be seen at ACE, but data gaps at ACE make it difficult to locate the shock. Again, the normalized magnetic field data inside the MC at ACE and Ulysses show a right-handed rotation in the maximum variance plane.

Figure 3-4 shows the data for Case 3 which has the largest separation (72°) in

latitude between ACE and Ulysses. Depressed proton temperature and magnetic field rotation combined with enhanced helium abundance are used to determine the boundaries. The velocity and magnetic field fluctuations are strongly anti-correlated outside the MC both at ACE and Ulysses, which indicates the presence of Alfvén waves; this wave activity also occurs within the MC but at a reduced fluctuation level. The eigenvalue ratio $\lambda_x : \lambda_y : \lambda_z$ from the MVA is 6.8 : 1 : 0.3 for ACE measurements and 3.4 : 1 : 0.1 for Ulysses observations. Smooth rotations of about 180° in the magnetic field (bottom panels) indicate a left-handed chirality.

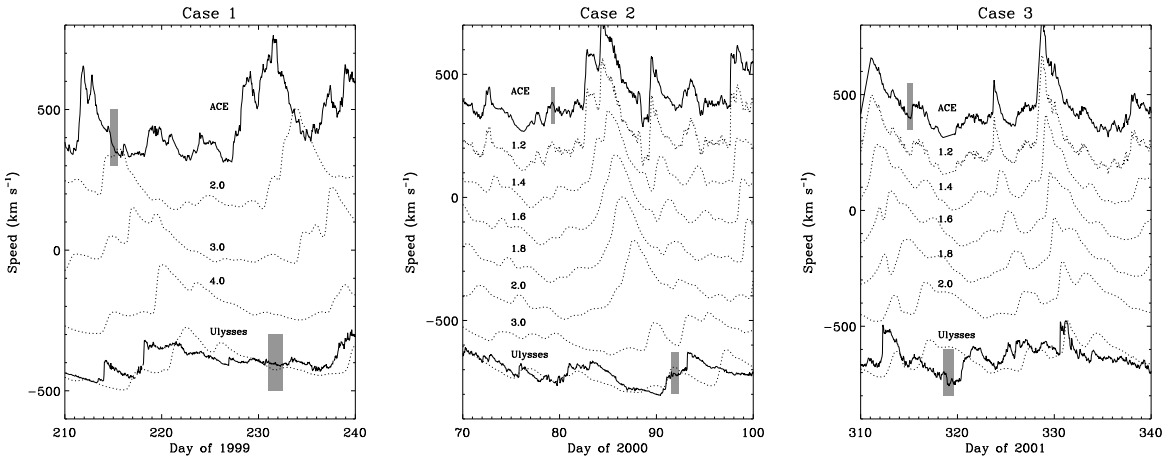

Figure 3-5: Evolution of solar wind speed from ACE to Ulysses for the three cases in Table 3.1 via the 1-D MHD model. The upper and lower solid lines show the solar wind speeds observed at ACE and Ulysses, while the dotted lines indicate the speed profiles predicted by the model at distances (in AU) marked by the numbers. Shaded regions represent the period where the MC was observed at ACE and Ulysses. Each speed curve is decreased by 200 km s^{-1} (left panel) and 160 km s^{-1} (middle and right panels) with respect to the previous one so that the individual line shapes can be easily deciphered. For Case 3 (right panel), the profile at Ulysses is shifted downward by 1360 km s^{-1} from the observed speed, while the model output at 2.3 AU is shifted by 1040 km s^{-1} to line up with the Ulysses data; the model output at Ulysses underestimates the observed speed by 320 km s^{-1}.

We propagate the ACE data to Ulysses using the 1-D MHD model described in section 3.2. Figure 3-5 shows the velocity profiles observed at ACE and Ulysses (solid lines), and the model profiles at certain distances (dotted lines) for the three cases. In all of these cases, larger streams at 1 AU persist to Ulysses as clearly shown by the traces and model-data comparison at Ulysses, while smaller ones smooth out. For Cases 1 and 2 (left and middle panels), the model outputs at Ulysses agree qualitatively well with the observed speed profiles. Note that the model-predicted and observed speeds were not shifted to produce this agreement. For Case 3 (right panel), the model predicts a slower solar wind than observed at Ulysses, which is reasonable given the large latitudinal separation (72°) between ACE and Ulysses and possible differences in the ambient solar wind. Based on the good stream alignment

and data similarities shown in Figures 3-2, 3-3 and 3-4, we conclude that the two spacecraft see the same events.

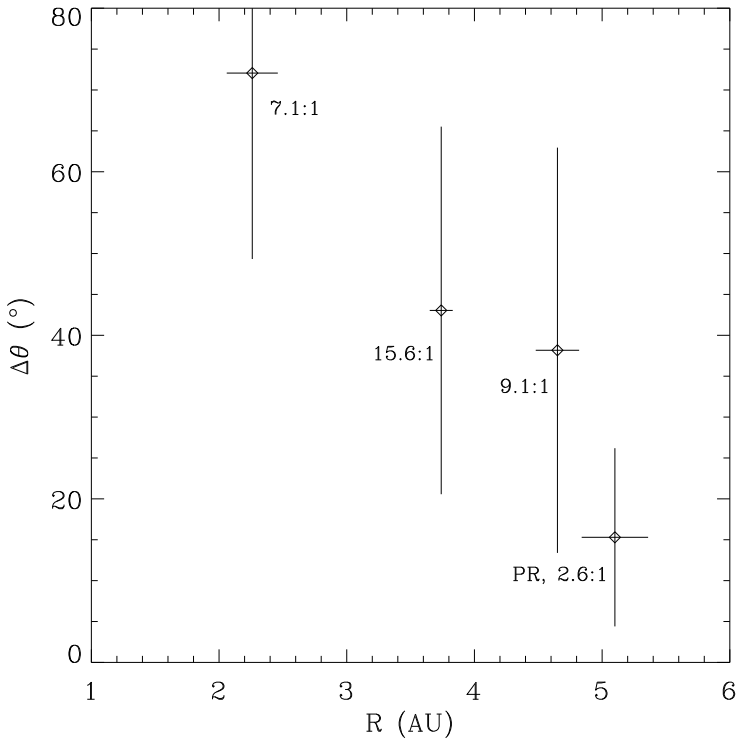

Figure 3-6: Latitudinal separation between ACE and Ulysses for the MCs listed in Table 3.1 as a function of Ulysses' heliocentric distance. The horizontal bars show the radial width of the MCs, and the vertical bars indicate the lower limit of the transverse size (converted to a length scale). Text depicts the corresponding ratio of the two scales.

The MCs listed in Table 3.1 offer observational evidence for the large transverse size of ICMEs. In order to quantify the transverse size, we examine the latitudinal separation between ACE and Ulysses for these MCs. The latitudinal separation ($\Delta\theta$) serves as a measure of the transverse size, S_t, expressed as

$$S_t = R\Delta\theta, \tag{3.6}$$

where R is the heliocentric distance of the MCs at Ulysses. This equation explicitly assumes that the latitudinal extent of the MCs is constant during their propagation through the solar wind. The results for the present MCs are plotted in Figure 3-6. The transverse size given by the above equation is much larger than the MCs' radial width obtained from their average speed multiplied by the time duration. As can seen from Figure 3-6, the largest aspect ratio is 15.6 : 1. The PR event has a ratio of 2.6 : 1 since $\Delta\theta$ is only 15.3° for this case. Figure 3-6 reveals that the MCs have a cross section greatly elongated in the latitudinal direction.

The large transverse size can also be inferred from the shock standoff distance d ahead of fast MCs written as [Russell and Mulligan, 2002]

$$\frac{d}{L} = 0.41 \frac{(\gamma - 1)M^2 + 2}{(\gamma + 1)(M^2 - 1)},$$

where $\gamma = \frac{5}{3}$, M is the Mach number of the preceding shock, and L is the characteristic scale of MCs, presumably a measure of S_t. From the superposed epoch data of 18 near-Earth MCs with preceding shocks (see Chapter 5), we have $M = 3.4$ and $d = 0.17$ AU on average. Substitution of these values into the above equation gives $L = 1.2$ AU, which corresponds to a latitudinal extent of $\sim 69°$ obtained from equation (3.6). Consistent with our direct evidence, the transverse size of MCs (or ICMEs in general) could be very large.

3.4 Curvature of Magnetic Clouds

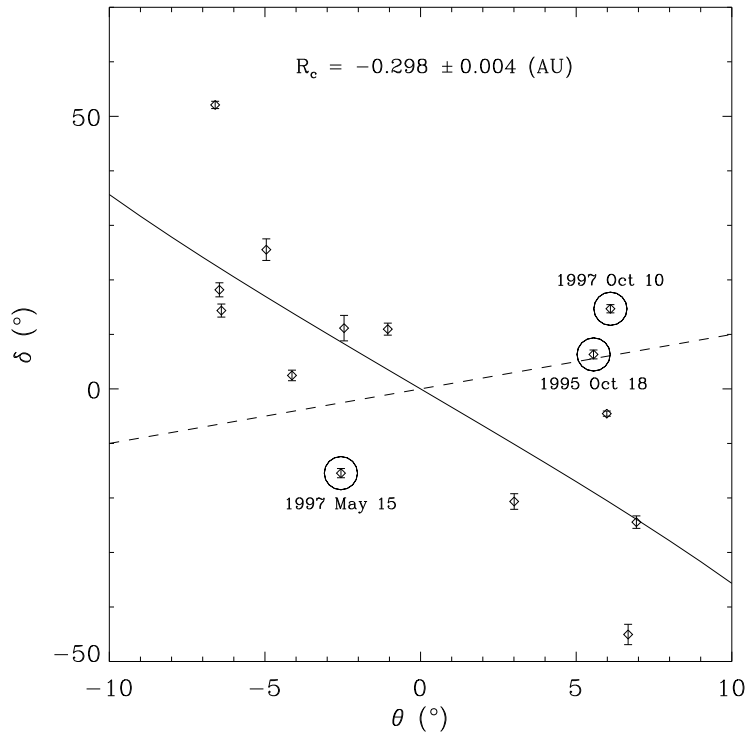

Figure 3-7: Elevation angles of the MC normal from the solar equatorial plane as a function of WIND's heliographic latitude. Circles with a nearby date indicate events that do not have an inverse correlation. The solid line represents the best fit of the data that obey the relationship using equation (3.1). The radius of curvature resulting from the fit is given by the text in the figure. The dashed line shows what would be expected if the MCs were convex outward with a radius of curvature of 1 AU.

A direct consequence of the large transverse size is that MCs encounter different solar wind flows in the meridianal plane. MCs can thus be highly distorted depending on the ambient solar wind conditions. The simplified scenario described in section 3.1 indicates that MCs should be ideally concave outward at solar minimum and convex outward during solar maximum. This curvature effect results in an inverse correlation between δ and θ at solar minimum and a positive correlation near solar maximum as shown by equation (3.1). Note, however, that this is a greatly simplified picture. In reality, the shape of MCs will be determined by the speed at which they travel with respect to the background solar wind, ambient magnetic fields, the presence of other ICMEs or obstacles nearby, and other features that are beyond the scope of this work.

As discussed in section 3.2, the distortion effect by solar wind flows would be most prominent if MCs have axes close to the solar equator and perpendicular to the radial direction. In order to have enough events for our curvature analysis, we include all the MCs whose axes lie within 30° of the solar equatorial plane and more than 30° away from the radial direction.

3.4.1 MCs in a Structured Solar Wind

Close to solar minimum, the solar wind is well ordered with fast wind originating from polar coronal holes and slow wind near the solar equatorial plane. WIND observations from 1995 - 1997 are used to assess the distortion effect of the latitudinal flow gradient on MCs. Figure 3-7 shows the normal elevation angles for the 14 events observed at WIND. Estimated parameters of these events are listed in Table A.1 of Appendix A. The error bars are obtained from equation (3.5). An inverse correlation is observed between δ and θ, except for three events. The MCs are expected to be concave outward during solar minimum, which is largely observed, made evident by the inverse relationship plotted as a solid line. The three events where δ and θ have the same sign indicate a convex outward curvature, contrary to the solar minimum prediction. A closer look at the 1997 May 15 event reveals an increasing speed profile indicative of a high-speed stream interacting with the sunward edge of the MC. As a result, the MC is bent to be convex outward. Note that the simplified picture described in section 3.1 assumes a minimum solar wind speed at the solar equator. It is conceivable that δ and θ may have the same sign if the minimum speed shifts away from the zero latitude. Although the breakdown of the assumption is a possible explanation for the other two exceptions, this effect may be negligible since most of the events in Figure 3-7 have the inverse correlation. The best fit to the data that show the inverse correlation, obtained with a least squares analysis of equation (3.1), gives a radius of curvature of -0.3 AU. Compared with the convex-outward representation (dashed line), the data clearly show the trend pictured by the right panel of Figure 3-1.

3.4.2 MCs in a Uniform-Speed Solar Wind

At solar maximum, the solar wind speed tends to be more uniform over heliographic latitude. We use Ulysses observations between 1999 and 2003 to quantify the curvature effect of solar wind spherical expansion on MCs. Our prescription yields 13

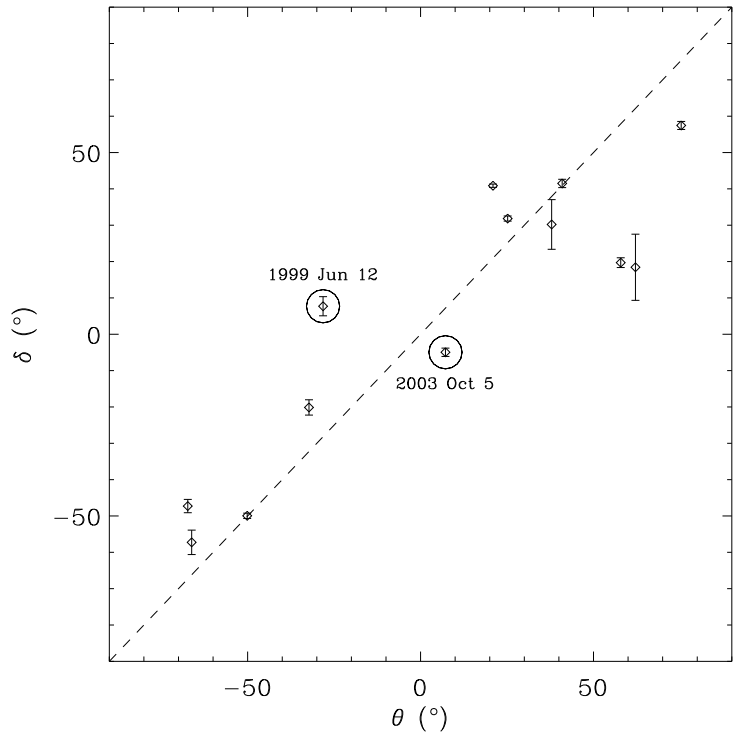

Figure 3-8: Elevation angles of the MC normal from the solar equatorial plane as a function of Ulysses' heliographic latitude. Circles with a nearby date indicates events that do not have a positive correlation. The dashed line represents $\delta = \theta$.

events shown in Figure 3-8. These MCs are also listed in Table A.2 of Appendix A, together with their parameters. In a uniform solar wind the MCs would have a radius of curvature equal to their distance from the Sun, which results in a proportional relationship, i.e., $\delta = \theta$ from equation (3.1). Only two events do not have a positive correlation. More specifically, δ and θ have opposite signs for the two events. They are the first and last ones in the time series of the MCs; as indicated by the dates, they may not truly come from the solar maximum environment. The data nearby the $\delta = \theta$ curve (dashed line) manifest a convex-outward structure at solar maximum as illustrated by the left panel of Figure 3-1.

3.5 Summary and Discussion

We have investigated the transverse size and curvature of the MC cross section, based on ACE, WIND and Ulysses observations. The results provide compelling evidence that MCs are highly stretched in the latitudinal direction and curved in a fashion depending on the background solar wind.

Three MCs, whose axes are close to the solar equator and roughly perpendicular to the radial direction, are shown to pass ACE and Ulysses (widely separated in latitude)

successively. The MVA method combined with the GS reconstruction technique is used to determine the axis orientation and the observations at ACE and Ulysses are linked using a 1-D MHD model. The latitudinal separation between ACE and Ulysses gives a lower limit to the MCs' transverse size. Varying from 40° to 70°, it reveals that the transverse size can be very large. The flattened cross section is a natural result of a flux rope subtending a constant angle as it propagates from the Sun through the heliosphere (see Figure 3-1).

The radius of curvature is obtained from a simple relationship between the MC normal elevation angle and the latitude of an observing spacecraft. The curvature of MCs in the solar wind with a latitudinal speed gradient at solar minimum differs from that in the uniform-speed solar wind near solar maximum. At solar minimum, MCs are bent concave-outward by the structured solar wind with a radius of curvature of about 0.3 AU; at solar maximum, they tend to be convex outward with the radius of curvature proportional to their heliographic distance. The distortion of MCs, resulting from the interaction with the ambient solar wind, is mainly a kinematic effect since magnetic forces are dominated by the flow momentum [Riley et al., 2004].

Improvement of our knowledge of the global structure of MCs (or generic ICMEs) is of critical importance for heliosphere physics and space weather prediction. Proper estimates of the magnetic flux and helicity of ICMEs require knowledge of the structure to quantify their connection with the coronal origin and to assess the modulation of heliospheric flux by CMEs. The existing flux-rope models, based on a single spacecraft cut through the large structure, may not capture the true dimension and distortion of ICMEs. The flux content and helicity can be significantly underestimated since these quantities are highly sensitive to the flux-rope scale. The large transverse size and curvature can alter the global configuration of the interplanetary magnetic field as ICMEs sweep through the heliosphere. Numerical simulations show that the ambient magnetic field extending from the Sun to high latitudes may bend poleward to warp around the flattened flux rope [e.g., Manchester et al., 2004], as initially proposed by Gosling and McComas [1987] and McComas et al. [1988]. The field line draping leads to favorable conditions for the formation of plasma depletion layers and temperature anisotropy instabilities in the sheath region of fast ICMEs (see Chapter 5). A magnetic field bent southward would also allow for strong coupling between the solar wind and the magnetosphere via field line merging [Dungey, 1961]. The curvature of ICMEs could modify the shape of preceding shock fronts, affecting plasma flows and particle acceleration at the shocks.

How general ICMEs are distorted remains unaddressed. Since their magnetic field is not well organized, the difficulty resides in how to best estimate their axis orientation. Future STEREO observations will provide perspectives for their geometry and also quantitatively test our results for MCs. Interestingly, the magnetic field within some ICMEs with low density and/or field strength also has a signature of rotation but is rather turbulent; the turbulent manifestation in the maximum variance plane is scatter deviating from the rotation trace. These ICMEs can be termed expanded MCs (EMCs). A good example of EMCs is the 1 April 2001 event at ACE (not shown here); three days later it is observed at Ulysses, and the field becomes even more turbulent. As Kumar and Rust [1996] suggest, an expanding flux rope loses magnetic

energy which may be dissipated as heat. The evolution of turbulence within the EMC leads us to conjecture the expansion and interaction with the ambient solar wind as a possible mechanism for turbulence generation inside ICMEs which is sought by Chapter 4.

The content of this chapter has been published in the *Journal of Geophysical Research* [see Liu et al., 2006c].

Chapter 4

Thermodynamic Structure of ICMEs

We investigate the thermodynamic structure of interplanetary coronal mass ejections (ICMEs) using combined surveys of the ejecta between 0.3 and 20 AU. ICMEs are shown to have a moderate expansion in the solar wind compared with theoretical predictions. The expansion seems to be governed by a polytrope with $\gamma \sim 1.3$ in this distance range. We find that Coulomb collisions are important contributors to the ion-ion equilibration process in the ICME plasma. The alpha-proton differential speed quickly drops to below 10 km s^{-1} due to strong Coulomb collisions. However, the two species of particles are far from thermal equilibrium with a temperature ratio T_α/T_p = 4 - 6, suggestive of a preferential heating of alpha particles. The plasma heating rate as a function of heliocentric distance required for the temperature profile is deduced by taking into account the expansion and energy transfer between protons and alphas via Coulomb collisions. The turbulence dissipation rate is also inferred from the inertial range power spectrum of magnetic fluctuations within ICMEs. Comparison of the turbulence dissipation rate with the required heating rate shows that turbulence dissipation seems sufficient to explain the ICME heating. Sources powering the turbulence are also investigated by examining the instabilities induced by temperature anisotropies and energy deposition by pickup ions.

4.1 Introduction

In situ measurements show that ICMEs usually have a depressed temperature compared to the ambient solar wind [e.g., Richardson and Cane, 1993]. This low temperature would make the ICME plasma collision-dominated as the plasma expansion time may be close to or even larger than the Coulomb collision time. The importance of the strongly collisional nature of the ICME plasma in regulating ion properties will be studied in this chapter. ICMEs often undergo expansion in the solar wind since their leading edges usually move faster than the trailing edges and/or their internal pressures are higher than in the ambient solar wind. As a result, the ICME plasma is expected to expand and be collision-dominated, which has significant consequences

for modeling the realistic thermodynamics of ICMEs.

Recent global MHD modeling of ICMEs [e.g., Odstrcil et al., 2002; Riley et al., 2003; Manchester et al., 2004] provides a useful tool for interpreting the observations. In these simulations a polytropic gas with index $\gamma < 5/3$ is assumed to keep the physics of energy transport simple while retaining a fair amount of plasma heating. The polytropic process, in theory, is entropy-conserving and thus reversible, whereas the actual heating may be irreversible. Leamon et al. [1998b] examine the properties of magnetic fluctuations within an ICME at 1 AU and find that the power spectrum of the fluctuations shows a steepening at high frequencies, indicative of the onset of magnetic dissipation. Dissipation of turbulence has been considered the mechanism responsible for the solar wind heating in the past decade [e.g., Goldstein et al., 1995; Matthaeus et al., 1999; Smith et al., 2001]. The magnetic fluctuations represent nonlinear interacting modes of the system. The nonlinear interactions produce a flow of energy originating from low frequencies (large scales), which cascades through the inertial range (typically with a $f^{-5/3}$ form) and is then converted to thermal energy in the dissipation range (small scales). This spectral transfer can lead to significant heating of the plasma and is inherently irreversible. This intrinsic difference between the polytropic process and turbulence dissipation makes the modeling of the thermodynamic state of ICMEs a challenge. There is a large gap in our understanding of the micro-physics governing the energy transport process and the ICME signatures.

Observations of ICMEs over a range of radial distances in the heliosphere can constrain models of their thermodynamic structure. Liu et al. [2005] perform a statistical study of ICMEs from 0.3 to 5.4 AU using a multi-spacecraft survey. Wang and Richardson [2004] extend this research out to 30 AU based on the observations of Voyager 2. Combining these surveys with theoretical analysis, this chapter investigates the thermodynamic state and kinetic properties of the ICME plasma. In the next section, we demonstrate that ICMEs expand and Coulomb collisions are important within ICMEs. Section 4.3 contains theoretical analysis of the heating problem along with a discussion of the source of the turbulence. We close by summarizing our results in section 4.4.

4.2 Observations and Data Analysis

Two difficulties have stymied the development of a comprehensive view of ICMEs individually and as a class. The first is how to best identify ICMEs in the solar wind. Despite the plethora of ICME signatures, the identification of ICMEs still remains subjective. No individual characteristic is necessary and sufficient to define the presence of an ICME. Second, spacecraft are usually sparsely distributed and rarely radially aligned. Tracking specific ICMEs through the heliosphere is thus generally not possible.

A statistical representation of ICME properties bypasses the second difficulty, although the first one still applies. In this work, we combine different surveys of ICMEs to study their radial evolution. The first survey is conducted by Liu et al. [2005] from the Helios 1 and 2, WIND, ACE and Ulysses data. These spacecraft are at heliospheric

distances ranging from 0.3 to 5.4 AU. The criteria used to select ICMEs are that the observed proton temperature, T_p, is less than 0.5 of the expected temperature, T_{ex}, and the density ratio of alpha particles to protons, n_α/n_p, is larger than 8%. The expected temperature, essentially the typical temperature for normal solar wind, is inferred from the well-established relationship between the solar wind temperature and speed [e.g., Lopez, 1987]. By including the radial temperature gradient, this relationship can be applied at different radial distances. Wang and Richardson [2004] use the temperature criterion to identify ICMEs from Voyager 2 data out to 30 AU. Both of these surveys incorporate other signatures to determine the ICME boundaries. In order to make the statistical average more reliable, we search the Voyager 1 data for more events employing the same method as Wang and Richardson. Details about the ICME signatures and identification are described in Chapter 1. We cut off the study at 20 AU since the temperature criterion may become less reliable due to the heating by pickup ions. Furthermore, we use only the data within $\pm 20^\circ$ in latitude to assure a meaningful comparison of different data sets.

4.2.1 Expansion of ICMEs

Under these constraints, the above surveys yield about 280 ICMEs at Helios 1 and 2, Ulysses, Voyager 1 and 2. Figure 4-1 shows the radial widths of ICMEs versus distance from 0.3 to 20 AU. The radial width is the time duration of the ICME multiplied by the average speed. The best power law fit, obtained with least squares analysis, is represented by the solid line. The radial width increases with distance, with average values of about 0.22 AU at 1 AU and about 1.33 AU at 10 AU. A large scatter is seen in the outer heliosphere. Wang and Richardson [2004] show that about 40% of the solar wind is ICME material at 15-20 AU near solar maximum.

Two factors may contribute to the expansion of ICMEs. First, the magnetic field inside most ICMEs in the inner heliosphere is larger than in the ambient solar wind (see Figure 4-2). The higher magnetic field, which dominates the internal pressure of ICMEs, may cause the ICME plasma to expand. The magnetic pressure, however, may be balanced by the magnetic tension for a force-free configuration of the field [e.g., Suess, 1988; Cargill et al., 1997]. A magnetic field $\mathbf{B}$ is said to be force-free if the current density, $\mathbf{j}$, is aligned with the field. Magnetic clouds (MCs), a subset of ICMEs with smooth rotation of the magnetic field, have often been described by such a topology. In general, $\mathbf{j}$ and $\mathbf{B}$ are not exactly parallel due to the existence of a finite thermal pressure, p. The angle χ between the current density and the magnetic field can be estimated from $\sin\chi = \frac{|\mathbf{j}\times\mathbf{B}|}{jB}$. Consider MHD equilibrium, i.e., $\mathbf{j}\times\mathbf{B} - \nabla p = 0$. It can be readily shown that

$$\sin\chi \simeq \frac{p}{B^2/\mu_0} = \frac{1}{2}\beta,$$

where μ_0 is the permeability of free space. Here we assume that the length scales for the spatial variations of the magnetic field and gas pressure are of the same order in magnitude. The observed proton beta is usually 0.1-0.2 and the electron temperature

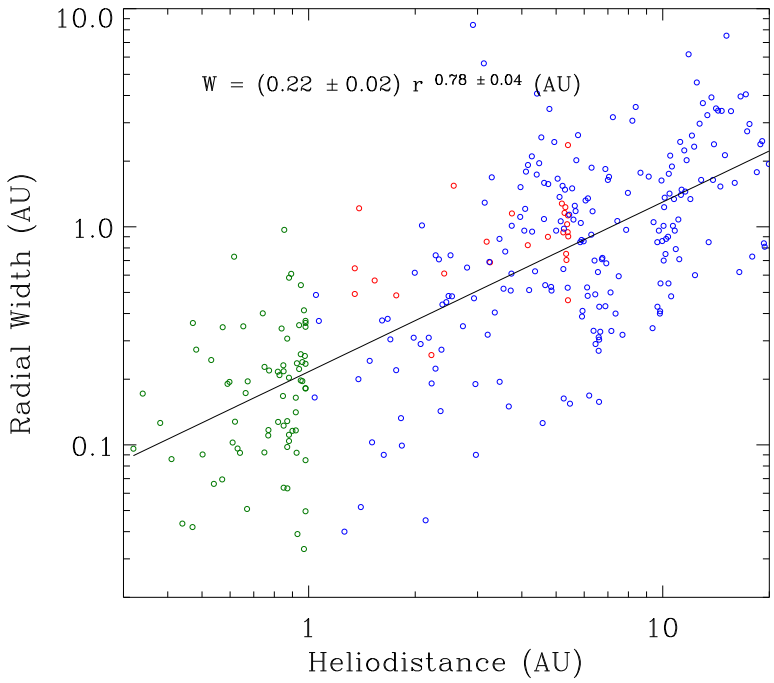

Figure 4-1: Radial widths of ICMEs observed by Helios 1 and 2 (green circles), Ulysses (red circles) and Voyager 1 and 2 (blue circles). The solid line shows the best power law fit to the data. The fit result is given by the text in this figure.

is ~ 3 times the proton temperature in ICMEs [Liu et al., 2005]. Therefore, the total plasma beta is 0.4-0.8, which gives an angle χ = 12-24° from the above equation. Considerable departures from force-free equilibrium exist for common ICMEs, so the overpressure may result in the ICME expansion. Second, the leading edges of ICMEs usually move faster than the trailing edges. The speed difference may result from the overpressure within ICMEs or may be a residual effect of the initiation of CMEs in the solar atmosphere. In the outer heliosphere (5-10 AU), ICMEs are frequently seen as low pressure regions accompanied by declining speed profiles. This characteristic provides evidence for the over-expansion of ICMEs but may also indicate the effect of the speed difference on the expansion. The contribution from the speed difference may be dominant in MC expansion with a small magnetic force involved.

The expansion of ICMEs can also be inferred from the plasma observations. Figure 4-2 displays the radial variation of the proton density n_p, bulk speed v_p, proton temperature T_p and the magnetic field magnitude B. The solid and dotted lines show the best power law fits to the ICME and solar wind data, respectively. Fit results are given by the text in each panel. The top and bottom panels indicate that the density and magnetic field within ICMEs decrease faster with distance than in the ambient solar wind, as expected if the ICMEs expand. ICMEs have a larger magnetic field than the ambient solar wind within 1 AU, which may contribute to the expansion of ICMEs as discussed above. The second panel suggests that the average ICME speed

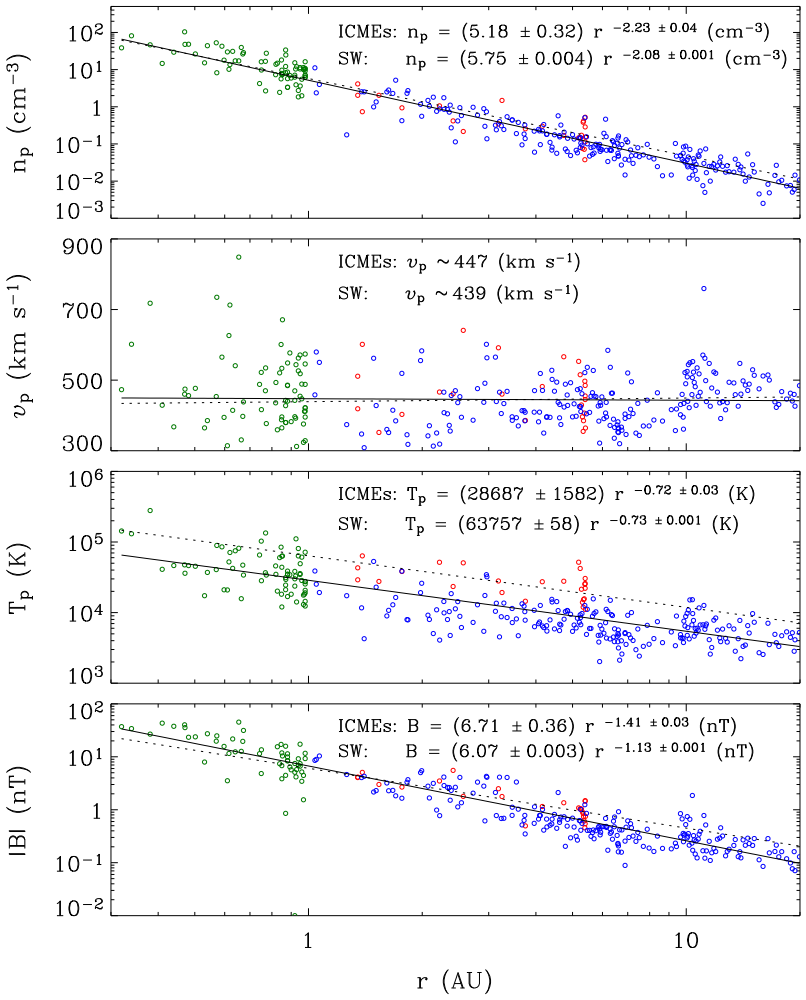

Figure 4-2: The average proton density, speed, temperature and the magnetic field strength in each ICME. Also displayed are fits to the ICME data (solid lines) and fits to the ambient solar wind (dotted lines), together with corresponding fit parameters (text). The color codes are the same as in Figure 4-1.

is comparable to the solar wind speed and remains constant in this distance range. The third panel shows that lower temperatures are seen within ICMEs than in the solar wind, as required by the ICME selection criteria. The expansion of ICMEs might be expected to result in a faster temperature decrease in ICMEs than that of the background solar wind due to adiabatic cooling. However, the temperature has a similar slope for ICMEs and the solar wind. Suppose that the ICME plasma can be described by a polytrope. The polytropic index, derived from the relation $T_p n_p^{1-\gamma} =$ const, is ~ 1.3 based on the fits in Figure 4-2, which is less than the adiabatic value 5/3. The physical interpretation is that local heating of the plasma must occur as ICMEs expand and move outward. We will investigate the heating mechanism in the next section.

4.2.2 Coulomb Collisions and Ion Properties

Understanding the thermodynamic state of ICMEs requires knowledge of the kinematic properties of the different ions in the ICME plasma and how they differ from those in the solar wind. Extensive studies of the solar wind show that heavy ions usually move faster than protons with the relative motion along the local magnetic field and are significantly hotter than protons [e.g., Feldman et al., 1974; Neugebauer, 1976; Marsch et al., 1982; Neugebauer et al., 1996; Reisenfeld et al., 2001]. Since the ICME plasma has a much lower temperature, ion properties in ICMEs may be different from those in the solar wind. An important consequence of the low temperature is that the Coulomb collision time between different particles, proportional to $T^{1.5}/n$ (see equations (4.4) and (4.5)), may be small compared to the expansion time of the plasma. Coulomb collisions should thus play an important role in the ion-ion equilibration process in the ICME plasma.

A typical example of an ICME is displayed in Figure 4-3 (hatched area). This event is observed by Helios 1 at 0.98 AU. Enhanced helium abundance (top panel) and depressed proton temperature (second panel) are used to identify this event. The third panel shows the expansion time τ_e divided by the Coulomb collision time $\tau_{\alpha p}$ (see section 4.3.1). This ratio, typically larger than unity within this event, is greatly boosted by the low temperature but drops to the order of 10^{-1} in the ambient solar wind. Particles in the ICME plasma therefore have plenty of time for collisions. Due to the strong Coulomb collisions the differential speed between alphas and protons, $v_{\alpha p} = |\mathbf{v}_\alpha - \mathbf{v}_p|$, is very small, which can be clearly seen in the fourth panel. The temperature ratio, T_α/T_p, is shown in the fifth panel. The short collision time suggests that the ions should be in thermal equilibrium. Surprisingly, T_α/T_p is higher within the ICME than in the ambient solar wind. The alpha particles must be preferentially heated; the preferential heating is not balanced by the energy loss to protons via Coulomb collisions. The above situation also occurs on days 38-39 when the temperature is reduced together with a small increase in the helium density. Also shown in this figure is the velocity of protons (bottom panel), which decreases across the ICME, suggestive of expansion of the event.

A global view of the differential speed and temperature ratios between alphas and protons in different plasmas is shown in Figure 4-4, based on 40 s averages of Helios 1 measurements. The whole data set, containing about 800,000 spectra, is binned into cells in the (n_α/n_p, T_p/T_{ex}) plane; wherever the data density permits, the bins are further subdivided, but each bin contains at least 1000 data points. The color bars indicate the average values in each bin for the two parameters. The black contours show the relative density of the measurements at the levels of 0.1, 0.3, 0.5, 0.7 and 0.9. The most probable state of the solar wind between 0.3 and 1 AU has $v_{\alpha p} \sim 30$ km s^{-1} and $T_\alpha/T_p \sim 3-4$, but note that radial variations may be present in the two quantities. Comparing the two panels, we find that the differential speed $v_{\alpha p}$ and the temperature ratio T_α/T_p are anti-correlated. The regions with high helium density and/or low proton temperature can be classified as the ICME plasma. In these regions the differential streaming is reduced by strong Coulomb collisions to below 10 km s^{-1}, whereas the alpha-to-proton temperature ratio is about 5 or even

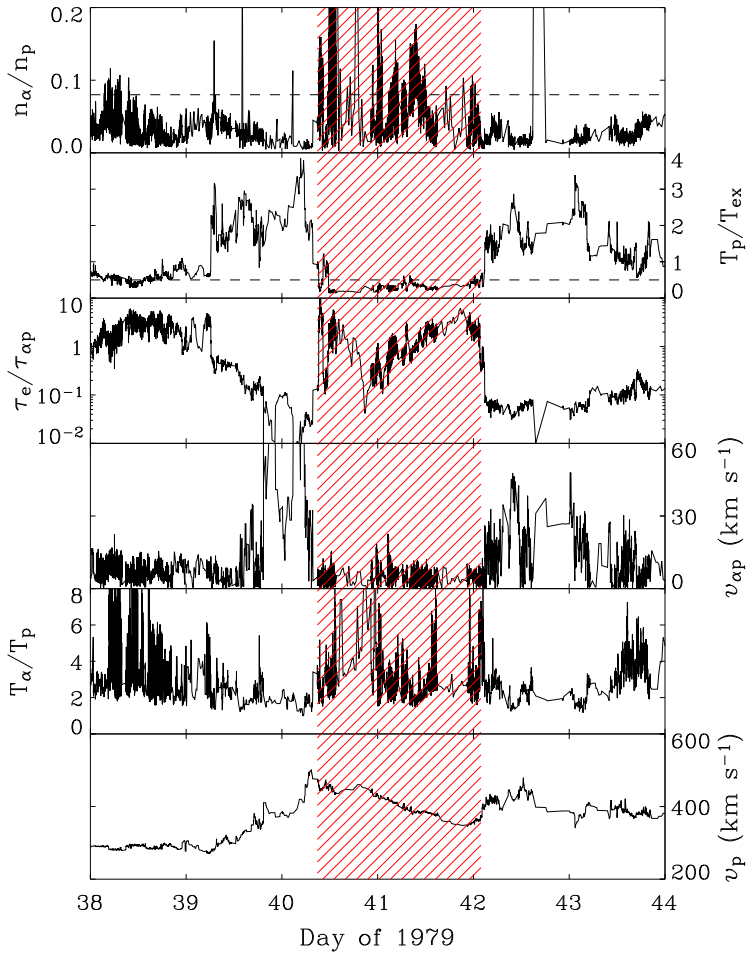

Figure 4-3: An ICME (hatched area) observed by Helios 1 at 0.98 AU. From top to bottom the panels show the alpha-to-proton density ratio, the observed-to-expected temperature ratio of protons, the expansion time over the Coulomb collision time, the differential speed between alphas and protons, the alpha-to-proton temperature ratio and the bulk speed of protons. The dashed lines in the upper two panels mark the limits of the identification criteria.

higher. This picture is in agreement with the scenario for the individual case discussed above. Another interesting area is the lower right corner of the panels with low helium density and high proton temperature. The extremely high temperature suggests that Coulomb collisions are of negligible importance for energy transfer between particles. In support of this point, the speed difference reaches 60-70 km s^{-1}, the highest value shown by the left color bar. However, the temperature ratio of alphas to protons is only 1-2 in this area, the lowest level indicated by the right color bar.

The radial evolution of T_α/T_p and $v_{\alpha p}$ from 0.3 to 5.4 AU is shown in Figure 4-5, with diamonds and dots corresponding to ICMEs and solar wind, respectively. Only the Helios and Ulysses data are shown as measurements for alpha particles are not routinely available from the Voyager missions. The Ulysses ion spectrometer has an

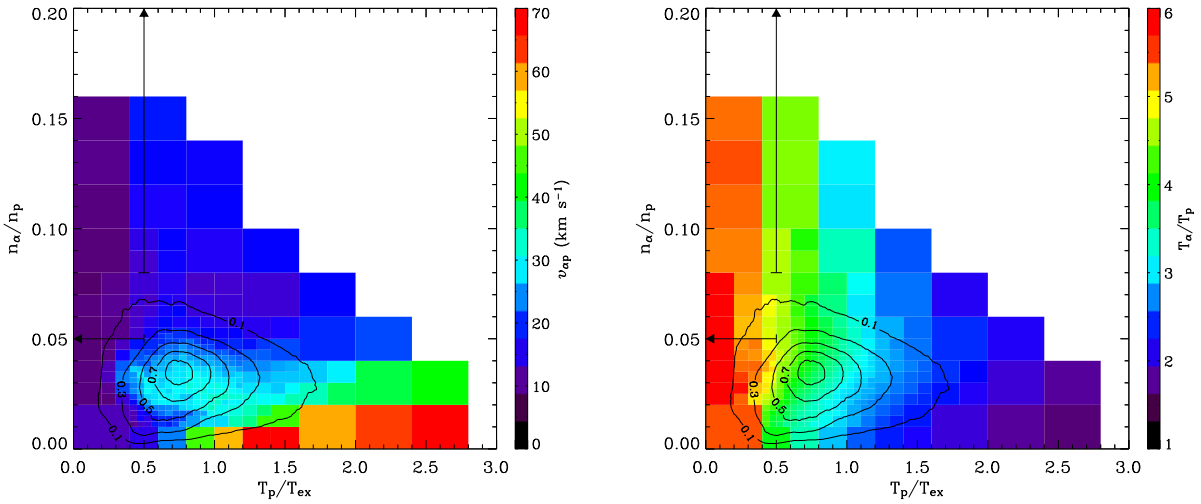

Figure 4-4: Surveys of the differential streaming $v_{\alpha p}$ (left panel) and the temperature ratio T_α/T_p (right panel) between alphas and protons, as a function of the density ratio n_α/n_p and the normalized temperature T_p/T_{ex}. The whole Helios 1 data set is used and divided into cells in the plane; regions with dense measurements contain more cells while no cell has less than 1000 spectra. The color scales indicate the average values within the bins. Black contours show the two-dimensional histogram of the data. The regions with $n_\alpha/n_p \geq 8\%$ or $T_p/T_{ex} \leq 0.5$ are shown by the arrows.

angular resolution of 5° in the polar direction, so the perpendicular velocity has large uncertainties. To overcome this difficulty, we follow the approach of Reisenfeld et al. [2001] and calculate the differential speed as $v_{\alpha p} = |\frac{v_\alpha - v_p}{\cos\theta_B}|$, using the fact that the relative streaming is along the magnetic field [e.g., Marsch et al., 1982]. The variables v_α and v_p are the velocities of the alpha particles and protons respectively, and θ_B is the angle between the magnetic field vector and the radial direction. Only the data with $|\cos\theta_B| \geq 0.3$ is included to guarantee a reliable differential speed. For an individual ICME, this procedure eliminates many data points; we use only the cases where over 60% of the points remain. Since Helios observations are at low latitudes, we use only Ulysses data within ±20° of the ecliptic plane. The solar wind data with ICMEs removed is binned over 0.1 AU intervals inside 1 AU and over 0.5 AU intervals beyond 1 AU. Binning is also performed for ICMEs, with the bin size indicated by the horizontal bars; the bounds of each bin are chosen to ensure enough points for the average. The standard deviation for each ICME bin is represented by the error bars. Radial dependences of solar wind parameters have previously been compiled [e.g., Marsch et al., 1982; Neugebauer et al., 1996; Reisenfeld et al., 2001]. Note that here we only include the low latitude data and do not differentiate between fast and slow streams.

The differential streaming in the solar wind (lower panel) shows a fairly steady decrease with distance, probably due to the accumulative effect of Coulomb collisions, in agreement with Marsch et al. [1982] and Neugebauer et al. [1996]. In contrast to the solar wind, the ICME $v_{\alpha p}$ decreases to less than 10 km s^{-1} by 0.4 AU. The

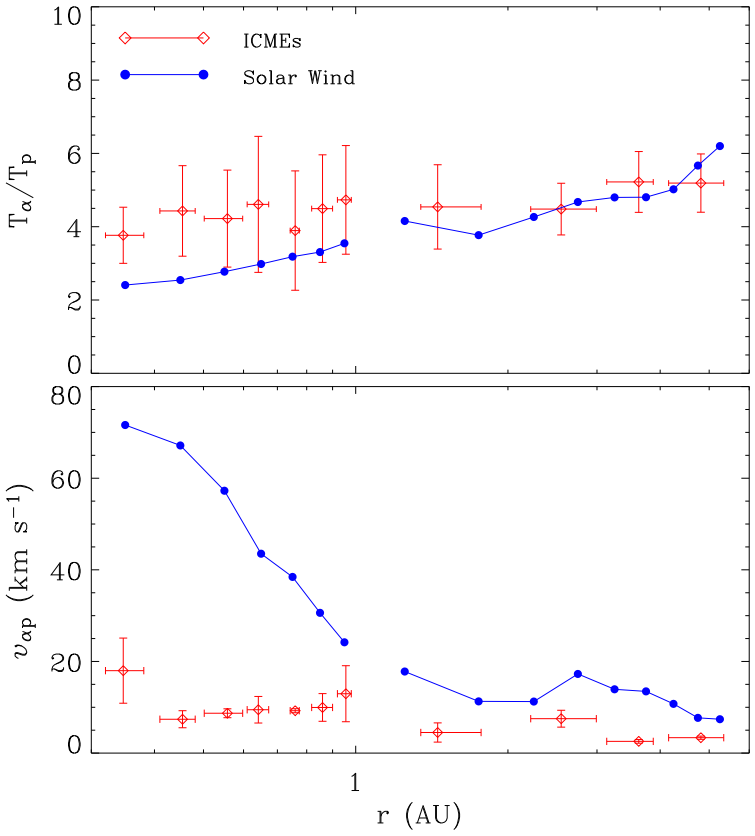

Figure 4-5: Radial variations of T_α/T_p (upper panel) and $v_{\alpha p}$ (lower panel) for ICMEs (diamonds) and solar wind (filled circles). For ICMEs, the horizontal bars indicate the bounds of the bins while the error bars show the standard deviation of the parameters within the bins. The solar wind levels are represented by the average values over 0.1 AU bins within 1 AU and 0.5 AU bins beyond. All the data are within $\pm 20°$ in latitude.

temperature ratio T_α/T_p does not vary with distance in ICMEs but does in the solar wind. Evidently, this ratio is larger than that of the solar wind inside 1 AU but roughly the same magnitude beyond 1 AU. The invariance of the ICME temperature ratio with distance implies the existence of a local mechanism responsible for heating the alphas. One may consider that the free energy associated with the differential streaming is converted into the thermal energy of the plasma. Reisenfeld et al. [2001] find a rough balance between the free energy and the required heat input for the alpha particles in the high-latitude solar wind. It is not likely that the free energy preferentially goes to alphas through Coulomb collisions. In addition, the differential speed within ICMEs is very small outside about 0.4 AU, but the temperature ratio is conserved at much larger distances. We conclude that the differential streaming, a relic in the initial helium acceleration in the solar atmosphere, does not account for the observed ICME heating.

4.3 Heating Mechanism and Energy Budget

The expansion of ICMEs is governed by a polytrope of $\gamma \sim 1.3$. This result implies thermal input into the ICME plasma. Kumar and Rust [1996] propose a current-core flux-rope model for MCs in which the energetics of the expansion are controlled by the magnetic helicity conservation. Their theoretical calculation shows that at least 58% of the magnetic energy lost in the expansion is available for the heating. Thus they suggest that the heating may result from the local magnetic dissipation. In the case of the solar wind, this dissipation usually appears as a spectral break in the power spectrum of magnetic fluctuations in association with the proton gyrofrequency [e.g., Goldstein et al., 1995, and references therein]. Similar results are also obtained in a case study of ICMEs, but the spectrum shows less steepening in the dissipation range compared with that of the solar wind [Leamon et al., 1998b]. Magnetic dissipation is considered by the turbulence interpretation to be the ultimate fate of the low-frequency magnetic power residing at large scales. In this section, we will examine the role of magnetic turbulence in the heating of ICMEs.

4.3.1 Collisions and Transport in an Expanding Plasma

Before going further, we first describe collisions and energy transport for an expanding plasma. Consider a parcel of ICME plasma with volume V moving away from the Sun with a constant velocity v. The plasma expands in the solar wind and is characterized by a large temperature difference between the interacting alpha particles and protons. The effect of electrons can be ignored in the Coulomb energy transfer between different species of particles since their mass is very small. We start with the first law of thermodynamics for alpha particles

$$dU_\alpha = dQ_\alpha - P_\alpha dV, \tag{4.1}$$

where dU_α is the change in the thermal energy of alphas, dQ_α is the heat added to them, and P_α is the alpha pressure. The internal energy can be expressed as

$$dU_\alpha = \frac{3}{2} N_\alpha k_\mathrm{B} dT_\alpha, \tag{4.2}$$

where N_α is the total number of alphas in the volume and k_B is the Boltzmann constant. In the presence of strong Coulomb collisions the quantity dQ_α includes heat transfer with protons and the energy from other sources. We treat the Coulomb energy exchange separately.

To do so, we first consider an isolated plasma containing protons and alpha particles. If the plasma components have a large temperature difference but a small relative drift, the thermal equilibration via Coulomb collisions is described by

$$\left.\frac{dT_\alpha}{dt}\right|_c = \frac{T_p - T_\alpha}{\tau_{\alpha p}}. \tag{4.3}$$

The Coulomb collision time scale $\tau_{\alpha p}$ can be written as

$$\tau_{\alpha p} = \frac{m_p + m_\alpha}{2 m_\alpha \nu_{\alpha p} \psi_{p\alpha}}, \tag{4.4}$$

where m_p and m_α are the masses of protons and alphas, respectively. By assuming Maxwellian velocity distributions for the ion species, the momentum transfer frequency $\nu_{\alpha p}$ [Burgers, 1969] is given by

$$\nu_{\alpha p} = \frac{16\pi^{1/2}}{3} \frac{n_p m_p}{m_p + m_\alpha} \left(\frac{2 k_\mathrm{B} T_r}{m_r} \right)^{-3/2} \frac{e_p^2 e_\alpha^2}{m_r^2} \ln \Lambda, \tag{4.5}$$

where e_p and e_α are the charges of protons and alphas, respectively. All units in the expressions are cgs except where noted. The reduced mass and temperature are defined by

$$m_r = \frac{m_p m_\alpha}{m_p + m_\alpha}, \quad T_r = \frac{m_p T_\alpha + m_\alpha T_p}{m_p + m_\alpha}. \tag{4.6}$$

The Coulomb logarithm [Spitzer Jr., 1962] can be written for the ICME plasma as

$$\ln \Lambda \simeq 8.51 + 1.5 \ln T_p - 0.5 \ln n_p \tag{4.7}$$

by taking its radial dependence into account. The correction factor $\psi_{p\alpha}$ for the relative drift in equation (4.4) is given by [Burgers, 1969; Schunk, 1977]

$$\psi_{p\alpha} = \exp\left(-\frac{v_{\alpha p}^2}{v_t^2} \right), \tag{4.8}$$

where $v_{\alpha p}$ is the differential speed between alphas and protons and v_t is the effective thermal speed defined as

$$v_t = \left(\frac{2 k_\mathrm{B} T_r}{m_r} \right)^{1/2}. \tag{4.9}$$

Evidently $\psi_{p\alpha} = 1$ in the limit of very small drifts ($v_{\alpha p} \ll v_t$), so it has a negligible effect in the case of ICMEs but may be significant for the solar wind.

For the original problem, we write the heat dQ_α as

$$dQ_\alpha = \left(\frac{3}{2} N_\alpha k_\mathrm{B} dT_\alpha \right)\Big|_c + N_\alpha m_\alpha \varepsilon_\alpha dt, \tag{4.10}$$

where the first term is the energy exchange through Coulomb collisions with protons and the second term is heat input from unknown sources. The quantity ε_α represents the specific heating rate of alphas with units J kg^{-1} s^{-1}. Combining equations (4.2), (4.3) and (4.10) we can reduce equation (4.1) to

$$\frac{dT_\alpha}{dt} = \frac{T_p - T_\alpha}{\tau_{\alpha p}} + \frac{2 m_\alpha \varepsilon_\alpha}{3 k_\mathrm{B}} - \frac{2 T_\alpha}{3V} \frac{dV}{dt}, \tag{4.11}$$

where the ideal gas law $P_\alpha V = N_\alpha k_\mathrm{B} T_\alpha$ is invoked. Conservation of the number of particles yields $\frac{dn_\alpha}{n_\alpha} = -\frac{dV}{V}$. We can then eliminate the volume V from the above equation, arriving at

$$\frac{dT_\alpha}{dr} = \frac{T_p - T_\alpha}{v\tau_{\alpha p}} - \frac{2T_\alpha}{3v\tau_e} + \frac{2m_\alpha \varepsilon_\alpha}{3k_\mathrm{B} v}. \tag{4.12}$$

Note that $dr = vdt$ is adopted for a purely radial outflow. We define τ_e as the expansion time of the plasma which is expressed in the form

$$\tau_e = -\left(v\frac{d}{dr}\ln n_\alpha\right)^{-1} = -\left(v\frac{d}{dr}\ln n_p\right)^{-1}. \tag{4.13}$$

For simplicity we assume that alphas and protons have the same bulk speed in the above equation. In observations their relative drift inside ICMEs quickly approaches zero due to strong Coulomb collisions. Any free energy associated with the drift can be included in the heating rate, ε_α.

Note that the adiabatic cooling due to the expansion is described by the second term on the right hand side of equation (4.12). The adiabatic temperature profile $T_\alpha \propto r^{-4/3}$ can be recovered for the steady state with $n_\alpha \propto r^{-2}$ by omitting the first and third terms. Any expansion faster than r^{-2}, which will result in a faster temperature decrease without heating sources, can also be described by this equation. Whether the plasma is collision dominated is determined by the magnitude of the ratio of $\tau_e/\tau_{\alpha p}$. Since ICMEs are characterized by very low temperatures but comparable densities with the solar wind, theoretically Coulomb collisions should be important in the transport equation, which can be readily seen from equations (4.4), (4.12) and (4.13).

Similarly we can obtain the temperature equation for protons. It has the form

$$\frac{dT_p}{dr} = \frac{T_\alpha - T_p}{v\tau_{p\alpha}} - \frac{2T_p}{3v\tau_e} + \frac{2m_p \varepsilon_p}{3k_\mathrm{B} v}, \tag{4.14}$$

where ε_p is the corresponding specific rate of energy deposition to the protons. Note that in the above equation $\tau_{p\alpha}$ is related to $\tau_{\alpha p}$ by $\frac{\tau_{\alpha p}}{\tau_{p\alpha}} = \frac{n_\alpha}{n_p}$ (refer to equations (4.4) and (4.5)), which depends on what particles are treated as test particles. Here we use $\tau_{\alpha p}$ as an indicator for the Coulomb collision time, following the approach found in most of the literature [e.g., Neugebauer, 1976; Marsch et al., 1982; Neugebauer et al., 1996].

4.3.2 Required Heating Rate

As described above, we derive the equations of temperature evolution for protons and alphas, taking into account the Coulomb energy transfer between them. Knowing the properties of the ICME expansion, we can use these equations to determine the heating rate required to produce the observed temperature profile. Inversion of equations (4.12) and (4.14) results in the specific heating rates of protons and alphas

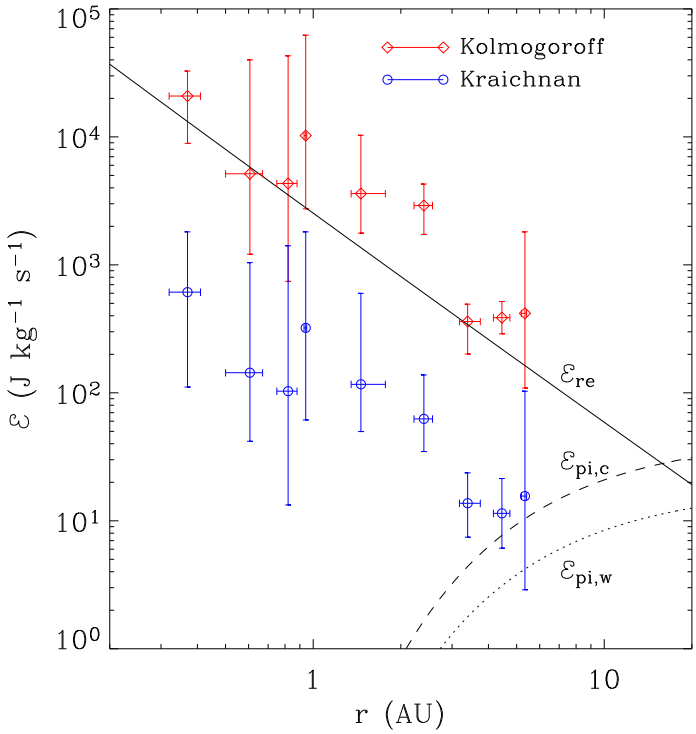

Figure 4-6: Energy dissipation rate of magnetic fluctuations within ICMEs deduced from Kolmogoroff's law (diamonds) and from Kraichnan's formulation (circles), respectively. Binning is similar to Figure 4-5; the error bars indicate the lower and upper bounds of the data for each bin. Also plotted are the required heating rate (solid line) determined from equation (4.16) and the energy deposition rate by pickup ions inferred from the collision approach (dashed line) and from wave excitation (dotted line).

expressed as

$$\varepsilon_p = \frac{k_B T_p}{m_p}\left[\frac{3v}{2}\frac{d}{dr}\ln T_p - \frac{3(\frac{T_\alpha}{T_p}-1)}{2\tau_{p\alpha}} + \frac{1}{\tau_e}\right],$$
$$\varepsilon_\alpha = \frac{k_B T_\alpha}{m_\alpha}\left[\frac{3v}{2}\frac{d}{dr}\ln T_\alpha - \frac{3(\frac{T_p}{T_\alpha}-1)}{2\tau_{\alpha p}} + \frac{1}{\tau_e}\right]. \quad (4.15)$$

The total required heating rate is then simply

$$\varepsilon_{re} = \varepsilon_p + \varepsilon_\alpha. \quad (4.16)$$

Based on the power-law fits to the data in Figure 4-2, we can quantitatively evaluate the required heating rate as a function of heliocentric distance. We assume fixed density and temperature ratios for protons and alphas within ICMEs, i.e., $\frac{n_\alpha}{n_p} \simeq 0.08$

and $\frac{T_\alpha}{T_p} \simeq 4.5$ (see Figure 4-5). Note that the density profile, which helps determine the time scales of τ_e, $\tau_{\alpha p}$ and $\tau_{p\alpha}$, is also needed in the calculation. The resulting heating rate is displayed in Figure 4-6 as a solid line. It spans almost three orders in magnitude, starting at about 19,000 J kg^{-1} s^{-1} at 0.3 AU and reaching about 19 J kg^{-1} s^{-1} at 20 AU. The partition between alphas and protons, $\varepsilon_\alpha/\varepsilon_p$, decreases from ~ 2.4 at 0.3 AU to ~ 1.3 at 20 AU, so more of the heating goes into the alpha particles and helps maintain their higher temperatures. The average required heating rate at 1 AU is about 2550 J kg^{-1} s^{-1}, with only 900 J kg^{-1} s^{-1} deposited to protons. Smith et al. [2001] test a phenomenological theory for the turbulent heating of the solar wind. By fitting Voyager 2 observations, they give an estimate for the proton heating rate at 1 AU to be 1600 J kg^{-1} s^{-1}, which is approximately 1.8 times the proton heating rate of ICMEs. As shown by equation (4.15), the proton heating rate ε_p is proportional to the temperature T_p. Given that the temperature is about 2 times higher in the solar wind than inside ICMEs, we consider the two estimates to be consistent.

4.3.3 Turbulence and Energy Dissipation Rate

Examination of magnetic fluctuations within an ICME shows a power spectrum of the form $f^{-5/3}$ at spacecraft frequencies less than 0.5 Hz [Leamon et al., 1998b]. Such an inertial range spectrum of the Kolmogoroff form indicates strong nonlinear couplings and quasi-steady spectral transfer. It is still not clear whether this property generally exists within ICMEs. We therefore consider two different theories that can be applied to the turbulence. One of them, Kolmogoroff phenomenology [Kolmogoroff, 1941], gives a simple expression for the inertial range omni-directional spectrum of the turbulent energy (per unit mass per unit wave number)

$$E(k) = C_{\rm ko}\varepsilon^{2/3}k^{-5/3} \tag{4.17}$$

in terms of the energy transfer rate ε and the wave number k. The numerical constant is $C_{\rm ko} \simeq 1.6$. Kolmogoroff's theory describes incompressible hydrodynamic turbulence but is also applicable to magnetic fluctuations of the solar wind. Kraichnan [1965] modified the theory to include the effect of the magnetic field, which gives the MHD equivalent for the energy spectrum

$$E(k) = C_{\rm kr}(\varepsilon v_{\rm A})^{1/2}k^{-3/2}, \tag{4.18}$$

where $v_{\rm A}$ is the Alfvén velocity. The above two formulations can be linked together by a phenomenological argument of the characteristic spectral transfer time [Matthaeus and Zhou, 1989]: the Kolmogoroff spectrum corresponds to the limit of weak magnetic fields while the Kraichnan spectrum applies to the case of strong fields. The relation between the constants $C_{\rm kr}$ and $C_{\rm ko}$ is $C_{\rm kr} = C_{\rm ko}^{3/4}$ resulting from this argument, which gives $C_{\rm kr} \simeq 1.42$.

The trace of the observed power spectral matrix is related to the omni-directional

spectrum by (see equations (3.4.17) and (3.4.18) in Batchelor [1953])

$$P(k) = P_{xx} + P_{yy} + P_{zz} = \int_k^{+\infty} \frac{E(k')}{k'} dk', \tag{4.19}$$

where P_{xx}, P_{yy} and P_{zz} are the power spectra of magnetic fluctuations in the x, y and z components, respectively. Substituting equations (4.17) and (4.18) into the above equation, we can obtain the reduced Kolmogoroff and Kraichnan spectra $P(k)$ separately. Conversion of the power spectrum from the plasma-frame wave number k to the spacecraft-frame frequency f requires a correction for the Doppler shift, i.e., $k = \frac{2\pi f}{v \pm v_{\rm w}(k)}$ for wave structures moving with velocity $v_{\rm w}(k)$ superposed on the plasma speed v outward from (+) or toward (-) the Sun. Since the plasma flow speed is much larger than the characteristic speed of the fluctuations, this relation is simplified to $k = \frac{2\pi f}{v}$. Using this relation as well as $P(k)dk = P(f)df$ yields the reduced Kolmogoroff spectrum in terms of the spacecraft-frame frequency f

$$P(f) = \frac{3}{5} C_{\rm ko} \varepsilon^{2/3} \left(\frac{2\pi}{v}\right)^{-2/3} f^{-5/3} \tag{4.20}$$

and the Kraichnan counterpart

$$P(f) = \frac{2}{3} C_{\rm kr} (\varepsilon v_{\rm A})^{1/2} \left(\frac{2\pi}{v}\right)^{-1/2} f^{-3/2}. \tag{4.21}$$

Rearrangement of equations (4.20) and (4.21) gives the turbulence cascade rate

$$\varepsilon_{\rm ko} = \left(\frac{5}{3C_{\rm ko}}\right)^{3/2} \frac{2\pi}{v} f^{5/2} [P(f)]^{3/2} \tag{4.22}$$

deduced from the Kolmogoroff spectrum and

$$\varepsilon_{\rm kr} = \frac{9\pi}{2C_{\rm ko}^2} \frac{1}{v v_{\rm A}} f^3 [P(f)]^2 \tag{4.23}$$

from the MHD equivalent. Note that $P(f)$ is the observed power spectral density in the inertial range. By inserting it into equations (4.22) and (4.23), two different specific dissipation rates can be obtained. Determination of the turbulence dissipation rate for the solar wind has been performed in this way by Coleman Jr. [1968] and Leamon et al. [1999]. In addition, fitting the observed spectrum to a power law gives the spectral index. Comparison of the deduced heating rates with the required rates determines whether turbulence dissipation can explain the heating of ICMEs; together with the spectral index, this comparison will also determine which theory applies to the turbulence.

We compute the power spectrum of magnetic fluctuations inside ICMEs from the magnetic field observations. We use 6 s averages of the magnetic field from the Helios missions and 1 s measurements from Ulysses. The Nyquist frequency for the Helios data is 0.083 Hz, which is usually below the proton gyro-frequency, so the dissipation

range spectrum is not seen. In constructing the power spectrum, we first rotate the magnetic field observations into a field-aligned coordinate system following the approach of Bieber et al. [1996]. In this system, the z axis is aligned with the mean magnetic field and points away from the Sun, the x axis is in the plane defined by the mean field and the radial direction and also points away from the Sun, and the y axis completes the right-handed system. More specifically, the orthogonal mean field coordinates ($\hat{\mathbf{x}}$, $\hat{\mathbf{y}}$, $\hat{\mathbf{z}}$) are the normalized ($\langle\mathbf{B}\rangle\times\hat{\mathbf{r}}\times\langle\mathbf{B}\rangle$, $\langle\mathbf{B}\rangle\times\hat{\mathbf{r}}$, $\langle\mathbf{B}\rangle$), where $\langle\mathbf{B}\rangle$ is the mean field vector and $\hat{\mathbf{r}}$ is the unit vector in the radial direction. We divide the ICME data into 1-hour intervals and the coordinates are set up using these 1-hour averages. In the new system, the B_z component is roughly the magnitude of the magnetic field and the components B_x and B_y are transverse fluctuations of the field. Trends in the B_x and B_y components are thereby automatically eliminated. Linear trends in the B_z component are subtracted after the coordinate system is established. Note that the coordinate system changes from one interval to another since the direction of the mean field $\langle\mathbf{B}\rangle$ changes. Intervals with more than 10% of the data missing are rejected; data gap filling is then performed for the rest of the intervals by a linear interpolation to ensure an equally spaced data record. The resulting intervals for each ICME are concatenated to form a series of data large enough to ensure sufficient frequency points in the inertial range of the power spectrum. The justification for this step is that the data are in the field-aligned coordinates with trends removed. Moreover, the inertial range power spectrum is associated with intermediate scale structures extending to the gyro-radius of protons, while the dissipation range corresponds to even smaller structures. Presumably these spectra are the same for different intervals of an ICME.

The power spectrum of solar wind fluctuations is often estimated by the Blackman-Tukey technique [e.g., Matthaeus and Goldstein, 1982; Leamon et al., 1998a]. The starting point of this method is that the spectral density is equal to the Fourier transform of the autocorrelation function. This method requires that the maximum lag used in calculating the autocorrelation function should be much smaller than the number of data samples to guarantee positive definiteness of the spectrum. In practice, a maximum lag is usually selected to be 10% of the length of the data for statistical validity. In the case of ICMEs, we frequently find that significant autocorrelation of the data exists even at much larger lags; the truncation of the function at 10% of the length thus gives a spurious spectrum. Here we use an improved periodogram estimator, the so-called Welch method (refer to the review by Ghil et al. [2002]). The data sequence of ICMEs is segmented into bins of the same length with adjacent bins half overlapping. The number of bins or the length of the bin is dictated by the trade-off between the frequency resolution and estimated variance. A rule of thumb is to take the length M to be no larger than $N/5$ or $N/10$, where N is the number of data samples; in practice, we find that with $N/M = 8$ adequate statistical validity can be obtained. Each segment is then smoothed by the Hamming window before computing the transform, which helps attenuate the power leakage. The final spectrum is achieved by averaging the estimate over the bins in order to reduce the bias and variance. This procedure gives a robust spectrum which mostly lies above the 95% significance level in the frequency domain.

Applying the above procedures to each component of the magnetic field, we obtain

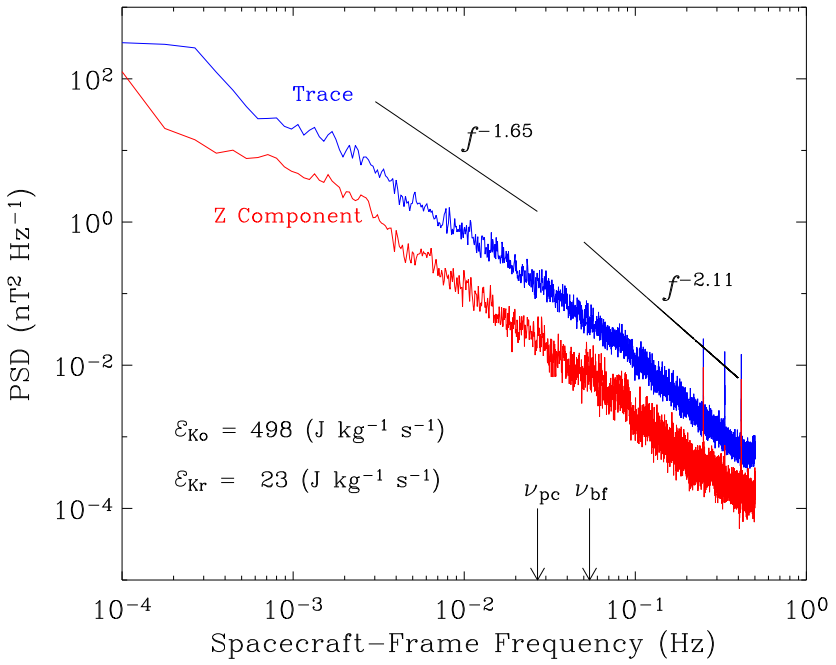

Figure 4-7: Power spectral density of magnetic fluctuations within an ICME observed by Ulysses at 3.25 AU. The inertial and dissipation ranges are shown by the power law fits with corresponding spectral indices. The proton cyclotron and spectral break frequencies are denoted by the arrows. Text in the lower left corner depicts the turbulence dissipation rates deduced from the Kolmogoroff and Kraichnan formulations, respectively.

the power spectra P_{xx}, P_{yy} and P_{zz} respectively. In the field-aligned coordinates, P_{zz} is the power spectrum of fluctuations parallel to the field, i.e., $P_{\parallel} = P_{zz}$; the power of fluctuations perpendicular to the field is $P_{\perp} = P_{xx}+P_{yy}$ as discussed above. Figure 4-7 gives a typical ICME power spectrum calculated from 1 s magnetic field measurements by Ulysses at 3.25 AU on Days 156-158.6 of 1991 from the list of Liu et al. [2005]. As required by the spectral estimator, data segmentation is implemented, and a frequency resolution of about 10^{-4} Hz is acquired. The trace of the power spectral matrix, i.e., $P = P_{xx} + P_{yy} + P_{zz}$, is shown in the figure as well as the z component P_{zz}. The power spectra show a slight but discernable steepening at high frequencies, indicative of the onset of magnetic dissipation. We fit the trace of the spectral matrix with a power law in the inertial and dissipation ranges separately; points close to the break frequency are omitted. The fit results are displayed in the plot. The spectral index in the inertial range is about 1.65 ± 0.02, in good agreement with the Kolmogoroff prediction of 5/3. The dissipation range spectrum has a slightly steeper form with an index of about 2.11 ± 0.01, smaller than the solar wind average level of 3.04 [Leamon et al., 1998a]. Accordingly, the spectral cascade within ICMEs may tend to be low. The intersection of the two power laws enables us to compute the frequency

at which the spectral break occurs. The resulting break frequency, ν_{bf}, is about 0.054 Hz, comparable to but larger than the proton gyro-frequency $\nu_{pc} = 0.027$ Hz. The dissipation range of the spectrum is hence associated with the fluctuations with spatial scales smaller than the gyro-radius of protons, which may indicate the presence of proton cyclotron damping. The energy cascade rate calculated from equation (4.22) is about 498 J kg^{-1} s^{-1}, much larger than the Kraichnan prediction of 23 J kg^{-1} s^{-1} from equation (4.23). In computing the dissipation rate, the power law fit of the inertial range $P(f)$ shown in Figure 4-7 is scaled to velocity units and then inserted into the two equations separately, and a geometric mean (the same as the arithmetic mean in this case) is taken over 270 frequency points in the range of 0.003 Hz up to the gyro-frequency. As can be seen from Figure 4-6, the required heating rate at 3.3 AU is about 400 J kg^{-1} s^{-1}, consistent with the Kolmogoroff dissipation rate but not the Kraichnan counterpart. This result, as well as the inertial range index, favors the Kolmogoroff turbulence theory.

Repeating the same procedure for each ICME yields the inertial range spectral index and the turbulent dissipation rate as a function of heliocentric distance. In fitting the inertial range spectrum, typically 100-200 frequency points in the range 0.005-0.05 Hz are used for the Helios 6 s averages depending on the sample length; for the Ulysses 1 s measurements, we adopt the frequency range from 0.005 Hz to the proton gyro-frequency containing about 300 spectral estimates. The turbulence cascade rates determined from equations (4.22) and (4.23) are displayed in Figure 4-6 to make a comparison with the required heating rate. The data are binned as in Figure 4-5, with the bin size denoted by the horizontal bars. The error bars show the range of data distribution within each bin. The dissipation rate, deduced from either the Kolmogoroff or Kraichnan formulations, shows a clear decrease with distance. The rate predicted by the Kraichnan theory is about 2 orders of magnitude lower than the Kolmogoroff prediction and it is well below the rate required by the temperature profile. The dissipation rate determined from the Kolmogoroff formulation is sufficient to explain the heating of the ICME plasma. Leamon et al. [1999] study magnetic dissipation based on a model of kinetic Alfvén waves and find that about 58% of the total dissipated energy in the solar wind goes to the heating of protons. They suggest that the remaining energy goes into electron heating. The required heating rate given here does not include the energy for electron heating, but the turbulence cascade rate still appears to be adequate if electron heating is included. The Kolmogoroff dissipation rate shows a large variation close to 1 AU, so a rigorous comparison with the solar wind counterpart is not available.

The derived inertial-range spectral index q is shown in Figure 4-8, represented by the averages within the same bins as in Figure 4-6. The standard deviations for the bins are plotted as error bars. The spectral index, with an average of 1.71, is generally larger than the Kraichnan prediction 3/2 but close to the Kolmogoroff index value of 5/3. Combined with the dissipation rate, this result verifies that the Kolmogoroff law, a crucial theorem for the inertial range turbulence, may also apply in the ICME plasma.

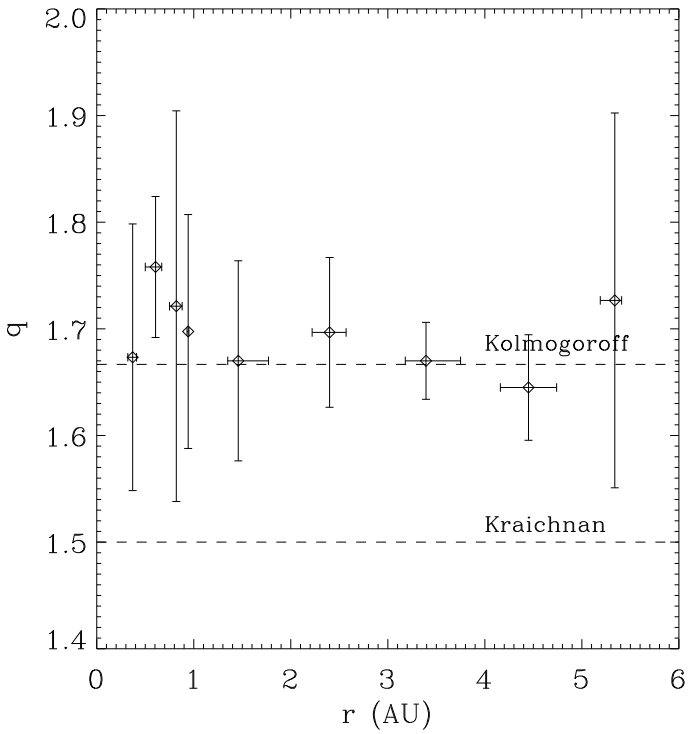

Figure 4-8: Inertial-range spectral indices as a function of heliocentric distance. The horizontal bars show the same bins as in Figure 4-6 and the error bars indicate the standard deviation of the data inside the bins. The Kolmogoroff index 5/3 and the Kraichnan level 3/2 are marked by the dashed lines.

4.3.4 Source of Turbulence

The Kolmogoroff form of the inertial range spectrum shows that magnetic fluctuations within ICMEs are essentially nonlinear. What is interesting here is that wave structures and large-scale flow gradients are not frequently seen within ICMEs. A question thus arises regarding what sources drive the turbulence.

Enhanced magnetic fluctuations can derive from instabilities induced by temperature anisotropies. The free energy associated with the temperature anisotropy feeds rapidly growing magnetic fluctuations when the proton temperature ratio $T_{\perp p}/T_{\parallel p}$ exceeds certain threshold conditions. We thus examine these instabilities as possible mechanisms for generating magnetic turbulence in ICMEs. The thresholds for the onset of these instabilities can be written as [e.g., Gary et al., 1994]

$$\frac{T_{\perp p}}{T_{\parallel p}} - 1 = \frac{S}{\beta_{\parallel p}^{\alpha}},$$

where the parallel plasma beta is defined as $\beta_{\parallel p} = \frac{n_p k_B T_{\parallel p}}{B^2/2\mu_0}$. Here S and α are free parameters which can be derived from solutions of the Vlasov dispersion equation or

single fluid MHD equations. The lower bound of the temperature anisotropy is an MHD mode with $T_{\perp p} < T_{\|p}$, the so-called firehose instability, which has $S = -2$ and $\alpha = 1$ [Parker, 1958]. The upper bound is imposed by the cyclotron and mirror instabilities. By fitting the numerical solutions of the Vlasov dispersion equation, Gary et al. [1997] obtain $S = 0.64$ and $\alpha = 0.41$ for the cyclotron instability at the maximum growth rate $\gamma_m = 0.01\Omega_p$ in the domain $0.1 \leq \beta_{\|p} \leq 10$, and $S = 0.87$, $\alpha = 0.56$ for the mirror instability at the same maximum growth rate over $5 \leq \beta_{\|p} \leq 50$. The enhanced magnetic fluctuations induced by the cyclotron instability are predominantly transverse while the mirror instability leads to predominantly compressive fluctuations. Detailed description about these instabilities is given in Chapter 5.

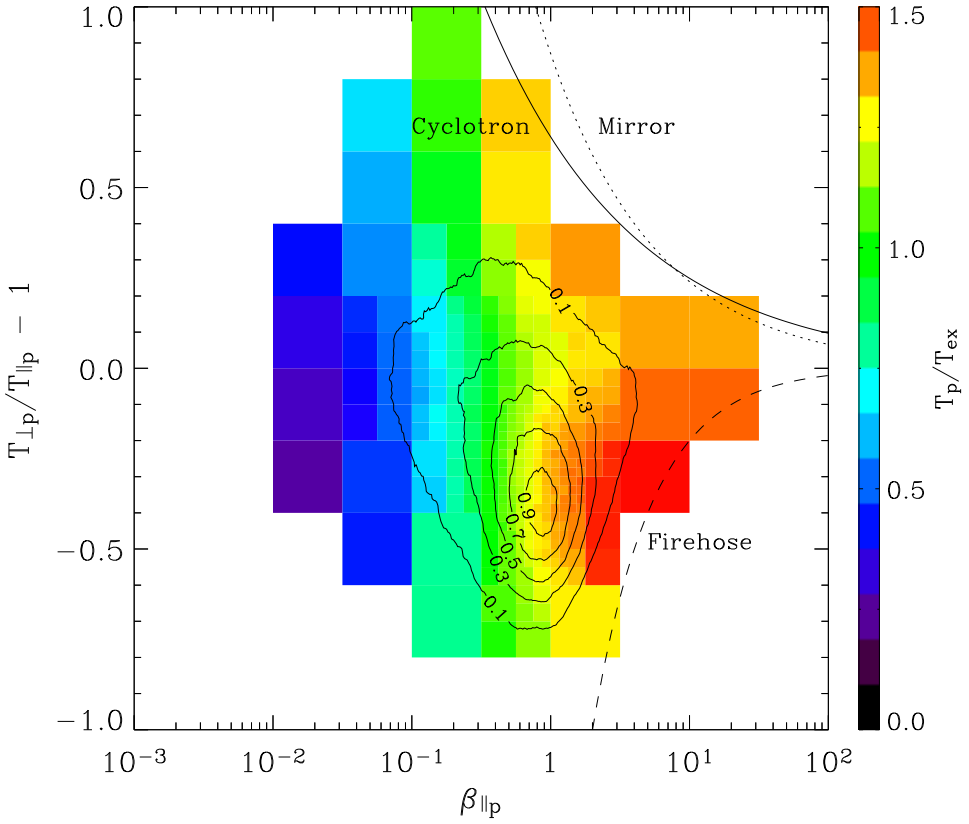

Figure 4-9: Survey of WIND measurements of the normalized proton temperature T_p/T_{ex} as a function of the temperature anisotropy and parallel plasma beta of protons. Bins are smaller in regions of higher density measurements, but each bin contains at least 1000 spectra. The average values of T_p/T_{ex} within the bins are indicated by the color shading. Black contours show the density of observations at levels of [0.1, 0.3, 0.5, 0.7, 0.9]. Also shown are the thresholds for the firehose (dashed line), cyclotron (solid line) and mirror (dotted line) instabilities.

Figure 4-9 illustrates the temperature ratio T_p/T_{ex} as a function of the temperature anisotropy and parallel plasma beta of protons. The procedure for creating this plot is the same as in Figure 4-4, but now it is applied to 100 s averages of the WIND

observations which contain more than 640,000 spectra recorded between 1994 and 2004. Again, regions with denser measurements in the two dimensional plane contain more cells, but no cell has less than 1000 data points. The data distribution is described by the black contours. As indicated by the contours, the typical solar wind has an anisotropy of ~ -0.35 and a parallel plasma beta of ~ 0.8. Therefore, $T_{\perp p} \simeq 0.65 T_{\parallel p}$ on average at 1 AU. The threshold conditions of the instabilities are denoted by the lines of different styles in the figure. As can be seen, the majority of the data is constrained by the thresholds. This evidence confirms that the upper and lower bounds indeed exist for the temperature anisotropies. In this figure the color scale, given by the bar on the right, indicates the average values of T_p/T_{ex} within the intervals. The high temperature regions are near the thresholds. The enhanced magnetic fluctuations lead to significant plasma heating when the instabilities rise above the thresholds; the heating continues until the damping of instabilities pushes the temperature anisotropy back into the constrained regime. Also note that the proton temperature is more enlarged near the threshold for the firehose instability than near the upper bound. Since the firehose instability is a large-scale MHD mode, more energy may be transferred to the particles from the damping of this instability. These results provide the first consistent view of the plasma heating by instabilities driven by temperature anisotropies. As mentioned in Chapter 1, $T_p/T_{ex} \leq 0.5$ is an indicator of ICME plasma. This figure clearly shows that the ICME region with low temperatures is characterized by $\beta_{\parallel p} \leq 0.1$ and located far away from the instability thresholds. A similar graph can also be constructed for the density ratio of n_α/n_p in the same plane (not shown here). Consistently, the high-density helium region roughly takes the same place in the plot. We conclude that instabilities due to temperature anisotropies do not play a role in the heating of ICMEs. Hence, the source of the turbulence seen inside ICMEs in the inner heliosphere is still an open question.

In the outer heliosphere (outside the ionization cavity), interactions between solar wind ions and interstellar neutrals are probably responsible for the solar wind heating. Since interstellar neutrals can freely penetrate plasmas, this interaction also occurs in ICMEs. Low-frequency MHD fluctuations can be generated by the damping of waves excited by pickup ions formed by the ionization of interstellar neutrals. In a steady state, this production of energy will be balanced by the dissipation rate. The heating rate associated with pickup ions can be estimated by [e.g., Williams and Zank, 1994]

$$\varepsilon_{\rm pi} = \frac{f_D v_p v_{\rm A} n_H}{n_p^0 \tau_{\rm ion}^0}, \tag{4.24}$$

where n_p^0 is the number density of protons at 1 AU taken from the fit in Figure 4-2, and $\tau_{\rm ion}^0$ is the neutral ionization time at 1 AU which is about 10^6 s. Here the Alfvén speed $v_{\rm A}$ is assumed to have a fixed value 50 km s^{-1}. We use the standard cold distribution for the density of interstellar neutrals [Vasyliunas and Siscoe, 1976]

$$n_H = n_H^\infty \exp(-\lambda/r), \tag{4.25}$$

where n_H^∞ is the interstellar neutral density at the termination shock, and λ is the

length scale of the ionization cavity taken to be 8 AU. The parameter f_D gives the faction of the available energy dissipated to the thermal core of protons. The value of f_D is ~ 0.05 based on fitting Voyager 2 observations assuming $n_H^\infty = 0.1$ cm^{-3} [Smith et al., 2001].

For completeness, we compare the above dissipation rate with the energy deposition calculated by McNutt Jr. et al. [1998] from the Boltzmann collision integrals. The charge exchange of interstellar neutrals with ions provides a source of both momentum and thermal energy. From their evaluation, the thermal energy can be expressed as

$$\begin{aligned} Q_t &= 2k_{\rm B}(T_H - T_p)\sigma(v^*)n_p n_H v^* \\ &\quad + \frac{1}{2}m_p(v_H - v_p)^2\sigma(v_m^*)n_p n_H v_m^*, \end{aligned} \tag{4.26}$$

where T_H is the temperature of interstellar neutrals taken to be 10^4 K, and v_H is their speed assumed to be 20 km s^{-1}. The charge exchange cross section used in the above expression can be written as

$$\sigma(v) = (2.1 \times 10^{-7} - 9.2 \times 10^{-9} \ln v)^2 \text{ cm}^2 \tag{4.27}$$

with speed v in units of cm s^{-1}. The two terms in equation (4.26) are associated with thermal energy exchange and momentum transfer between protons and neutrals, respectively. The characteristic speeds corresponding to the two exchanges can be approximated by

$$v^* = \sqrt{\frac{4}{\pi}\left(\frac{2k_{\rm B}T_p}{m_p} + \frac{2k_{\rm B}T_H}{m_p}\right) + (v_H - v_p)^2}, \tag{4.28}$$

and

$$v_m^* = \sqrt{\frac{64}{9\pi}\left(\frac{2k_{\rm B}T_p}{m_p} + \frac{2k_{\rm B}T_H}{m_p}\right) + (v_H - v_p)^2}. \tag{4.29}$$

The energy deposition rate is related to the thermal energy by

$$\varepsilon_{\rm pi} = \frac{f_D Q_t}{n_p m_p}. \tag{4.30}$$

Similarly, the energy partition factor f_D is also applied concerning the uncertainties.

The energy deposition rates by pickup ions, estimated from equations (4.24) and (30) based on the fits in Figure 4-2, are plotted in Figure 4-6. The deposition rates determined from the two equations differ by a factor of 2, which indicates a rough consistency of the two approaches. The deposition rate shows a steady increase as distance and seems to match the required heating rate of ICMEs around 20 AU. Therefore, the pickup ions should be the dominant source for the heating of the ICME plasma in the outer heliosphere. An increase in the ICME temperature might be expected since the deposition rate by pickup ions continues to grow with distance.

One consequence is that the temperature criterion used in identifying ICMEs may not work beyond 20 AU. The identification of ICMEs is hence particularly difficult at large distances, which in turn makes the observational confirmation of the temperature increase hard to achieve.

4.4 Summary and Discussion

We have presented a statistical study of the thermodynamic structure and kinetic properties of the ICME plasma based on combined surveys of the ejecta between 0.3 and 20 AU from Helios 1 and 2, Ulysses, and Voyager 1 and 2 data. The results are summarized and discussed as follows.

We confirm the ICME expansion reported by Liu et al. [2005]. It is interesting to compare the observed expansion with theoretical predictions. In the flux-rope model of MCs proposed by Kumar and Rust [1996], the predicted expansion gives a radial width $W \sim r$, number density $n \sim r^{-3}$, magnetic field strength $B \sim r^{-2}$ and temperature $T \sim r^{-1}$. In this model the magnetic field configuration is essentially force-free within the flux rope, but the authors argue that a small angle of 4° between the current and the magnetic field can provide the necessary force to drive the expansion. Compared with the fits in Figures 4-1 and 4-2, the model yields a rather faster expansion. In good agreement with our results, the polytropic index obtained from the theoretical expansion is also $\gamma \sim 1.3$, so the ICME expansion is not adiabatic due to the local heating of the plasma.

The ICME plasma is collision dominated. The expansion time of the plasma is generally comparable to or even larger than the Coulomb collision time. Restricted by the strong collisions, the differential speed between alpha particles and protons rapidly diminishes to below 10 km s^{-1} within ICMEs. However, the alpha particles have a higher temperature than protons with a typical temperature ratio $T_\alpha/T_p = 4$ - 6. The preferential heating of alphas, which overwhelms the energy loss to protons through Coulomb collisions, must be accounted for in any local heating mechanism.

Note that CMEs at the Sun are usually modeled as a collisionless plasma. It is interesting how the ICME plasma becomes collision dominated. Consider the particle mean free path expressed as a product of the thermal speed and collision time, namely,

$$\lambda = v_t \tau_c \sim \frac{T^2}{n}.$$

ICME expansion decreases the plasma temperature as well as the density. For an adiabatic expansion with a density profile $n \sim r^{-\delta}$ ($\delta > 0$), equation (4.12) gives $T \sim r^{-2\delta/3}$ when particle collisions are neglected. The resulting mean free path is $\lambda \sim r^{-\delta/3}$, so the expansion would actually decrease the mean free path, which is not expected. Consequently, particle collisions become strong during the expansion. Close to the Sun, CMEs undergo a violent expansion and the CME plasma should quickly become collision dominated. When CMEs move further out, plasma cooling is alleviated by turbulence dissipation (or heat conduction owing to particle collisions), but the expansion would go to a quasi-steady state with $n \sim r^{-2}$; the mean free path

may increase at this stage.

Magnetic dissipation is sufficient to explain the in situ heating of the ICME plasma. The inertial range spectrum of magnetic fluctuations within ICMEs frequently shows the Kolmogoroff form with spectral index 5/3, and the dissipation range, which begins at frequencies slightly larger than the proton cyclotron frequency, has a steeper slope. From the observed power spectrum in the inertial range, we deduce the energy dissipation rate and compare it with the required heating rate. We find that the Kolmogoroff law applies to the magnetic turbulence inside ICMEs and the dissipation rate determined from this formulation is adequate to produce the temperature profile.

The occurrence of magnetic dissipation at frequencies comparable to the proton cyclotron frequency suggests resonant cyclotron damping of the fluctuations. The resonant cyclotron interaction is capable of accelerating and heating heavy ions preferentially [e.g., Hollweg and Turner, 1978]. Isenberg and Hollweg [1983] investigate the preferential heating and acceleration of solar wind alpha particles by this interaction with parallel-propagating ion cyclotron waves. Hu and Habbal [1999] extend this study by including the dispersive effect imposed by the alpha particles. Both of the studies show that the alpha particles can be preferentially heated by the cyclotron interaction to more than 4 times the proton temperature. The energy for this interaction is assumed to come from a nonlinear cascade of low-frequency Alfvén waves. However, Alfvén waves are seldom seen inside ICMEs and the ejecta show a relative lack of sources to drive the turbulence. We investigate the sources for the turbulence, particularly the instabilities driven by temperature anisotropies and energy deposition by pickup ions. The ICME plasma is not near the instability thresholds, so the instabilities may not contribute to the turbulence generation. A rough estimate shows that the free energy associated with pickup ions is the dominant source for the ICME heating beyond 20 AU.

Some other results should also be noted, although they are not of particular relevance to the purpose of this work. In the collisionless regime of the solar wind plasma with extremely high temperature and low helium abundance, the alpha particles and protons approach thermal equilibrium while they have a large relative drift (see Figure 4-4). The free energy associated with the differential streaming apparently does not feed the heating of this plasma; resonant cyclotron damping also seems unable to produce the high temperatures since it will preferentially heat the alpha particles and thus make them substantially hotter than protons. This plasma heating is not understood. Another interesting outcome is that temperature anisotropies of the solar wind are constrained by the threshold conditions for the firehose, mirror and cyclotron instabilities (refer to Figure 4-9). Significant plasma heating occurs when the instabilities rise above the thresholds.

The content of this chapter has been published in the *Journal of Geophysical Research* [see Liu et al., 2006a]. Some of our work, relevant but not included here, is also published [see Richardson et al., 2004; Liu et al., 2005; Richardson et al., 2006].

Chapter 5

Sheath Regions of ICMEs

We find that the sheath regions between fast interplanetary coronal mass ejections (ICMEs) and their preceding shocks are often characterized by plasma depletion and mirror wave structures, analogous to planetary magnetosheaths. A case study of these signatures in the sheath of a magnetic cloud (MC) shows that a plasma depletion layer (PDL) coincides with magnetic field draping around the MC. In the same event, we observe an enhanced thermal anisotropy and plasma beta as well as anti-correlated density and magnetic fluctuations which are signatures of mirror mode waves. We perform a superposed epoch analysis of ACE and WIND plasma and magnetic field data from different classes of ICMEs to illuminate the general properties of these regions. For MCs preceded by shocks, the sheaths have a PDL with an average duration of 6 hours (corresponding to a spatial span of about 0.07 AU) and a proton temperature anisotropy $\frac{T_{\perp p}}{T_{\parallel p}} \simeq$ 1.2 -1.3, and are marginally unstable to the mirror instability. For ICMEs with preceding shocks which are not MCs, plasma depletion and mirror waves may also be present but at a reduced level. ICMEs without shocks are not associated with these features. The differences between the three ICME categories imply that these features depend on the ICME geometry and the extent of upstream solar wind compression by the ICMEs. We discuss the implications of these features for a variety of crucial physical processes including magnetic reconnection, formation of magnetic holes and energetic particle modulation in the solar wind.

5.1 Introduction

Plasma depletion layers (PDLs) and mirror mode waves are common features of planetary dayside magnetosheaths [e.g., Kaufmann et al., 1970; Crooker et al., 1979; Hammond et al., 1993; Violante et al., 1995; Hill et al., 1995]. The physical explanation for the plasma depletion is that the plasma is squeezed out of the local noon region as the magnetic field drapes around the magnetosphere [Zwan and Wolf, 1976]. Combining this model with the double-adiabatic equations derived by Chew et al. [1956], Crooker and Siscoe [1977] predict that a temperature anisotropy of $T_\perp > T_\parallel$ is a direct consequence of the field line draping and plasma depletion, where $\perp$ and $\parallel$ denote the directions perpendicular and parallel to the magnetic field. When the temperature

anisotropy exceeds the instability threshold, mirror mode waves are generated.

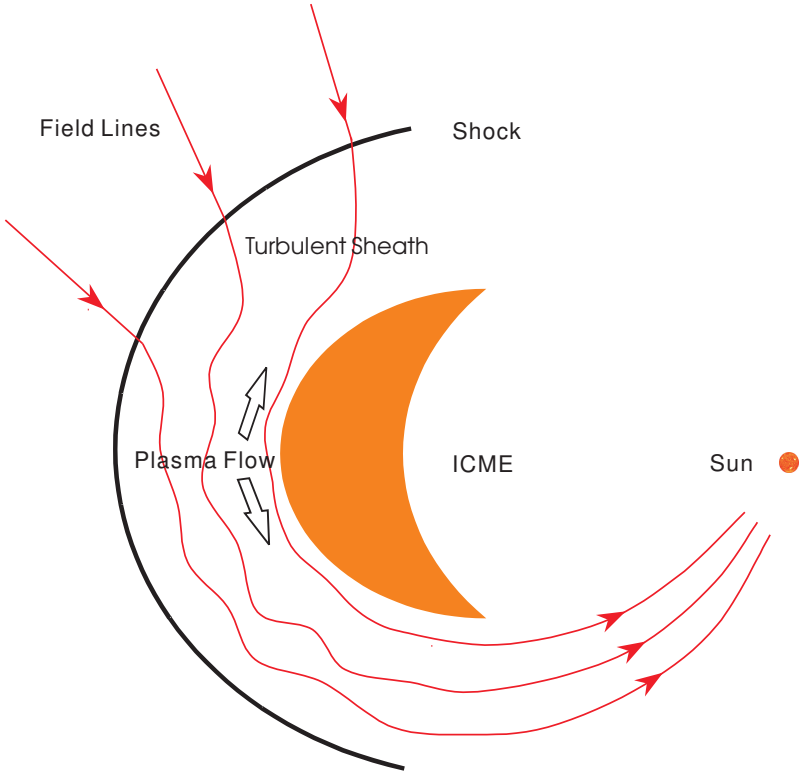

Figure 5-1: Schematic diagram of the turbulent sheath between an ICME and the preceding shock in the solar equatorial plane, illustrating the field line draping and consequent plasma flow.

Magnetic field draping may occur in front of an obstacle in the solar wind if the magnetized plasma cannot penetrate the obstacle. CMEs, large-scale magnetic structures expelled from the Sun, form large obstacles as they propagate into the solar wind. The ambient magnetic field may be draped around fast ICMEs, similar to the case of planetary magnetosheaths [Gosling and McComas, 1987; McComas et al., 1988]. Figure 5-1 shows an idealized sketch of this field line draping. An ICME with its axis lying in the solar equatorial plane creates a preceding shock if its speed relative to the ambient solar wind exceeds the fast-mode speed. Note that the ICME may still remain magnetically connected to the Sun. In front of the shock, the ambient magnetic field has the form of a Parker spiral. Between the shock and ICME is the sheath region where the magnetic field becomes stretched and turbulent. The shocked solar wind plasma is compressed in the direction perpendicular to the magnetic field, which may cause the plasma to flow along the draped field lines and result in formation of a PDL. The plasma temperature is enhanced in the perpendicular direction by the compression and depressed along the magnetic field by the parallel flow. As a result, anisotropic ion distributions are produced [e.g., Crooker and Siscoe, 1977]. When the threshold condition

$$\frac{T_{\perp p}}{T_{\parallel p}} - 1 > \frac{1}{\beta_{\perp p}} \tag{5.1}$$

is satisfied, the plasma is unstable to the mirror mode instability [Chandrasekhar et al., 1958]. The perpendicular plasma beta of protons is defined as $\beta_{\perp p} = \frac{n_p k_B T_{\perp p}}{B^2/2\mu_0}$ with n_p, k_B, B and μ_0 representing the proton density, Boltzmann constant, magnetic field strength and permeability of free space, respectively. This picture should apply to ICMEs with any axis orientation. Therefore, PDLs and mirror mode waves are expected to form ahead of fast ICMEs. The presence and properties of these features may depend on the geometry of the ejecta and how much the magnetic field is draped and compressed. Unlike the case of planetary magnetosheaths, ICMEs expand in the solar wind and the spatial span of their sheath regions increases since the preceding shock usually moves faster than the ejecta.

A possible PDL lasting about 3 hours in front of an ICME was identified and investigated by Farrugia et al. [1997], based on an ideal magnetohydrodynamic (MHD) theory developed by Erkaev et al. [1995]. Mirror mode structures which appear to be ahead of an ICME were also found in the solar wind [Tsurutani et al., 1992]. In this chapter, we use a case study and statistical analysis to investigate plasma depletion and mirror waves associated with ICMEs. Section 5.2 describes the observational data and data analysis. Section 5.3 gives theoretical description of the temperature anisotropy instabilities and derivation of formulations used in the analysis. Section 5.4 shows an example of a PDL and mirror waves in the sheath region of an ICME. A superposed epoch analysis (SEA) of ICMEs, presented in section 5.5, provides evidence that these features are usually observed ahead of ICMEs preceded by shocks. We test the SEA in section 5.6 and close by summarizing and discussing the results in section 5.7. This work presents the first consistent view of plasma depletion and mirror waves in the environment of ICMEs.

5.2 Observations and Data Reduction

We use solar wind plasma and magnetic field observations at 1 AU from ACE and WIND. Particularly important are the temperature anisotropy data which are needed to identify mirror mode waves. The ACE and WIND plasma teams use two different algorithms to calculate $T_\perp$ and $T_\parallel$. The WIND team fits the measured ion velocity distributions with a convecting bi-Maxwellian function, using the magnetic field data to determine the parallel and perpendicular directions [e.g., Kasper et al., 2002]. The accuracy of their thermal anisotropies may be affected by angular fluctuations of the magnetic field; spectra with angular fluctuations over 15° are rejected. The ACE team calculates the second moment integrals of the measured distributions to obtain the temperature anisotropy. The resulting temperature matrix is then rotated into a field-aligned frame, which gives two perpendicular and one parallel temperatures [e.g., Gary et al., 2001]. If the plasma is gyrotropic (i.e., particle gyration in a plane perpendicular to the magnetic field has no preferred direction), the two perpendicular temperatures should be the same; we only include the data for which the ratio of the two perpendicular temperatures is less than 1.3.

We use mainly ICMEs from the list of Liu et al. [2005] which are observed at both ACE and WIND. Events with $T_p/T_{ex} \leq 0.5$ and $n_\alpha/n_p \geq 8\%$ were qualified as ICMEs,

where T_p, T_{ex} and n_α are the proton temperature, expected proton temperature and alpha density separately. The expected temperature is calculated from the observed temperature-speed relationship at each spacecraft using the method of Lopez [1987]. We did not require the two criteria to be satisfied everywhere in an ICME interval. The boundaries of ICMEs are adjusted by incorporating other signatures of ICMEs. The ICMEs are further sorted into three categories: MCs and ICMEs (non-MCs) with preceding shocks and ICMEs without preceding shocks. Events with large data gaps in the sheath region are rejected, which gives a total 18 MCs preceded by shocks, 21 ICMEs (non-MCs) with forward shocks and 56 ICMEs without shocks between 1998 and 2005. All the shocks upstream of the ICMEs are quasi-perpendicular fast shocks across which the magnetic field strength increases abruptly. We note that although identification of ICMEs is a subjective art, the study of sheath regions by definition requires a preceding shock. Since almost all shocks inside 2 - 3 AU are generated by ICMEs, the uncertainties inherent in identifying ICMEs are not a major difficulty for this work.

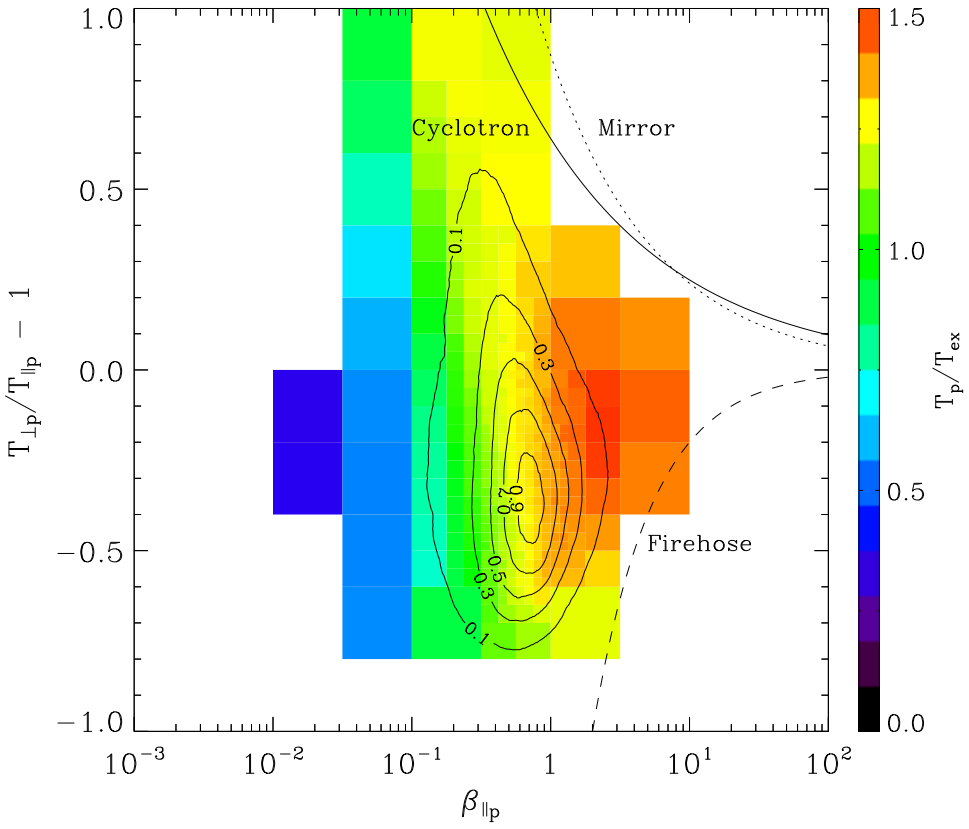

Figure 5-2: ACE measurements of the normalized proton temperature T_p/T_{ex} over the thermal anisotropy and parallel plasma beta of protons. The color shading indicates the average values of T_p/T_{ex} for the data binning. Black contours display the 2-D histogram overlaid on the data at levels of [0.1, 0.3, 0.5, 0.7, 0.9]. Also shown are the thresholds for the firehose (dashed line), cyclotron (solid line) and mirror (dotted line) instabilities.

We compare the thermal anisotropies determined from the WIND non-linear fittings to those obtained from the ACE moment integrals for different plasma regimes. Figure 5-2 shows ACE observations of the normalized temperature T_p/T_{ex} as a function of the temperature anisotropy and parallel plasma beta of protons. The parallel plasma beta of protons is defined as $\beta_{\|p} = \frac{n_p k_B T_{\|p}}{B^2/2\mu_0}$. A similar plot for WIND data is given in Chapter 4 (Figure 4-9). The 1.7×10^6 ACE 64 s temperature averages from 1998 - 2005 are divided into two-dimensional bins of temperature anisotropy and plasma beta; bins with dense spectra are further subdivided, with the requirement that each cell contains at least 2000 data points. The curves indicate the threshold conditions

$$\frac{T_{\perp p}}{T_{\|p}} - 1 = \frac{S}{\beta_{\|p}^{\alpha}} \tag{5.2}$$

for the cyclotron, mirror and firehose instabilities, respectively. The free parameters, S and α, are determined from solutions to the single-fluid MHD equations or to the Vlasov dispersion relation [Parker, 1958; Gary et al., 1997]. The firehose instability has $S = -2$ and $\alpha = 1$, while $S = 0.64$, $\alpha = 0.41$ for the cyclotron instability over the range $0.1 \leq \beta_{\|p} \leq 10$ and $S = 0.87$, $\alpha = 0.56$ for the mirror mode in the domain $5 \leq \beta_{\|p} \leq 50$ at the maximum growth rate $\gamma_m = 0.01\Omega_p$. Here Ω_p denotes the proton cyclotron frequency. These parameters are also given in section 4.3.4. Most of the data are constrained by these thresholds; when the thermal anisotropy is close to the thresholds, the plasma is heated by the induced instabilities. As indicated by the contour lines, the most probable temperature anisotropy for the solar wind at 1 AU is $T_{\perp p}/T_{\|p} = 0.6$ - 0.7. This ratio can be increased in the sheath regions of fast ICMEs to 1.1 - 1.3 (see below). The ICME plasma, characterized by $T_p/T_{ex} \leq 0.5$, lies far away from the instability thresholds. These results are consistent with the picture described by WIND data. We conclude that the two methods used to derive the thermal anisotropies give similar results.

5.3 Temperature Anisotropy Instabilities

In a magnetized plasma, the magnetic field can modify the particle distribution and make it anisotropic with respect to the field. A direct consequence is that the magnetic field is involved in the thermal properties of the plasma. The distribution anisotropy, however, cannot go without limits. Three modes of plasma instabilities arise when the anisotropy exceeds certain thresholds; the induced instabilities produce pitch angle scattering of ions, which helps inhibit the anisotropy to grow. As discussed above, the lower bound is called the firehose instability with $T_{\perp p} < T_{\|p}$. Plasma regimes with $T_{\perp p} > T_{\|p}$ are constrained by two competitive instabilities, the mirror and ion cyclotron instabilities, if the electron temperature is not much larger than the ion temperature. The firehose instability is an MHD mode, while the other two requires a kinetic description.

5.3.1 Firehose Instability

Derivation of the firehose instability and identification of corresponding waves require the anisotropic MHD conception, or the CGL theory [Chew et al., 1956]. For a bi-Maxwellian distribution with $T_\perp \neq T_\parallel$,

$$f(v_\parallel, \mathbf{v}_\perp) = n\left(\frac{m}{2\pi k_\mathrm{B} T_\perp}\right)\left(\frac{m}{2\pi k_\mathrm{B} T_\parallel}\right)^{1/2} \exp\left(-\frac{m v_\perp^2}{2k_\mathrm{B} T_\perp} - \frac{m v_\parallel^2}{2k_\mathrm{B} T_\parallel}\right), \tag{5.3}$$

the ideal MHD equations can be written as

$$\frac{\partial \rho}{\partial t} + \nabla \cdot (\rho \mathbf{v}) = 0, \tag{5.4}$$

$$\rho \frac{d\mathbf{v}_\perp}{dt} + \nabla_\perp \left(P_\perp + \frac{B^2}{2\mu_0}\right) - \frac{(\mathbf{B}\cdot\nabla)\mathbf{B}}{\mu_0}\left(\frac{P_\perp - P_\parallel}{B^2/\mu_0} + 1\right) = 0, \tag{5.5}$$

$$\rho \frac{d\mathbf{v}_\parallel}{dt} + \nabla_\parallel P_\parallel + (P_\perp - P_\parallel)\left(\frac{\nabla B}{B}\right)_\parallel = 0, \tag{5.6}$$

$$\frac{P_\perp}{\rho B} = \text{const}, \tag{5.7}$$

$$\frac{P_\parallel B^2}{\rho^3} = \text{const}, \tag{5.8}$$

$$\frac{\partial \mathbf{B}}{\partial t} = \nabla \times (\mathbf{v} \times \mathbf{B}), \tag{5.9}$$

where ρ and $\mathbf{v}$ are the plasma density and velocity, respectively. Linearizing the above equations gives three basic MHD modes in a double-Maxwellian plasma. We assume a background field $\mathbf{B}_0$ along the z direction in Cartesian coordinates, so the perturbation in the field strength

$$B_1 = B_{1z}. \tag{5.10}$$

The wave vector is taken to be $\mathbf{k} = k_\parallel \hat{\mathbf{z}} + k_\perp \hat{\mathbf{x}}$. Any perturbed quantities, represented by the subscript 1, are thus in the form $\exp[i(k_\perp x + k_\parallel z - \omega t)]$, where ω is the angular frequency. The background quantities are indicated by the subscript 0. For simplicity, we consider the problem in the plasma frame so that $\mathbf{v}_0 = 0$.

Derivation of the MHD modes and associated relationships in perturbed quantities at the presence of pressure anisotropy are nontrivial compared with the usual MHD theory, but they cannot be found in textbooks. Here we give the detailed derivation. Equation (5.4) can be readily reduced to

$$\rho_1 = \frac{\rho_0}{\omega}(k_\perp v_{1x} + k_\parallel v_{1z}) \tag{5.11}$$

for the density perturbation. The pressure perturbations can be obtained from equa-

tions (5.7) and (5.8) respectively, i.e.,

$$P_{\perp 1} = P_{\perp}\left(\frac{\rho_1}{\rho_0} + \frac{B_{1z}}{B_0}\right) \tag{5.12}$$

and

$$P_{\parallel 1} = P_{\parallel}\left(\frac{3\rho_1}{\rho_0} - \frac{2B_{1z}}{B_0}\right), \tag{5.13}$$

where equation (5.10) is invoked. Equation (5.9) gives the relationship between field and velocity perturbations

$$\begin{aligned} B_{1x} &= -\frac{k_{\parallel} v_{1x}}{\omega} B_0, \\ B_{1y} &= -\frac{k_{\parallel} v_{1y}}{\omega} B_0, \\ B_{1z} &= \frac{k_{\perp} v_{1x}}{\omega} B_0. \end{aligned} \tag{5.14}$$

The linearized form of equation (5.6) is

$$\rho_0(-i\omega)v_{1z} + ik_{\parallel}P_{\parallel 1} + (P_{\perp} - P_{\parallel})ik_{\parallel}\frac{B_{1z}}{B_0} = 0.$$

Substituting equations (5.11), (5.13) and (5.14) into the above equation yields

$$k_{\parallel}k_{\perp}P_{\perp}v_{1x} - \left(\omega^2\rho_0 - 3k_{\parallel}^2 P_{\parallel}\right)v_{1z} = 0. \tag{5.15}$$

Equation (5.5) describes fluid motion in the x and y directions. Consider the x direction first,

$$\rho_0(-i\omega)v_{1x} + ik_{\perp}\left(P_{\perp 1} + \frac{B_0 B_{1z}}{\mu_0}\right) - \frac{B_0 ik_{\parallel}B_{1x}}{\mu_0}\left(\frac{P_{\perp} - P_{\parallel}}{B_0^2/\mu_0} + 1\right) = 0.$$

Inserting equations (5.12) and (5.14) into this equation, we have

$$\left[\omega^2\rho_0 - 2k_{\perp}^2 P_{\perp} - k_{\perp}^2\frac{B_0^2}{\mu_0} - k_{\parallel}^2\left(P_{\perp} - P_{\parallel} + \frac{B_0^2}{\mu_0}\right)\right]v_{1x} - k_{\perp}k_{\parallel}P_{\perp}v_{1z} = 0. \tag{5.16}$$

The dispersion relation for the slow and fast modes can be obtained by letting the determinant of equations (5.15) and (5.16) equal to zero, namely,

$$\begin{aligned} \frac{\omega^2}{k^2} = \frac{1}{2\rho}\Bigg[\frac{B^2}{\mu_0} + P_{\perp}(1+\sin^2\theta) + 2P_{\parallel}\cos^2\theta \\ \pm \sqrt{\left(\frac{B^2}{\mu_0} + P_{\perp} + P_{\perp}\sin^2\theta - 4P_{\parallel}\cos^2\theta\right)^2 + 4P_{\perp}^2\sin^2\theta\cos^2\theta}\Bigg], \end{aligned} \tag{5.17}$$

where the subscript 0 has been omitted from ρ and B. The wave vector has been rewritten as $k_\perp = k\sin\theta$ and $k_\parallel = k\cos\theta$, where θ is the angle between $\mathbf{k}$ and $\mathbf{B}$. The fast and slow modes correspond to the plus and minus signs in equation (5.17), respectively. Now consider the y direction,

$$\rho_0(-i\omega)v_{1y} - \frac{B_0 i k_\parallel B_{1y}}{\mu_0}\left(\frac{P_\perp - P_\parallel}{B_0^2/\mu_0} + 1\right) = 0.$$

The dispersion relation for the intermediate mode is derived by inserting equation (5.14) into the above equation, i.e.,

$$\frac{\omega^2}{k^2} = v_{\rm A}^2\left(\frac{P_\perp - P_\parallel}{B^2/\mu_0} + 1\right)\cos^2\theta, \tag{5.18}$$

where $v_{\rm A}$ denotes the Alfvén speed. It is clear that the intermediate mode reduces to the oblique Alfvén wave when $P_\perp = P_\parallel$.

The relationship between density and magnetic field perturbations is obtained by inserting equations (5.14) and (5.16), or (5.15), into equation (5.11). We get

$$\frac{\delta n}{n} = \left(\frac{P_\perp \sin^2\theta}{n m_p}\right)^{-1}\left[\frac{\omega^2}{k^2} - \frac{B^2}{\mu_0 n m_p} - \frac{P_\perp}{n m_p} + \frac{P_\parallel\cos^2\theta}{n m_p}\right]\frac{\delta B}{B} \tag{5.19}$$

for the slow and fast modes, where m_p is the proton mass. We have rewritten $\delta n = \rho_1/m_p$ and $\delta B = B_1$. It can be shown from equations (5.17) and (5.19) that the fast mode always gives positively correlated δn and δB whereas the slow mode could yield anti-correlated density and field perturbations. For the intermediate mode, the velocity perturbation v_{1y} is not involved in the density fluctuation expressed by equation (5.11), so $\delta n = \delta B = 0$ across this mode as in the ordinary MHD theory. The relationship between the density and field fluctuations will be used below.

For perpendicular propagation ($\theta = \pi/2$), equation (5.17) is reduced to

$$\frac{\omega^2}{k^2} = \frac{B^2}{\mu_0\rho} + \frac{2P_\perp}{\rho},$$

which is the stable magnetosonic wave. For parallel propagation ($\theta = 0$), there are two solutions, the sound wave

$$\frac{\omega^2}{k^2} = \frac{3P_\parallel}{\rho}$$

and another mode with dispersion relation

$$\frac{\omega^2}{k^2} = \frac{1}{\rho}\left(\frac{B^2}{\mu_0} + P_\perp - P_\parallel\right). \tag{5.20}$$

It overlaps with the intermediate mode as can be seen from equation (5.18). Note

that ω becomes imaginary when

$$P_{\parallel} > P_{\perp} + \frac{B^2}{\mu_0}.$$

This is the firehose instability, and the above condition can be reduced to the firehose threshold expressed by equation 5.2. It is evident that $\beta > 2$ for the firehose instability to occur, which requires very low magnetic field or strong thermal pressure. This is possible in the solar wind or in some neutral sheets. Once excited, the firehose instability will give rise to strong transverse magnetic fluctuations.

The name of the firehose instability derives from its analogue, an ordinary firehose with a rapid water flow. In an anisotropic plasma, a magnetic flux tube corresponds to the hose, and particles moving along the field correspond to the flowing water. These particles exert a centrifugal force and drive a bend (perturbation) in the field line. The centrifugal force is proportional to the parallel pressure ($P_{\parallel}$). The perpendicular pressure ($P_{\perp}$) and the tension of the magnetic field (B^2/μ_0), however, would restrict the perturbation. The firehose instability, or a blowup in the field line bending, arises if the driving force $P_{\parallel}$ cannot be balanced by the stabilizing factors of $P_{\perp}$ and B^2/μ_0.

5.3.2 Mirror Instability

The mirror instability is complementary to the firehose instability. However, the mirror mode is non-oscillatory and its proper treatment requires kinetic theory [e.g., Hasegawa, 1969; Southwood and Kivelson, 1993]. Mirror waves arise as the result of the mirror instability which is a purely growing mode. They propagate nearly perpendicular to the magnetic field and induce compressive magnetic fluctuations. The kinetic dispersion relation has the form [Hasegawa, 1969]

$$\frac{\omega^2}{k^2} = \frac{c^2}{\varepsilon_{yy}},$$

where ε_{yy} is the appropriate element of the plasma dielectric tensor with y being the direction transverse to both $\mathbf{B}$ and $\mathbf{k}$, and c is the speed of light. The electron contribution to the dispersion relation is factored out by assuming a cold electron distribution. The above equation can be reduced to

$$\omega = i\xi\mu^{1/2}\left[\eta - \left(1 + \frac{\mu}{\nu}\right)\frac{e^{\nu}}{I_0(\nu) - I_1(\nu)}\right], \tag{5.21}$$

where

$$\xi = \left(\frac{2}{\pi}\right)^{1/2}\left(\frac{T_{\parallel}}{T_{\perp}}\right)^{3/2}\frac{\Omega_p}{\beta_{\perp}},$$

$$\eta = \beta_{\perp}\left(\frac{T_{\perp}}{T_{\parallel}} - 1\right),$$

$$\mu = \frac{k_\parallel^2}{\Omega_p^2}\frac{k_\mathrm{B}T_\perp}{m_p},$$
$$\nu = \frac{k_\perp^2}{\Omega_p^2}\frac{k_\mathrm{B}T_\perp}{m_p}.$$

Here I_0 and I_1 are the modified Bessel functions of the first kind with order 0 and 1, respectively. This dispersion relation includes the effect of finite Larmor radius which will limit the maximum growth rate of the instability. The wave frequency ω is purely imaginary and as a result the mirror wave is non-propagating. This point contradicts the perspective of fluid theory.

The onset condition expressed by equation (5.1) is derived from the above equation in the long wavelength limit when the perpendicular wave number $k_\perp$ is much larger than the parallel wave number $k_\parallel$, i.e.,

$$\nu \ll 1,\ \frac{\mu}{\nu} \ll 1.$$

Correspondingly,

$$I_0(\nu) \sim 1,\ I_1(\nu) \sim 0,$$

which gives

$$\omega = i\xi\mu^{1/2}\left(\eta - 1\right). \tag{5.22}$$

The instability occurs when $\eta > 1$, the same condition as represented by equation (5.1). Therefore, η can be considered as a measure of the overshoot of the mirror instability. Here we use equation (5.21) to estimate the maximum growth rate of the mirror instability. As shown by this equation, the growth rate is proportional to $k_\parallel$. While $k_\perp \gg k_\parallel$, the maximum growth rate will be restricted by the effect of finite Larmor radius since the perpendicular wavelength cannot be smaller than the ion Larmor radius. Taking derivatives of equation (5.21) with respect to μ and ν and equating them to zero, i.e.,

$$\frac{\partial\omega}{\partial\mu} = 0,\ \frac{\partial\omega}{\partial\nu} = 0,$$

we obtain

$$k_\perp \simeq \frac{\sqrt{6}}{6}\Omega_p\left(\frac{k_\mathrm{B}T_\perp}{m_p}\right)^{-1/2}\left(\eta-1\right)^{1/2},\quad k_\parallel \simeq \frac{\sqrt{6}}{12}\Omega_p\left(\frac{k_\mathrm{B}T_\perp}{m_p}\right)^{-1/2}\left(\eta-1\right).$$

Substituting the expression of $k_\parallel$ into equation (5.22) results in the maximum growth rate

$$\gamma_m = \left(\frac{3}{\pi}\right)^{1/2}\frac{1}{6\beta_\perp}\left(\frac{T_\perp}{T_\parallel}\right)^{-3/2}\left(\eta-1\right)^2\Omega_p \tag{5.23}$$

in the long wavelength limit. The theoretical growth rate is displayed in Figure 5-3 over the two dimensional plane of the parallel plasma beta and thermal anisotropy under the constraint of $\eta > 1$. As is evident from the figure, a significant growth rate occurs only in high beta regions when the thermal anisotropy is moderate. The best

power law fit to the $0.01\Omega_p$ level of the growth rate over the range $5 \leq \beta_{\parallel p} \leq 50$ in the form of equation (5.2) gives $S = 1.05$ and $\alpha = 0.85$, close to but lower than the the numerical evaluation of Gary et al. [1997] in the same domain.

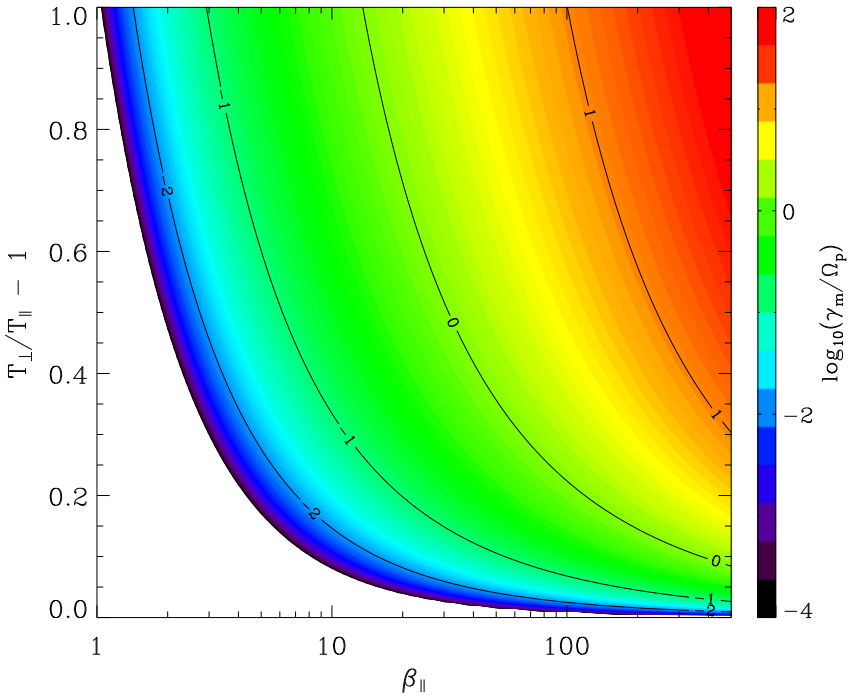

Figure 5-3: Theoretical growth rate of the mirror instability as a function of the parallel plasma beta and temperature anisotropy. The color bar indicates the logarithmic scale of the growth rate in units of the proton cyclotron frequency. Contour lines show the growth rate levels of $[10^{-2}, 10^{-1}, 10^{0}, 10^{1}] \times \Omega_p$.

The name of the mirror instability may be attributed to the mirror focusing of the field. The mirror instability was first observed in the dayside magnetosheath where the shocked solar wind plasma is preferentially heated in the perpendicular direction (see Chapter 6); at the same time the field-aligned flow around the magnetopause lowers the parallel temperature, which may also give favorable conditions for the instability to develop. To see how this instability arises, we write the pressure perturbation as [Hasegawa, 1969]

$$\delta P_\perp \sim -2P_\perp \left(\frac{T_\perp}{T_\parallel} - 1\right) \frac{\delta B}{B}.$$

At low frequencies, the perpendicular pressure responds in anti-phase to a compressional change in the field. When the temperature anisotropy is large enough, a decrease in the field strength will result in an increase in the total pressure. To restore the pressure balance, the field needs to further decrease, hence driving the instability.

Mirror mode instabilities produce anti-correlated density and magnetic field fluc-

tuations, namely,

$$\frac{\delta n}{n} = -\left(\frac{T_\perp}{T_\parallel} - 1\right)\frac{\delta B}{B} \tag{5.24}$$

for a bi-Maxwellian plasma [e.g., Hasegawa, 1969]. As described above the slow mode, alone among the three basic MHD modes, also has a density variation out of phase with the magnetic fluctuation in the same low frequency regime. It is still not clear how the mirror instability evolves to the non-linear stage. Kivelson and Southwood [1996] suggest that the fully evolved state would be such that the plasma is marginally stable to the mirror instability (i.e., $\eta \sim 1$) and the field configuration is characterized by large depressions or "holes" in the field strength.

5.3.3 Ion Cyclotron Instability

There is a second instability that occurs at frequencies below the ion gyro-frequency and competes with the mirror instability, the ion cyclotron instability. While the mirror mode is a high β instability, the ion cyclotron instability would dominate in low β plasma regimes. Unlike the mirror mode, the ion cyclotron instability has a real frequency ω_r and maximum growth rate at a wave vector parallel to the background field.

As shown above, the mirror instability recovers from the kinetic dispersion relations when $\mathbf{k}$ is highly oblique to $\mathbf{B}$. Here we show that the ion cyclotron and firehose instabilities recover from the kinetic dispersion relation when $\mathbf{k} \parallel \mathbf{B}$. In this case, $k_\perp = 0$, and $k_\parallel = k$. For bi-Maxwellian distributions as expressed by equation (5.3), the dispersion relation for the parallel propagation is of the form [Gary, 1993]

$$\omega^2 = k^2c^2 - \sum_j \omega_j^2 \left[A + \frac{(A+1)\omega \pm A\Omega_j}{kw_{\parallel j}} Z\left(\frac{\omega \pm \Omega_j}{kw_{\parallel j}}\right)\right], \tag{5.25}$$

where ω_j and Ω_j are the plasma frequency and gyro-frequency for particle species j, and

$$A = \frac{T_{\perp j}}{T_{\parallel j}} - 1,$$

$$w_{\parallel j} = \sqrt{\frac{2k_{\mathrm{B}}T_{\parallel j}}{m_j}}.$$

The plasma dispersion function $Z(\zeta)$ is defined as

$$Z(\zeta) = \frac{1}{\sqrt{\pi}} \int_{-\infty}^{+\infty} dx \frac{\exp(-x^2)}{x - \zeta}.$$

The summation extends over ions and electrons. The + (−) labels in equation (5.25) refer to waves with right (left) hand circular polarization. Let $\omega = \omega_r + i\gamma$, and suppose $|\gamma| \ll |\omega_r|$. Under these conditions, equation (5.25) gives the wave growth

rate

$$\gamma = \frac{\sqrt{\pi}}{2\omega_r} \sum_j \frac{\omega_j^2}{w_{\parallel j}} \left[-\frac{T_{\perp j}}{T_{\parallel j}} \frac{\omega_r}{k} \pm \left(1 - \frac{T_{\perp j}}{T_{\parallel j}} \right) \frac{\Omega_j}{k} \right] \exp \left[\frac{(\omega_r \pm \Omega_j)^2}{k^2 w_{\parallel j}^2} \right]. \tag{5.26}$$

The plasma is unstable when $\gamma > 0$. It is clear from this expression that, when $\omega_r \ll |\Omega_j|$, the right-handed (+) mode is unstable for an ion species with $T_{\perp j} < T_{\parallel j}$, which corresponds to the firehose instability; the left-handed mode (−) is unstable for species with $T_{\perp j} > T_{\parallel j}$, which recovers the ion cyclotron instability. The opposite is true for electrons since they have a negative Ω. Note that the mirror instability is not covered by the above equation since equation (5.25) is the dispersion relation for waves propagating along the magnetic field.

The above analysis indicates that the ion cyclotron instability would have a left-hand circular polarization whereas the firehose instability would be right-hand circularly polarized. Both of these instabilities have maximum growth rate at $\mathbf{k} \parallel \mathbf{B}$ and lead to transverse magnetic fluctuations, which is distinct from the mirror instability. The ion cyclotron instability is also found in the magnetosheath but predominantly in the plasma depletion layer. The firehose instability has not been identified in detail, but our theoretical analysis shows that it could be present downstream of a quasi-parallel shock (see Chapter 6).

There is no fluid picture for the generation of the ion cyclotron instability. It evolves out of the Alfvén or ion cyclotron wave if the temperature anisotropy is gradually increased. As can be seen from equation (5.26), the generation of the instability is related to cyclotron resonance through which waves and particles exchange energy. This process occurs when the Doppler shifted frequency of the wave is close to the ion cyclotron frequency, i.e., $\omega - kv_\parallel \sim \Omega_j$, where $v_\parallel$ is the particle velocity along the magnetic field. Particles are accelerated by the electric field of the wave when they are slightly slower than the phase velocity but are decelerated when they are slightly faster than the phase velocity. If the temperature anisotropy is such that there are more fast particles than slow particles fulfilling the resonance condition, the ion cyclotron instability occurs.

5.4 Case Study

We first present a study of the association of a PDL and mirror mode waves with an ICME observed by ACE and WIND on 16 - 17 April (day 106 - 107) 1999. Figure 5-4 shows the ACE data, with the ICME interval indicated by the shaded area (the same event as shown in Figure 1-3). The ICME was identified based on the enhanced helium/proton density ratio, declining speed, and depressed proton temperature; the smooth, strong magnetic field and large rotation of the B_y component indicate that this event is an MC. A forward shock driven by the event passed the spacecraft at 10:34 UT on 16 April, with simultaneous sharp increases in the proton density, bulk speed, temperature and magnetic field strength. Within the sheath region, between the shock and the leading edge of the MC, the proton density first increases due to the

compression at the shock and then decreases closer to the MC. This density decrease is the plasma depletion mentioned above. As shown by the bottom panel, fluctuations in the density and magnetic field strength are out of phase during the density increase; the correlation coefficient is about -0.6 for the data subtracted by the backgrounds (refer to section 5.4.3) between 11:00 and 15:30 UT on 16 April. This signature is typical for mirror waves. The second to last panel shows the temperature anisotropy and instability threshold conditions calculated from equation (5.2) for mirror and cyclotron instabilities. The dotted line in this panel shows WIND data scaled and time shifted to match the sheath and MC intervals seen at ACE. Anisotropies derived from WIND fit and ACE moment integrals are in agreement. The thermal anisotropy, $\frac{T_{\perp p}}{T_{\|p}} - 1$, is near zero inside the MC but drops to ~ -0.4 in the ambient solar wind. In the sheath region, the anisotropy is as high as 0.5 (exceeding the instability thresholds) and has an average value of 0.2 - 0.3 (very close to the thresholds). The plasma beta (its effect is also reflected by the instability thresholds) is very high in the sheath after 12:29 UT on 16 April, with values sometimes exceeding 50. As is evident from Figure 5-2, the mirror threshold is lower than the cyclotron limit when $\beta_{\|p} > 6$, which is also indicated in Figure 5-4. Therefore, mirror instabilities are excited in the sheath and give rise to the anti-correlated density and magnetic field fluctuations. More evidence is provided below for the plasma depletion and mirror mode structures.

5.4.1 Flux Rope and Shock Orientation

The mechanism described in section 5.1 for generation of PDLs and mirror mode waves may fit these observations. To test this fit requires knowledge of the MC and shock orientation. Minimum variance analysis (MVA, see section 3.2.2) provides estimates of the MC axis orientation using the measured magnetic field vectors [e.g., Lepping et al., 1990; Bothmer and Schwenn, 1998]. Eigenvectors of the magnetic variance matrix, $\hat{\mathbf{x}}^*$, $\hat{\mathbf{y}}^*$, $\hat{\mathbf{z}}^*$, corresponding to the eigenvalues in descending order, form a right-handed orthogonal coordinate system. MCs are oriented along the intermediate variance direction ($\hat{\mathbf{y}}^*$). Application of the MVA method to the normalized magnetic field measurements within the MC gives an axis, in terms of the azimuthal (Θ) and longitudinal (Φ) angles, of $\Theta = -69^\circ$ and $\Phi = 91^\circ$ in the geocentric solar ecliptic (GSE) coordinates. We also determine the axis orientation with a flux-rope reconstruction technique, based on the Grad-Shafranov equation [Hau and Sonnerup, 1999; Hu and Sonnerup, 2002]; the resulting axis orientation is very close to the MVA estimate.

Figure 5-5 is a 3-D view of the MC modeled as a cylindrical flux rope with a diameter of 0.23 AU (obtained from the average speed multiplied by the MC duration in Figure 5-4) in the GSE system. Note that the x axis points from the Earth to the Sun, so the Sun lies at (1, 0, 0) AU in the system. The flux rope is viewed from (-2, 1.5, 0) AU relative to the origin (Earth) of the system and is almost perpendicular to the ecliptic plane. The dark belt around the MC represents part of the shock surface which is approximated as a sphere centered at the Sun. The distance between the shock and the MC is about 0.08 AU along the ACE trajectory. The upper arrow

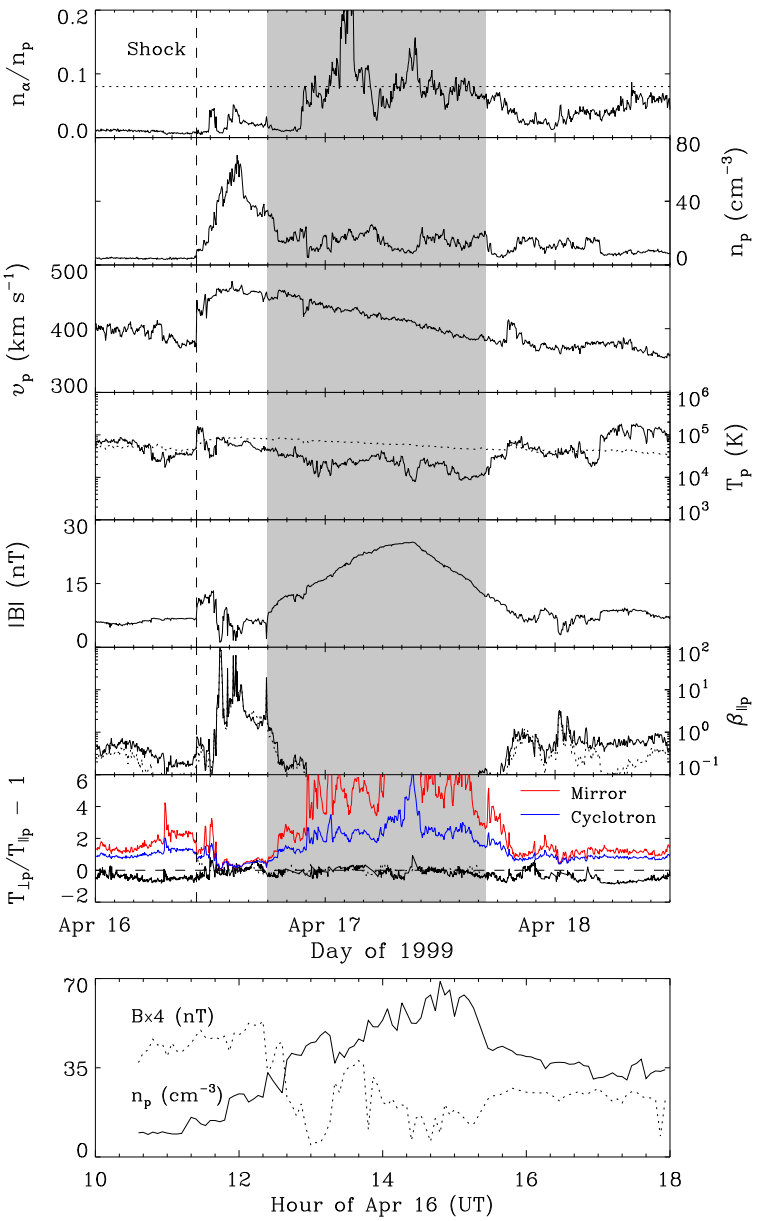

Figure 5-4: Solar wind plasma and magnetic field parameters measured by ACE for a 2.5-day interval in 1999. From top to bottom, the panels show the alpha-to-proton density ratio, proton density, bulk speed, proton temperature, magnetic field strength, parallel proton beta $\beta_{\|p}$, thermal anisotropy, and an expanded view of the magnetic and density fluctuations within the sheath. The shaded region shows an MC. Dashed lines indicate the arrival time of the MC-driven shock and the zero level of the anisotropy, respectively. Dotted lines denote the 8% level of the alpha/proton density ratio (top panel), the expected proton temperature (fourth panel), the perpendicular proton beta $\beta_{\perp p}$ (sixth panel), and the scaled WIND data (seventh panel). Mirror and cyclotron thresholds (computed from ACE data) are shown by the colored lines.

points in the direction of the shock normal with $\Theta = 7°$ and $\Phi = 178°$ determined from a least squares fit to the Rankine-Hugoniot relations [Viñas and Scudder, 1986]. Magnetic coplanarity gives a comparable result using the average magnetic field vectors upstream and downstream of the shock. The angle between the shock normal and upstream magnetic field is about 61°, so the shock is oblique. The shock normal makes an angle of about 96° with the flux-rope axis. Therefore, the whole situation can be pictured as a flux rope nearly perpendicular to the ecliptic plane moving away from the Sun (along the $-x$ direction) and driving an oblique shock ahead of it. In the MC frame, the ambient field lines may be draped around the MC, analogous to planetary magnetosheaths.

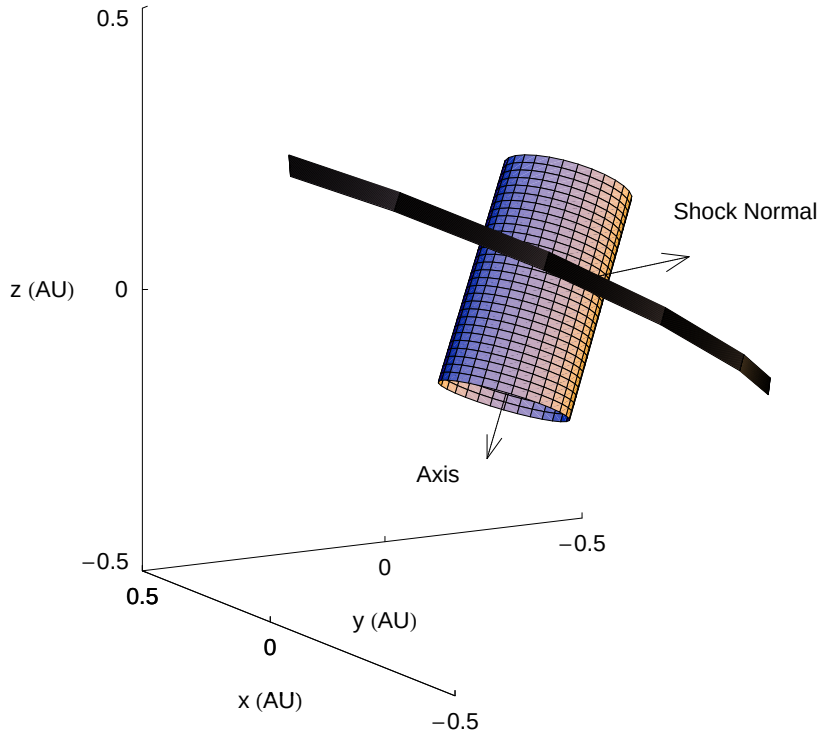

Figure 5-5: A 3-D rendering of the MC in GSE coordinates. Arrows indicate the axis orientation and shock normal, respectively. The belt around the flux rope approximates the shock surface.

The shock speed can be calculated from $v_s = \frac{n_2 v_2 - n_1 v_1}{n_2 - n_1}$ given by the conservation of mass across the shock. Substituting the upstream density $n_1 = 4$ cm^{-3} and velocity $v_1 = 375$ km s^{-1} and the downstream $n_2 = 9$ cm^{-3} and $v_2 = 430$ km s^{-1}, we obtain $v_s \simeq 474$ km s^{-1}, slightly larger than the MC leading-edge speed of 450 km s^{-1}. The size of the sheath, between the MC and shock, is thus expected to increase with distance. The MC is also expanding in the solar wind, as shown by the speed difference between the leading and trailing edges (see Figure 5-4). These two factors may affect the formation of PDLs and anisotropic ion distributions within the sheath.

5.4.2 Plasma Depletion and Magnetic Field Draping

Figure 5-6 provides an expanded view of the PDL and shows that it is associated with field line draping. The dashed lines bracket the PDL, in which the proton density decreases by a factor of 2 within 2.6 hours. Within the MC the B_y component, not B_z as usually seen in MCs, exhibits a large rotation, which confirms our MC axis determination. Interestingly, the magnetic field is nearly radial inside this PDL as indicated by the comparison of the B_x component with the field strength. Note that the spiral magnetic field makes an angle of 45° with the radial direction on average near the Earth; a radial field seldom occurs. The bottom panel shows the dot product of the field direction with the axis orientation, which is typically near zero in the PDL, so the field lines in the PDL are perpendicular to the MC axis. This product reaches its maximum close to the MC center. In contrast, the dot product between the field direction and the minimum variance direction ($\hat{\mathbf{z}}^*$) of the MC magnetic field is almost -1 in the PDL but roughly constant throughout the MC interval. The configurations of the flux rope and field lines within the PDL give direct evidence for field line draping. The good time coincidence between the density decrease and field line draping strengthens confidence for these features.

5.4.3 Wave Structures

As shown above, the mirror instability as well as the slow mode induces anti-correlated density and magnetic field fluctuations in the low frequency domain. A possible way to distinguish these two modes is to look at the wave amplitudes predicted by them. Identification of the wave also requires the propagation angle (θ) of the wave with respect to the background magnetic field. The direction of the wave vector can be estimated using MVA on the measured magnetic field. For plane waves, the propagation vector lies along the minimum variance direction. The best estimate of the direction is roughly normal to the magnetic field with an average value of 93° for the interval with active fluctuations in the sheath region, so the waves may be highly oblique. Therefore, equation (5.19) is reduced to

$$\frac{\delta n}{n} = -\left(1 + \frac{2}{\beta_\perp}\right)\frac{\delta B}{B} \tag{5.27}$$

for the slow mode. Equations (5.24) and (5.27) can be used to compare data with theoretical predictions.

Figure 5-7 displays the density variations within a 4-hour interval in the sheath region. Note that the fluctuations seem to be periodic at later times. A frequency of 1.04×10^{-3} Hz stands out in the power spectrum of the fluctuations, which corresponds to a period of about 960 s. The smooth density profile is obtained by applying a Butterworth low-pass filter to the frequency space of the data and then converting it back to the time domain. We set the cutoff frequency of the filter to 5×10^{-4} Hz, smaller than the present wave frequency. The same filter is also applied to the magnetic field data to get the background field strength. The filter removes fluctu-

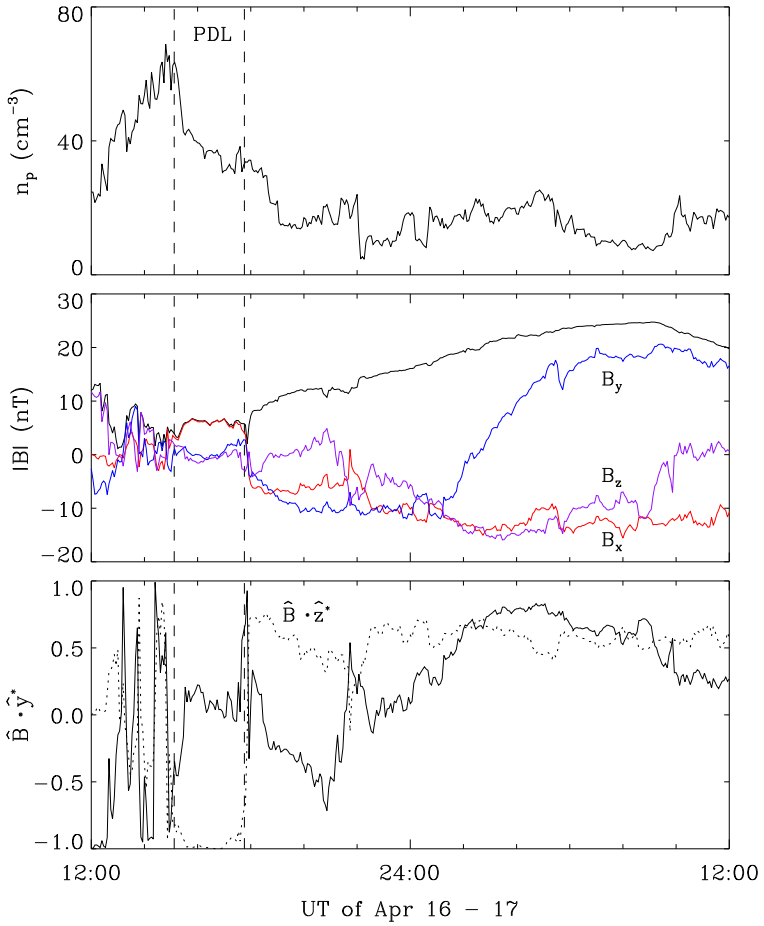

Figure 5-6: Proton density (upper panel), magnetic field magnitude with its components denoted by the colored lines (middle panel), and the dot product of the field direction with the MC axis orientation (lower panel) encompassing the PDL between the vertical dashed lines. The dotted line in the bottom panel shows the dot product between the field direction and the minimum variance direction of the MC magnetic field.

ations with frequencies higher than the cutoff frequency, so the smoothed quantities represent the unperturbed profiles. Using these background quantities and the field variations, we obtain the density perturbations predicted by the mirror and slow modes from equations (5.24) and (5.27), respectively. Figure 5-7 compares the observed and predicted density fluctuations. The density variations predicted by the mirror mode agree fairly well with observations after 12 UT on 16 April; only one spike is missed at 14:17 UT. The slow mode also predicts the phase of the variation correctly, but gives much larger fluctuation amplitudes than observed. As implied by equation (5.24), the mirror mode density perturbation relative to the background is smaller in amplitude than the corresponding magnetic field variation for a moderate anisotropy, while the opposite is true across slow mode waves as described by equation (5.27). Stasiewicz [2004] reinterpreted the mirror mode fluctuations in the

terrestrial magnetosheath as trains of slow mode solitons using Hall-MHD theory. In order to suppress the density variations, the author adopts $\kappa = 0$, $\gamma = 1.7$ for the relationship $P_\perp \sim n^\gamma B^\kappa$, whereas the CGL theory gives $\kappa = 1$, $\gamma = 1$ as required by the conservation of the magnetic moment. In addition, the present high β indicates breakdown of Hall-MHD theory (see section 6.3.3). We conclude that the wave activity is driven by the mirror mode. The density and magnetic field fluctuations in the PDL are significantly reduced (see Figure 5-4), probably due to the decrease in the plasma beta.

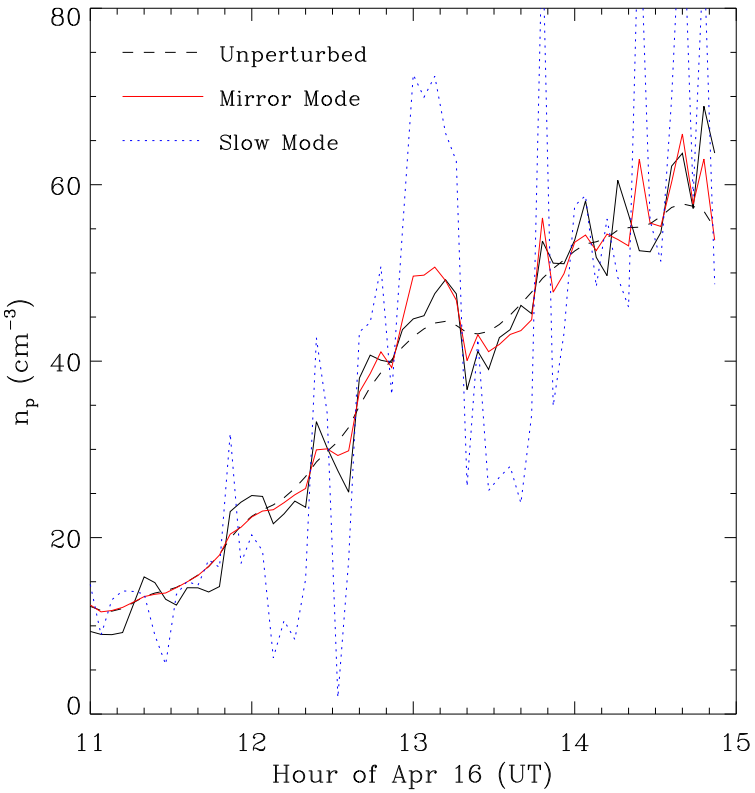

Figure 5-7: Expanded view of the density fluctuations ahead of the PDL. Colored lines indicate density variations predicted by the slow and mirror modes, respectively. The background profile obtained from a low-pass filter is represented by the dashed line.

Note that the mirror mode may couple to propagating waves, for instance, the drift wave produced by magnetic field and density gradients [Hasegawa, 1969], and then convect away. The oscillatory structure in Figure 5-7 may result from this wave coupling. The maximum growth rate can be estimated using equation (5.23). The average observed values $\beta_{\perp p} \simeq 12$ and $\frac{T_{\perp p}}{T_{\parallel p}} \simeq 1.2$ result in $\gamma_m = 0.02\Omega_p$, which seems reasonable for the overshoot of the instability of $\eta \simeq 2.4$.

5.5 Superposed Epoch Analysis

In the previous section, we presented an example showing the presence of a PDL and mirror mode waves in front of an MC. ICME data in the literature often show these features, e.g., Neugebauer and Goldstein [1997, Figure 3], Bothmer and Schwenn [1998, Figures 4, 5, 6, 7 and 8], Webb et al. [2000, Figure 6], Mulligan and Russell [2001, Figures 1 and 2], Richardson et al. [2002, Figure 2], Richardson et al. [2004, Figure 1], Zurbuchen and Richardson [2006, Figure 2], and Gosling et al. [2005, Figure 1]; all these ICMEs are preceded by shocks. In this section, we use a superposed epoch analysis (SEA) to give a broad-based view of these features. We define the ICME arrival time as the zero epoch and superpose the ICME-related data for the three ICME classes (MCs with shocks, non-MC ICMEs with shocks, ICMEs without shocks) separately. Typical uncertainties in identifying the beginning of an ICME are estimated to be 1 - 2 hours depending on the time resolution of the data. ICMEs with preceding shocks are scaled into a 30 hour long interval (the average duration of an ICME at 1 AU) and the sheath regions are scaled into 14 hour intervals (the average duration of the sheath at 1 AU); ICMEs without shocks are scaled into the same interval, but since there is no sheath region we use the 14 hours of data ahead of the ICMEs. Thus we line up the data in a fixed time relation to the ICME arrival times as if we had many observations of a single event. By averaging the superposed data for each time, real signals would be preserved but noise would tend to average out [e.g., Haurwitz and Brier, 1981; Prager and Hoenig, 1989].

Figure 5-8 displays the superposed 4 m averages of ACE plasma and magnetic field data for the three categories of ICMEs. As required by our ICME identification criteria, the ICME intervals (the data after the zero epoch) have a depressed proton temperature and the MCs (left panels) possess a strong magnetic field. The first two classes of ICMEs have expansion speeds (the speed difference between the leading and trailing edges) of about 90 km s^{-1}; the third class of ICMEs, those without preceding shocks, has an expansion speed of about 20 km s^{-1}. As a result of this expansion, the first two ICME classes have a lower average plasma density than the third class. Using the ambient solar wind density $n = 6.5$ cm^{-3}, temperature $T = 10^5$ K and magnetic field strength $B = 7$ nT derived from the data ahead of the ICMEs in the right panels, we estimate the fast mode speed from $v_f \sim (v_A^2 + \frac{5k_BT}{3m_p})^{1/2}$ to be around 70 km s^{-1}. The expansion speed can be regarded as the ICME speed relative to the ambient solar wind, which is larger than the fast mode speed for the first two ICME classes. Consequently, shock waves should be driven ahead of the fast ICMEs, consistent with the data in Figure 5-8. For all ICMEs, the expansion speed is of order of the Alfvén speed, 50 - 60 km s^{-1} at 1 AU. This result is in agreement with previous findings [e.g., Burlaga et al., 1981; Liu et al., 2005].

In the left and middle panels, the superposed shock occurs 14 hours before the arrival time of the ICMEs; between the shock and the ICME is the sheath region where PDLs and mirror mode waves may occur. For MCs with preceding shocks (left panels), a PDL is present beginning about six hours ahead of the ICME in which the proton density decreases by a factor of about 1.7 and the field magnitude gradually increases. The anti-correlated density and magnetic field fluctuations, with some times marked

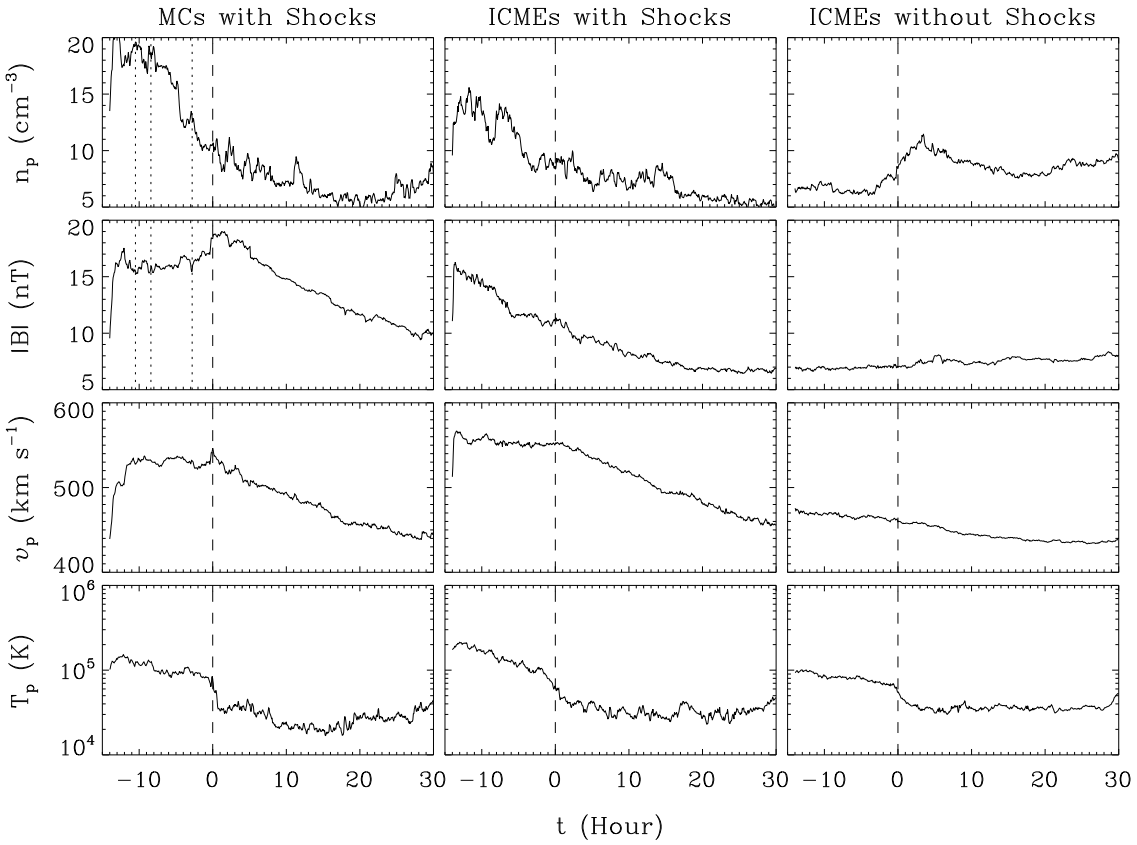

Figure 5-8: Superposed epoch plots of the proton density, magnetic field strength, bulk speed and proton temperature for the three classes of ICMEs. The zero time (dashed lines) is the ICME forward boundary. Dotted lines align some magnetic field dips with the corresponding density spikes in the MC sheath.

by the dotted lines, show that wave structures are also present. Presumably these structures are induced by the mirror instability; the superposed thermal anisotropy supports this interpretation (see Figure 5-9). Plasma depletion may also occur in the sheath region of ICMEs with shocks (middle panels). The plasma is rarefied in the layer adjacent to these ICMEs, but the magnetic field magnitude remains roughly constant. The density and magnetic field have high-frequency fluctuations, but no coherent structure is apparent. The sheath regions of the first two ICME classes thus show a different association with the PDL and mirror waves, which may reveal the dependence of these features on the ICME geometry. MCs are better organized than common ICMEs in terms of magnetic structure and may lead to favorable conditions for such features to develop. The ICMEs not associated with shocks (right panels) do not have PDLs and the density and magnetic fluctuations are even further reduced. The compression of the ambient solar wind by these ICMEs is apparently not large enough to produce these features, contrary to the suggestion of Farrugia et al. [1997] that a PDL may form irrespective of whether ICMEs drive shocks or not. Figure 5-8 indicates that shocks may be necessary to produce these features, since their formation

is closely related to the extent of the compression. Observations of PDLs in planetary magnetosheaths show a gradual increase in the magnetic field simultaneous with the density decrease [e.g., Crooker et al., 1979; Hammond et al., 1993; Violante et al., 1995]. This increase in the field strength may not be required in ICME sheaths. The upstream field compression by ICMEs may be alleviated by the sheath expansion as the preceding shocks move away from the ejecta.

The speed and field strength profiles within ICMEs are smooth compared with the turbulent profiles of the density and temperature. As is well known, Alfvén waves give rise to correlated velocity and magnetic field fluctuations [e.g., Stix, 1962]. The low-frequency Alfvén waves may be responsible for solar wind heating and acceleration through a non-linear cascade process of energy [e.g., Isenberg and Hollweg, 1983; Goldstein et al., 1995; Leamon et al., 1999; Hu and Habbal, 1999]. Radial evolution of ICMEs is investigated in Chapter 4; we find that the ICME temperature decreases more slowly with distance than an adiabatic profile. This plasma heating may not be powered by Alfvén waves since they are not prevalent within ICMEs as implied by the smooth speed and magnetic field profiles.

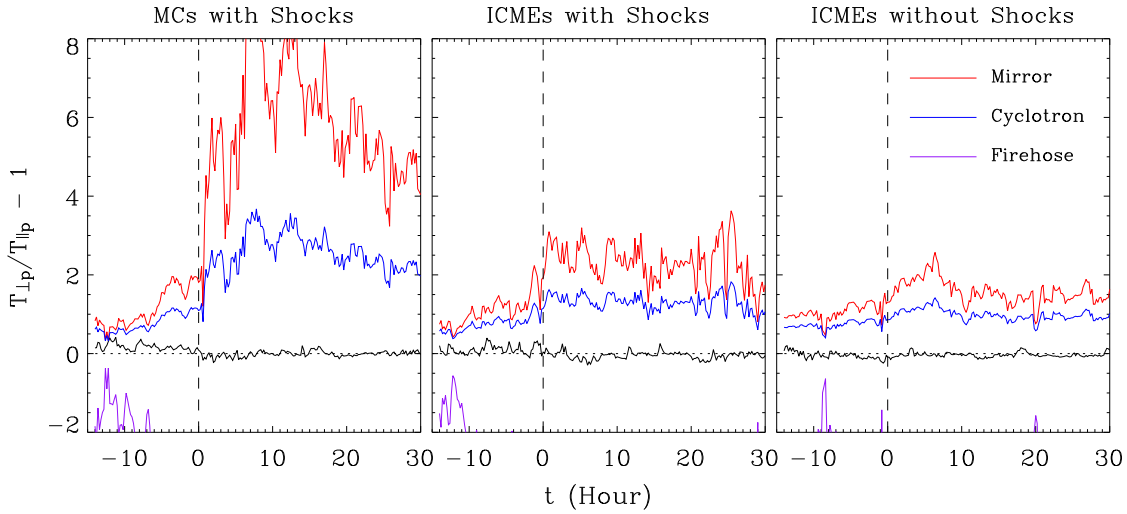

Figure 5-9: Superposed epoch plots of proton thermal anisotropy for the same three classes of ICMEs as in Figure 5-8. Dashed lines mark the ICME arrival times while dotted lines show the zero level of the anisotropy. Threshold conditions for the instabilities are represented by the colored lines.

Mirror waves can also be evidenced by the temperature anisotropy. Figure 5-9 shows the superposed thermal anisotropy data from WIND for the three classes of ICMEs. The instability threshold conditions, calculated from the superposed parallel plasma beta $\beta_{\parallel p}$ using equation (5.2), are plotted to allow comparison with the anisotropy. An abrupt increase in the mirror and cyclotron thresholds can be seen at the leading edge of the first two groups of ICMEs (left and middle panels); it is stronger in the first case, indicating that the plasma beta is low within these MCs. For the third ICME class (right panel), the onset conditions inside and outside the

ICMEs are similar. The ICME plasma typically has an anisotropy near zero, so it is stable with respect to temperature anisotropy instabilities. This point is consistent with the picture described by Figures 4-9 and 5-2. The thermal anisotropy increases to 0.1 - 0.4 in the sheath regions of the first ICME category (left panel) and is very close to the instability thresholds at some epochs. The sheath plasma may be marginally unstable to the mirror and cyclotron instabilities. As a result, mirror waves may be induced under certain conditions and then be carried away by plasma flows. This interpretation is in accord with the anti-correlated density and magnetic field fluctuations seen in Figure 5-8 (left panels). The temperature anisotropy may also be enhanced in the sheaths of the second ICME class (middle panel), but not as strongly, so the fluctuations are reduced as shown in Figure 5-8 (middle panels). For the third ICME group (right panel), the thermal anisotropy does not deviate from zero across the sheath and ICME intervals, so mirror waves do not appear.

The superposed parallel proton beta $\beta_{\|p}$ ranges from 0.5 to 5.5 in the sheath regions of the MCs with preceding shocks. In this regime, the instabilities are dominated by the cyclotron mode since it has a lower threshold than the mirror mode (refer to Figure 5-2). Gary [1992] showed through numerical evaluation of the Vlasov dispersion relation that the cyclotron instability has a higher linear growth rate. The temperature anisotropy can be rapidly reduced by the cyclotron instability and thus the mirror mode may not develop to a significant level. However, Price et al. [1986] found that the introduction of a small fraction of minor ions would substantially lower the growth rate of the cyclotron instability while leaving the mirror mode unaffected. Since helium ions are always present in the solar wind, the mirror mode would be able to grow given the observed plasma beta and thermal anisotropy.

It should be noted that the SEA smoothes the data. Consequently, the superposed field magnitude and density do not exhibit large fluctuations. The smoothed profiles of the threshold conditions and thermal anisotropy also underestimate the marginal instability to the mirror mode. Examining ICMEs individually is the best way to see the mirror mode structures, as demonstrated by the case study in section 5.4. The references listed in the first paragraph of section 5.5 give ICMEs that often show the mirror mode fluctuations (and PDLs) in their sheath regions; large dips in the magnetic field strength serve as a good identifier for the mirror mode structures.

5.6 Test of Superposed Epoch Analysis

Superposed epoch analysis (SEA) is useful to identify the association of individual features with key events (here defined as the ICME arrival times) in time series data. The statistical significance of the association can be determined by a randomization technique which avoids the assumptions of normality, random sampling and sample independence made by parametric testing [e.g., Haurwitz and Brier, 1981; Prager and Hoenig, 1989]. The null hypothesis is that plasma depletion and mirror waves are not associated with ICMEs. Under this null hypothesis, any time in the data can be considered as a key event, i.e., an ICME arrival time.

We use the 4 m averages of ACE proton density data from 1998 - 2005 as a proxy

for the significance test. We repeatedly draw random sets of locations for the key event and their corresponding background times from the data. Key events closer than a minimum spacing of 27 days are discarded to avoid the effect of solar sector crossings. Each randomization yields 39 positions of simulated ICME arrival times and 660 background spectra corresponding to each key event (210 before and 450 after). For each set, we compute the t-statistic defined as

$$t = \frac{\bar{E} - \bar{B}}{\sqrt{\frac{(m+n)(m\sigma_E^2 + n\sigma_B^2)}{mn(m+n-2)}}},$$

where σ_E and σ_B are the standard deviations of the $m = 39$ key events and $n = 660 \times 39$ background times respectively, and $\bar{E}$, $\bar{B}$ are their corresponding means. This statistic obeys Student's t-distribution with degrees of freedom $m + n - 2$ for normally distributed and independent data. The observed t-statistic is calculated from the true arrival times of the 39 ICMEs with preceding shocks used in our analysis. The frequency distribution of the simulated t-statistic resulting from 10,000 runs of the randomization is displayed in Figure 5-10 as a histogram with a bin size of 0.1. Compared with the Gaussian fit, the distribution skews toward the high-value tail. The significance level can be estimated from the relative frequency with which the simulated t-statistic is smaller than or equal to the observed one. The observed statistic is about 0.91, corresponding to a significance level of 91%. In contrast, the standard t-distribution gives 82% for the observed statistic.

5.7 Conclusions and Discussion

In analogy with planetary magnetosheaths, we propose that PDLs and mirror mode structures form in the sheath regions of fast ICMEs. The upstream field compression by fast ICMEs and their leading shocks results in field line draping and anisotropic plasma heating in the sheath. An extensive case study and statistical analysis of ICMEs observed by ACE and WIND show that these two features occur in the sheaths ahead of fast events.

The association of plasma depletion and mirror waves with ICMEs is demonstrated by an MC example observed at ACE and WIND on 16 April 1999. This event drives a forward oblique shock with its axis perpendicular to the shock normal. Downstream of the shock, the proton density decreases by a factor of 2 within 2.6 hours (corresponding to 0.03 AU in length) ahead of the MC. At the same time the magnetic field is stretched to be nearly radial and normal to the MC axis. Anti-correlated density and field strength fluctuations are seen inside the sheath region between the MC and the shock and are consistent with mirror mode waves; the thermal anisotropy exceeds the mirror mode onset condition and the plasma beta is high. Analytical growth rates of the mirror instability limited by the effect of finite Larmor radius are obtained as a function of plasma beta and temperature anisotropy. From the observed overshoot of the mirror instability the maximum growth rate is estimated to be around $0.02\Omega_p$.

We perform a SEA on three classes of ICMEs to investigate the general properties

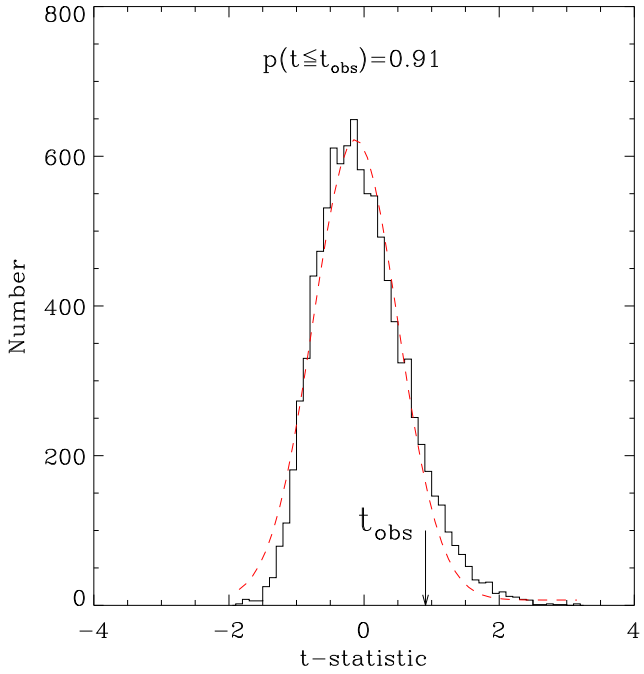

Figure 5-10: Histogram distribution of the t-statistic from the Monte Carlo simulations with its Gaussian fit denoted by the dashed line. The arrow indicates the value of the real statistic while the upper text shows the significance level.

of PDLs and mirror mode waves associated with these different kinds of events. On average, the sheath region is about 14 hours long (roughly 0.17 AU) at 1 AU in comparison with the 0.2 - 0.3 AU span of ICME intervals. For MCs preceded by shocks, PDLs are observed to have an average density decrease of a factor of 1.7 which lasts about 6 hours and is accompanied by a gradual increase in the field magnitude. The average thermal anisotropy $\frac{T_{\perp p}}{T_{\parallel p}} \simeq 1.2$ - 1.3, close to the threshold for the mirror instability, leads to anti-correlated fluctuations in the density and magnetic field strength. Compared with the MCs, non-MC ICMEs with forward shocks have a thinner plasma depletion layer close to their leading edges. The thermal anisotropy is only slightly enhanced, so fluctuations in the density and magnetic field are smaller and do not have a definite structure. This difference between the two classes may indicate the effect of the ICME geometry in creating the features. The third category, ICMEs without shocks, is not associated with plasma depletion and mirror waves. The occurrence of these signatures may be determined by the extent of the upstream field compression by ICMEs. As a measure of the compression, an ICME speed of about 90 km s^{-1} relative to the ambient solar wind seems necessary to drive shocks and produce the features. As revealed by the SEA, all the ICME plasma is stable to the temperature anisotropy instabilities, consistent with the finding in Chapter 4.

These results reveal important physical processes which alter the ICME environment and provide another setting in which to study PDLs and mirror mode waves. As

noted by Zwan and Wolf [1976], PDLs can only develop in the absence of significant magnetic reconnection; otherwise, flux tubes that are compressed against the magnetosphere would merge with geomagnetic field lines before they are diverted around the obstacle. The same condition should hold in ICME sheaths for the squeezing process to be operative. An ideal MHD simulation of plasma flow behind MC-driven shocks also seems to confirm that the PDL becomes thinner with a small increase in the reconnection rate [Erkaev et al., 1995]. McComas et al. [1988, 1994] suggest that magnetic reconnection should commonly take place between fast ICMEs and the upstream ambient solar wind in the same manner as occurs at the dayside of the magnetopause. Direct evidence for the local reconnection in the solar wind was not provided until recently, but none of the reconnection sites are at the interface between ICMEs and the upstream solar wind [Gosling et al., 2005]. Given the frequency of PDLs in ICME sheaths, magnetic reconnection may not be prevalent or locally important in the sheath regions of fast ICMEs.

Observations of planetary magnetosheaths indicate that mirror waves can make large depressions, i.e., holes in the background magnetic field [e.g., Kaufmann et al., 1970; Tsurutani et al., 1992; Violante et al., 1995]. This point is emphasized by Winterhalter et al. [1994] who made a survey of magnetic holes observed at Ulysses and examined their relationship with mirror instabilities. Consistent with the results of Klein and Burlaga [1980], they find that the holes tend to occur in the interaction regions where fast streams overtake the ambient solar wind and the mirror mode is marginally stable. Non-linear saturation mechanisms of the mirror instability are qualitatively discussed by Kivelson and Southwood [1996]. In the non-linear saturation process, marginal stability can be achieved by large reductions in the magnetic field, so the fully evolved state would be characterized by holes in the background magnetic field rather than alternate field enhancements and depressions. However, Bavassano Cattaneo et al. [1998] suggest that mirror waves make field enhancements as well as dips based on Voyager observations of Saturn's magnetosheath. According to Figure 5-3, the mirror instability will grow quickly and consequently make a series of holes when the plasma beta is high; adjacent holes are so close that the magnetic field appears to be alternately enhanced and depressed. When the plasma beta is occasionally high, the hole will be isolated. Their observed plasma beta profile seems to support this explanation. If the interpretation that magnetic holes are remnants of mirror mode structures is correct, the mechanism suggested here would be able to explain the creation of some magnetic holes localized in the solar wind in a self-consistent manner.

Mirror waves may contribute to energetic particle modulation and acceleration in the sheath regions of ICMEs. Various studies of the cosmic ray modulation in the solar wind show that enhanced magnetic turbulence in the sheath is particularly effective in producing Forbush decreases [e.g., Badruddin et al., 1991; Ifedili, 2004], probably due to particle scattering by waves or their non-linear evolved states. According to Kivelson and Southwood [1996], the final evolved state of mirror waves would be such that the total perpendicular pressure (plasma plus field) is constant along the field line. Particles with small pitch angles will be constrained by the mirror force $F = -\mu\nabla_{\parallel}B$, where μ is the magnetic moment; if the magnetic moment and total

energy are invariant, motion of these particles into weak field regions along the field line will convert perpendicular energy to parallel and kinetic energy, which can serve to suppress growth of the mirror instability. Particles with large pitch angles may be excluded from strong field regions, also leading to the pressure balance.

This work reveals some universal physical processes that occur in different environments (also see Chapter 6). It relates a diversity of phenomena that can be explained in a self-consistent manner. The content of this chapter has been published in the *Journal of Geophysical Research* [see Liu et al., 2006b].

Chapter 6

Comparative Shocks and Sheaths in the Heliosphere

We extend the study of ICME sheaths to planetary magnetosheaths and the heliosheath, and generalize some universal processes including temperature anisotropy instabilities, magnetic field draping and plasma depletion in these regions. We show that temperature anisotropies induced at a shock can account for interplanetary and planetary bow shock observations. Shocked plasma with enhanced plasma β is preferentially unstable to the mirror instability downstream of a quasi-perpendicular shock and to the firehose instability downstream of a quasi-parallel shock, consistent with magnetic fluctuations observed downstream of a large variety of shocks. Our theoretical analysis of the solar wind termination shock suggests that the magnetic holes observed by Voyager 1 in the heliosheath are produced by the mirror instability. The results are also of astrophysical interest, providing an energy source for plasma heating.

6.1 Introduction

Planetary bow shocks and interplanetary shocks serve as a unique laboratory for the study of shock waves in collisionless plasmas. Observations of these shocks usually show that ion distributions are anisotropic with respect to the background magnetic field downstream of the shocks. Mirror mode waves associated with this anisotropy are observed downstream of quasi-perpendicular shocks (defined by the angle between the shock normal and the upstream magnetic field $\theta_{Bn} > 45°$) when the plasma β is high ($\beta > 1$) [Kaufmann et al., 1970; Tsurutani et al., 1992; Violante et al., 1995; Bavassano Cattaneo et al., 1998; Liu et al., 2006b]. Mirror mode waves do not grow in low β regions where the ion cyclotron mode dominates [e.g., Anderson et al., 1994; Czaykowska et al., 2001]. Magnetic fluctuations downstream of quasi-parallel shocks ($\theta_{Bn} < 45°$) have not been identified in detail, but hybrid simulations show that the firehose instability can occur downstream of these shocks for certain ranges of upstream Alfvén Mach number (M_A) and plasma β, for instance, $M_A \geq 3$ at $\beta \sim 0.5$ [Kan and Swift, 1983; Krauss-Varban and Omidi, 1991]; observations seem to confirm

this point [e.g., Greenstadt and Fredricks, 1979; Bavassano Cattaneo et al., 2000]. Quasi-perpendicular shocks are characterized by a sharp increase in the magnetic field strength, but quasi-parallel shocks are often more turbulent, with shock ramps containing large-amplitude waves which spread upstream and downstream.

The recent crossing of the termination shock (TS) by Voyager 1 [Burlaga et al., 2005; Decker et al., 2005; Gurnett and Kurth, 2005; Stone et al., 2005] provides an opportunity to study the TS and shock-induced waves in the heliosheath. The sharp increase in the magnetic field strength across the TS and the downstream magnetic field configuration suggest that the TS is quasi-perpendicular [Burlaga et al., 2005]. As in planetary magnetosheaths downstream of a quasi-perpendicular bow shock, the heliosheath shows compressive magnetic fluctuations in the form of magnetic holes [Burlaga et al., 2006a,b].

The idealized picture of ICMEs with shocks shown in Figure 5-1 is analogous to planetary magnetosheaths and the heliosheath for northward interplanetary magnetic fields, in which case magnetic reconnection at the dayside magnetopause and heliopause is absent. The ICME preceding shock is analogous to the planetary bow shock and the TS, and the ICME driver is analogous to the magnetospheric and interstellar medium obstacles. This suggests that excitation of proton temperature anisotropy instabilities in these sheaths should be similar. Magnetosheath observations [e.g., Anderson et al., 1994] have shown that mirror mode fluctuations occur in the relatively high β plasma downstream of the shock, whereas the low β plasma depletion layer (PDL) is the location of proton cyclotron instabilities. Therefore, by analogy the same should hold for fluctuations in ICME sheaths and the heliosheath: mirror mode fluctuations should be likely in the high β region and proton cyclotron fluctuations should be likely in the low β depletion layer. In addition to these instabilities, other processes such as magnetic field draping and plasma depletion should also be qualitatively similar.

In this chapter, we perform a comparative study of interplanetary shocks, planetary bow shocks and the TS and their corresponding sheaths. We propose a theoretical explanation in section 6.2 for the temperature anisotropies and associated instabilities induced at a shock. Section 6.3 provides observations in planetary magnetosheaths, ICME sheaths and the heliosheath; we show that, based on the theoretical analysis, the magnetic holes observed in the heliosheath could be mirror mode fluctuations. We summarize and discuss the results in section 6.4. The present results provide a prototype for understanding shocks in various astrophysical contexts, such as gamma-ray bursts, supernova explosions and active galactic nuclei.

6.2 Theory

An anisotropic ion distribution requires use of a pressure tensor in the magnetohydrodynamic (MHD) equations. Observations show that the shock structure and dynamics depend on the shock geometry and upstream M_{A1} and β_1, so we examine the temperature anisotropy $A_2 = T_{\perp 2}/T_{\parallel 2}$ as a function of these parameters, where $T_\perp$ and $T_\parallel$ are the plasma temperature perpendicular and parallel to the magnetic

field. The subscripts 1 and 2 indicate physical parameters upstream and downstream of a shock. Assuming a bi-Maxwellian plasma, we write the jump conditions across a shock as [Hudson, 1970]

$$[B_n] = 0, \tag{6.1}$$

$$[\rho v_n] = 0, \tag{6.2}$$

$$[v_n \mathbf{B}_t - \mathbf{v}_t B_n] = 0, \tag{6.3}$$

$$\left[P_\perp + (P_\parallel - P_\perp)\frac{B_n^2}{B^2} + \frac{B_t^2 - B_n^2}{2\mu_0} + \rho v_n^2\right] = 0, \tag{6.4}$$

$$\left[\frac{B_n \mathbf{B}_t}{\mu_0}\left(\frac{P_\parallel - P_\perp}{B^2/\mu_0} - 1\right) + \rho v_n \mathbf{v}_t\right] = 0, \tag{6.5}$$

$$\left[\rho v_n \left(\frac{2P_\perp}{\rho} + \frac{P_\parallel}{2\rho} + \frac{v^2}{2} + \frac{B_t^2}{\mu_0 \rho}\right) + \frac{B_n^2 v_n}{B^2}(P_\parallel - P_\perp) - \frac{(\mathbf{B}_t \cdot \mathbf{v}_t)B_n}{\mu_0}\left(1 - \frac{P_\parallel - P_\perp}{B^2/\mu_0}\right)\right] = 0, \tag{6.6}$$

where μ_0 is the permeability of free space, ρ is the plasma density, and $\mathbf{v}$ and $\mathbf{B}$ are the plasma velocity and magnetic field with subscripts t and n denoting the tangential and normal components with respect to the shock surface. The square brackets indicate the difference between the preshock (1) and postshock (2) states. The above equations describe conservation of the normal component of the magnetic field, the mass flux, the tangential component of the electric field, the normal and tangential components of the momentum flux, and the energy flux, respectively. They are obtained from Maxwell's equations and the energy momentum tensor of anisotropic fluids. The velocity is measured in the shock frame. For simplicity, we assume that the bulk velocity is parallel to the shock normal. The perpendicular and parallel plasma pressures are defined as $P_\perp = \rho k_\mathrm{B} T_\perp / m_p$ and $P_\parallel = \rho k_\mathrm{B} T_\parallel / m_p$, where k_B and m_p represent the Boltzmann constant and proton mass, respectively. The components of the magnetic field upstream of the shock are given by $B_{n1} = B_1 \cos\theta_{Bn}$ and $B_{t1} = B_1 \sin\theta_{Bn}$. Different forms of the solutions to these equations have been derived based on various assumptions [Chao et al., 1995; Erkaev et al., 2000]. The focus of the present analysis is to investigate under what conditions the shocked plasma is unstable to the thermal anisotropy instabilities.

The thermal anisotropy serves a free energy source which can feed magnetic fluctuations when it exceeds certain threshold conditions. As shown in section 5.3, the thresholds can be expressed as $A = 1 - 2/\beta_\parallel$ for the firehose instability, the lower bound of the temperature anisotropy, and $A = 1 + 1/\beta_\perp$ for the mirror mode instability, the upper bound; the ion cyclotron instability, competing with the mirror mode, has the onset condition $A = 1 + 0.64/\beta_\parallel^{0.41}$. The perpendicular and parallel plasma β's are defined as $\beta_\perp = P_\perp/(B^2/2\mu_0)$ and $\beta_\parallel = P_\parallel/(B^2/2\mu_0)$.

For a perpendicular shock, equations (6.2) and (6.3) give the shock strength

$$r_s = \frac{\rho_2}{\rho_1} = \frac{v_1}{v_2} = \frac{B_2}{B_1}. \tag{6.7}$$

To write the temperature anisotropy as a function of the upstream plasma β_1, we define

$$P = \frac{2P_\perp + P_\parallel}{3}.$$

In association with $A = P_\perp/P_\parallel$, the perpendicular and parallel pressures can be written as

$$P_\perp = \frac{3AP}{2A+1}, \quad P_\parallel = \frac{3P}{2A+1}.$$

The temperature anisotropy A_2 can thus be obtained from equations (6.4), (6.5) and (6.6),

$$A_2 = \frac{\frac{3A_1\beta_1}{2A_1+1} + 2M_{A1}^2(1-1/r_s) + 1 - r_s^2}{\frac{3A_1\beta_1}{2A_1+1}(4r_s - 4 + r_s/A_1) + 2M_{A1}^2(r_s + 3/r_s - 4) + 4(r_s - 1)}, \tag{6.8}$$

where $\beta = P/(B^2/2\mu_0)$. To compare with the thresholds, we derive $\beta_{\perp 2}$ from equation (6.4) as

$$\beta_{\perp 2} = \frac{3A_1\beta_1}{(2A_1+1)r_s^2} + \frac{2M_{A1}^2}{r_s^2}(1-1/r_s) - 1 + \frac{1}{r_s^2}. \tag{6.9}$$

For $2M_{A1}^2 \gg \beta_1$, we have

$$\beta_{\perp 2} \sim \frac{2M_{A1}^2}{r_s^2}(1-1/r_s), \tag{6.10}$$

so the shocked plasma would have a high β independent of β_1, consistent with the findings in the magnetosheaths of outer planets [Russell et al., 1990]. Since $M_A^2 = \rho v^2/(B^2/\mu_0)$, $M_{A1}^2 \gg \beta_1$ means that the upstream thermal energy density can be neglected compared to the kinetic energy density. At the shock front some kinetic energy is converted to the thermal energy added to the original one which is very small, so the downstream plasma β_2 would be independent of the upstream β_1. As can be seen from the mirror-mode threshold, high values of $\beta_{\perp 2}$ favor the onset of the mirror mode instability. Similarly,

$$A_2 \sim \frac{1}{r_s - 3}, \tag{6.11}$$

under the same condition, so $A_2 \geq 1$ since the shock strength cannot be larger than 4, also favoring the mirror mode onset.

As required by the second law of thermodynamics, the entropy has to increase across a shock. For a bi-Maxwellian plasma, there are two entropy functions associated with the two adiabatic equations corresponding to the perpendicular and parallel degrees of freedom, i.e.,

$$S_\perp = k_\mathrm{B} \ln\left(\frac{P_\perp}{\rho B}\right), \quad S_\parallel = \frac{1}{2}k_\mathrm{B} \ln\left(\frac{P_\parallel B^2}{\rho^3}\right),$$

where the entropies are referred to an individual particle. The variations of the

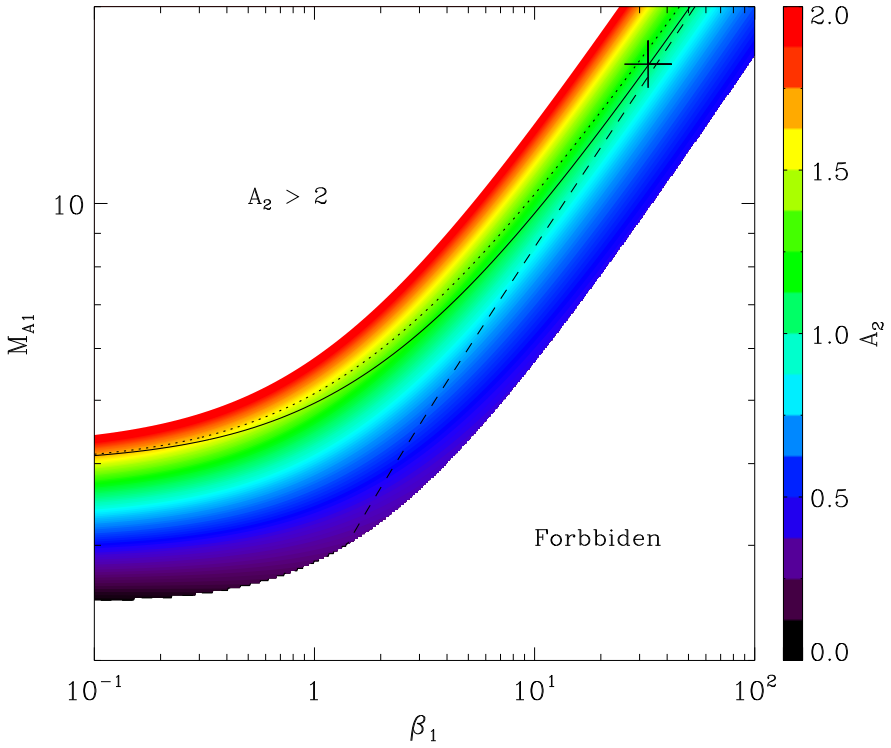

Figure 6-1: Temperature anisotropy downstream of a perpendicular shock with $r_s = 3$ and $A_1 = 1$ as a function of β_1 and $M_{\rm A1}$. The color shading denotes the values of A_2. The lower region is forbidden for a $r_s = 3$ shock since the entropy does not increase across the shock. Also shown are the thresholds for the mirror mode (solid line), ion cyclotron (dotted line) and firehose (dashed line) instabilities. Regions above the mirror/ion cyclotron threshold are unstable to the mirror/ion cyclotron mode and regions below the firehose onset are unstable to the firehose instability. The plus sign marks the TS location.

entropies can be written as

$$T_\parallel dS_\parallel = q + q_1, \quad T_\perp dS_\perp = -q + q_2,$$

where q is the exchange heat flux between the perpendicular and parallel degrees of freedom, and q_1 and q_2 are thermal energy extracted from the kinetic energy inside the shock front. Adding the above two expressions together, we obtain

$$dS = \frac{q(T_\perp - T_\parallel)}{T_\perp T_\parallel} + \frac{q_1}{T_\parallel} + \frac{q_2}{T_\perp}, \tag{6.12}$$

where the total entropy is

$$S = S_\parallel + S_\perp = \frac{1}{2} k_{\rm B} \ln\left(\frac{P_\perp^2 P_\parallel}{\rho^5}\right). \tag{6.13}$$

The second and third terms in equation (6.12) are always positive because they are associated with the thermal dissipation of the plasma flow. The first term is also positive since by definition $q > 0$ when $T_\perp > T_\parallel$ and $q < 0$ when $T_\perp < T_\parallel$. Therefore, the entropy change dS across a shock must be positive in all cases.

The temperature anisotropy expressed by equation (6.8) has to be restricted by the entropy principle. The entropy requirement $S_2 > S_1$ reduces to

$$\frac{P_{\perp 2}^3}{P_{\perp 1}^3}\frac{A_1}{A_2}\frac{1}{r_s^5} > 1,$$

where the ratio of the pressures is

$$\frac{P_{\perp 2}}{P_{\perp 1}} = 1 + \frac{2A_1+1}{3A_1\beta_1}\left(1 - r_s^2 + 2M_{A1}^2 - \frac{2M_{A1}^2}{r_s}\right)$$

given by equation (6.4). These two expressions, combined with equation (6.8), indicate plasma regimes which are "forbidden" or "allowed" by the entropy requirement.

Figure 6-1 shows the temperature anisotropy A_2 for $r_s = 3$ and $A_1 = 1$ as a function of M_{A1} and β_1. Only values of $0 \leq A_2 \leq 2$ are shown. The region which breaks the entropy principle is show as "Forbidden" in Figure 6-1. The majority of the allowed area has $A_2 \geq 1$ as expected and is preferentially unstable to the mirror mode instability. The mirror mode has a lower threshold than the cyclotron mode in this plasma regime, so the temperature anisotropy would be quickly reduced by the mirror mode before the ion cyclotron mode could develop. The TS with $\beta_1 \simeq 32.8$ and $M_{A1} \simeq 16.3$ (see section 6.3.3), indicated by the plus sign, is located slightly above the mirror mode threshold. Interplanetary and planetary bow shocks have a large variation in M_{A1} and β_1; many of them would also be above the mirror mode threshold as indicated by the large area with $A_2 \geq 1$. Consequently, mirror mode instabilities should be a frequent feature downstream of quasi-perpendicular shocks.

For a parallel shock, $B_1 = B_2$ across the shock, so a large jump in the field strength would imply a quasi-perpendicular shock. The shock strength is now

$$r_s = \frac{\rho_2}{\rho_1} = \frac{v_1}{v_2}. \tag{6.14}$$

The temperature anisotropy

$$A_2 = \frac{\frac{3\beta_1 r_s}{2A_1+1}(A_1 + \frac{3}{2} - \frac{3}{2r_s}) + M_{A1}^2(r_s + 2/r_s - 3)}{\frac{3\beta_1}{2A_1+1} + 2M_{A1}^2(1 - 1/r_s)}, \tag{6.15}$$

and the downstream parallel plasma beta

$$\beta_{\parallel 2} = \frac{3\beta_1}{2A_1+1} + 2M_{A1}^2(1 - 1/r_s). \tag{6.16}$$

For $2M_{A1}^2 \gg \beta_1$,

$$\beta_{\parallel 2} \sim 2M_{A1}^2(1 - 1/r_s), \tag{6.17}$$

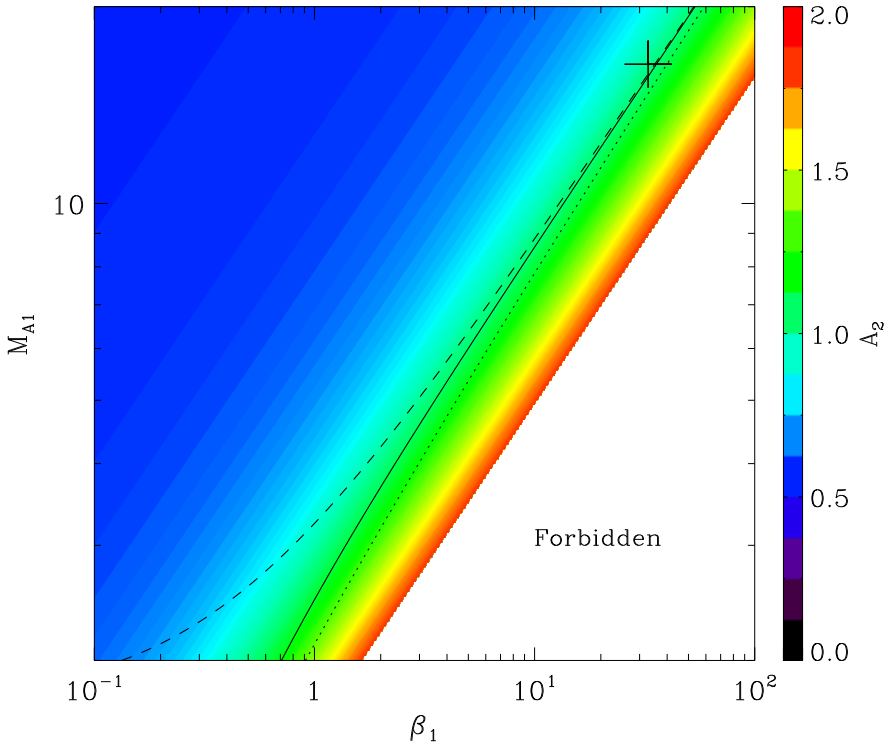

Figure 6-2: Same format as Figure 6-1, but for temperature anisotropy downstream of a parallel shock with $r_s = 3$ and $A_1 = 1$ as a function of β_1 and M_{A1}. Regions below the mirror/ion cyclotron threshold are unstable to the mirror/ion cyclotron mode and regions above the firehose onset are unstable to the firehose instability.

which makes the thresholds close to 1, and

$$A_2 \sim \frac{r_s - 2}{2} \leq 1, \tag{6.18}$$

giving favorable conditions for the onset of the firehose instability. For the parallel shock, we write the entropy principle as

$$\frac{P_{\parallel 2}^3}{P_{\parallel 1}^3} \frac{A_2^2}{A_1^2} \frac{1}{r_s^5} > 1$$

with the pressure ratio

$$\frac{P_{\parallel 2}}{P_{\parallel 1}} = 1 + \frac{2M_{A1}^2}{3\beta_1}(2A_1 + 1)\left(1 - \frac{1}{r_s}\right)$$

obtained from equation (6.4). The above two expressions, together with equation (6.15), indicate plasma regimes which obey the entropy principle. Figure 6-2 displays the temperature anisotropy A_2 over various upstream conditions for $r_s = 3$ and $A_1 = 1$

under the entropy requirement. Compared with Figure 6-1, higher values of M_{A1} at a given β_1 would otherwise lead to smaller A_2. Most of the area shown has $A_2 \leq 1$, as expected for a quasi-parallel shock, and is unstable to the firehose instability. The TS would induce firehose instabilities in the downstream plasma if it were quasi-parallel, as indicated by its location in the plot. Many quasi-parallel interplanetary and planetary bow shocks will also give rise to firehose instabilities as implied by the large area with $A_2 \leq 1$.

Observations show that a quasi-parallel bow shock becomes unsteady as the Alfvén Mach number $M_{\rm A1}$ exceeds ~ 3 for $\beta_1 \sim 0.5$ [Greenstadt and Fredricks, 1979] and is often associated with large transverse magnetic fluctuations [Bavassano Cattaneo et al., 2000; Czaykowska et al., 2001]. A closer look at Figure 6-2 gives $A_2 \simeq 0.97$ at $M_{A1} = 2$ for $\beta_1 = 0.5$, a noticeable thermal anisotropy but not large enough to exceed the firehose onset; at $M_{A1} = 3$, the thermal anisotropy rises above the firehose threshold, generating firehose instabilities which will disturb the shock structure. The firehose instability is an MHD mode and produces large-amplitude transverse waves. The results from this simple calculation agree with hybrid simulations [Kan and Swift, 1983; Krauss-Varban and Omidi, 1991].

Here we examine some limiting cases for the temperature anisotropy A_2 expressed by equations (6.8) and (6.15). For a perpendicular shock, in the limit of $A_2 \to 0$ and $M_{A1}^2 \gg \beta_1$ equation (6.8) reduces to

$$2M_{A1}^2(1 - 1/r_s) + 1 - r_s^2 = 0,$$

which gives a simple expression for the shock strength

$$r_s = \frac{1}{2}\left(\sqrt{1 + 8M_{A1}^2} - 1\right).$$

This analytical formula shows that the jump at the shock increases strongly with the Alfvén Mach number for low anisotropy rate and β_1. For a parallel shock, the minimum anisotropy is bounded by the firehose instability as can be seen from Figure 6-2, so the limit of $A_2 \to 0$ has no physical sense. Now consider the limit $A_2 \to \infty$. As revealed by Figure 6-1, this is possible for a perpendicular shock when β_1 goes to zero. In this case, equation (6.8) would lead to

$$2M_{A1}^2(r_s + 3/r_s - 4) + 4(r_s - 1) = 0,$$

from which we obtain the shock strength

$$r_s = \frac{3M_{A1}^2}{M_{A1}^2 + 2}.$$

This limiting case corresponds to the usual MHD solutions for an polytropic index $\gamma = 2$ (the 2-D case[1]). In the case of a parallel shock, the limit of $A_2 \to \infty$ and

[1]In isotropic MHD theory, the polytropic index depends on the dimensionality d as $\gamma = (d+2)/d$ given by thermodynamics. 1-D, $\gamma = 3$; 2-D, $\gamma = 2$; 3-D, $\gamma = 5/3$.

$\beta_1 \to 0$ results in $r_s = 1$, also physically meaningless.

6.3 Observational Evidence

The theoretical analysis described above suggests that the shocked plasma with high β is unstable to the mirror or firehose instability depending on the shock geometry. Different shocks, such as interplanetary shocks (often ICME-driven), planetary bow shocks and the solar wind termination shock, have been observed in the heliosphere. Observations of these shocks and corresponding sheath regions enable us to do a comparative study of the shock and sheath phenomena and test our theory. Here we give data for these shocks and associated sheaths and discuss characteristics of the shocks, instabilities, magnetic holes, magnetic field draping and PDLs.

6.3.1 Planetary Magnetosheaths

Planetary bow shock observations show that a quasi-parallel shock usually bears a distinct structure from a quasi-perpendicular one. A quasi-perpendicular shock is characterized by a sharp ramp. In contrast, a quasi-parallel shock is often highly irregular, with the shock ramp obscured by surrounding large waves. The turbulence is higher downstream of a quasi-parallel shock than downstream of a quasi-perpendicular one, and accordingly the plasma regimes downstream of quasi-parallel and quasi-perpendicular bow shocks are often called "disturbed" and "quiet" magnetosheaths, respectively.

Bow shocks of outer planets offer ideal environments to study shock-induced instabilities. Compared with the terrestrial environment, these shocks have higher Alfvén Mach numbers in the upstream solar wind and higher β's in the magnetosheath [Russell et al., 1990], favorable for the instability onset as revealed in section 6.2. Figure 6-3 shows 48 s averages of the magnetic field data and 96 s averages of the plasma data observed by Voyager 2 during its inbound pass of Saturn's bow shock at 0026 UT on day 237, 1981. In Saturn planetary system, the crossing of the bow shock occurs at a distance $23.6R_S$ (R_S being Saturn's radius), latitude 15° and local time 1308 LT. The abrupt increase in the field strength suggests that the shock is quasi-perpendicular; a rough estimate gives a shock speed $v_s \simeq 66$ km s^{-1}, geometry $\theta_{Bn} \simeq 77°$ and strength $r_s \simeq 3.6$. Upstream of the shock, the plasma is extremely steady with $\beta_{p1} \simeq 0.32$ and $M_{A1} \simeq 7.2$. It is clear that the condition of $2M_{A1}^2 \gg \beta_1$ is satisfied, and equation (6.10) yields the downstream $\beta_{p2} \sim 8$, consistent with the observed value of 10. The mirror threshold is estimated to be $A_c = 1 + 1/\beta_2 \sim 1.1$, smaller than the downstream anisotropy 1.7 as calculated from equation (6.11), which implies generation of mirror mode instabilities in the magnetosheath.

The magnetic field direction is relatively constant during the entire transition except a polarity reversal around 0250 UT. The magnetic fluctuations throughout the magnetosheath are thus compressive and also out of phase with the density oscillations, which are characteristics of mirror mode waves. The propagation direction of the wave is estimated to be $\sim 80°$ with respect to the background magnetic field,

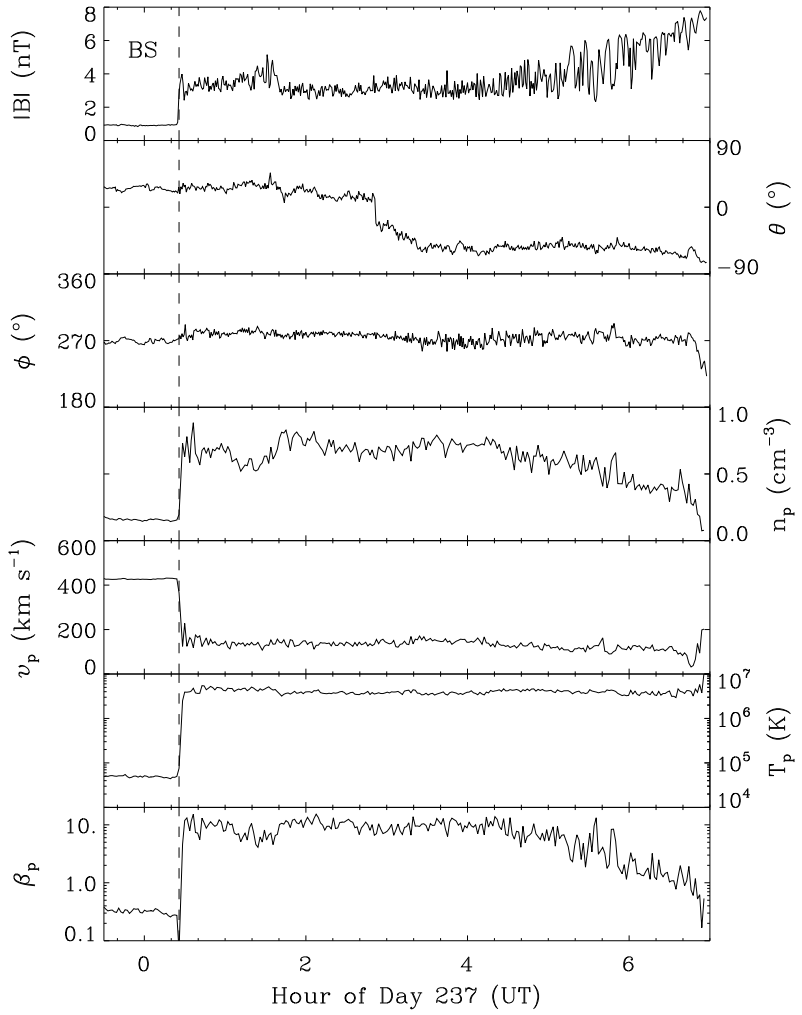

Figure 6-3: Plasma and magnetic field data during the inbound crossing of Saturn's bow shock by Voyager 2. Plotted from top to bottom are the magnetic field magnitude, field elevation (θ) and azimuthal (ϕ) angles in RTN coordinates, proton density, bulk speed, proton temperature, and proton β, respectively. The dashed line marks the location of the bow shock (BS). The bow shock is quasi-perpendicular.

based on minimum variance analysis of the measured fields in the magnetosheath. The amplitude of the waves first increases, reaching its maximum between 0500 and 0600 UT, and then decreases toward the magnetopause. The evolution of the wave can be explained by the dependence of the mirror instability on the plasma β. As shown by Figure 5-3, the growth rate of the mirror instability increases with β for a moderate temperature anisotropy. In the first half of the magnetosheath transition, the plasma β is as high as 10, so the mirror instability will grow quickly and make dense holes in the field strength such that the field looks alternately enhanced and depressed; closer to the magnetopause, the plasma β becomes low, so the depressions in the field strength are isolated and appear broad relative to the background field. The

temperature anisotropy data are not available but can be estimated from the density and field fluctuations using equation (5.24). The resulting anisotropy is about 1.4, comparable to but smaller than the value 1.7 estimated above; non-linear saturation of the wave would suppress the anisotropy and leave the plasma marginally unstable.

The magnetic field strength gradually increases from about 0420 UT to the magnetopause by a factor of 2. The plasma density shows a simultaneous decrease, but first decreases from ~ 0.7 to about 0.3 cm^{-3} and then has a steeper gradient in the last 10 min. During the last 10 min, the plasma velocity, temperature and field direction also vary dramatically. The trends in the plasma and field conditions are typical of PDLs in planetary magnetosheaths. Presumably the field is compressed and draped around the magnetopause without significant magnetic reconnection at the magnetopause; at the same time the plasma is squeezed to flow along the draped field, forming a PDL ahead of the magnetopause. The PDL in this case lasts about 2.7 hours. Magnetic holes in the PDL have a typical convection time of ~ 1 min, which corresponds to $\sim 20R_L$ in terms of the proton gyroradius given the observed field strength and plasma conditions.

Magnetic fluctuations downstream of this quasi-perpendicular shock is relatively moderate. The magnetosheath can be qualified as a "quiet" one. Turbulence downstream of a quasi-parallel shock is often higher, but its nature is still not clear. Figure 6-4 shows 48 s magnetic field data and 96 s plasma data during Voyager 1 outbound crossing of Saturn's bow shock at 0605 UT on day 321, 1980. The bow shock crossing occurs at $77.9R_S$ in Saturnian system, the dawn flank of the shock. The shock ramp is not sharp in the field magnitude and seems blurred by large magnetic fluctuations, a typical signature of a quasi-parallel shock. In this case, the shock has $\theta_{Bn} \sim 30^\circ$, speed $v_s \sim 360$ km s^{-1} and strength $r_s \sim 2.2$. The turbulence spreads from the magnetosheath into the upstream plasma which has $\beta_{p1} \sim 0.46$ and $M_{A1} \sim 2.5$. The condition of $2M_{A1}^2 \gg \beta_{p1}$ results in the downstream $\beta_{p2} \sim 6.8$ as calculated from equation (6.17). The proton β in the magnetosheath is sometimes as high as 5. Given the uncertainties in the shock parameters brought about by the large magnetic fluctuations, we consider the estimate of β_{p2} to be roughly consistent with the observed value. The firehose threshold is estimated to be $A_c = 1 - 2/\beta_2 \sim 0.6$ for $\beta_2 \sim 5$, while equation (6.18) gives a much smaller temperature anisotropy of ~ 0.1, so the firehose instability is expected to be induced at the shock.

Unlike the fluctuations shown in Figure 6-3, the magnetic field shows large fluctuations in its direction, so the waves are mainly transverse. The angle between the wave vector and the background field, estimated from minimum variance analysis, is generally below 30° [Bavassano Cattaneo et al., 2000]. The turbulence is violent, and even the plasma speed and temperature are disturbed, which is remarkably different from the turbulence downstream of the quasi-perpendicular shock. Waves observed in the foreshock region are similar to those in the magnetosheath, probably excited by the back-streaming ions. A polarization analysis further shows that the waves across the shock are right-hand polarized. As discussed in section 5.3, the firehose instability is an MHD mode, has maximum growth rate at a wave vector parallel to the background field and generates right-hand polarized transverse waves. The observed characteristics of the waves are qualitatively consistent with generation of

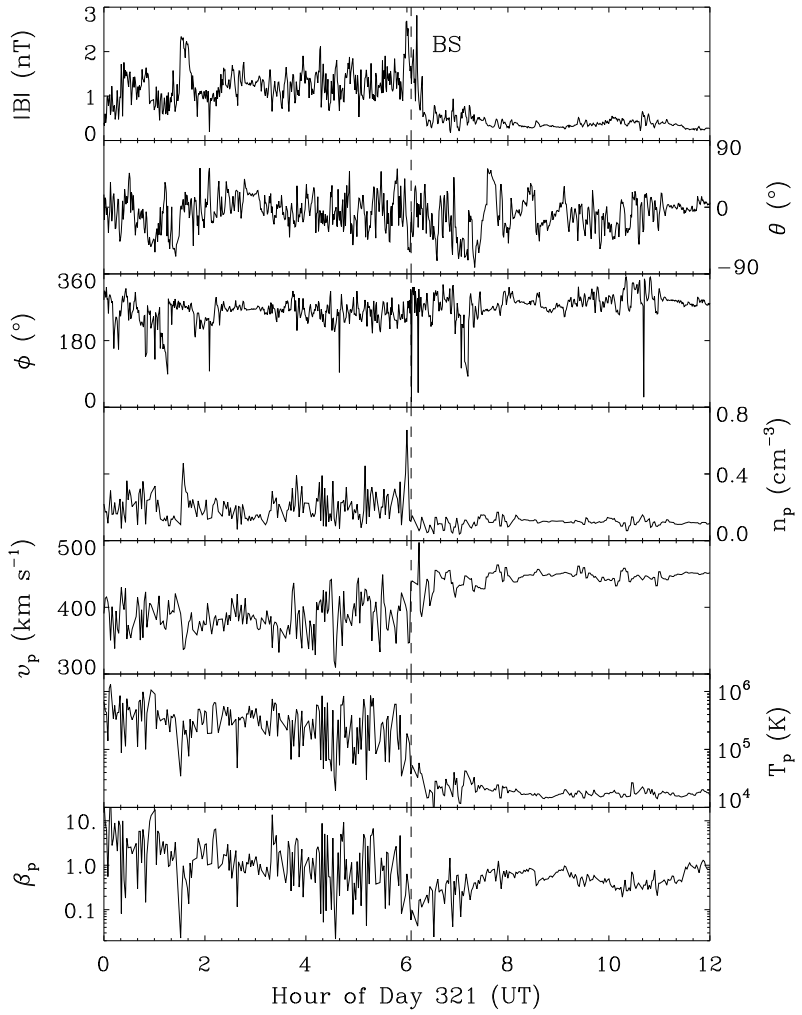

Figure 6-4: Same format as Figure 6-3, but for the outbound crossing of Saturn's bow shock by Voyager 1. The bow shock is quasi-parallel.

the firehose instability.

It should be noted that waves induced by the firehose instability are a mix of Alfvénic and magnetosonic fluctuations as indicated by equations (5.18) and (5.20). The large disturbance in the plasma speed seems to confirm this point. Mode conversion is likely to occur due to the wave interaction. As a result, the nature of the fluctuations generated by the firehose instability could be difficult to identify. Bavassano Cattaneo et al. [2000] think that the foreshock waves, which are convected by the solar wind flow and amplified at the shock front, are the source of the transverse fluctuations in the magnetosheath. Our analysis indicates that the firehose instability is excited at the shock and gives rise to the transverse waves which spread downstream and upstream.

6.3.2 ICME Sheaths and MIRs

Mirror instabilities and PDLs ahead of ICMEs are extensively investigated in Chapter 5. Here we examine how the ICME driven shocks and sheath regions compare to other shock-sheath phenomena in the heliosphere. Figure 6-5 displays two adjacent ICMEs observed at ACE. These events are identified by a combination of the enhanced helium density, low proton temperature and smooth magnetic field. The B_z component of the field (in GSE coordinates) shows a rotation from southward to northward within the first event and the other way around inside the second one, suggestive of two magnetic clouds (MCs). The smooth rotation of the field allows us to determine the boundaries of these two events without large ambiguities. The two MCs are relatively small, with a convection time of 4.7 hours for the first one and 9 hours for the second one. The sheath region, between the preceding shock and the first MC, has a passage time of about 5.1 hours. A sharp increase in the field strength is apparent at the preceding shock, so the shock is quasi-perpendicular. Similar to the quasi-perpendicular shock shown in Figure 6-3, the plasma is steady upstream of the shock but has compressive magnetic fluctuations downstream. The magnetic fluctuations are characterized by large magnetic holes, a good indicator of mirror mode waves. The occurrence of magnetic holes coincides with high β_p in the sheath region. The bottom-left panel shows that the magnetic fluctuations in the sheath are anti-correlated with the density oscillations. All these features imply the presence of mirror mode waves.

Between the two MCs is a merged interaction region (MIR) which is created by the interaction of the two events and characterized by an enhanced density and temperature. The MIR lasts about 2.5 hours. It is interesting that magnetic holes are also present in the MIR. These magnetic holes are very similar to those downstream of the shock: they also occur in a high β region and are out of phase with the density perturbations as revealed by the bottom-right panel. These holes are thus predominantly mirror mode. However, they cannot be produced by the shock. It is likely that the plasma temperature in the MIR is preferentially increased in the direction perpendicular to the magnetic field owing to the compression by the two MCs; the mirror instability is triggered when the temperature anisotropy exceeds the mirror threshold. The observed temperature anisotropy is indeed close to the threshold, both in the sheath and MIR, which is consistent with this scenario. It should be emphasized that MIRs, formed by compression of transient events, have been thought to be characterized by enhanced field strength, but the compression may actually lead to depressions in the field.

Similarly, the mirror instability can also occur in interaction regions where fast streams overtake slow streams. Winterhalter et al. [1994] find that magnetic holes tend to occur in these interaction regions and are marginally mirror stable. Interplanetary shocks and interaction regions as shown in Figure 6-5 are common in the heliosphere, providing environments for the creation of magnetic holes. In these regions the anisotropic heating of the plasma, which leads to the mirror instability, would be a natural explanation for the generation of magnetic holes localized in the solar wind. The size of holes in Figure 6-5, in terms of the proton gyroradius, is as

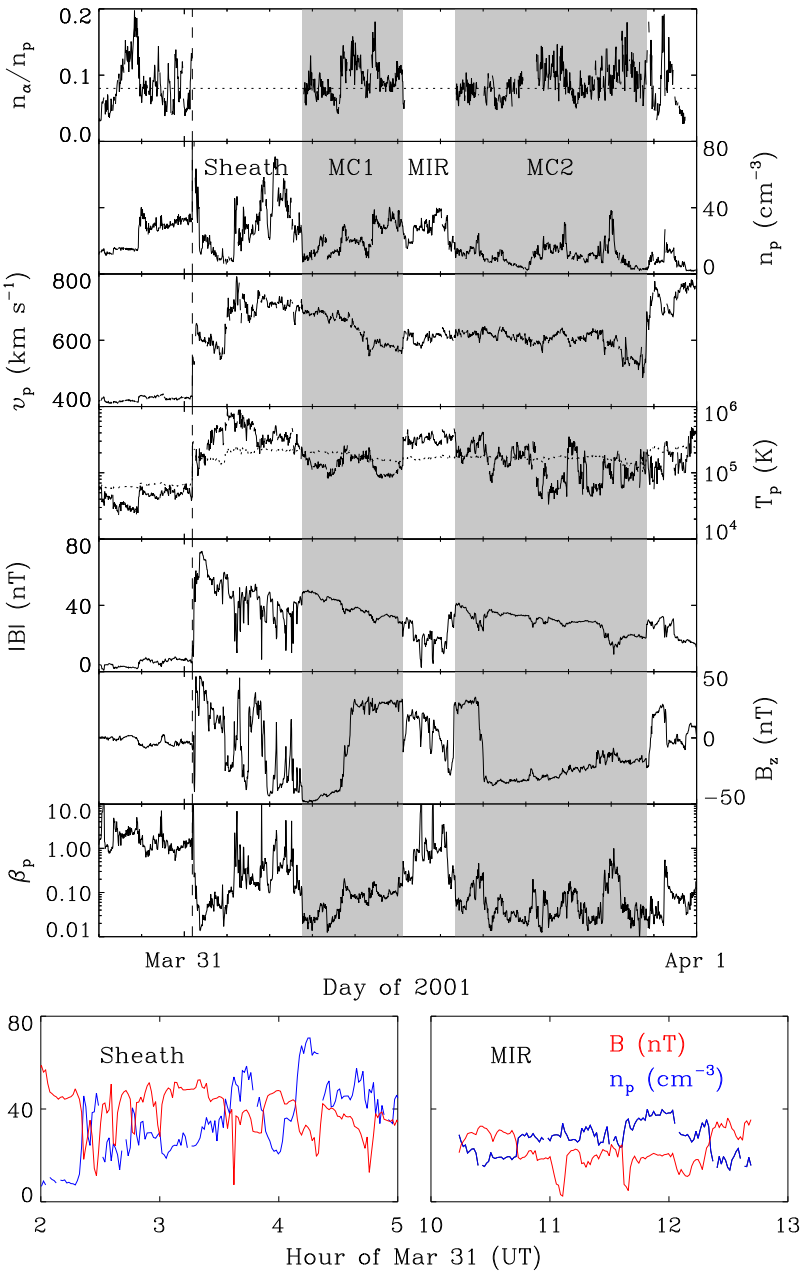

Figure 6-5: Solar wind plasma and magnetic field parameters across two adjacent MCs observed by ACE on 31 March 2001. From top to bottom, the panels show the alpha-to-proton density ratio, proton density, bulk speed, proton temperature, magnetic field strength, B_z component, proton β, and an expanded view of the magnetic and density fluctuations within the sheath and MIR. Shaded regions show the MCs. The dashed line indicates the arrival time of the preceding shock. Dotted lines denote the 8% level of the alpha/proton density ratio (top panel) and the expected proton temperature (fourth panel).

large as $1000R_L$ for a passage time of 1 min. They look larger than magnetic holes in planetary magnetosheaths, probably due to the fast plasma speed, low temperature and strong magnetic field downstream of the shock and in the MIR.

There is a brief PDL ahead of the first MC where the plasma density decreases by a factor of about 3 within 1 hour. Different from the PDL in a magnetosheath, the magnetic field does not increase at the same time, which may indicate pressure unbalance. The density ahead of the second MC also seems reduced but the layer is even shorter. It is not clear whether this is a real PDL or simply a part of the second MC concerning the uncertainty in the leading edge of the MC.

6.3.3 The Heliosheath

Voyager 1 crossed the TS on 16 December 2004 (day 351) at 94 AU and is making the first measurements in the heliosheath. Figure 6-6 shows the hourly averages of the magnetic field data across the TS. Downstream of the TS, the direction of the magnetic field is fairly constant, indicating that the magnetic fluctuations are mainly compressive. The magnetic fluctuations in the heliosheath are characterized by a series of depressions in the field magnitude, or magnetic holes. These fluctuations are similar to those observed downstream of quasi-perpendicular interplanetary and planetary bow shocks that have been identified as mirror mode structures (see Figures 6-3 and 6-5).

The TS is expected to be highly oblique with $\theta_{Bn} \sim 86°$ at Voyager 1, so we use equations (6.8) and (6.9) to determine whether mirror mode instabilities occur in the heliosheath. MHD simulations give the average preshock plasma density $n_1 \simeq 8\times10^{-4}$ cm^{-3}, speed $v_1 \simeq 380$ km s^{-1}, and temperature $T_1 \simeq 5.4\times10^5$ K [Whang et al., 2004], which yields

$$M_{A1} \simeq 16.3, \quad \beta_1 \simeq 32.8$$

combined with the observed field strength $B_1 \simeq 0.03$ nT. The shock strength r_s is ~ 3 estimated from the jump in the field magnitude [Burlaga et al., 2005] and from the spectral slope of TS accelerated particles [Stone et al., 2005]. The typical thermal anisotropy of the solar wind is $A \sim 0.7$ near the Earth (see Figures 4-9 and 5-2). Expansion of the solar wind would further decrease the value of A if the magnetic moment $\mu \sim T_\perp/B$ is invariant; when the thermal anisotropy exceeds the firehose threshold, firehose instabilities will be induced and help suppress the growth of the anisotropy. The two competing processes will arrive at a balance close to the threshold $A \simeq 1 - 2/\beta_\parallel$, i.e.,

$$A \simeq \frac{3\beta - 2}{3\beta + 4},$$

which gives $A_1 \simeq 0.94$ for $\beta \simeq 32.8$. Introduction of pickup ions in the outer heliosphere would not significantly change this value. The newly-born pickup ions gyrate about the interplanetary magnetic field, forming a ring-beam distribution; this configuration is unstable to the generation of MHD waves, which scatter the ions quickly toward isotropy [Lee and Ip, 1987; Bogdan et al., 1991]. We have also shown that A_2 does not depend on A_1 when $2M_{A1}^2 \gg \beta_1$. Substituting the values of M_{A1},

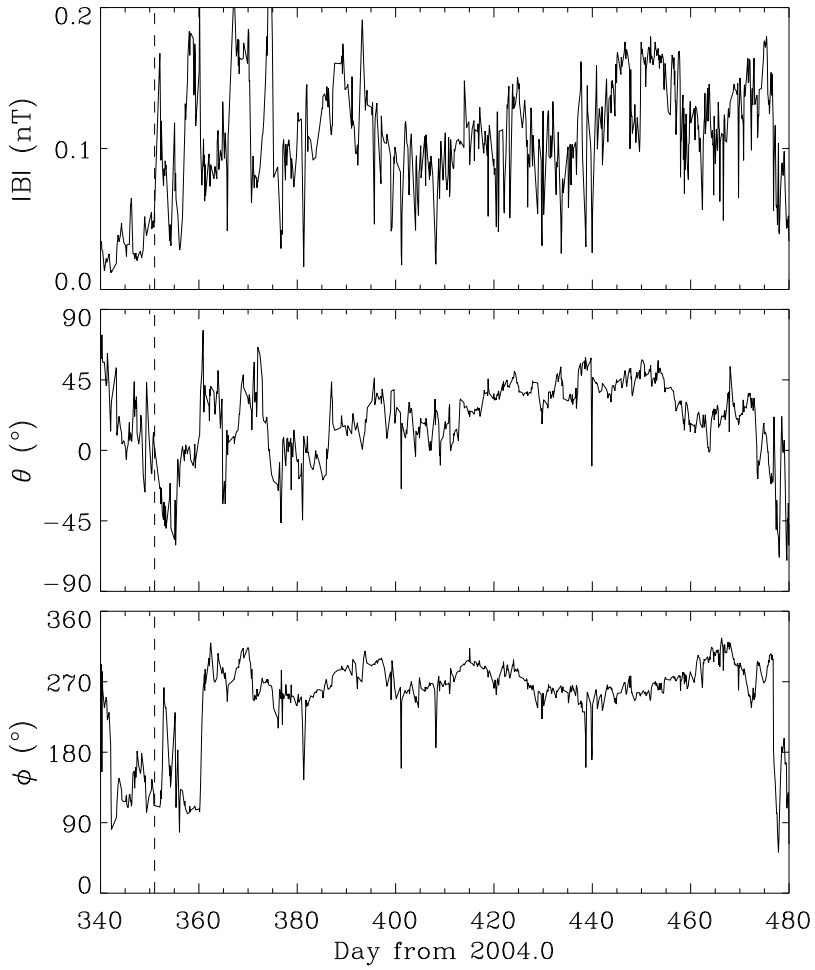

Figure 6-6: Hourly averages of the magnetic field strength (top), elevation angle (middle), and azimuthal angle (bottom) across the TS (indicated by the dashed line) as a function of time measured in days from the beginning of 2004.

β_1, r_s and A_1 into equations (6.8) and (6.9) gives $A_2 \simeq 1.03$ and $\beta_{\perp 2} \simeq 42.2$. The threshold of the mirror mode is $1 + 1/\beta_{\perp 2} \simeq 1.02$, smaller than the downstream anisotropy. As indicated by Figure 6-1, even an A_2 slightly larger than 1 can meet the mirror mode onset at high β_1, so mirror mode instabilities should be induced in the heliosheath.

For the upstream temperature, we have used the density-weighted average of the pickup ion, solar wind proton and electron temperatures [Whang et al., 2004]. However, the result can be shown to be self-consistent. From equation (6.10) we have the downstream temperature $T_2 \sim 2 \times 10^6$ K, given the average field magnitude $B_2 \simeq 0.09$ nT and density $n_2 \simeq 0.002$ cm^{-3} obtained from equation (6.7). Approximating the TS as a hydrodynamic shock because of the high plasma β, we have

$$\frac{n_2}{n_1} = \frac{(\gamma+1)M^2}{(\gamma-1)M^2+2}, \tag{6.19}$$

$$\frac{T_2}{T_1} = \frac{[2\gamma M^2 - (\gamma - 1)][(\gamma - 1)M^2 + 2]}{(\gamma + 1)^2 M^2}. \tag{6.20}$$

The shock Mach number is estimated to be $M \simeq 3$ from equation (6.19) with $n_2/n_1 \simeq 3$ and $\gamma = 5/3$. With this Mach number, equation (6.20) gives $T_1 \sim 5 \times 10^5$ K, consistent with the MHD simulation result.

Given the absence of plasma measurements across the TS, it is hard to estimate the uncertainties brought about by the upstream conditions and the shock parameters. A revisit to equations (6.1) - (6.6) assuming a 10% error in the upstream conditions and the shock geometry and strength gives $A_2 = 1.03 \pm 0.42$ and a mirror mode threshold 1.02 ± 0.01. Note that the uncertainty of A_2 is determined largely by the shock strength, since $A_2 \sim 1/(r_s - 3)$ in the case of the TS. If we use $r_s = 2.6^{+0.4}_{-0.2}$ inferred from the particle spectra [Stone et al., 2005] with other parameters fixed, then the temperature anisotropy $A_2 = 1.03$ - 4.19, so the mirror mode would be more likely to occur. Interestingly, the shock strength cannot be smaller than 2.2 at the present conditions; otherwise A_2 would be negative. It should be emphasized that turbulence induced by the mirror mode instability would leave the threshold marginally satisfied, so we expect $A_2 = 1.02 \pm 0.01$ in the evolved state.

The mirror mode instability has a maximum growth rate at a wave vector highly oblique to the background magnetic field. The minimum variance direction of the measured magnetic fields has an angle of about 75° with respect to the background field when magnetic holes are present [Burlaga et al., 2006b]. Mirror mode waves are non-propagating and appear to be static structures, consistent with the observed magnetic fluctuations with a fairly constant field direction. Mirror mode waves are also characterized by anti-correlated density and magnetic fluctuations. The density measurements are not available, so we cannot verify the mirror mode from density fluctuations. The density perturbation δn can be estimated from equation (5.24) using the derived temperature anisotropy. The fluctuation amplitude $\delta B/B$ is ~ 0.4 - 0.9 in the heliosheath, which results in $\delta n/n \sim 0.01$ - 0.03, too small to be resolved by future Voyager 2 observations.

The non-linear evolution of mirror mode instabilities would generate holes in the background field strength [Kivelson and Southwood, 1996]. Magnetic holes in planetary magnetosheaths which are predominately produced by mirror mode waves have a typical size of $20R_L$ [Kaufmann et al., 1970; Bavassano Cattaneo et al., 1998]. The average passage time of the magnetic holes from day 400 - 440 in Figure 6-6, when the holes are dense, is ~ 0.2 day estimated from the full width at half maximum of a Gaussian fit. The downstream temperature $T_2 \sim 2 \times 10^6$ K and field strength $B_2 \sim 0.09$ nT yield $R_L \sim 20\,000$ km. Given a plasma convection speed of ~ 20 km s^{-1} for this period [Decker et al., 2005], the hole size is also about $20R_L$ on average.

Magnetic holes in planetary magnetosheaths were also explained as slow mode solitons based on Hall-MHD theory [Stasiewicz, 2004]. In general, Ohm's law can be written for a collisionless plasma as

$$\mathbf{E} + \mathbf{v} \times \mathbf{B} = \frac{1}{en}(\mathbf{j} \times \mathbf{B} - \nabla P_e),$$

where $\mathbf{E}$ is the electric field, e is the electron charge, and P_e is the electron pressure. Hall-MHD theory only includes the $\mathbf{j} \times \mathbf{B}$ term, the so-called Hall term. The importance of the pressure gradient relative to the Hall term can be evaluated through the ratio of the ion Larmor radius (R_L) to the ion inertial length (λ_i), namely,

$$\frac{|\nabla P|}{|\mathbf{j} \times \mathbf{B}|} = \frac{R_L}{\lambda_i} = \sqrt{\frac{\beta}{2}}.$$

The ion inertial length is defined as $\lambda_i = v_{\rm A}/\Omega_i$, where $v_{\rm A}$ is the Alfvén speed and Ω_i is the ion cyclotron frequency. In a low β plasma, the finite ion inertial length dominates over the finite Larmor radius, so Hall-MHD theory is valid. In a high β plasma, the effect of the finite Larmor radius comes into play through the pressure gradient. The plasma β in the heliosheath is ~ 40 as estimated above; in this case the ion Larmor radius is much larger than the ion inertial length, so Hall-MHD theory breaks down. A similar argument can also be made based on the dispersion relation in terms of the length scales [Pokhotelov et al., 2005].

Deep in the heliosheath, magnetic field lines may be draped and compressed against the heliopause if there is no significant reconnection between the solar wind and interstellar fields. Analogous to planetary magnetosheaths, the plasma would be squeezed and flow along the draped field lines, leading to a PDL close to the heliopause. The plasma β is reduced in this layer, so the mirror mode instability may be inhibited and ion cyclotron waves may be generated. Damping of these waves would suppress the thermal anisotropy and heat the plasma (see section 4.3.4).

6.4 Summary and Discussion

We present a comparative study of planetary bow shocks, interplanetary shocks and the TS and their corresponding sheath regions in the heliosphere. Some universal processes, including temperature anisotropy instabilities, magnetic field draping and plasma depletion, are found to occur in these sheaths and have similar characteristics. These physical processes can be explained by the same mechanisms even though the sheaths are quite different in spatial scales. The present results also provide a substantial basis for shock-induced anisotropies which act as an energy source for plasma heating in various space and astrophysical environments.

A simple calculation based on temperature anisotropy instabilities explains a variety of observations associated with these shocks. A shock modifies the velocity distribution of particles at its surface, producing instabilities downstream of the shock which give rise to different types of waves. The mirror instability is preferentially produced downstream of a quasi-perpendicular shock when the plasma β is high, as commonly observed in planetary magnetosheaths. We show that mirror mode waves are also present in ICME sheaths preceded by a shock and interaction regions in the heliosphere. This has a significant consequence for production of magnetic holes in the solar wind; since these regions are common, mirror-mode magnetic holes should be frequently observed. Examples are given for planetary magnetosheaths, ICME

sheaths and MIRs. Similar to these sheaths, the heliosheath is characterized by compressive magnetic fluctuations. Our calculation predicts that mirror mode waves form downstream of the TS, which is consistent with the observed fluctuations. The high Alfvén Mach number, upstream of bow shocks of outer planets and the TS, leads to a high β downstream of these shocks regardless of the upstream β, also consistent with our theoretical calculation.

Examples of the ion cyclotron instability are not provided in this thesis, but it can grow in a low β plasma downstream of a quasi-perpendicular shock. Ion cyclotron waves induced by this instability are observed largely in PDLs of planetary magnetosheaths [e.g., Anderson et al., 1994; Czaykowska et al., 2001]. In PDLs, draping of the field lines and the consequent parallel plasma flow can also generate anisotropic plasma heating in addition to shock compression. Anderson et al. [1994] find that magnetic fluctuations, downstream of a quasi-perpendicular bow shock, progress from the predominant compressive mirror mode in the magnetosheath proper to the predominant transverse ion-cyclotron mode in the PDL. The observed ion cyclotron waves are left-hand polarized, which agrees with the theoretical description in section 5.3.

Our calculation also shows that a high β plasma downstream of a quasi-parallel shock may be unstable to the firehose instability. Dictated by this instability, there is a critical Alfvén Mach number $M_{A1} \sim 2.5$ at $\beta_1 \sim 0.5$, where a quasi-parallel shock transits from a steady to an unsteady structure. Such a transition has been observed [e.g., Greenstadt and Fredricks, 1979]. We present an example of quasi-parallel bow shocks and demonstrate that the transverse waves downstream of the shock are qualitatively consistent with generation of the firehose instability.

Magnetic holes produced by the mirror instability are similar in ICME sheaths, planetary magnetosheaths and the heliosheath, except that they tend to be larger in ICME sheaths. Plasma depletion in ICME sheaths may not be accompanied by a simultaneous increase in the field strength as usually observed in planetary magnetosheaths, but it coincides with magnetic field draping around the obstacle. A possible explanation is that the pressure in an ICME sheath is not balanced since the preceding shock moves away from the ejecta. The analogy of these sheaths leads us to conjecture that plasma depletion and field draping may also occur in the heliosheath. A slight increase in the field magnitude is indeed observed as Voyager 1 moves deep in the heliosheath (L. F. Burlaga, presentation in the Oxnard heliospheric workshop). As the exact size of the heliosheath is not known, it is not clear whether the field increase is due to the field draping against the heliopause or produced by a plasma structure in the heliosheath.

Some work of this chapter has been published in the *Astrophysical Journal* [see Liu et al., 2007a]. Another paper, reviewing shocks and sheaths in the heliosphere, is in preparation.

Chapter 7

Future Work

We did not intend for this thesis to give a complete characterization of CMEs and ICMEs. The vast knowledge achieved by more than thirty years of observations cannot be covered in a single thesis. Instead, we focused on some outstanding problems that have not been thoroughly studied up to now. These problems include the magnetic field orientation of CMEs, the global morphology of ICMEs inferred from multi-point observations, and the underlying mechanisms governing ICME thermodynamic structure and physical processes in their surroundings. In this concluding chapter, we briefly summarize and discuss the results of the thesis, their relevance to observations and theoretical modeling, and ideas for future work.

7.1 Faraday Rotation Observations

Given a coronal temperature of 2×10^6 K, the coronal magnetic field cannot be measured by the conventional technique of Zeeman splitting. Without coronal field observations, an effective constraint on various CME initiation theories is not possible. Predictions of the CME influence on the terrestrial environment also require knowledge of the CME magnetic field. We propose a new method to measure the CME field orientation based on the Faraday rotation (FR) of a polarized radio signal through the CME plasma. We have shown that the FR technique can yield a two-dimensional (2-D) mapping of CMEs. The FR mapping is similar to white-light imaging but can give the CME field orientation two to three days before the CMEs reach the Earth.

The FR mapping takes advantage of background radio sources distributed in the vicinity of the Sun. A radio array, which can simultaneously probe these background sources, makes our method practical. The Mileura Widefield Array (MWA) is being designed for this purpose and will see the first light in 2009. Technical issues, involving calibration of FR through the ionosphere, should not be a major difficulty, since a difference mapping in FR can be used. It should be noted, however, that one should avoid inferring the CME size and orientation using a flux-rope fitting method. The flux-rope fitting method is possible for single-point local measurements because the hypothesis of invariance along a flux rope may be valid at that point, although the

flux-rope dimension is usually not properly estimated. In contrast, FR measurements may cover a whole CME, and different lines of sight explore different part of the CME. Given the curved structure of CMEs, flux-rope fitting with FR observations has to make significant assumptions for a flux-rope structure as to how it is curved. In addition, plasma conditions are not available and more free parameters go into the flux-rope fitting. These assumptions and free parameters may make the fitting results physically meaningless.

We think that FR mapping is the best approach, as demonstrated in Chapter 2. One advantage of FR mapping is that it can give the magnetic field orientation of CMEs without prior knowledge of the electron density. While the field orientation indicates whether a CME is geoeffective, the field strength would determine how geoeffective the CME is. Joint coronagraph measurements are needed to estimate the electron density, which is made feasible by modern coronagraphs like LASCO (see Chapter 1). The SECCHI instrument (discussed below) has a suite of wide-angle coronagraphs which provide even better resolution and larger fields of view. It is thus possible to evaluate the CME field strength from FR observations, given the electron density. Research of this kind is expected to be routine in the future, when radio arrays such as the MWA begin to collect data.

Another area of future research is verification or calibration of the FR technique. As shown in Chapter 2, the CME speed projected on the sky can be determined from the FR mapping. CME speeds derived this way may be compared to those obtained from while-light imaging. In situ measurements near the L1 point give the field orientation as well as the field magnitude. These measurements can be used to verify the field orientation (or CME orientation as a whole) predicted by the FR method. Comparison of the field magnitude given by local and FR observations may also be made by assuming a specific dependence of the field with distance. For example, a power-law dependence has been observed (see Chapter 4).

As described in Chapter 1, CMEs typically appear as a three-part structure. It is still not clear how this three-part structure compares to the flux-rope geometry identified in magnetic clouds (MCs). If the bright front of a CME is the leading edge of a helical flux rope, then what is the role of the erupted prominence in the low-density cavity? Since FR responds to the magnetic field, a careful comparison of the CME structure viewed in FR mapping with white-light images could give important information on which feature is which within CMEs. Remote sensing of the solar atmosphere (for example, imaging at various wavelengths and photospheric magnetograms) can also be linked with in situ measurements by FR observations. An integrated study of CMEs and ICMEs, from the Sun to the terrestrial environment, is thus possible with FR observations.

7.2 Global Morphology of CMEs/ICMEs

Single-point measurements have greatly limited our understanding of the global structure of ICMEs. Their cross section, magnetic flux, and magnetic helicity cannot be properly estimated from a single cut through the large-scale structure, although var-

ious flux-rope fitting techniques have been developed. Near-Earth observations and high-latitude Ulysses measurements show that the transverse size of MCs could be very large. We have presented a simple model to investigate curvature of the MC cross section and find a rough dependence of the curvature on the ambient solar wind state. These results improve our knowledge of the global structure of MCs in the pre-STEREO era. Generic ICMEs are thought to have a similar structure, but they are more distorted, making it hard to specify their morphology.

In the future, the Solar TErrestrial RElations Observatory (STEREO) will provide a unique view of the 3-D structure of CMEs and ICMEs. STEREO has twin spacecraft, one preceding the Earth and the other trailing behind in its orbit about the Sun. Mounted on each of the two spacecraft are Sun Earth Connection Coronal and Heliospheric Investigation (SECCHI), In-situ Measurements of Particles and CME Transients (IMPACT), PLAsma and SupraThermal Ion Composition (PLASTIC) and WAVES.

SECCHI has two coronagraphs, COR1 and COR2 which cover 1.4 - 4 $R_{\odot}$ and 2 - 15 $R_{\odot}$ respectively, and a Heliospheric Imager (HI) which observes the heliosphere from 12 - 318 $R_{\odot}$. Combined with LASCO/SOHO, these coronagraphs can observe CME speeds viewed from different points. The HI can obtain the direct imaging of ICMEs in interplanetary space. These stereoscopic observations can be used to constrain the global MHD modeling of CME propagation from the Sun to the Earth. This can be done by calculating the polarization brightness of the simulated CME and then comparing it to the observed brightness. The boundary and initial conditions and the propagation trajectory of CMEs in the modeling need to be adjusted to match observations. The best match between MHD simulations and observations can give the global structure of CMEs and their propagation through the interplanetary medium. The comparison between MHD modeling and observations may also indicate the key factors controlling ICME trajectories, leading to advances in space weather prediction.

IMPACT and PLASTIC provide in situ characterization of ICMEs at different locations at 1AU. Since tracking of the CME evolution is made feasible by imaging over a large distance, timing studies of these in situ measurements and remote sensing observations would further verify the propagation and structure of CMEs predicted by global MHD modeling. Our method of studying the global structure of MCs, presented in Chapter 3, can also be applied to data from the STEREO mission. Analysis of the in situ measurements, based on either minimum variance analysis or the Grad-Shafranov technique, gives the MC axis orientation and magnetic helicity. Since the twin spacecraft are widely separated, correlation studies of their data can give the lower limit of the longitudinal or transverse size with the derived axis. Curvature analysis can be similarly performed. Such a study will be superior to the present one, because one will have two identical spacecraft at different locations to verify the curvature derived at one location or to tell how MCs are curved at different locations. The MC size and curvature can be compared to global MHD simulations.

It should be noted that more spacecraft can be used to give coordinated measurements of the same event. WIND and ACE are located near L1, and Ulysses is in the inner heliosphere over part of its orbit. Together with the twin STEREO space-

craft, a single ICME could thus be observed at five different locations. These in situ measurements from clustered points will give a clearer 3-D structure of ICMEs.

7.3 Thermodynamic Structure of CMEs/ICMEs

There is a large gap in our understanding of the underlying physics governing energy transport and signatures inside ICMEs. We have demonstrated for the first time that ICME expansion leads to strong Coulomb collisions in the ICME plasma. Protons and alpha particles have a reduced relative drift within ICMEs, but surprisingly the alpha particles undergo preferential heating. We have also shown that turbulence dissipation seems sufficient for ICME heating. These results provide insight into the thermodynamic state of the ICME plasma and impose constraints on models of ICME evolution.

It will be interesting to look at plasma properties of CMEs in their acceleration region. The ultraviolet spectroscopy of SOHO Ultraviolet Coronagraph Spectrometer (UVCS/SOHO) presents a unique opportunity to study the thermodynamic structure of CMEs in the solar corona [Kohl et al., 2006, and references therein]. UVCS has observed several hundred CMEs at distances where they experience maximum acceleration. Along the UVCS slit, spectral lines of low ionization species usually show a sudden brightening in the CME plasma. Spectroscopic diagnostic techniques, based on line profiles and intensity ratios, can thus be used to determine electron and ion kinetic temperatures and velocity distributions, ion bulk flow speeds, charge states and compositions. These properties will characterize the CME plasma from the ambient coronal plasma. Empirical models, comparing observed and predicted line emissions, can give the heating rate in CMEs and place a strong constraint on CME heating mechanisms near the Sun. These results would also reveal how plasma heating and particle acceleration in CMEs are quantitatively different from solar wind heating and acceleration.

CME plasma properties derived from UVCS observations can be compared to in situ measurements described above. This highlights the importance of joint analysis of in situ data and UVCS observations for a specific event. Combined remote and in situ observations of a CME open the possibility of tightly constraining the thermal evolution of the ejected plasma. Physical interpretation of various ICME signatures, especially the compositional anomalies, may also be clarified.

7.4 Shocks and Sheath Regions

Sheath regions of ICMEs show interesting features on both global and micro scales, and these features are crucial in our comprehensive view of ICMEs and related phenomena. We have found that plasma depletion layers (PDLs) and mirror mode waves often occur in ICME sheaths preceded by a shock, analogous to planetary magnetosheaths. Our theoretical calculation indicates that a shock produces temperature anisotropies downstream of the shock; mirror, ion cyclotron and firehose instabilities

may be generated depending on the shock geometry. A comparative study of different shocks and sheath turbulence seems to confirm the theoretical analysis. These results reveal some universal processes that occur in different environments but are governed by the same mechanisms. They also present a new topic which is the subject of increasing attention.

Unlike planetary magnetosheaths, PDLs in ICME sheaths do not show a clear increase in the magnetic field close to the ejecta. This pressure unbalanced structure may be associated with sheath stretching as well as ICME expansion. Global MHD simulations are needed to look at the ICME sheath, primarily focusing on plasma flows, magnetic field draping, and formation of a PDL. ICME expansion and sheath stretching would be key factors that need to be adjusted in the modeling. The dependence of these processes on ICME expansion and sheath stretching would be revealed in such studies. Modeling of ICME sheaths may also help illuminate the formation of southward fields in these regions and why the sheaths are effective in particle modulation. Note that the sheath is an intermediate-scale structure in the solar wind, which requires fine grids in the modeling; special schemes are also needed to capture the preceding shock.

Ion cyclotron waves are expected to occur in PDLs of ICME sheaths downstream of a quasi-perpendicular shock when the plasma β is low, but they have not yet been identified. The PDLs are often short, so high time resolution data are needed. As described in section 5.3, ion cyclotron waves are transverse, left-hand polarized waves, and propagate along the magnetic field. These signatures can be seen from power spectral calculations, polarization and minimum variance analyses.

Firehose instabilities are also expected to occur but in high β sheaths downstream of a quasi-parallel shock. Waves induced by the firehose instability are similar to ion cyclotron waves, except that they are right-hand polarized and are associated with $T_{\parallel} > T_{\perp}$. The firehose instability is difficult to identify; it induces large waves that will greatly disturb the plasma, and mode conversion is likely to occur. Nevertheless, a careful analysis of the shock geometry, particle distributions that may give any evidence of $T_{\parallel} > T_{\perp}$, and transverse waves (separated from longitudinal waves) that show a right-hand polarization should be able to give clues on the excitation of the firehose instability.

Other universal processes may also be associated with these shock-sheath regions, including particle acceleration at the shock, probability distributions of magnetic fluctuations in the sheath, and magnetic reconnection at the obstacle boundary. A surprise in Voyager 1 observations of the termination shock is that the flux of anomalous cosmic rays continues to increase across the shock [Stone et al., 2005], which was thought to be the source of these particles. A possible interpretation is that the acceleration process depends on the shock topology. ICME-driven shocks may bear a curvature similar to ICMEs as described in Chapter 3; the relevance of the shock curvature to the acceleration process needs to be investigated. The distribution of magnetic fluctuations becomes Gaussian in the heliosheath, whereas it is log normal in the solar wind [Burlaga et al., 2005]. For planetary magnetosheaths and ICME sheaths, we should be able to see if the distribution is Gaussian as in the heliosheath, but we note that the distribution may depend on whether the shock

is quasi-perpendicular or quasi-parallel. Magnetic reconnection, when the interplanetary magnetic field is southward, may also be similar in these regions. It will be interesting to see how PDLs depend on the reconnection rate.

CME-driven shocks in the solar corona may have similar features, which can be determined unambiguously by the UVCS spectroscopy. Shock compression will cause a sudden increase in the line emission and broadening due to the increased temperature and density, which helps locate the shock front. Observations show that the electron temperature is smaller than the proton temperature in ICME sheaths and planetary magnetosheaths; inefficient electron heating also seems to occur downstream of supernova remnant shocks [e.g., Ghavamian et al., 2001]. The electron temperature, derived from Thomson scattering and/or line intensity ratios, will help differentiate the sheath and CME plasmas; temperature anisotropies in the sheath region can be determined from line emissivities via empirical models [Kohl et al., 2006, and references therein] and give indication of possible wave activities downstream of the shock. Comparison of these observations with in situ measurements and theoretical modeling will constrain the shock geometry and strength. Combined with the coronal density and outflow velocity, they can also help to establish the relationship to type II radio bursts and particle acceleration at the shock. Caution must be taken since the shocked region passes the UVCS slit quickly.

Appendix A

Magnetic Clouds for Curvature Analysis

The following tables list the magnetic clouds (MCs) and their parameters for the curvature study in Chapter 3. The start and end of the MCs are given in a fractional day of year (DOY). The elevation angle of the MC normal (δ) and its uncertainty ($\Delta\delta$) are estimated from the minimum variance analysis (MVA) of the normalized magnetic fields within the MCs as described in Chapter 3. The MVA also yields the elevation angle (Θ) and azimuthal angle (Φ) of the MC axis orientation. Note that the axis azimuthal angle is given in GSE coordinates for WIND observations and RTN coordinates for Ulysses measurements. Our curvature analysis of MCs requires that the MC axis is within 30° of the solar equatorial plane and more than 30° away from the Sun-spacecraft direction. All the MCs listed here meet this requirement.

It is clear that the MCs observed by WIND at solar minimum roughly have an inverse relationship between θ and δ, while a positive correlation can be seen for the MCs observed by Ulysses during solar maximum. This interesting relationship reflects the curvature of the MC cross section resulting from the distortion by the ambient solar wind. See details in Chapter 3.

Table A.1: Estimated parameters of MCs at WIND for the curvature study

Date	Start DOY	End DOY	θ^a (°)	ϕ^a (°)	δ^b (°)	$\Delta\delta^b$ (°)	Θ^c (°)	Φ^c (°)
8-FEB-1995	39.24	40.03	-6.46	63.54	18.18	1.29	-7.30	284.85
3-APR-1995	93.33	94.45	-6.40	118.10	14.37	1.20	-28.87	88.32
22-AUG-1995	234.89	235.80	6.93	253.95	-24.43	1.15	-14.58	279.49
18-OCT-1995	291.82	293.05	5.56	310.04	6.32	0.82	-3.92	284.08
27-MAY-1996	148.64	150.30	-1.05	171.72	10.96	1.11	-1.10	123.30
1-JUL-1996	183.72	184.43	3.01	204.57	-20.65	1.43	7.26	100.58
10-JAN-1997	10.22	11.10	-4.13	34.52	2.47	0.97	-22.50	243.89
10-FEB-1997	41.14	41.77	-6.60	65.85	52.09	0.67	22.72	315.13
21-APR-1997	111.60	113.27	-4.96	136.84	25.54	1.98	-24.18	147.72
15-MAY-1997	135.38	136.05	-2.56	159.31	-15.45	0.85	-21.60	110.07
16-MAY-1997	136.25	136.58	-2.46	159.98	11.15	2.33	-21.79	290.15
3-AUG-1997	215.59	216.08	5.98	235.55	-4.54	0.48	2.37	33.88
1-OCT-1997	274.68	275.95	6.67	293.61	-45.04	1.86	-27.07	318.56
10-OCT-1997	283.99	285.03	6.10	302.71	14.70	0.76	-7.72	262.52

[a] Heliographic inertial latitude and longitude of the spacecraft.
[b] Normal elevation angle with respect to the solar equatorial plane and its errors, estimated from MVA.
[c] Axis elevation angle with respect to the solar equatorial plane and azimuthal angle in GSE coordinates, estimated from MVA.

Table A.2: Estimated parameters of MCs at Ulysses for the curvature study

Date	Start DOY	End DOY	R^a (AU)	θ^a (°)	ϕ^a (°)	δ^b (°)	$\Delta\delta^b$ (°)	Θ^c (°)	Φ^c (°)
12-JUN-1999	163.50	169.88	4.84	-28.19	86.40	7.71	2.64	-15.54	263.59
19-AUG-1999	231.00	232.50	4.65	-32.27	87.40	-20.13	2.11	-7.08	283.92
31-MAR-2000	91.50	92.30	3.74	-50.14	93.09	-49.95	0.72	19.06	112.23
10-AUG-2000	223.50	226.30	2.99	-66.18	104.18	-57.25	3.36	-29.70	56.58
23-JAN-2001	23.90	24.70	1.87	-67.31	236.45	-47.27	1.83	11.69	82.30
14-NOV-2001	318.50	319.60	2.26	75.37	39.53	57.46	1.10	-16.63	104.74
18-JAN-2002	18.20	19.50	2.70	62.14	61.97	18.43	9.11	5.33	309.67
11-FEB-2002	42.70	43.80	2.86	57.88	65.03	19.70	1.35	14.78	83.50
14-JUN-2002	165.40	174.00	3.60	40.95	72.40	41.50	1.15	-14.04	73.10
17-JUL-2002	198.70	199.70	3.75	37.90	73.30	30.21	6.84	-16.54	300.77
13-DEC-2002	347.00	350.80	4.40	25.19	76.40	31.83	0.70	-5.36	78.46
13-FEB-2003	44.00	45.80	4.61	20.94	77.30	40.87	0.45	-15.92	276.79
5-OCT-2003	278.10	279.50	5.18	7.20	79.80	-4.95	1.15	-18.80	128.42

[a] Heliographic inertial distance, latitude and longitude of the spacecraft.
[b] Normal elevation angle with respect to the solar equatorial plane and its errors, estimated from MVA.
[c] Axis elevation angle with respect to the solar equatorial plane and azimuthal angle in RTN coordinates, estimated from MVA.

Bibliography

J. J. Aly. How much energy can be stored in a three-dimensional force-free magnetic field? *Astrophys. J.*, 375:L61, 1991.

B. J. Anderson, S. A. Fuselier, S. P. Gary, and R. E. Denton. Magnetic spectral signatures in the Earth's magnetosheath and plasma depletion layer. *J. Geophys. Res.*, 99:5877, 1994.

V. E. Andreev, A. I. Efimov, L. N. Samoznaev, I. V. Chashei, and M. K. Bird. Characteristics of coronal Alfvén waves deduced from Helios Faraday rotation measurements. *Solar Phys.*, 176:387, 1997.

S. K. Antiochos, C. R. DeVore, and J. A. Klimchuk. A model for solar coronal mass ejections. *Astrophys. J.*, 510:485, 1999.

M. Badruddin, D. Venkatesan, and B. Y. Zhu. Study and effect of magnetic clouds on the transient modulation of cosmic-ray intensity. *Solar Phys.*, 134:203, 1991.

S. J. Bame, J. R. Asbridge, W. C. Feldman, E. E. Fenimore, and J. T. Gosling. Solar wind heavy ions from flare-heated coronal plasma. *Solar Phys.*, 62:179, 1979.

G. K. Batchelor. *The Theory of Homogeneous Turbulence*. Cambridge Univ. Press, New York, 1953.

M. B. Bavassano Cattaneo, C. Basile, G. Moreno, and J. D. Richardson. Evolution of mirror structures in the magnetosheath of Saturn from the bow shock to the magnetopause. *J. Geophys. Res.*, 103:11961, 1998.

M. B. Bavassano Cattaneo, G. Moreno, G. Russo, and J. D. Richardson. MHD turbulence in Saturn's magnetosheath downstream of a quasi-parallel bow shock. *J. Geophys. Res.*, 105:23141, 2000.

J. W. Bieber, W. Wanner, and W. H. Matthaeus. Dominant two-dimensional solar wind turbulence with implications for cosmic ray transport. *J. Geophys. Res.*, 101: 2511, 1996.

M. K. Bird, E. Schrüfer, H. Volland, and W. Sieber. Coronal Faraday rotation during solar occultation of PSR0525 + 21. *Nature*, 283:459, 1980.

M. K. Bird et al. White-light and radio sounding observations of coronal transients. *Solar Phys.*, 98:341, 1985.

T. J. Bogdan, M. A. Lee, and P. Schneider. Coupled quasi-linear wave damping and stochastic acceleration of pickup ions in the solar wind. *J. Geophys. Res.*, 96:161, 1991.

G. Borrini, J. T. Gosling, S. J. Bame, and W. C. Feldman. Helium abundance enhancements in the solar wind. *Solar Phys.*, 87:7370, 1982.

V. Bothmer and R. Schwenn. The structure and origin of magnetic clouds in the solar wind. *Ann. Geophys.*, 16:1, 1998.

G. E. Brueckner et al. The Large Angle Spectroscopic Coronagraph (LASCO). *Solar Phys.*, 162:357, 1995.

G. E. Brueckner et al. Geomagnetic storms caused by coronal mass ejections (CMEs): March 1996 through June 1997. *Geophys. Res. Lett.*, 25:3019, 1998.

J. M. Burgers. *Flow Equations for Composite Gases.* Academic Press, New York, 1969.

L. F. Burlaga. Magnetic clouds and force-free fields with constant alpha. *J. Geophys. Res.*, 93:7217, 1988.

L. F. Burlaga and K. W Behannon. Magnetic clouds - Voyager observations between 2 and 4 AU. *Solar Phys.*, 81:181, 1982.

L. F. Burlaga, E. Sittler, F. Mariani, and R. Schwenn. Magnetic loop behind an interplanetary shock: Voyager, Helios and IMP 8 observations. *J. Geophys. Res.*, 86:6673, 1981.

L. F. Burlaga, N. F. Ness, and M. H. Acuña. Magnetic fields in the heliosheath: Voyager 1 observations. *Astrophys. J.*, 642:584, 2006a.

L. F. Burlaga, N. F. Ness, and M. H. Acuña. Trains of magnetic holes and magnetic humps in the heliosheath. *Geophys. Res. Lett.*, 33:L21106, 2006b.

L. F. Burlaga et al. Crossing the termination shock into the heliosheath: Magnetic fields. *Science*, 309:2027, 2005.

L. F. Burlaga et al. A magnetic cloud containing prominence material - January 1997. *J. Geophys. Res.*, 10:277, 1998.

H. V. Cane and I. G. Richardson. Interplanetary coronal mass ejections in the near-Earth solar wind during 1996-2002. *J. Geophys. Res.*, 108:1156, 2003.

P. J. Cargill, D. S. Spicer, and S. T. Zalesak. Magnetohydrodynamic simulations of Alfvénic pulse propagation in solar magnetic flux tubes: two-dimensional slab geometries. *J. Geophys. Res.*, 488:854, 1997.

P. J. Cargill, J. Schmidt, D. S. Spicer, and S. T. Zalesak. Magnetic structure of overexpanding coronal mass ejections: Numerical models. *J. Geophys. Res.*, 105: 7509, 2000.

S. A. Chandrasekhar, A. N. Kaufman, and K. M. Watson. The stability of the pinch. *Proc. Roy. Soc. London, Ser. A*, 245:435, 1958.

J. K. Chao, X. X. Zhang, and P. Song. Derivation of temperature anisotropy from shock jump relations: Theory and observations. *Geophys. Res. Lett.*, 22:2409, 1995.

I. V. Chashei, M. K. Bird, A. I. Efimov, V. E. Andreev, and L. N. Samoznaev. Five-minute magnetic field fluctuations in the solar wind acceleration region. *Solar Phys.*, 189:399, 1999.

I. V. Chashei, A. I. Efimov, L. N. Samoznaev, M. K. Bird, and M. Pätzold. The spectrum of magnetic field irregularities in the solar corona and in interplanetary space. *Adv. Space Res.*, 25:1973, 2000.

J. Chen. Theory of prominence eruption and propagation: Interplanetary consequences. *J. Geophys. Res.*, 101:27499, 1996.

G. F. Chew, M. L. Goldberger, and F. E. Low. The Boltzmann equation and the one-fluid hydromagnetic equations in the absence of particle collisions. *Proc. Roy. Soc. London, Ser. A*, 236:112, 1956.

C. Cid, M. A. Hidalgo, T. Nieves-Chinchilla, J. Sequeiros, and A. F. Viñas. Plasma and magnetic field inside magnetic clouds: A global study. *Solar Phys.*, 207:187, 2002.

P. J. Coleman Jr. Turbulence, viscosity, and dissipation in the solar-wind plasma. *Astrophys. J.*, 153:371, 1968.

N. U. Crooker and E. W. Cliver. Postmodern view of M-regions. *J. Geophys. Res.*, 99:23383, 1994.

N. U. Crooker and G. L. Siscoe. A mechanism for pressure anisotropy and mirror instability in the dayside magnetosheath. *J. Geophys. Res.*, 82:185, 1977.

N. U. Crooker, T. E. Eastman, and G. S. Stiles. Observations of plasma depletion in the magnetosheath at the dayside magnetopause. *J. Geophys. Res.*, 84:869, 1979.

A. Czaykowska, T. M. Bauer, R. A. Treumann, and W. Baumjohann. Magnetic field fluctuations across the Earth's bow shock. *Ann. Geophys.*, 19:275, 2001.

S. Dasso, C. H. Mandrini, P. Démoulin, M. L. Luoni, and A. M. Gulisano. Large scale MHD properties of interplanetary magnetic clouds. *Adv. Space Res.*, 35:711, 2005.

R. B. Decker et al. Voyager 1 in the foreshock, termination shock, and heliosheath. *Science*, 309:2020, 2005.

J. W. Dungey. Interplanetary magnetic field and the auroral zones. *Phys. Rev. Lett.*, 6:47, 1961.

A. I. Efimov, M. K. Bird, V. E. Andreev, and L. N. Samoznaev. On the detection of Alfvén waves in circumsolar plasma by radio sounding using linearly polarized signals. *Astron. Lett.*, 22:785, 1996.

N. V. Erkaev, C. J. Farrugia, H. K. Biernat, L. F. Burlaga, and G. A. Bachmaier. Ideal MHD flow behind interplanetary shocks driven by magnetic clouds. *J. Geophys. Res.*, 100:19919, 1995.

N. V. Erkaev, D. F. Vogl, and H. K. Biernat. Solution for jump conditions at fast shocks in an anisotropic magnetized plasma. *J. Plasma Phys.*, 64:561, 2000.

C. J. Farrugia, N. V. Erkaev, H. K. Biernat, L. F. Burlaga, R. P. Lepping, and V. A. Osherovich. Possible plasma depletion layer ahead of an interplanetary ejecta. *J. Geophys. Res.*, 102:7087, 1997.

W. C. Feldman, J. R. Asbridge, and S. J. Bame. The solar wind He^{2+} to H^{+} temperature ratio. *J. Geophys. Res.*, 79:2319, 1974.

E. E. Fenimore. Solar wind flows associated with hot heavy ions. *Astrophys. J.*, 235: 245, 1980.

T. G. Forbes. A review on the genesis of coronal mass ejections. *J. Geophys. Res.*, 105:23153, 2000.

T. G. Forbes et al. CME theory and models. *Space Sci. Rev.*, 123:251, 2006.

A. B. Galvin. Minor ion composition in CME-related solar wind. In N. Crooker, J. A. Joselyn, and J. Feynman, editors, *Coronal Mass Ejections, Geophysical Monograph 99*, page 253, 1997.

S. P. Gary. The mirror and the ion cyclotron anisotropy instabilities. *J. Geophys. Res.*, 97:8519, 1992.

S. P. Gary. *Theory of Space Plasma Mircroinstabilities*. Cambridge Univ. Press, New York, 1993.

S. P. Gary, M. E. McKean, D. Winske, B. J. Anderson, R. E. Denton, and S. A. Fuselier. The proton cyclotron instability and the anisotropy $/\beta$ inverse correlation. *J. Geophys. Res.*, 99:5903, 1994.

S. P. Gary, J. Wang, D. Winske, and S. A. Fuselier. Proton temperature anisotropy upper bound. *J. Geophys. Res.*, 102:27159, 1997.

S. P. Gary, R. M. Skoug, J. T. Steinberg, and C. W. Smith. Proton temperature anisotropy constraint in the solar wind: ACE observations. *Geophys. Res. Lett.*, 28:2759, 2001.

P. Ghavamian, J. Raymond, R. C. Smith, and P. Hartigan. Balmer-dominated spectra of nonradiative shocks in the Cygnus Loop, RCW 86, and Tycho supernova remnants. *Astrophys. J.*, 547:995, 2001.

M. Ghil et al. Advanced spectral methods for climatic time series. *Rev. Geophys.*, 40:1003, 2002.

S. E. Gibson and B. C. Low. A time dependent three-dimensional magnetohydrodynamic model of the coronal mass ejection. *Astrophys. J.*, 493:460, 1998.

M. L. Goldstein, D. A. Roberts, and W. H. Matthaeus. Magnetohydrodynamic turbulence in the solar wind. *Ann. Rev. Astron. Astrophys.*, 33:283, 1995.

J. T. Gosling. Coronal mass ejections and magnetic flux ropes in interplanetary space. In C. T. Russell, E. R. Priest, and L. C. Lee, editors, *Physics of Magnetic Flux Ropes, Geophysical Monograph 58*, page 343, 1990.

J. T. Gosling. The solar flare myth. *J. Geophys. Res.*, 98:18937, 1993.

J. T. Gosling. Coronal mass ejections - An overview. In N. Crooker, J. A. Joselyn, and J. Feynman, editors, *Coronal Mass Ejections, Geophysical Monograph 99*, pages 9–16, 1997.

J. T. Gosling and D. J. McComas. Field line draping about fast coronal mass ejecta: A source of strong out-of-ecliptic interplanetary magnetic fields. *Geophys. Res. Lett.*, 14:355, 1987.

J. T. Gosling, J. R. Asbridge, S. J. Bame, W. C. Feldman, and R. D. Zwickl. Observations of large fluxes of He^+ in the solar wind following an interplanetary shock. *J. Geophys. Res.*, 85:3431, 1980.

J. T. Gosling, D. J. McComas, J. L. Philips, and S. J. Bame. Geomagnetic activity associated with Earth passage of interplanetary shock disturbances and coronal mass ejections. *J. Geophys. Res.*, 96:7831, 1991.

J. T. Gosling, J. Birn, and M. Hesse. Three-dimensional magnetic reconnection and the magnetic topology of coronal mass ejection events. *Geophys. Res. Lett.*, 22:869, 1995a.

J. T. Gosling, R. M. Skoug, D. J. McComas, and C. W. Smith. Direct evidence for magnetic reconnection in the solar wind near 1 AU. *J. Geophys. Res.*, 110:A01107, 2005.

J. T. Gosling et al. A CME-driven solar wind disturbance observed at both low and high heliographic latitudes. *Geophys. Res. Lett.*, 22:1753, 1995b.

J. T. Gosling et al. Bidirectional solar wind electron heat flux events. *J. Geophys. Res.*, 92:8519, 1987.

E. W. Greenstadt and R. W. Fredricks. In L. J. Lanzerotti, C. F. Kennel, and E. N. Parker, editors, *Solar System Plasma Physics*, page 3, Amsterdam, 1979. North-Holland.

C. P. T. Groth, D. L. De Zeeuw, T. I. Gombosi, and K. G. Powell. Global three-dimensional MHD simulation of a space weather event: CME formation, interplanetary propagation, and interaction with the magnetosphere. *J. Geophys. Res.*, 105: 25053, 2000.

D. A. Gurnett and W. S. Kurth. Electron plasma oscillations upstream of the solar wind termination shock. *Science*, 309:2025, 2005.

C. M. Hammond, J. L. Phillips, S. J. Bame, E. J. Smith, and C. G. Maclennan. Ulysses observations of the planetary depletion layer at Jupiter. *Planet. Space Sci.*, 41:857, 1993.

C. M. Hammond et al. Latitudinal structure of a coronal mass ejection inferred from Ulysses and Geotail observations. *Geophys. Res. Lett.*, 22:1169, 1995.

A. Hasegawa. Drift mirror instability in the magnetosphere. *Phys. Fluids*, 12:2642, 1969.

L.-N. Hau and B. U. Ö. Sonnerup. Two-dimensional coherent structures in the magnetopause: Recovery of static equilibria from single-spacecraft data. *J. Geophys. Res.*, 104:6899, 1999.

M. W. Haurwitz and G. W. Brier. A critique of the superposed epoch analysis method: Its application to solar-weather relations. *Mon. Wea. Rev.*, 109:2074, 1981.

T. Henke et al. Ionization state and magnetic topology of coronal mass ejections. *J. Geophys. Res.*, 106:10597, 2001.

J. Heyvaerts and E. R. Priest. Thermal evolution of current sheets and flash phase of solar flares. *Solar Phys.*, 47:223, 1975.

M. A. Hidalgo, C. Cid, A. F. Viñas, and J. Sequeiros. A non-force-free approach to the topology of magnetic clouds in the solar wind. *J. Geophys. Res.*, 107:1002, 2002a.

M. A. Hidalgo, T. Nieves-Chinchilla, and C. Cid. Elliptical cross-section model for the magnetic topology of magnetic clouds. *Geophys. Res. Lett.*, 29:1637, 2002b.

P. Hill, G. Paschmann, R. A. Treumann, W. Baumjohann, N. Sckopke, and H. Lühr. Plasma and magnetic field behavior across the magnetosheath near local noon. *J. Geophys. Res.*, 100:9575, 1995.

J. Hirshberg, S. J. Bame, and D. E. Robbins. Solar flares and solar wind helium enrichments: July 1965 - July 1967. *Solar Phys.*, 23:467, 1972.

J. V. Hollweg and J. M. Turner. Acceleration of solar wind He^{++}: 3. Effects of resonant and nonresonant interactions with transverse waves. *J. Geophys. Res.*, 83:97, 1978.

J. V. Hollweg, M. K. Bird, H. Volland, P. Edenhofer, C. T. Stelzried, and B. L. Seidel. Possible evidence for coronal Alfvén waves. *J. Geophys. Res.*, 87:1, 1982.

R. A. Howard, D. J. Michels, N. R. Sheeley Jr., and M. J. Koomen. The observation of a coronal transient directed at Earth. *Astrophys. J.*, 263:L101, 1982.

R. A. Howard, J. D. Moses, and D. G. Socker. Sun-Earth connection coronal and heliospheric investigation (SECCHI). *Proc. SPIE*, 4139:259, 2000.

Q. Hu and B. U. Ö. Sonnerup. Reconstruction of magnetic clouds in the solar wind: Orientations and configurations. *J. Geophys. Res.*, 107:1142, 2002.

Y.-Q. Hu and S. R. Habbal. Resonant acceleration and heating of solar wind ions by dispersive ion cyclotron waves. *J. Geophys. Res.*, 104:17045, 1999.

P. D. Hudson. Discontinuities in an anisotropic plasma and their identification in the solar wind. *Planet. Space Sci.*, 18:1611, 1970.

A. Hundhausen. Coronal mass ejections. In K. T. Strong, J. L. R. Saba, B. M. Haisch, and J. T. Schmelz, editors, *The many faces of the sun : A summary of the results from NASA's Solar Maximum Mission*, page 143, 1999.

A. J. Hundhausen. An introduction. In N. Crooker, J. A. Joselyn, and J. Feynman, editors, *Coronal Mass Ejections, Geophysical Monograph 99*, pages 1–7, 1997.

S. O. Ifedili. The two-step Forbush decrease: An empirical model. *J. Geophys. Res.*, 109:A02117, 2004.

P. A. Isenberg and J. V. Hollweg. On the preferential acceleration and heating of solar wind heavy ions. *J. Geophys. Res.*, 88:3923, 1983.

L. Jian, C. T. Russell, J. G. Luhmann, and R. M. Skoug. Properties of interplanetary coronal mass ejections at one AU during 1995-2004. *Solar Phys.*, 239:393, 2006.

S. W. Kahler and D. V. Reames. Probing the magnetic topologies of magnetic clouds by means of solar energetic particles. *J. Geophys. Res.*, 96:9419, 1991.

J. R. Kan and D. W. Swift. Structure of the quasi-parallel bow shock - Results of numerical simulations. *J. Geophys. Res.*, 88:6919, 1983.

J. C. Kasper, A. J. Lazarus, and S. P. Gary. Wind/SWE observations of firehose constraint on solar wind proton temperature anisotropy. *Geophys. Res. Lett.*, 29: 1839, 2002.

R. L. Kaufmann, J.-T. Horng, and A. Wolfe. Large-amplitude hydrodynamic waves in the inner magnetosheath. *J. Geophys. Res.*, 75:4666, 1970.

A. V. Khrabrov and B. U. Ö. Sonnerup. DeHoffmann-Teller analysis. In G. Paschmann and P. W. Daly, editors, *Analysis Methods for Multi-Spacecraft Data*, page 221, 1998.

M. G. Kivelson and D. J. Southwood. Mirror instability II: The mechanism of nonlinear saturation. *J. Geophys. Res.*, 101:17365, 1996.

L. Klein and L. F. Burlaga. Interplanetary sector boundaries 1971 - 1973. *J. Geophys. Res.*, 85:2269, 1980.

J. L. Kohl, G. Noci, S. R. Cranmer, and J. C. Raymond. Ultraviolet spectroscopy of the extended solar corona. *Astron. Astrophy. Rev.*, 13:31, 2006.

A. N. Kolmogoroff. Dissipation of energy in the locally isotropic turbulence. *C. R. Acad., Sci. URSS*, 32:16, 1941.

R. H. Kraichnan. Inertial range of hydromagnetic turbulence. *Phys. Fluids*, 8:1385, 1965.

D. Krauss-Varban and N. Omidi. Structure of medium Mach number quasi-parallel shocks - Upstream and downstream waves. *J. Geophys. Res.*, 96:17715, 1991.

A. Kumar and D. M. Rust. Interplanetary magnetic clouds, helicity conservation, and current-core flux ropes. *J. Geophys. Res.*, 101:15667, 1996.

R. J. Leamon, C. W. Smith, N. F. Ness, W. H. Matthaeus, and H. K. Wong. Observational constraints on the dynamics of the interplanetary magnetic field dissipation range. *J. Geophys. Res.*, 103:4775, 1998a.

R. J. Leamon, C. W. Smith, and N. F. Ness. Characteristics of magnetic fluctuations within coronal mass ejections: The January 1997 event. *Geophys. Res. Lett.*, 25: 2505, 1998b.

R. J. Leamon, C. W. Smith, N. F. Ness, and H. K. Wong. Dissipation range dynamics: Kinetic Alfvén waves and the importance of β_e. *J. Geophys. Res.*, 104:22331, 1999.

M. A. Lee and W.-H. Ip. Hydromagnetic wave excitation by ionised interstellar hydrogen and helium in the solar wind. *J. Geophys. Res.*, 92:11041, 1987.

R. P. Lepping, J. A. Jones, and L. F. Burlaga. Magnetic field structure of interplanetary magnetic clouds at 1 AU. *J. Geophys. Res.*, 95:11957, 1990.

G. S. Levy, T. Sato, B. L. Seidel, C. T. Stelzried, J. E. Ohlson, and W. V. T. Rusch. Pioneer 6: Measurement of transient Faraday rotation phenomena observed during solar occultation. *Science*, 166:596, 1969.

J. Lin and T. G. Forbes. Effects of reconnection on the coronal mass ejection process. *J. Geophys. Res.*, 105:2375, 2000.

J. Lin, T. G. Forbes, P. A. Isenberg, and P. Démoulin. The effect of curvature on flux-rope models of coronal mass ejections. *Astrophys. J.*, 504:1006, 1998.

J. A. Linker, Z. Mikić, R. Lionello, P. Riley, T. Amari, and D. Odstrcil. Flux cancellation and coronal mass ejections. *Phys. Plasmas*, 10:1971, 2003.

Y. Liu, J. D. Richardson, and J. W. Belcher. A statistical study of the properties of interplanetary coronal mass ejections from 0.3 to 5.4 AU. *Planet. Space Sci.*, 53:3, 2005.

Y. Liu, J. D. Richardson, J. W. Belcher, J. C. Kasper, and H. A. Elliott. Thermodynamic structure of collision-dominated expanding plasma: Heating of interplanetary coronal mass ejections. *J. Geophys. Res.*, 111:A01102, 2006a.

Y. Liu, J. D. Richardson, J. W. Belcher, J. C. Kasper, and R. M. Skoug. Plasma depletion and mirror waves ahead of interplanetary coronal mass ejections. *J. Geophys. Res.*, 111:A09108, 2006b.

Y. Liu, J. D. Richardson, J. W. Belcher, C. Wang, Q. Hu, and J. C. Kasper. Constraints on the global structure of magnetic clouds: Transverse size and curvature. *J. Geophys. Res.*, 111:A12S03, 2006c.

Y. Liu, J. D. Richardson, J. W. Belcher, and J. C. Kasper. Temperature anisotropy in a shocked plasma: Mirror-mode instabilities in the heliosheath. *Astrophys. J.*, 659:L65, 2007a.

Y. Liu, W. B. Manchester IV, J. C. Kasper, J. D. Richardson, and J. W. Belcher. Determining the magnetic field orientation of coronal mass ejections from Faraday rotation. *Astrophys. J.*, accepted, 2007b.

R. E. Lopez. Solar cycle invariance in solar wind proton temperature relationships. *J. Geophys. Res.*, 92:11189, 1987.

R. E. Lopez and J. W. Freeman. Solar wind proton temperature-velocity relationship. *J. Geophys. Res.*, 91:1701, 1986.

B. C. Low and D. F. Smith. The free energies of partially-open coronal magnetic fields. *Astrophys. J.*, 410:413, 1993.

S. Lundquist. Magnetohydrostatic fields. *Ark. Fys.*, 2:361, 1950.

P. MacNeice, S. K. Antiochos, A. Phillips, D. S. Spicer, C. R. DeVore, and K. Olson. A numerical study of the breakout model for coronal mass ejection initiation. *Astrophys. J.*, 614:1028, 2004.

W. B. Manchester et al. Modeling a space weather event from the Sun to the Earth: CME generation and interplanetary propagation. *J. Geophys. Res.*, 109:A02107, 2004.

E. Marsch, K.-H. Mühlhäuser, H. Rosenbauer, R. Schwenn, and F. M. Neubauer. Solar wind helium ions: Observations of the Helios solar probes between 0.3 and 1 AU. *J. Geophys. Res.*, 87:35, 1982.

R. G. Marsden, T. R. Sanderson, C. Tranquille, K.-P. Wenzel, and E. J. Smith. ISEE 3 observations of low-energy proton bidirectional events and their relation to isolated interplanetary magnetic structures. *J. Geophys. Res.*, 92:11009, 1987.

W. H. Matthaeus and M. L. Goldstein. Measurements of the rugged invariance of Magnetohydrodynamic turbulence in the solar wind. *J. Geophys. Res.*, 87:6011, 1982.

W. H. Matthaeus and Y. Zhou. Extended inertial range phenomenology of magnetohydrodynamic turbulence. *Phys. Fluids B*, 1:1929, 1989.

W. H. Matthaeus, G. P. Zank, C. W. Smith, and S. Oughton. Turbulence, spatial transport, and heating of the solar wind. *Phys. Rev. Lett.*, 82:3444, 1999.

D. J. McComas, J. T. Gosling, D. Winterhalter, and E. J. Smith. Interplanetary magnetic field draping about fast coronal mass ejecta in the outer heliosphere. *J. Geophys. Res.*, 93:2519, 1988.

D. J. McComas, J. T. Gosling, C. M. Hammond, M. B. Moldwin, J. L. Phillips, and R. J. Forsyth. Magnetic reconnection ahead of a coronal mass ejection. *Geophys. Res. Lett.*, 21:1751, 1994.

D. J. McComas et al. Ulysses' return to the slow solar wind. *Geophys. Res. Lett.*, 25: 1, 1998.

R. L. McNutt Jr., J. Lyon, and C. C. Goodrich. Simulations of the heliosphere: Model. *J. Geophys. Res.*, 103:1905, 1998.

Z. Mikić and J. A. Linker. Disruption of coronal magnetic field arcades. *Astrophys. J.*, 430:898, 1994.

T. Mulligan and C. T. Russell. Multispacecraft modeling of the flux rope structure of interplanetary coronal mass ejections: Cylindrically symmetric versus nonsymmetric topologies. *J. Geophys. Res.*, 106:10581, 2001.

M. Neugebauer. The role of Coulomb collisions in limiting differential flow and temperature differences in the solar wind. *J. Geophys. Res.*, 81:78, 1976.

M. Neugebauer and R. Goldstein. Particle and field signatures of coronal mass ejections in the solar wind. In N. Crooker, J. A. Joselyn, and J. Feynman, editors, *Coronal Mass Ejections, Geophysical Monograph 99*, page 245, 1997.

M. Neugebauer, B. E. Goldstein, E. J. Smith, and W. C. Feldman. Ulysses observations of differential alpha-proton streaming in the solar wind. *J. Geophys. Res.*, 101:17047, 1996.

D. Oberoi and J. C. Kasper. LOFAR: The potential for solar and space weather studies. *Planet. Space Sci.*, 52:1415, 2004.

D. Odstrcil, P. Riley, and X. P. Zhao. Numerical simulation of the 12 May 1997 interplanetary CME event. *J. Geophys. Res.*, 109:A02116, 2004.

D. Odstrcil et al. Merging of coronal and heliospheric numerical two-dimensional MHD models. *J. Geophys. Res.*, 107:1493, 2002.

M. J. Owens, V. G. Merkin, and P. Riley. A kinematically distorted flux rope model for magnetic clouds. *J. Geophys. Res.*, 111:A03104, 2006.

E. N. Parker. Dynamical instability in an anisotropic ionized gas of low density. *Phys. Rev.*, 109:1874, 1958.

M. Pätzold and M. K. Bird. The Pioneer 6 Faraday rotation transients - On the interpretation of coronal Faraday rotation data. *Geophys. Res. Lett.*, 25:2105, 1998.

M. Pätzold, M. K. Bird, H. Volland, G. S. Levy, B. L. Seidel, and C. T. Stelzried. The mean coronal magnetic field determined from Helios Faraday rotation measurements. *Solar Phys.*, 109:91, 1987.

K. I. Paularena, C. Wang, R. von Steiger, and B. Heber. An ICME observed by Voyager 2 at 58 AU and by Ulysses at 5 AU. *Geophys. Res. Lett.*, 28:2755, 2001.

O. A. Pokhotelov, M. A. Balikhin, R. Z. Sagdeev, and R. A. Treumann. Comment on "Theory and observations of slow-mode solitons in space plasmas". *Phys. Rev. Lett.*, 95:129501, 2005.

M. H. Prager and J. M. Hoenig. Superposed epoch analysis: A randomization test of environmental effects on recruitment with application to chub Mackerel. *Trans. Amer. Fish. Soc.*, 118:608, 1989.

C. P. Price, D. W. Swift, and L. C. Lee. Numerical simulation of nonoscillatory mirror waves at the Earth's magnetosheath. *J. Geophys. Res.*, 91:101, 1986.

D. B. Reisenfeld et al. Helium energetics in the high-latitude solar wind: Ulysses observations. *J. Geophys. Res.*, 106:5693, 2001.

I. G. Richardson and H. V. Cane. Identification of interplanetary coronal mass ejections at 1 AU using multiple solar wind plasma composition anomalies. *J. Geophys. Res.*, 109:A09104, 2004.

I. G. Richardson and H. V. Cane. Signatures of shock drivers in the solar wind and their dependence on the solar source location. *J. Geophys. Res.*, 98:15295, 1993.

I. G. Richardson and H. V. Cane. Regions of abnormally low proton temperature in the solar wind (1965-1991) and their association with ejecta. *J. Geophys. Res.*, 100:23397, 1995.

J. D. Richardson, K. I. Paularena, C. Wang, and L. F. Burlaga. The life of a CME and the development of a MIR: From the Sun to 58 AU. *J. Geophys. Res.*, 107: 1041, 2002.

J. D. Richardson, Y. Liu, and J. W. Belcher. Propagation and evolution of ICMEs in the solar wind. In J.-A. Sauvaud and Z. Němeček, editors, *Multiscale Processes in the Earth's Magnetosphere: From Interball to Cluster, NATO Sci. Ser. II, Math., Phy. Chem.*, page 1, 2004.

J. D. Richardson, Y. Liu, C. Wang, and L. F. Burlaga. ICMES at very large distances. *Adv. Space Res.*, 38:528, 2006.

P. Riley and N. U. Crooker. Kinematic treatment of coronal mass ejection evolution in the solar wind. *Astrophys. J.*, 600:1035, 2004.

P. Riley et al. Using an MHD simulation to interpret the global context of a coronal mass ejection observed by two spacecraft. *J. Geophys. Res.*, 108:1272, 2003.

P. Riley et al. Fitting flux ropes to a global MHD solution: A comparison of techniques. *J. Atmos. Sol. Terr. Phys.*, 66:1321, 2004.

C. T. Russell and T. Mulligan. On the magnetosheath thicknesses of interplanetary coronal mass ejections. *Planet. Space Sci.*, 50:527, 2002.

C. T. Russell, R. P. Lepping, and C. W. Smith. Upstream waves at Uranus. *J. Geophys. Res.*, 95:2273, 1990.

J. E. Salah, C. J. Lonsdale, D. Oberoi, R. J. Cappallo, and J. C. Kasper. Space weather capabilities of low frequency radio arrays. *Proc. SPIE*, 5901:124, 2005.

K. Schindler, D. Pfirsch, and H. Wobig. Stability of two-dimensional collision-free plasmas. *Phys. Plasmas*, 15:1165, 1973.

R. W. Schunk. Mathematical structure of transport equations for multispecies flows. *Rev. Geophys. Space Phys.*, 15:429, 1977.

G. M. Simnett. The relationship between prominence eruptions and coronal mass ejections. *J. Atmos. Sol. Terr. Phys.*, 62:1479, 2000.

R. M. Skoug et al. Radial variation of solar wind electrons inside a magnetic cloud observed at 1 and 5 AU. *J. Geophys. Res.*, 105:27269, 2000.

C. W. Smith, W. H. Matthaeus, G. P. Zank, N. F. Ness, S. Oughton, and J. D. Richardson. Heating of the low-latitude solar wind by dissipation of turbulent magnetic fluctuations. *J. Geophys. Res.*, 106:8253, 2001.

B. U. Ö. Sonnerup and L. J. Cahill Jr. Magnetopause structure and attitude from Explorer 12 observations. *J. Geophys. Res.*, 72:171, 1967.

B. U. Ö. Sonnerup and M. Scheible. Minimum and maximum variance analysis. In G. Paschmann and P. W. Daly, editors, *Analysis Methods for Multi-Spacecraft Data*, page 185, 1998.

D. J. Southwood and M. G. Kivelson. Mirror instability: 1. Physical mechanism of linear instability. *J. Geophys. Res.*, 98:9181, 1993.

L. Spitzer Jr. *Physics of Fully Ionized Gases*. Interscience, New York, 2nd edition, 1962.

O. C. St. Cyr et al. Properties of coronal mass ejections: SOHO LASCO observations from January 1996 to June 1998. *J. Geophys. Res.*, 105:18169, 2000.

K. Stasiewicz. Reinterpretation of mirror modes as trains of slow magnetosonic solitons. *Geophys. Res. Lett.*, 31:L21804, 2004.

C. T. Stelzried et al. The quasi-stationary coronal magnetic field and electron density as determined from a Faraday rotation experiment. *Solar Phys.*, 14:440, 1970.

T. H. Stix. *The Theory of Plasma Waves*. McGraw-Hill, New York, 1962.

E. C. Stone et al. Voyager 1 explores the termination shock region and the heliosheath beyond. *Science*, 309:2017, 2005.

P. A. Sturrock. Maximum energy of semi-infinite magnetic field configurations. *Astrophys. J.*, 380:655, 1991.

P. A. Sturrock. *Plasma Physics: An Introduction to the Theory of Astrophysical, Geophysical and Laboratory Plasmas*. Cambridge Univ. Press, New York, 1994.

S. T. Suess. Magnetic clouds and the pinch effect. *J. Geophys. Res.*, 93:5437, 1988.

Z. Švestka. On 'The solar flare myth' postulated by Gosling. *Solar Phys.*, 160:53, 1995.

B. T. Tsurutani, D. J. Southwood, E. J. Smith, and A. Balogh. Nonlinear magnetosonic waves and mirror mode structures in the March 1991 Ulysses interplanetary event. *Geophys. Res. Lett.*, 19:1267, 1992.

M. Vandas and E. P. Romashets. A force-free field with constant alpha in an oblate cylinder: A generalization of the Lundquist solution. *Astron. Astrophys.*, 398:801, 2003.

M. Vandas, S. Fischer, P. Pelant, and A. Geranios. Spheroidal models of magnetic clouds and their comparison with spacecraft measurements. *J. Geophys. Res.*, 98: 11467, 1993a.

M. Vandas, S. Fischer, P. Pelant, and A. Geranios. Evidence for spheroidal structure of magnetic clouds. *J. Geophys. Res.*, 98:21061, 1993b.

V. M. Vasyliunas and G. L. Siscoe. On the flux and energy spectrum of interstellar ions in the solar system. *J. Geophys. Res.*, 81:1247, 1976.

A. F. Viñas and J. D. Scudder. Fast and optimal solution to the 'Rankine-Hugoniot problem'. *J. Geophys. Res.*, 91:39, 1986.

L. Violante, M. B. Bavassano Cattaneo, G. Moreno, and J. D. Richardson. Observations of mirror waves and plasma depletion layer upstream of Saturn's magnetopause. *J. Geophys. Res.*, 100:12047, 1995.

M. F. Vogt, C. M. S. Cohen, P. Puhl-Quinn, V. K. Jordanova, C. W. Smith, and R. M. Skoug. Space weather drivers in the ACE era. *Space Wea.*, 4:S09001, 2006.

C. Wang and J. D. Richardson. Interplanetary coronal mass ejections observed by Voyager 2 between 1 and 30 AU. *J. Geophys. Res.*, 109:A06104, 2004.

C. Wang, J. D. Richardson, and J. T. Gosling. A numerical study of the evolution of the solar wind from Ulysses to Voyager 2. *J. Geophys. Res.*, 105:2337, 2000.

C. Wang, J. D. Richardson, and K. I. Paularena. Predicted Voyager observations of the Bastille Day 2000 coronal mass ejection. *J. Geophys. Res.*, 106:13007, 2001.

D. F. Webb. CMEs and the solar cycle variation in their geoeffectiveness. In A. Wilson, editor, *Proceedings of the SOHO 11 Symposium on "From Solar Min to Max: Half a Solar Cycle with SOHO"*, pages 409–419, 2002.

D. F. Webb. The solar sources of coronal mass ejections. In Z. Švestka, B. V. Jackson, and M. E. Machado, editors, *Eruptive Solar Flares*, page 234, 1992.

D. F. Webb, S. W. Kahler, P. S. McIntosh, and J. A. Klimchuck. Large-scale structures and multiple neutral lines associated with coronal mass ejections. *J. Geophys. Res.*, 102:24161, 1997.

D. F. Webb, E. W. Cliver, N. U. Crooker, O. C. St. Cry, and B. J. Thompson. Relationship of halo coronal mass ejections, magnetic clouds, and magnetic storms. *J. Geophys. Res.*, 105:7491, 2000.

D. F. Webb, M. Tokumaru, B. V. Jackson, and P. P. Hick. Study of ICME structure using LASCO white light and STE Lab IPS observations of halo CMEs. *EOS*, 82: F1001, 2001.

D. R. Weimer et al. Variable time delays in the propagation of the interplanetary magnetic field. *J. Geophys. Res.*, 107:A81210, 2002.

Y. C. Whang, L. F. Burlaga, Y.-M. Wang, and N. R. Sheeley. The termination shock near 35° latitude. *Geophys. Res. Lett.*, 31:L03805, 2004.

L. L. Williams and G. P. Zank. Effect of magnetic field geometry on the wave signatures of the pickup ions of interstellar neutrals. *J. Geophys. Res.*, 99:19229, 1994.

D. Winterhalter, M. Neugebauer, B. E. Goldstein, E. J. Smith, S. J. Bame, and A. Balogh. Ulysses field and plasma observations of magnetic holes in the solar wind and their relation to mirror-mode structures. *J. Geophys. Res.*, 99:23371, 1994.

R. Woo. Evidence for the reversal of magnetic field polarity in coronal streamers. *Geophys. Res. Lett.*, 24:97, 1997.

S. T. Wu, W. P. Guo, S. P. Plunkett, B. Schmieder, and G. M. Simnett. Coronal mass ejections (CMEs) initiation: models and observations. *J. Atmos. Sol. Terr. Phys.*, 62:1489, 2000.

M. Zhang, L. Golub, E. DeLuca, and J. Burkepile. The timing of flares associated with the two dynamical types of solar coronal mass ejections. *Astrophys. J.*, 574: L97, 2002.

T. H. Zurbuchen and I. Richardson. In-situ solar wind and magnetic field signatures of interplanetary coronal mass ejections. *Space Sci. Rev.*, 123:31, 2006.

B. J. Zwan and R. A. Wolf. Depletion of solar wind plasma near a planetary boundary. *J. Geophys. Res.*, 81:1636, 1976.